

CONVECTIVE HEAT TRANSFER AND EXPERIMENTAL ICING AERODYNAMICS OF WIND TURBINE BLADES

By

Xin Wang

B.A. Sc. (Engineering) North China Electric Power University, 1989

M.A. Sc. (Engineering) Xi'an Jiaotong University, 1996

**A THESIS SUBMITTED IN PARTIAL FULFILMENT OF
THE REQUIREMENTS FOR THE DEGREE OF
DOCTOR OF PHILOSOPHY**

In

**THE FACULTY OF GRADUATE STUDIES
DEPARTMENT OF MECHANICAL AND
MANUFACTURING ENGINEERING**

UNIVERSITY OF MANITOBA

August, 2008

Copyright © Xin Wang 2008

Abstract

The total worldwide base of installed wind energy peak capacity reached 94 GW by the end of 2007, including 1846 MW in Canada. Wind turbine systems are being installed throughout Canada and often in mountains and cold weather regions, due to their high wind energy potential. Harsh cold weather climates, involving turbulence, gusts, icing and lightning strikes in these regions, affect wind turbine performance. Ice accretion and irregular shedding during turbine operation lead to load imbalances, often causing the turbine to shut off. They create excessive turbine vibration and may change the natural frequency of blades as well as promote higher fatigue loads and increase the bending moment of blades. Icing also affects the tower structure by increasing stresses, due to increased loads from ice accretion. This can lead to structural failures, especially when coupled to strong wind loads. Icing also affects the reliability of anemometers, thereby leading to inaccurate wind speed measurements and resulting in resource estimation errors. Icing issues can directly impact personnel safety, due to falling and projected ice. It is therefore important to expand research on wind turbines operating in cold climate areas. This study presents an experimental investigation including three important fundamental aspects: 1) heat transfer characteristics of the airfoil with and without liquid water content (LWC) at varying angles of attack; 2) energy losses of wind energy while a wind turbine is operating under icing conditions; and 3) aerodynamic characteristics of an airfoil during a simulated icing event. A turbine scale model with curved 3-D blades and a DC generator is tested in a large refrigerated wind tunnel, where ice formation is simulated by spraying water droplets. A NACA 63421 airfoil is used to study the characteristics of aerodynamics and convective heat transfer. The current, voltage, rotation of the DC generator and temperature distribution along the airfoil, which are used to calculate heat transfer coefficients, are measured using a Data Acquisition (DAQ) system and recorded with LabVIEW software. The drag, lift and moment of the airfoil are measured by a force balance system to obtain the aerodynamics of an iced airfoil. This research also quantifies the power loss under various icing conditions. The data obtained can be used to valid numerical data method to predict heat transfer characteristics while wind turbine blades worked in cold climate regions.

Table of contents

Abstract	I
Table of contents	II
Table of figures	V
Tables	X
Nomenclature	XI
Acknowledgements	XIV
Chapter 1	1
1.1 Background	1
1.1.1. Developing wind energy in the world	1
1.1.2. Effects of icing on wind energy	4
1.1.3. Ice types in cold climates	5
1.2 Objectives	9
1.3 Methodology	10
Chapter 2	16
2.1 Weather conditions for wind energy applications	17
2.2 The technology development of wind energy	19
2.3 Aerodynamics of wind turbine blades	21
2.3.1 Airfoils applied in wind turbines	21
2.3.2 The range of Reynolds number in the aerodynamics study	22
2.4 Design and application of wind turbine blades	23
2.5 Aerodynamics of the airfoils	25
2.5.1 Simulation of aerodynamics and theoretical study of airfoils	25
2.5.2 Experimental study of aeroelastics of airfoils	26
2.6 Aerodynamic study of wind turbines	29
2.6.1 Investigation of wind turbine blades	29
2.6.2 Flow characteristics study of wind turbines	30
2.7 Icing of wind turbines and blades	31

2.7.1	Operation of wind turbines under cold climates	31
2.7.2	Icing of airfoils on aircraft	33
2.7.3	Investigation of wind turbine blades with ice	36
2.8	Research on anti-icing and de-icing for wind turbine blades	38
2.8.1	Simulation study.....	38
2.8.2	Application of anti-icing or de-icing methods	39
2.9	Convective heat transfer	41
2.9.1	Correlation of heat transfer without droplets	41
2.9.2	Analytical and numerical convection heat transfer	42
2.9.3	Experimental procedures of convection heat transfer	43
2.9.4	Characteristics of water droplet spray	45
2.9.5	Multi-phase convective heat transfer	47
2.10	Operation of wind turbines.....	48
2.11	Summary	52
Chapter 3	55
3.1	Icing wind tunnel and instrumentation.....	56
3.1.1	Overall capability and sub-system components	56
3.1.2	Water spray system	59
3.2	HAWT with 3-D twisted blade operation under icing conditions.....	61
3.2.1	Fabrication of small wind turbine model	61
3.2.2	Measurement of rotation, current and voltage	65
3.3	Aerodynamic force characterization during icing.....	69
3.3.1	Force balance measurements.....	69
3.3.2	Aerodynamics measurements.....	72
3.4	Convective heat transfer characterization of wind blades.....	75
3.4.1	Setup of heat transfer for an airfoil	75
3.4.2	Temperature measurements.....	78
3.4.3	Test procedures and analysis.....	80
Chapter 4	82
4.1	Characteristics of the 3-blade wind turbine model.....	82
4.2	Ice thickness over the wind turbine blades.....	86

4.3 Glaze ice over wind turbine.....	87
4.4 Power losses with rime iced blades.....	91
4.5 Summary	96
Chapter 5	98
5.1 Cylinder measurements	99
5.2 Ice shapes on an airfoil.....	103
5.3 Aerodynamics of the iced airfoil.....	111
5.4 Discussion of iced wind turbine results.....	117
Chapter 6	120
6.1 Heat transfer characterization at 0 AOA	121
6.1.2 Sensitivity study for correlation coefficients	125
6.1.3 Comparison with past methods	128
6.2 Nusselt number at varying AOA.....	133
6.3 Heat transfer characterization with water droplets at 0 AOA	141
6.4 Modified hilpert correlation with LWC at varying AOA.....	148
6.5 Summary	159
Chapter 7	161
7.1 Conclusions	161
7.2 Recommendations for future research.....	164
References	166
Appendix A – Lists of published papers	187
Appendix B – Measurement uncertainties	189
Appendix C – Operation manual for force balance (A).....	192
Appendix D – Operation manual for force balance (B)	195

Table of figures

Figure 1.1: Growth rate of annual and cumulative installed capacities of world wind power (1999-2006) [2]	2
Figure 1.2: Global forecast (2005-2010) of annual installed and cumulate capacity (GW)	2
Figure 1.3: Distribution of icing and low temperature related consequences in Finland 1996-2002 [5].	5
Figure 1.4: Glaze ice in icing tunnel: a) rotating propellers and b) a wind turbine blade model	6
Figure 1.5: Simulated icing event showing rime ice: a) airfoil (icing phase) and b) cylinder (post icing).....	8
Figure 1.6: Icing event showing the pre-icing, icing and post icing regions	10
Figure 2.1: Wind turbines operating in cold or icing climates	17
Figure 2.2: Distribution of high wind speed regions in Manitoba [11].....	18
Figure 2.3: Severe Icing Map – From Manitoba Hydro.....	19
Figure 2.4: Growth in size and capacity of wind turbine design.....	20
Figure 3.1: Top view of wind tunnel.....	57
Figure 3.2: Side View of spray flow / ice tunnel.....	57
Figure 3.3: Nozzle distribution with heaters and thermocouples inside spray bar.....	59
Figure 3.4: Spray bar in the icing wind tunnel	60
Figure 3.5: Water flowmeter and air pressure controller.	61
Figure 3.6: Digitized blade: a) smooth blade and b) blade before smoothing	62
Figure 3.7: a) a blade model at 0 pitch angle and b) blades with adaptors.	63
Figure 3.8: a) hub and b) hub center	64

Figure 3.9: Wind turbine model with DC generator in the wind tunnel	65
Figure 3.10: Circuit diagram of current and voltage transducer with DC generator.....	67
Figure 3.11: PC-based data acquisition system.....	68
Figure 3.12: Structure of the side wall force balance.....	69
Figure 3.13: Side view of one balance wall with a shaft coupler.....	69
Figure 3.14: Data acquisition system: HBM MGC Plus and a Laptop	70
Figure 3.15: Acquisition of data from FMS force measurement system	71
Figure 3.16: Tunnel setup for icing of airfoil measurements	71
Figure 3.17: NACA 63421 airfoil with thermocouple locations (note: dimensions in mm).....	77
Figure 3.18: Test airfoil with a heater and thermocouples.....	77
Figure 3.19: Block panel of LabVIEW: temperature, voltage and frequency measurement	78
Figure 3.20: The front panel of Temperature, rotation and voltage measuring with LabView 8.	79
Figure 4.1: Power output at different pitch angles	83
Figure 4.2: Rotation at different pitch angles.....	84
Figure 4.3: Power output at different temperatures.....	85
Figure 4.4: Rotation variation at different temperatures	85
Figure 4.5: Glaze ice over a wind turbine	88
Figure 4.6: Icing of blades at -2°C for 2, 5 and 10 minutes	88
Figure 4.7: Comparison power losses for different ice thicknesses.....	89
Figure 4.8: Comparison rotation for different ice thicknesses	90
Figure 4.9: Power output and 4.2 mm ice thickness	91
Figure 4.10: Rime ice on the wind turbine blade	92

Figure 4.11: Power losses at extreme icing conditions	94
Figure 4.12: Rotation of the turbine working on extreme weather condition for different ice thicknesses	94
Figure 4.13: Wind energy losses under -20°C: a) power output; b) rotation	95
Figure 5.1: Shorter cylinder installed in the wind tunnel with force balance and shaft protectors	99
Figure 5.2: C_D of different diameter cylinders as a function of Reynolds numbers.....	100
Figure 5.3: Comparison with short and long cylinders for C_L and C_D	101
Figure 5.4: Rime iced cylinder at -9°C, 0.8 g/m ³ and 10 m/s at 30 minutes spraying	102
Figure 5.5: Two airfoils in tandem installed in the icing wind tunnel	103
Figure 5.6: Left side of the force balance with a camera	104
Figure 5.7: Photograph of an iced airfoil at -9°C, 10 m/s and 0.8 g/m ³	105
Figure 5.8: Ice shape over the airfoil at -9°C, 10 m/s and 0.8 g/m ³ during 45 minutes	106
Figure 5.9: Aerodynamics of iced airfoils with glaze ice at various AOA	113
Figure 5.10: Aerodynamics of iced airfoils with rime ice at various AOA and spraying duration: a) AOA = 0° & 6°; b) AOA = 3° & 9° with 0.8 g/m ³ LWC at 10 m/s wind speed	115
Figure 6.1: Average Nusselt number at varying Reynolds and Prandtl numbers	122
Figure 6.2: Normalized Nusselt function correlation.....	124
Figure 6.3: Local Nusselt number at varying chord positions (x/c).....	124
Figure 6.4: Average Nusselt number at varying a) c and b) m ($Re_c \leq 5 \times 10^5$)	126
Figure 6.5: Average Nusselt number at varying a) c and b) m ($Re_c > 5 \times 10^5$)	127
Figure 6.6: Local Nusselt number for cylinder and airfoil cases	129
Figure 6.7: Comparison between NACA airfoil, flat plate and circular cylinder results.....	132

Figure 6.8: Local Nusselt number distribution along dimensionless chord: a) low Re , and b) high Re	135
Figure 6.9: Measured data and Nusselt number correlation at various AOA (high Re_c)	136
Figure 6.10: Measured data and Nu correlation at 10° AOA (low Re_c).....	137
Figure 6.11: Measured data and Nu correlation at varying AOA from 5° to 25° (low Re_c)...	137
Figure 6.12: Comparison of measured data dotted at 10° and Nu correlations at 0° & 10° AOA	140
Figure 6.13: Comparison of experimental data with LWC and Nusselt function correlations without LWC: a) high Re and b) low Re	142
Figure 6.14: Local Nusselt number at varying chord positions (x/c).....	144
Figure 6.15: Predicted and measured Nu a) without and b) with droplets for $Re_c (1+W) > 6 \times 10^5$	145
Figure 6.16: Predicted and measured Nu a) without and b) with droplets for $Re_c (1+W) \leq 6 \times 10^5$	146
Figure 6.17: Measured data and predicted Nu correlation at a) high Re_c and b) low Re_c at 15° AOA	150
Figure 6.18: Comparison of measured data with LWC and Nu correlations without LWC at 15° AOA, as well as the predicted Nu correlation with LWC at 0° AOA	152
Figure 6. 19: Nusselt number at a) low and b) high Reynolds numbers with LWC at varying AOA	154
Figure 6.20: Predicted and measured Nu with droplets for $Re_c (1+W) > 6 \times 10^5$ at 15° AOA	157
Figure 6.21: Measured date and predicted Nu with droplets at varying angles of attack for high $Re_c (1+W)$	158

Figure 6.22: Predicted and measured Nu with droplets for $Re_c (1+W) \leq 6 \times 10^5$ at 15° AOA 158

Figure 6.23: Predicted and measured Nu with droplets for $Re_c (1+W) \leq 6 \times 10^5$ at varying AOA

..... 159

Tables

Table 1.1: Canada's wind energy Tracker by July 2007	3
Table 1.2: 'Ice Alarm' indication from Manitoba Hydro's System Control Centre 1999- 2006....	14
Table 3.1: Test content in the investigation	55
Table 3.2: Standard deviation of calibration results (6×39 Non-Iterative)	70
Table 3.3: Past literature for airfoils and range of Reynolds numbers.....	73
Table 3.4: Heat transfer and simulated icing conditions	75
Table 4.1: Wind turbine operating conditions.....	82
Table 4.2: Glaze ice thicknesses over the wind turbine blades (-3°C) (mm).....	86
Table 4.3: Rime ice thicknesses over the wind turbine blades (-10°C) (mm)	87
Table 4.4: Ice thicknesses at -20°C and -30°C on the wind turbine blades (mm)	87
Table 5.1: Icing conditions for aerodynamics studies.....	98
Table 5.2: Photos of glaze ice at various AOAs and spraying times at -5°C and 10 m/s	107
Table 5.3: Glaze ice shapes at various AOA and spraying duration at -5°C and 10 m/s	108
Table 5.4: Pictures of rime ice at various AOA and spraying duration at -9°C and 10 m/s	109
Table 5.5: Rime ice shapes at various AOA and spraying duration at -9°C and 10 m/s.....	110
Table 5.6: Data of ΔC_L , ΔC_D and ΔC_m at -5°C (0.8 g/m^3 LWC and 10 m/s wind speed).....	112
Table 5.7: Rime ice aerodynamics of the iced airfoil at tunnel temperature -9°C	113
Table 6.1: Experimental conditions during convective heat transfer.....	121
Table 6.2: The range of Prandtl numbers in the experiments	121

Nomenclature

c	chord of airfoil (m)
C_1, C_2	chord coefficient
C_D	drag coefficient
C_L	lift coefficient
c_m	moment center (m)
C_m	moment coefficient
D	diameter of wind turbine m,
D_1, D_2, D_3, D_4	arc angle coefficients
F_X	force in the X axis direction (N)
F_Z	measured force in the Z axis direction (N)
F_D	drag force (N)
F_L	lift force (N)
h_i	local convective heat transfer coefficient (W/m^2K)
\bar{h}	average heat transfer coefficient (W/m^2K)
i	local measurement point in the 2-D airfoil
k	thermal conductivity (W/mK)
k	height of ice (m)
K	dimensionless shear parameter
L	span of airfoil (m)
M_1, M_2, M_3	ice thickness at the middle of wind turbine No. 1, 2, 3 blades (mm)
M	moment (Nm)

Nu_x	local Nusselt number
\overline{Nu}	average Nusselt number
P	power output of the 3-blade wind turbine (W)
Pr	Prandtl number
P^*, P_{\max}^*	maximum power output of the 3-blade wind turbine at 20°C temperature (W)
q_{con}	convective heat flux (W)
q_{cd}	conductive heat flux (W)
R^2	curve regression coefficient
Re_c	Reynolds number (based on a chord reference length)
Re_D	Reynolds number (based on a diameter of the 3-blade wind turbine)
Re_m	Multiphase Reynolds number
Re_L	Reynolds number (based on a length of a flat plate)
Re_x	Reynolds number (based on a local position of a flat plate)
R_1, R_2, R_3	ice thickness at the root of wind turbine No.1, 2, 3 blades (mm)
s	circumference of the 2-D airfoil model
s	position of ice on an airfoil surface (m)
s_i	distance between two measurement points in the 2-D airfoil
T_{∞}	freestream temperature (°C)
T_{in}	inner surface temperature of airfoil (°C)
T_o	outer surface temperature of airfoil (°C)
W	non-dimensional liquid water content
u_{∞}	velocity of free stream m/s
AOA	angle of attack (°)

ANN	artificial neural networks
CFD	computational fluid dynamics
CHF	critical heat flux (W/m^2)
HTC	heat transfer coefficient
LCE	local collision efficiency
LWC	liquid water content (g/m^3)
MVD	mean volume diameter (μm)
NACA	National Advisory Committee for Aeronautics
NASA	National Aeronautics and Space Administration
NAG	numerical algorithms group
NREL	National Renewable Energy Laboratory
PDA	laser phase-doppler anemometry
PIV	particle image velocimetry
RPM	rotation of the 3-blade wind turbine (Hz)
RPM*	maximum rotation of the 3-blade wind turbine at 20°C temperature
TSR	tip speed ratio

Greek Symbol

μ	dynamic viscosity of air (kg/ms)
ρ	density of air (kg/m^3)
δ	average thickness of the airfoil (mm)
δ	ice thickness over the blades (mm)
α	angle of attack ($^\circ$)

Acknowledgements

My first and most earnest acknowledgment must go to my advisors: Dr. E.L. Bibeau and Dr. G.F. Naterer. Dr. Naterer and Dr. Bibeau have been instrumental in ensuring my academic, professional, financial and moral well being ever since I started to work with them. In every sense, none of this work would have been possible without them. They gave excellent advice to me about this research project and written thesis. Many thanks also to committee members Dr. J. Hanesiak and Dr. S. J. Ormiston. The financial support of the Natural Sciences and Research Council of Canada (NSERC), Manitoba Hydro NSERC Chair in Alternative Energy, Tier 1 Canada Research Chair in Advanced Energy Systems and the Canada Foundation for Innovation (CFI) are gratefully appreciated.

Far too many people to mention individually have assisted in so many ways during my research work at UM. They all have my sincere gratitude. In particular, I would like to thank Dr. Qingjin Peng for providing assistance in reverse engineering for a blade model, Mr. Qing Sun for help in experimental and research assistance, and technical help provided by Mr. Bruce Ellis and Mr. Paul Krueger.

I also wish to thank my family and friends for their encouragement and support. My final, and most heartfelt acknowledgment must go to my wife Xiaofei Pang who has worked diligently and successfully. Her support, encouragement, and companionship have converted my journey through graduate school into a pleasure.

Chapter 1

Introduction

1.1 Background

1.1.1. Developing wind energy in the world

Climate change could become one of the most important problems this century. Efforts must be made by all countries to reduce industrialized GHG emissions by at least 30% by 2020 according to calculations by the European Wind Energy Association [1] to keep the global mean temperature rise below 2°C. Many countries, including Canada, are developing wind power generation capacity to meet the rising demand for energy using renewable power. Figure 1.1 shows the annual growth in the world wind power market from 1999 to 2006 [2]. It is predicted that the total installed capacity of wind energy will increase to 135 GW worldwide and reach an average growth rate of 19.1% by 2010 as compared to the average 24.3% growth rate from 2002 to 2006 [2].

Figure 1.2 exhibits the planned growth rate from 2005 to 2010 [3] in the world. Comparing the capacity of the planned and installed capacities in 2005 and 2006, it can be found that global wind energy has developed faster than anticipated and this will be a booming industry for many years.

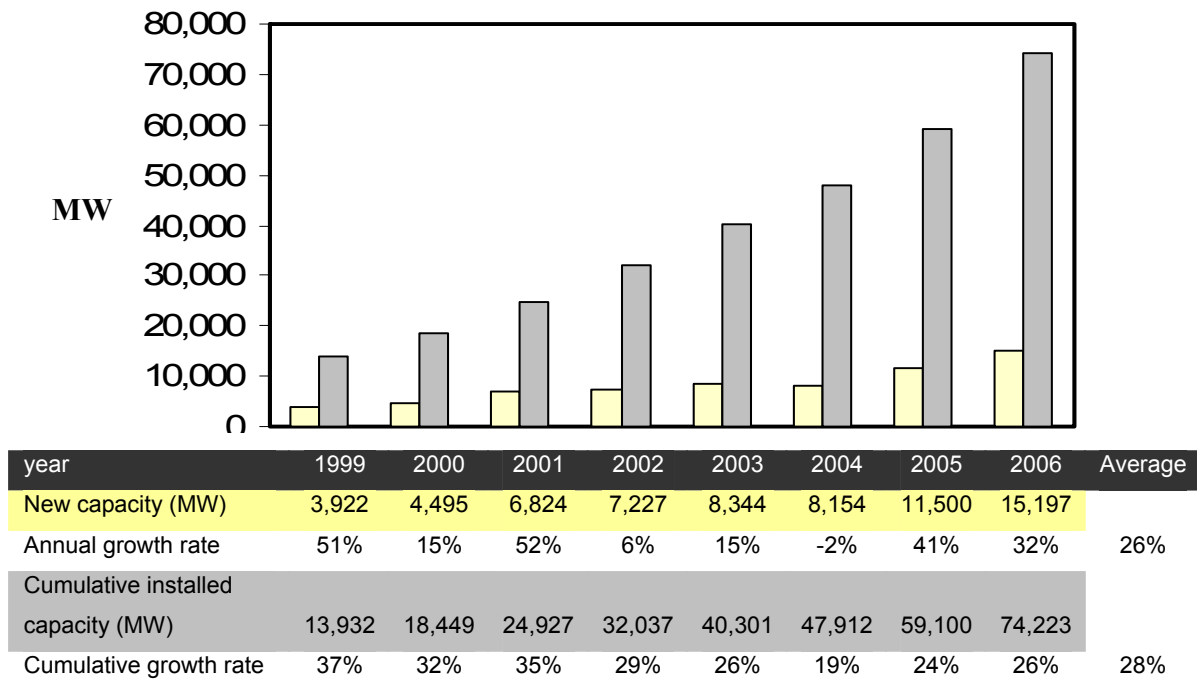


Figure 1.1: Growth rate of annual and cumulative installed capacities of world wind power (1999 – 2006) [2]

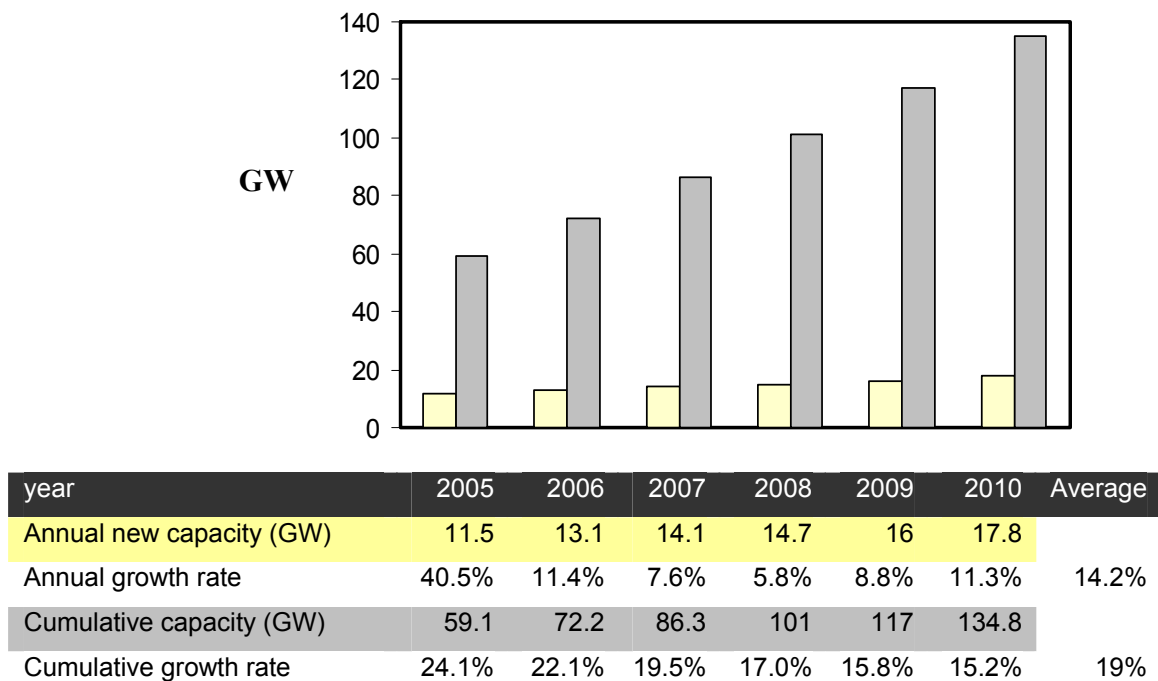


Figure 1.2: Global forecast (2005-2010) of annual installed and cumulate capacity (GW)

The previous figures provide an indication of projected wind energy capacity and a global outlook. Canada has a strong potential for wind energy development. Wind turbine systems are being installed throughout Canada and often in mountains and cold weather regions. The Canadian Federal Government expanded its Wind Power Incentive Program in the 2005 budget to support the development of an additional 4,000 MW of wind energy by 2010 [3]. Furthermore, from the GWEA 2007 annual report, Canada's provincial governments have now set targets and objectives for wind energy development that will have a minimum total of 12,000 MW by 2016 [2]. This includes wind energy in cold weather areas, such as Manitoba, which plans to develop 1,000 MW wind energy capacity from 2009 to 2014, according to the Manitoba Provincial Government. This can be compared with Quebec, which forecasts about 3,500 MW of wind energy by 2012 to offset the shortfall in power supply. Table 1.1 shows Canada's wind tracker by July 2007 [4]. It can be found that more and more wind energy facilities will be installed in cold and icing climate areas in Canada.

Table 1.1: Canada's wind energy Tracker by July 2007

Province	Installed	Proposed*
BC	0	325.2 MW
Alberta	442.6 MW	80.0 MW
Saskatchewan	171.2 MW	24.8 MW
Manitoba	103.9 MW	0.0 MW
Ontario	415.3 MW	1014.8 MW
Quebec	321.8 MW	1095.0 MW
Newfoundland	390.0 KW	51.0 MW
PEI	72.4 MW	79.2 MW
Nova Scotia	59.3 MW	1.2 MW
New Brunswick	0.0	96.0 MW
Yukon	810.0 kW	0.0
NWT	0.0	0.0
Nunavut	0.0	0.0
Total	1587.6 MW	2767.1 MW

*Under construction or awarded a PPA

1.1.2. Effects of icing on wind energy

Climatic conditions with turbulence, gusts, icing and lightning strikes in cold regions will affect wind turbine performance and cause idling of wind farms on windy days. In particular, ice accretion and irregular shedding during turbine operation cause large load imbalances as well as excessive turbine vibration. They can change the natural frequency of blades, promote higher fatigue loads, and increase the bending moment of blades. Icing affects the tower structure by increasing stresses due to increased loads from ice accretion. This can lead to structural failures, especially when coupled with strong wind loads. Icing also affects the reliability of anemometers and sensors, thereby leading to inaccurate wind speed measurements, thereby resulting in resource estimation errors. These icing issues can directly impact personnel safety due to falling ice. Figure 1.3 shows that the distribution of icing and low temperature related consequences in Finland from 1996 – 2002 included a total of 12,629 hours [5]. Ronsten [6] also reported a stoppage of over 7 weeks of a wind turbine due to icing, during the best operating period in southern Sweden. These facts show icing and cold conditions will in some cases significantly affect the operation of the wind turbines installed, or that will be serviced in the cold climate such as North America and North Europe. Also, a total 71% of consequences, including 54% iced wind turbine blades and other blade problems indicate that the wind turbine blades are the most important and frequent malfunctioning parts when a wind turbine is working in icing areas, due to ice on the blades. This can introduce important geometric changes to their leading edges and cause rapid variations in lift and drag. More research focused on icing of wind turbine blades is required to obtain insight of aerodynamics of airfoils and de-ice or anti-ice methods.

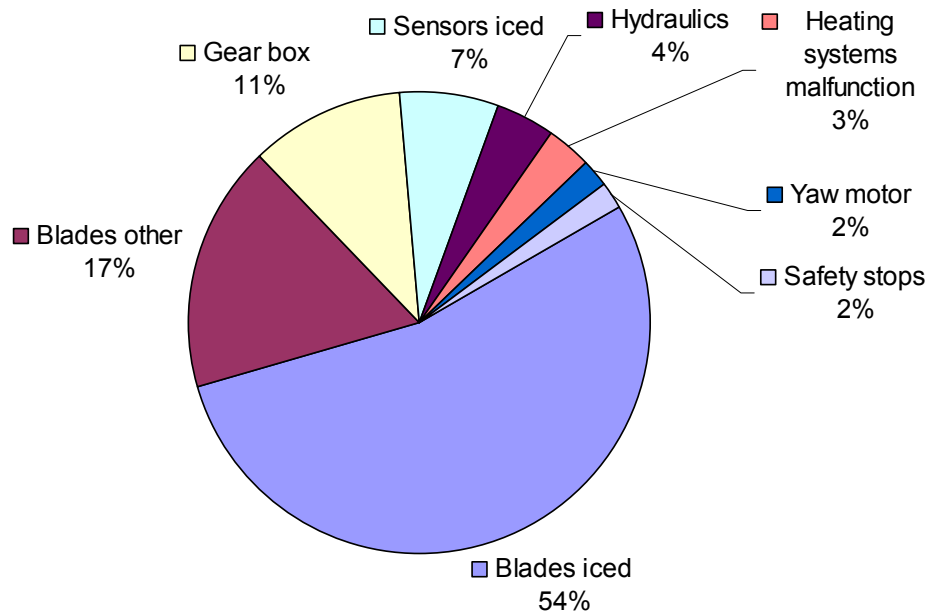


Figure 1.3: Distribution of icing and low temperature related events in Finland 1996-2002

1.1.3. Ice types in cold climates

Icing occurs at temperatures below 0°C when there is some liquid water in the air. The type, amount and density of ice depend on both meteorological conditions and on the water droplet dimensions and type of states, including moving and static. There also is different icing climates, such as in-cloud icing, when small water droplets in the cloud impact and freeze on the surface of structures under cold and extreme low temperature icing conditions.

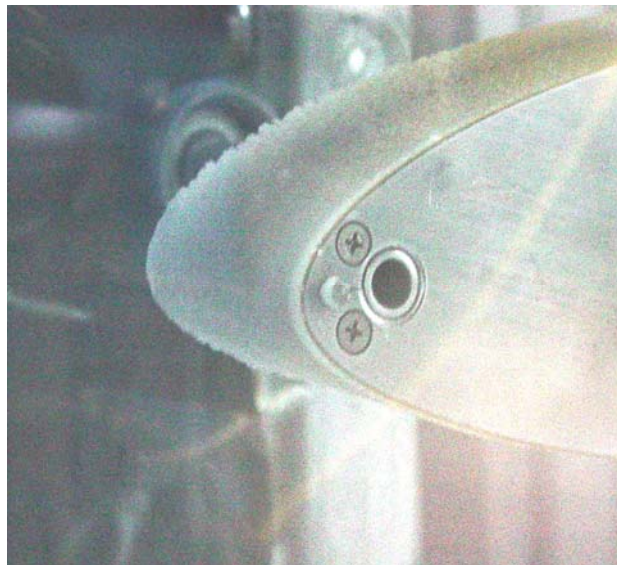
Two forms of atmospheric in-cloud icing are glaze and rime ice (including hard and soft rime ice) in icing events. Glaze ice, whose density varies from 0.8 to 0.9 g/cm³, has a hard, smooth and transparent appearance. Glaze ice is the result of liquid water droplets striking a surface below the freezing point. Glaze ice sticks well when it forms, as shown in Figure 1.4. The figure shows a propeller model forming glaze ice when rotating in a wind tunnel temperature at -5°C , 20 m/s velocity and 0.8 g/m³ LWC, with water droplets and glaze icing of a wind turbine blade model in the wind tunnel.



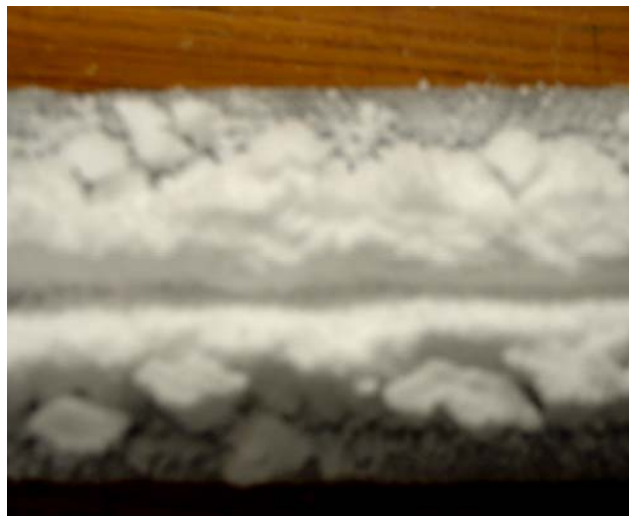
Figure 1.4: Glaze ice in icing tunnel: a) rotating propellers and b) a wind turbine blade model

Rime ice has a rough and opaque appearance and forms when the surface temperature is below the freezing point and it is exposed to supercooled water droplets. Due to the presence of air bubbles trapped inside, rime ice is opaque and its density ranges from 0.59 to 0.9 g/cm³, depending on the type of ice. Druez et al. [7] experimentally studied mechanical property variations of atmospheric ice, including rime ice, with air velocity, liquid water content (LWC) and temperature and median volume droplet diameter (MVD). The results showed that ice strengths in compression and adhesion increased when the LWC and MVD increased and the air temperature decreased during ice accretion. However, the density of ice decreased with increasing air temperature under rime icing conditions. Figure 1.5 shows rime ice on an airfoil blade and a cylinder. Unlike glaze ice, rime ice accretes horizontally and forms various shapes in the upwind direction. Another kind of icing is called precipitation icing, including wet snow and freezing rain. Freezing rain is anticipated to become more serious due to global warming.

Many studies have contributed to our present understanding of the aerodynamic effects of icing of wind turbine blades. Most of the work has focused on simulated ice shapes over airfoils in wind tunnels, at atmospheric conditions at very high wind velocity, such as iced wings of an aircraft. It is therefore important to expand research on wind turbines operating in cold climate areas and focus on developing a more fundamental understanding of these complex phase change phenomena for wind turbines.



a)



b)

Figure 1.5: Simulated icing events showing rime ice: a) airfoil (icing phase) and b) cylinder (post icing)

1.2 Objectives

This proposed research will concentrate on three important inter-related aspects of icing of wind turbine blades to improve our fundamental understanding of icing of wind turbines, with experiments performed during simulated icing events.

Operational Effects: A 3-D wind turbine model was built and it will be used to measure the power output at various pitch angles and icing conditions to relate the changes of the aerodynamic forces to power reduction, when a wind turbine is operating under icing conditions. Ice accretion and irregular shedding during turbine operation causes large load imbalances, creating excessive turbine vibration. They can change the natural frequency of blades, promoting higher fatigue loads and increases in the bending moment of blades. This thesis will quantify the power loss under various icing conditions, which is an important aspect to ensure proper operation by wind farm operators. Knowledge gained in determining the impact of aerodynamic forces and heat transfer characterization will provide new insights into these operational issues.

Aerodynamic Forces: An important part of the research will be to examine the aerodynamics of airfoils including the lift, drag and moment coefficient variations during a simulated icing event, which includes the pre-icing, icing and post icing periods. Special attention will be given to better understand the droplet capture efficiency of wind turbine blades. This aspect is important to predict ice accretion rates and provide transient icing data for numerical model validation. The pressure gradient at the leading edge of the blade affects both the heat transfer and the aerodynamic forces. Both aspects need to be understood. Determining how they are related is important to develop ice mitigation strategies.

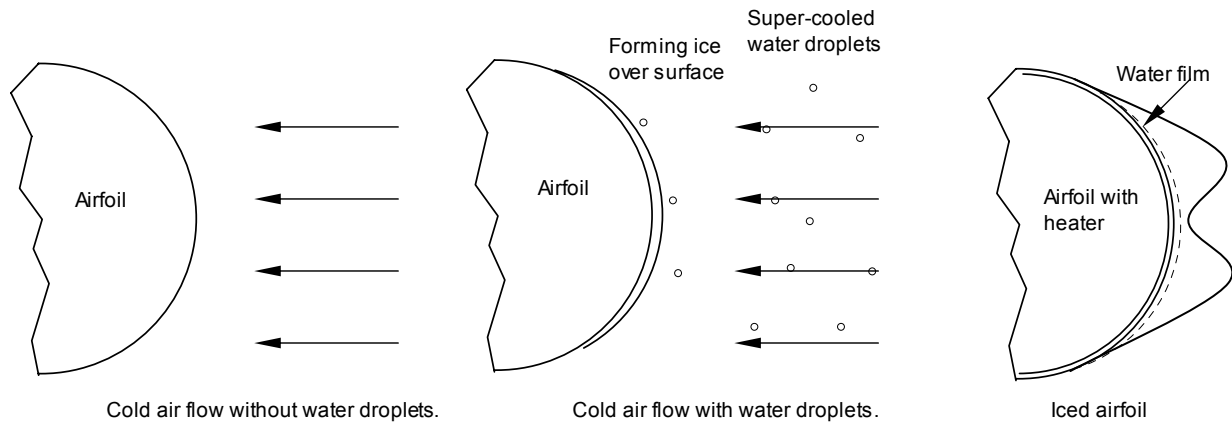


Figure 1.6: Icing event showing the pre-icing, icing and post icing stages

Heat Transfer: The objective of the proposed research is also to improve our knowledge of the mechanism of heat transfer, when air flows over a turbine blade under different conditions, representing some of the following icing stages, shown in Figure 1.6: low temperature experiment without liquid water content (LWC); room temperature with some LWC; and icing conditions with super-cooled water droplets. Heat transfer characterization at various points along the blade is a key requirement to develop effective heat and mass balance models over the turbine blade and predict power requirements for thermal mitigation strategies and blade performance changes. Better characterization of the heat transfer may lead, for example, to lower power requirements with electrical heating of the leading edge during an icing event.

1.3 Methodology

To achieve these research objectives, an icing wind tunnel is used. It includes a) a 3-blade scaled model to simulate wind turbine rotating blades, b) an image capture (digital camera) system to determine shapes of the iced airfoil, and c) a force balance to measure transient aerodynamic forces during an icing event and heat transfer characteristics, while air with

water droplets flow over an airfoil. A water spray system supplies super-cooled water droplets to simulate icing conditions under lower temperatures for rime and glaze icing conditions. Thermocouples and a Pitot tube are used to measure the temperature and air velocity, respectively. The experimental methodology to achieve the research objectives consists of the following three investigations.

- A rotating 3-blade wind turbine with an electrical generator is used to measure ice accretion rates during a simulated icing event. These results are used to estimate the power loss when wind turbines operate under icing conditions. By measuring the generator current, voltage, temperature, and velocity of wind in the tunnel, it is possible to study wind turbine behaviors during an icing event. More details about the proposed experimental work are discussed in Chapter 4. Developing a rotating wind turbine model is key for fundamental understanding of icing and subsequent mitigation strategies.
- A 2-D airfoil model is used to measure the lift, drag and moment at different angles of attack during a simulated icing event for rime and glaze conditions. A comparison between an un-iced airfoil and different iced airfoils is investigated. The measurement of force and moment is performed with a three-component strain gauge dynamometer force balance. This includes lift, drag and pitching moment. These experiments characterize the effects of aerodynamic forces during a simulated icing event, to provide insights into the complex phase change phenomena. Additional details are also provided in Chapter 5.
- A 2-D NACA 63421 airfoil model is tested in the icing tunnel to determine the convective heat transfer coefficient. These tests were developed to measure the heat transfer characteristics for atmospheric air, air with water droplets without phase change, and air with water droplets and phase change (icing conditions). Each of these tests corresponds to the pre-icing, icing and post icing regions, as shown in Figure 1.6. The proposed plan

of testing heat transfer characteristics is discussed in Chapter 6, including the experimental setup of the test model in the wind tunnel, measurement system, results and analysis. This research work is key to characterize the heat transfer from an airfoil to simulate icing conditions and provide theoretical background for heating de-icing or anti-icing.

These three sets of experiments for wind turbine blades during icing conditions provide a unique set of experimental data to explain heat transfer characteristics of icing of wind turbine blades. They also provide fundamental insights for better understanding of icing events and help the development of de-icing or anti-icing wind turbine blade technologies, as well as more accurate predictive models, and provide model validation data.

It is a challenge to simulate complex icing conditions under wind tunnel conditions, as scaling laws are not well formulated for sprayed water in wind tunnels. As a result, the predicted results may have differences compared to actual wind turbine icing conditions. It will be important to assess these differences. The proposed experiments will give useful data for better understanding of aerodynamics and heat transfer during wind turbine icing, while capturing also the important operational issues.

1.4 Significance of this study

This research has both theoretical and practical importance. Currently, there are relatively few experimental studies which focus on the operation of wind turbines in icing conditions. Some manufacturers have developed de-icing or anti-icing technology, such as a leading edge

heating foil or microwave de-icing system. However, fundamental knowledge needs to be improved to address the many technical challenges remaining to be overcome. This should lead to more cost-effective solutions for wind farms. Most investigations use simulated ice to measure the lift and drag coefficients of airfoils under icing conditions. Significantly less attention has been given to the characterization of heat transfer when air flows over the airfoil, under simulated operating conditions of a wind turbine. The study conducted in this research will provide useful data regarding heat transfer from blades.

A past article entitled “Prioritizing Wind Energy Research” by EWEA [8] ascertains that the barriers for developing wind energy include large wind turbine operation in cold climates. This theme is also reflected in the annual report of IEA [9]. An example here in Canada recently is the utilization of wind demonstration projects in the Northwest Territories and Nunavut [10] that show that wind generation in remote Canadian communities has been adversely affected by cold weather. For example, Sachs Harbour, Northwest Territories, installed 66 kW wind capacity at a capital cost of \$445,000. This operated for 15 months at a 1.5% operating capacity factor resulting in \$40.45 per kWh of power costs (lifetime, capital cost only). Kugluktuk, Nunavut which installed 160 kW at a capital cost of \$650,000, operated for 39 months at a 5.6% operating capacity factor, resulting in \$2.56 per kWh power costs (lifetime, capital cost only); and Rankin Inlet, Nunavut, installed 66 kW wind capacity at a capital cost of \$355,000, it has been operating since November 2000 at a 8.9% operating capacity factor, resulting in \$1.63 per kWh of power. These costs are significantly higher than the approximate \$0.09 per kWh normally reported for wind power and reflect the many operational challenges faced by remote communities, those include cold weather effects.

In addition, two monitoring wind stations operated by Manitoba Hydro collapsed in 2003—2004 during the winter due to icing. Table 1.2 depicts 13 MET stations including St.Leon, which report on average 44 wind turbine operating ice days per year from 1999 to 2006 [11]. It means that wind energy would be affected from icing issues when installed in Manitoba. Furthermore, with the proposed 1000 MW wind capacity in Manitoba, wind energy could theoretically supply more than 25% of power at any given time, making prior knowledge of icing events an absolute requirement to allow uninterrupted service to power consumers.

Table 1.2: ‘Ice Alarm’ indication from Manitoba Hydro’s System Control Centre 1999- 2006

	Ice Detection Alarm Data			MET Stations (Manitoba Hydro)					
	1999	2000	2001	2002	2003	2004	2005	2006	AVG
MELITA	12	20	22	15	36	25	31	30	23.9
PILOT MND	31	31	57	30	46	47	41	42	40.6
TREHERNE	19	19	39	20	38	29	32	33	28.6
ST.LEON	25	16	63	47	66	73	62	59	51.4
DARLINGFD	38	51	73	46	81	69	65	61	60.5
STANLEY	31	25	52	36	49	43	49	45	41.3
NIVERVILE	20	13	31	25	25	21	32	41	26.0
MINNEDOSA	35	19	41	28	35	51	27	61	37.1
PTG RADIO	13	14	22	16	32	28	32	55	26.5
STONEWALL	16	10	18	19	22	18	24	19	18.3
BIRTLE	21	16	28	17	20	32	48	59	30.1
RIVERTON	37	24	17	29	18	15	19	29	23.5
ASHERN	14	7	24	12	12	17	24	16	15.8

State-of-the-art laboratory testing is needed to develop a better understanding of the physics of large wind turbine operation when subjected to cold climates that result in a less than optimal use of renewable wind resources. This proposed research identifies important areas where fundamental knowledge needs to be improved. In the proposed research, a model of wind turbine, 2-D airfoils for wind turbine blades and an icing wind tunnel with water droplet production will be prepared for experimental measurements, including heat transfer and other characteristics of wind turbine operation under icing conditions. These characterization experiments will provide fundamental insight into the mechanism of wind turbine blade icing.

Analysis methods will be developed to better understand the physics of wind turbine blade icing. These tests will also be used to provide validation data for advanced numerical Computational Fluid Dynamics (CFD) models.

Chapter 2

Literature review

As one of the fastest growing renewable energies in the world, wind power has become a main source of energy for the future. However, wind energy continues to encounter problems that need to be addressed as the technology is deployed under various climatic conditions. Past research has shown progress towards better understanding of aerodynamic characteristics of wind turbines, icing of wind turbine blades, wind sensors, anemometers, nacelles, heating systems for de-icing or anti-icing of blades and computational simulations. The following literature review will present current status of icing of wind turbines in Manitoba and some of those achievements in past research that pertain to the growing issue of icing of wind turbine blades. The three main objectives of this review focus on operational effects, aerodynamic forces and characterization of heat transfer.

The literature review includes the following main themes that will be used throughout the research:

- Weather conditions for wind energy applications;
- The technology development of wind energy;
- Aerodynamics of wind turbine blades;
- Design and application of wind turbine blades;
- Aerodynamics of the airfoils;
- Aerodynamic study of wind turbines;
- Icing of wind turbines and blades;
- Research on anti-icing and de-icing for wind turbine blades;

- Convective heat transfer;
- Operation of wind turbines.

2.1 Weather conditions for wind energy applications

A cold climate is defined as one that experiences either icing events or temperatures lower than the operational limits of standard wind turbines [12]. Many wind turbines have been operating in regions that experience cold or icing climates, such as Scandinavia, North America, Europe, and Asia. Figure 2.1 shows that wind turbines are located in cold or icing climates [13]. Canada is not included in the map because the survey was pretty old and new map will have to include Canada because so many wind turbines installed in cold climates. However, as mentioned in Table 1.1, significant wind energy capacities have been projected or planned to be installed in most of the provinces in Canada, including Manitoba where cold climates with icing conditions occur (yellow circle in Figure 2.1 and red point including Manitoba, Quebec and Saskatchewan).

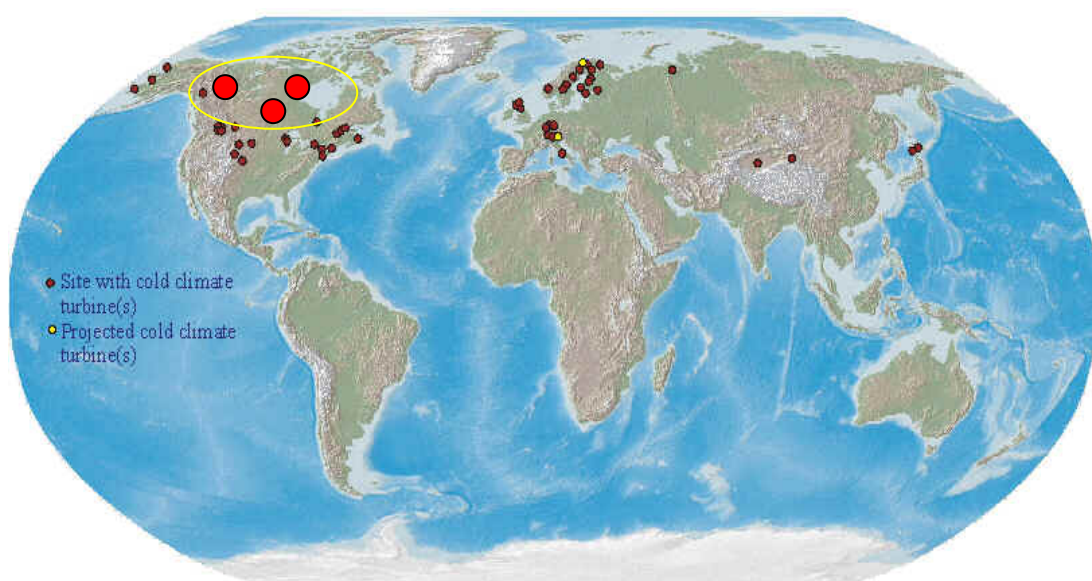


Figure 2.1: Wind turbines operating in cold or icing climates (2003) [13]

Figure 2.2 indicates the potential of wind energy sites in Manitoba. Regions of interest include R1 and R2, where locations include the Red River valley, which has a rich wind energy potential [11]. The recommendation in that installation for 300 MW of additional wind-generation in the R1 region is the best location, as well as 200 MW in the R2 area [11]. These regions are located in severe icing areas presented in Figure 2.3, where characteristics of cold climates can be experienced over several months between October and May. From the example of wind energy penetration in Manitoba, wind energy in cold climates can be effectively distinguished by the ability of the climate to negatively impact power generation of the wind turbine specific to the region in which the wind turbine will be located.

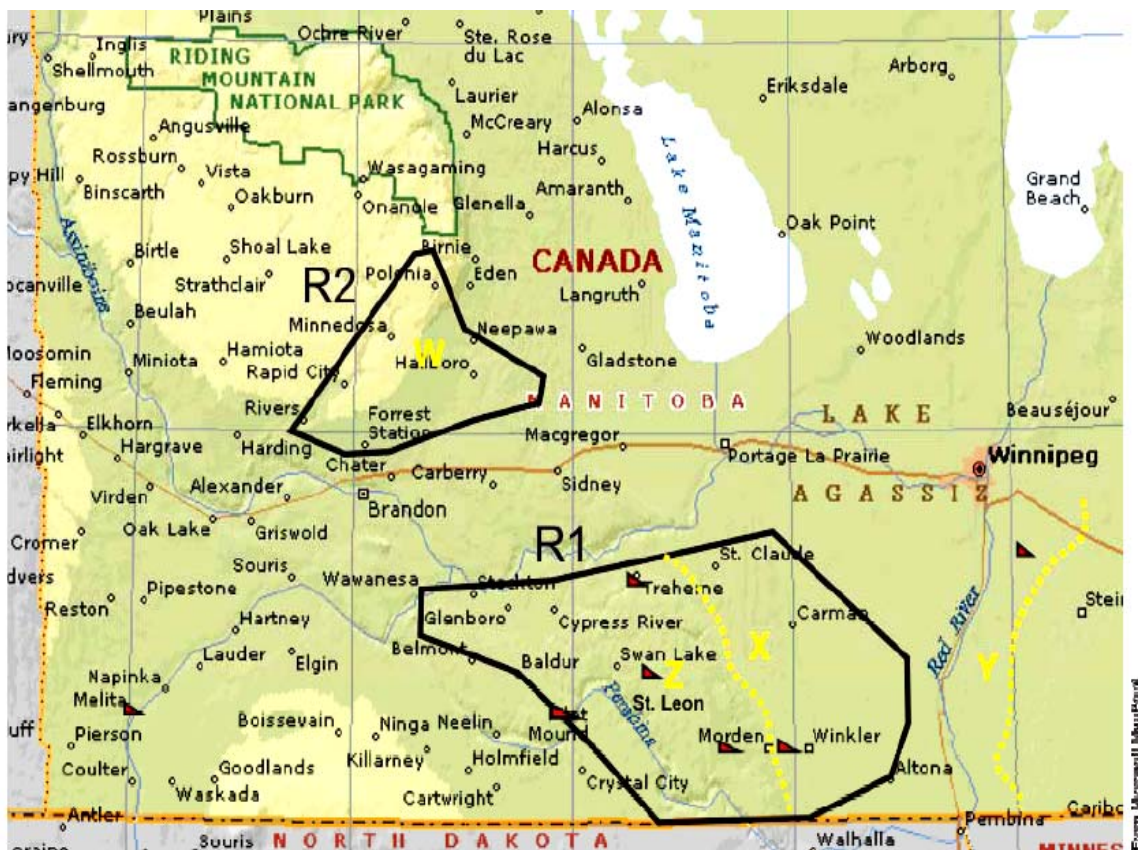


Figure 2.2: Distribution of high wind speed regions in Manitoba [11]

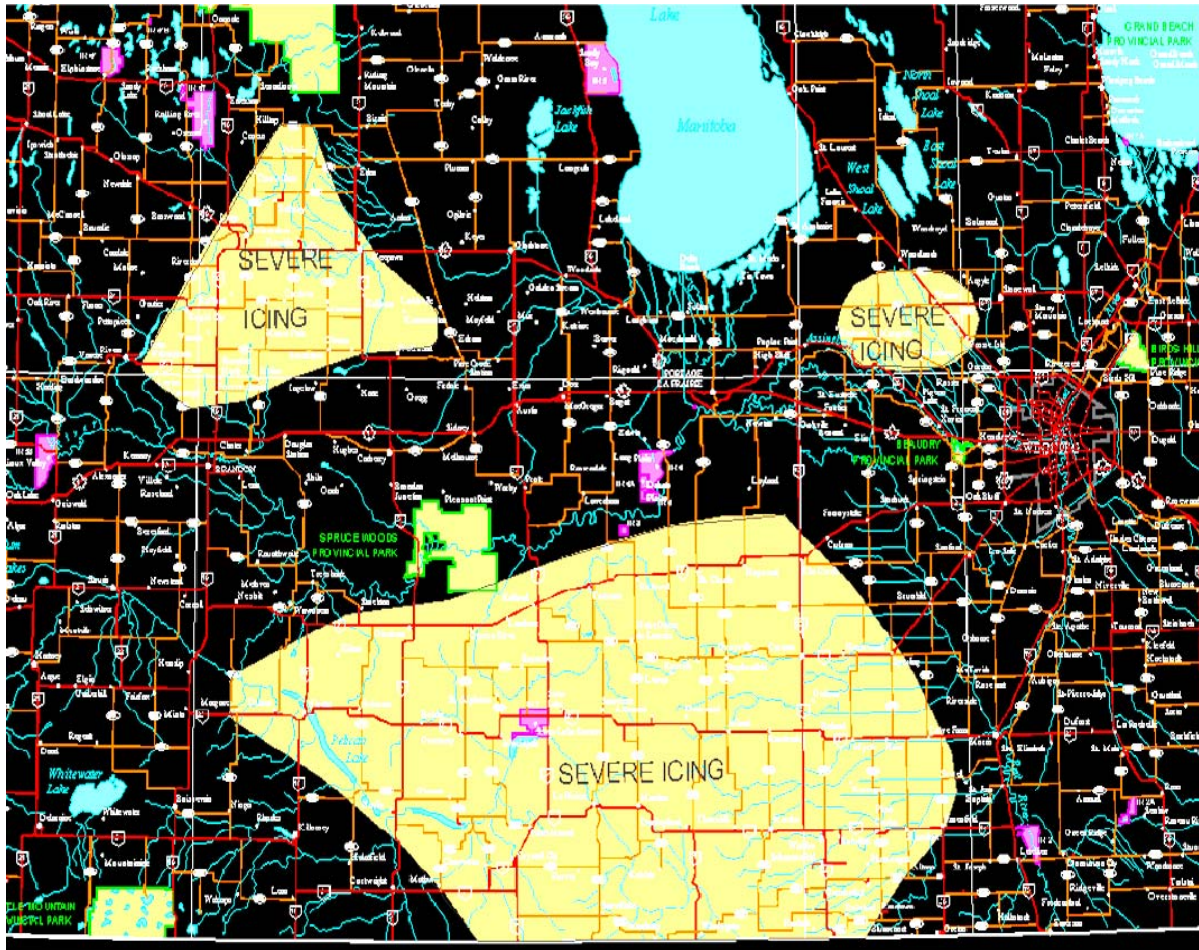


Figure 2.3: Severe Icing Map – From Manitoba Hydro [11]

2.2 The technology development of wind energy

There are two kinds of wind turbines that have been developed to transform wind kinetic energy into mechanical energy and then electric power. These include the horizontal axis wind turbines (HAWT) and vertical axis wind turbines (VAWT). Presently two kinds of wind turbines are being installed in the world, including mountains, valleys and offshore. Normally, the large capacity wind turbines are the horizontal axis type. The capacity of a wind turbine has been developed from 50 kW to 5000 KW [14] and the diameter of a wind turbine ranges from 12 m to 126 m (see Figure 2.4 [15]). From 1985 to 2003, the capacity increase of a single wind turbine has increased tenfold every decade.

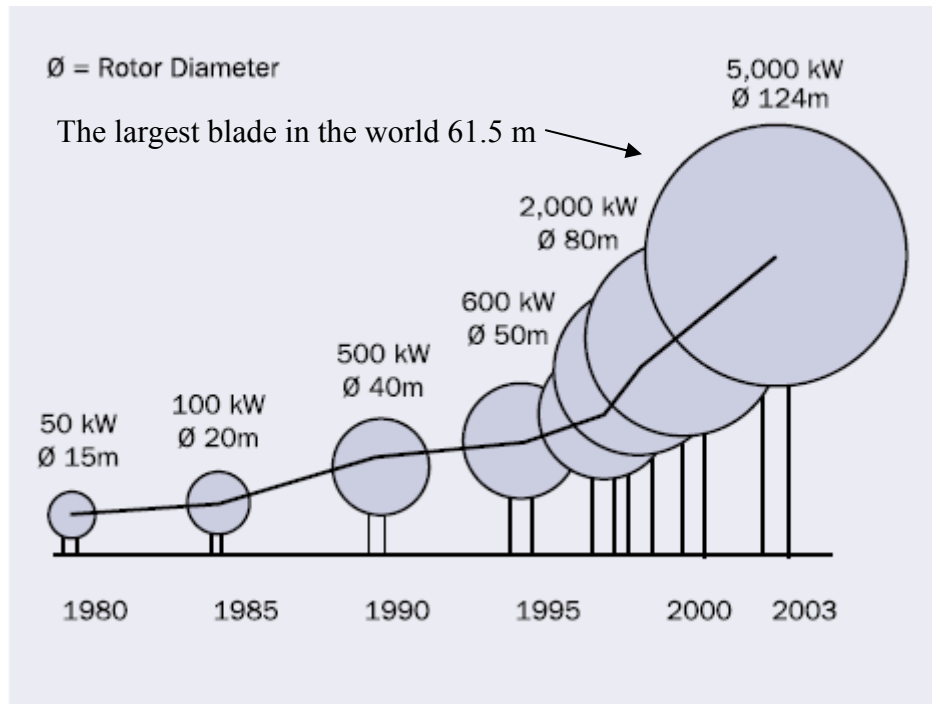


Figure 2.4: Growth in size (radius of blade) and capacity of wind turbine design

From 1995 to 2007, the globe installed capacity boomed almost 7-fold from 13,932 MW to 94,123 MW. Wind energy studies in Refs. [1- 3] have reported that wind energy is projected to grow significantly over the next decade. This may be attributed in part to the scaling up of the technology with typical wind turbines reaching 5 MW, having one single blade in 61.5 m [14] long in a 3-blade wind turbine.

With increased installed capacity and development of a single wind turbine, the aerodynamics of wind turbine blades has been improved by various researchers. The aerodynamics of wind turbine blades is key to developing more capacity of wind turbines. Airfoils adopted in wind turbines differ significantly from airfoils employed in aircraft. Specific requirements for wind turbine airfoils are: high lift-to-drag ratios, large thickness, insensitivity to changes in surface roughness, such as ice and insects, benign and well-defined stall characteristics. The

following section will discuss some studies focusing on the selection of airfoils for wind turbine blades and their aerodynamic characteristics.

2.3 Aerodynamics of wind turbine blades

With the development of wind turbines, the capacity of a single wind turbine increases and the length of wind turbine blades are increasingly longer and heavier. All these changes require the blades to satisfy more and more strict requirements of aerodynamics. The following section will discuss the development of airfoils for wind turbine blades.

2.3.1 Airfoils applied in wind turbines

Airfoils are utilized as wings or propellers in business aircraft. Every airfoil has an element of aerodynamics. Some of them may be used in wind turbines. The following literature describes some airfoil adaptations in wind energy system, due to their structure and specialties.

Coton et al. [16] compared aerodynamic calculations for a range of test cases in an Unsteady Aerodynamics Experiment (UAE) wind turbine with five different sets of 2D wind tunnel data, for the S809 aerofoil that was used for the turbine's blade section. Sohn et al. [17] considered a type of wind turbine blade for a 750 kW direct-drive wind turbine generator system. In this study, the profile of NACA 63 is distributed in position between (r/R_0) 68% and 100% from the blade root, in which the majority of the aerodynamic forces are produced. A circular profile is selected at the blade root to connect with a hub flange easily and ensure the strength of the inner part. A blade structure design was proposed by Kong et al. [18], using a NACA63 series as an airfoil in different sections for a 750 kW HAWT. The profile of the AE02 series is distributed up to 68% of the blade to confirm the structural strength. Jackson et al. [19] used FB 6300-1800, FB 5487-1216, FB 4286-0802, FB 3423-0596, FB

2700-0230, S830, S831 airfoil types to design 50 m in length wind turbine blades. Fuglsang and Bak [20] presented various kinds of airfoils, such as Risø-A1, which was developed for rotors of 600 kW and larger, Risø-P to replace the Risø-A1 in a larger capacity and Risø-B1, developed for variable speed operation with pitch control of large megawatt sized rotors. Bak et al. [21] studied a modification of the NACA 62₂-415, leading to better aerodynamic performance and overcoming causes for double stall.

Wind turbine blades made from NACA 4415 airfoils, as well as NACA 4613, NACA 3712 and NACA 4611 airfoils, in different positions were investigated by Grant et al.[22].

Past studies have shown that wind turbine blades were made with different airfoils. Recently, some airfoils employed for huge capacity wind turbines are the NACA 63 series and their modified airfoils. Different wind turbine blades with various airfoils will have differences in aerodynamics, with different wind distributions. In this research, a 2-D blade made from NACA 63421 is used as a test piece to perform experiments with heat transfer in icing conditions. Section 3.3 will give more details about how the test piece airfoil was fabricated for our research.

2.3.2 The range of Reynolds number in the aerodynamics study

Schreck and Robinson [23] studied unsteady aerodynamics experiments of surface pressure in the National Renewable Energy Laboratory (NREL), with a full-scale horizontal axis wind turbine and aerodynamics of a wind turbine blade, combined with the stationary blade conditions ($0.74 \times 10^6 < Re_c < 1.12 \times 10^6$). It was erected in the National Aeronautics and Space Administration (NASA) Ames 80 ft \times 120 ft wind tunnel. Rotational augmentation of

aerodynamic forces was found to be independent of the influence of Reynolds number. Insensitivity to the Reynolds number over the range $5 \times 10^5 - 1 \times 10^6$ was suggested in wind turbine blade research at various spans by Coton [16]. The Reynolds number range from $1 \times 10^6 < Re_c < 10 \times 10^6$ has been studied for a modified DU97-W-300 aerofoil by Timmer and Schaffarczyk [24].

A literature review in Section 2.7.3, investigation of wind turbine blades with ice, also includes past research at different Reynolds numbers for airfoils with ice. Some papers focus on airfoils for aircraft studied at higher Reynolds number, mentioned in Section 2.7.2, icing of wind turbines and blades.

These literature reviews revealed that the Reynolds number for wind turbine blades vary from $1 \times 10^5 - 1.12 \times 10^6$; This is less than the 10×10^6 value normal for aircraft airfoil tests. In this research, the Reynolds number for convective heat transfer from the airfoil will focus on the range between 1×10^5 and 1.3×10^6 , with some data collected at lower Reynolds numbers.

2.4 Design and application of wind turbine blades

The structure of the blades is very important for safe, reliable, and efficient operation of wind turbines. Maalawi and Negm [25] developed an optimal frequency approach for designing a typical blade structure. The main spar, optimization variables, optimal design, global optimality and structural analysis were considered in a blade design, to address the aeroelastic stability boundaries and steady-state response problems. Mejía et al. [26] developed a mathematical model to calculate the chord distribution of airfoils and blade twist along the

radius of the blade, as well as the power output curve under some wind speed distributions. Kong et al. [18] discussed the specific composite structure, fatigue of wind turbine blades under various loads, and a new blade root joint. They also presented a full size static structural test and compared the simulated results with measured data. Jureczko et al. [27] applied a commercial ANSYS code to optimize the wind turbine blades, in terms of the shapes of the blade, composite materials and aerodynamic loads of the blade.

Two wind-tunnel tests of the wake dynamics of an operational, horizontal-axis wind turbine and NACA 4415 airfoil were investigated by Grant et al. [22]. The closed type, low turbulence, wind tunnel was designed with axial dimensions of 10, 4.5 and 10 m at Heriot-Watt University. The 2 and 3 blade configuration wind turbine had an overall rotor diameter of 0.9 m and a hub diameter of 0.24 m. It was installed in the 2.3 m working section in the tunnel. The blade had an airfoil profile that approximately varied from the tip to the root as NACA 4613, NACA 3712 and NACA 4611 airfoils. They were untwisted, tapered and set at a pitch angle of 12° . The second closed-return, low-speed wind tunnel at the University of Glasgow had a working section of $2.13 \text{ m} \times 1.61 \text{ m}$ and a test air speed range from 7.5 m/s to a maximum of 9.3 m/s. The test model of the wind turbine was a two-bladed setup with a chord length of 0.1 m. It was manufactured from carbon fiber as a NACA 4415 airfoil. A laser sheet visualization (LSV) technique was used to measure the trajectories of the trailing vortices, under various conditions of turbine yaw and blade azimuth. Particles with an average diameter of $6 \text{ }\mu\text{m}$ had been utilized as seed particles to obtain the wake images and a uniform distribution across the measurement plane. The authors compared selected results in the experimental study with predictions of a prescribed wake model. Another feature of the wind turbine blades was ascertained for 600 kW and 750 kW wind turbines by Norwin [28]. The pitch changes were given with the length of the blade.

Previous literature gave some examples of how blades are made. The design of a wind turbine blade is complicated and it must have suitable aerodynamic characteristics. Research on wind turbine blades and wind turbines must be performed when some new blade design is introduced. The following section will discuss some aspects of the aerodynamics of wind turbines and blades.

2.5 Aerodynamics of the airfoils

Given a favourable wind resource, the basis of wind energy extraction is favourable aerodynamics of wind turbine blades. The characteristics of blades affect the power collection coefficient from the wind. Numerous past studies have focused on the aeroelasticity of airfoils and wind turbines, both in numerical and experimental studies. Past literature indicates that most research on wind energy has concentrated on theory and numerical simulations. The body of knowledge obtained is important when trying to understand the transient ice accretion on a rotating airfoil.

2.5.1 Simulation of aerodynamics and theoretical study of airfoils

Anttonen et al. [29] developed a proper orthogonal decomposition (POD) method to predict flows on a deforming grid. This technique was successfully used to simulate the aeroelastic problem, with flow on a pitching and plunging airfoil. Giering [30] employed a new automatic differentiation tool, TAF, to compute the Euler flow around a NACA airfoil. The performance of the NSC2KE adjoint and self-adjointness, using TAF, were discussed in

Giering's paper. Computational studies were expanded by Mittal et al. [31] for two-dimensional flow over a NACA 0012 airfoil. The research presented the separation point of the flow and the effects of the angles of attack.

Akbari and Price [32] used a Joukowski transformation by mapping a circle onto a physical domain to establish elliptic profiles of an airfoil. The flow over elliptic airfoils was simulated over pitching oscillators for a Reynolds number of 3000 and the effects of various parameters on the flow field were analyzed. A numerical study of the aerodynamic characteristics of a two-dimensional airfoil with the incompressible Navier–Stokes equations was simulated by Le Maître et al. [33]. Validation of the method and the flutter derivatives of an airfoil were examined for the aerodynamics coefficients. The authors predicted the effects of the Reynolds number and the thickness of the airfoil to estimate the flutter coefficients and it showed good agreement with the inviscid theory. The dependence of drag and lift of a four-element airfoil, with respect to the position of some flaps in Euler and turbulent Navier–Stokes flow, was reported by Slawig [34] through the automatic differentiation method. A two-dimensional (2 - D) compressible Navier–Stokes/Euler solver, NSC2KE, and a Numerical Algorithms Group (NAG) quasi-Newton optimization routine, were used to obtain the optimization of a cost functional, based on drag and lift with respect to the position of the flaps. An alternative model of dynamic stalls was investigated by Meyer and Matthies [35] to simulate the airfoil performance, aeroelastic stability and sensitivity analyses.

2.5.2 Experimental study of aeroelastics of airfoils

In addition to theoretical studies on the aeroelastics of airfoils, many past studies conducted experiments to gather further insight regarding the processes. Jung and Park [36] conducted

an experimental study of vortex-shedding characteristics in the wake of an oscillating airfoil at low Reynolds numbers. A NACA 0012 airfoil model with a 10 cm chord and 19.8 cm span was installed in a small open-circuit wind tunnel with a 20 cm \times 30 cm test-section, with a length of 120 cm. A constant-temperature hot-wire anemometer and four X-wire probes were used for the velocity measurements and the smoke-wire technique was utilized for flow visualization. The results showed that the shedding frequency decreased with an increasing angle of attack. Also, the frequency variation during the cycle of oscillation diminished as the frequency of oscillation increased. Ahmed and Sharma [37] experimentally studied the flow characteristics over a symmetrical airfoil, NACA 0015. They measured the pressure distribution, lift and drag coefficients, mean velocity profiles over the airfoil surface, as well as the wake region, and turbulence intensities at two stations downstream of the trailing edge, by varying the angle of attack from 0° to 10°. Higher values of the pressure coefficient and lift coefficient on the lower surface were observed when the airfoil was close to the ground. The pressure distribution on the upper surface did not change significantly with ground clearance for higher angles of attack.

Amitay et al. [38] investigated flow transients associated with controlled reattachment and separation of the flow over a stalled airfoil (NACA four-digit series symmetric airfoil with a 25.4 cm chord). The experiments were conducted in an open return wind tunnel with the airfoil model made from aluminum and the leading edge circular cylinder mounted within a fiberglass aerodynamic section. Phase-locked two-component hot-wire anemometry and Particle Image Velocimetry (PIV) were used to measure the response of the flow over the airfoil to time modulated control input. The flow mechanisms associated with the reattachment process and a new actuation technique were used to achieve an improvement in the efficiency of the jet actuators, by using pulse modulated excitation input. Also, lift

coefficients in these situations were given. Hillenherms et al. [39] experimentally studied the interaction of aerodynamic and structural forces on a 2-D rectangular wing section oscillating in transonic flow. The tests were conducted in a $0.4\text{ m} \times 0.4\text{ m}$ test section with a fixed 2-D adaptive wall wind tunnel. Piezo-resistive pressure sensors and a strain-gauge balance were installed in the wind tunnel to measure the pressure signals and the unsteady forces. The pressure distribution along the dimensionless chord and unsteady flow around the supercritical airfoil, undergoing free and forced pitch oscillations, were presented in the paper. Bak et al. [40] tested the characteristics of the NACA 63-415 and modified NACA 63-415 airfoils in a VELUX wind tunnel, which had an open test section with a $7.5\text{ m} \times 7.5\text{ m}$ cross section and a length of 10.5 m (closed return type). The models of airfoils were 0.6 m and 0.606 m in chord length, and 1.9 m in span. The aerodynamic properties of lift, drag and moment coefficient, as well as the influence of leading edge roughness, stall strips, vortex generators at various angles of attack and comparisons between two airfoils were investigated.

These studies of airfoils provide aerodynamic characteristics of different kinds of airfoils. According to the airfoil in the wind turbine blade from a manufactory, the 2-D NACA 63421 airfoil was selected to do research of aerodynamics with and without icing conditions. However, NACA 63421 is a blank in this field research. This part of past research will be used for wind turbine blades and wind energy research in this thesis. Comparing with past studies, this research will focus on force measurement at lift, drag and moment with different ice thicknesses by a force balance measurement system.

2.6 Aerodynamic study of wind turbines

2.6.1 Investigation of wind turbine blades

Beyond studying the aerodynamic characteristics of an airfoil, a large number of studies have focused on the aeroelastic properties of blades, an important aspect as it relates to possible deformation of the blade which can impact the de-icing and anti-icing phase. The turbulence characteristics of wind turbine blades, including lift, drag, pitching moment and pressure distributions, were investigated in a $2\text{ m} \times 2\text{ m}$ test section wind tunnel by Devinant et al. [41]. The 0.3 m chord model blade with the shape of a NACA 65₄-421 airfoil (span of 1.1 m) was installed in a wind tunnel and tested at angles of attack up to 90° . The aerodynamic properties in high turbulence conditions were measured by hot wire measurements. A viscous–inviscid interaction algorithm that coupled unsteady potential flow to a turbulent boundary layer was developed by Bermúdez et al. [42] to simulate turbulent unsteady flow over the airfoil of the wind turbine blade. This method has the capability to predict the turbulent boundary layer flow detachment point, up to 50% of the airfoil chord length with reasonable accuracy. Artificial neural networks (ANN) were used by Yurdusev et al. [43] to predict the optimal tip speed ratio (TSR) for NACA 4415 and LS-1 profile types with 3 and 4 blades. The results showed that the ANN structure was more successful than the conventional approach for estimating the TSR and power factor. The parametric model derived from CAD and a finite element model was used to evaluate the aerodynamic forces and dynamic behavior of the structure, respectively, by Younsi et al. [44]. The model was based on the theory of three-dimensional beams, under the assumption of variable sections of the NACA 4415 airfoil with a membrane. Transverse shear, flexion and free torsion effects were studied numerically. The research obtained numerical results with a Fluent code and the results were in accordance with the assumption of linear behavior according to the maximal deflection (no more than 10% of the blade length).

2.6.2 Flow characteristics study of wind turbines

Flow fields past a small wind turbine with a flanged diffuser were numerically and experimentally studied by Abe et al. [45] in a large wind tunnel. The measurement section has a 2.5 m width, 1.5 m height and a maximum wind velocity of 20 m/s. The experimental wind turbine was located 500 mm downstream of the wind tunnel exit with a 3-bladed rotor in a 388 mm diameter flanged diffuser. A hot wire technique was employed to measure the average velocity profiles behind the wind turbine. A much higher power output was obtained due to the effect of the flanged diffuser. The computational simulation corresponding to the experimental conditions was used to obtain more details with respect to the flow field, as well as comparisons with experimental results. A numerical simulation was presented by Bermúdez et al. [46] to predict the unsteady aerodynamic characteristics, based on time-dependent forces and moments, while a wind turbine was operating. The authors studied an application of a wind turbine with unsteady aerodynamics effects and the results showed agreement with experimental data. Another simulation model based on lifting line theory was developed by Badreddinne et al. [47] to optimize the aerodynamics of horizontal axis wind turbines. The code used a momentum theory and circulation at the trailing edge.

Vermeer et al. [48] reviewed past studies on the wake aerodynamics of horizontal axis wind turbines for both near and far wake regions. The paper included experiments on single turbines and wind farm effects, both experimental and simulated. Ebert and Wood [49 - 51] studied the velocity and turbulence of the near wake and vortices of the tip and hub of a 250 mm diameter 2-bladed turbine, with blades made from a NACA 4418 profile with a constant pitch of 10° . A technique of X-probe hot wire anemometry in six axial planes was used to measure the mean velocity and vorticity in the flow field. The wake structure, vorticity in the boundary layer and their effects were discussed in these papers. Thrust–torque and thrust–

energy methods were theoretically and experimental investigated to analyze the aerodynamic performance characteristics of a wind turbine by Kishinami et al. [52]. The results were presented for a NACA LS04 airfoil series of wind turbine blades. The studies involved a variable pitch control output system and NACA 4415 airfoil, with blades of a fixed pitch stall control method, because of aerodynamic characteristics and power, torque and thrust coefficients. The approach taken by these studies can be replicated but with icing on the blades.

2.7 Icing of wind turbines and blades

The aerodynamics of wind turbine blades will affect the efficiency of the system [53] and how much wind energy is transformed to electric power. In cold climate regions, icing of wind turbines can significantly affect the performance, safety and economics. Numerous wind farms have been built in the north of Europe and North America, in areas that have a cold climate and therefore, they have lengthy icing periods in the winter.

2.7.1 Operation of wind turbines under cold climates

External conditions, involving turbulence, gusts, icing and lightning strikes will affect significantly the wind energy source, as well as wind turbine working conditions. Durstewitz et al. [54], Schaffner [55], Morgan et al. [56] and Peinke et al. [57] studied a series of challenging problems for a Horizontal Axis Wind Turbine (HAWT), including turbulence in wind gusts and turbulent wind fields. Cheng et al. [58] simulated the extreme gusts and the effect of gusts on the turbine. Comparisons with stochastic and deterministic gusts were discussed. All extreme climates would affect the performance of wind turbines; the worst case is a wind turbine operating under icing conditions.

Many observations of icing on wind turbine blades, sensors and nacelles and power systems were reported in north arctic areas, such as Finland, Germany and Austria. The first arctic wind farm, Lammasoivi wind farm in Northern Finland, was discussed by Aarnio et al. [59]. They explained the technical availability, low temperature conditions, service and maintenance of a wind farm in a cold climate region. Tammelin and Santti [60] presented icing conditions in Europe, including the potential of wind energy in an icing climate environment. Fathomer, Antikainen and Peuranen [61] studied icing blades in different case studies. Tammelin et al. [62] discussed problems when large wind turbines are installed in cold climate regions. Various ice shapes were noted during the wind turbine operation, including standstill or idling of the turbines at lower wind speeds when a heating system on the blades was working. Plastic heating foils were installed at the leading edge. The real ice structures on a wind turbine, wind sensor and power lines were investigated by Tammelin [63] in Europe. Pictures of rime ice accretion on wind turbine blades were also recorded in this paper. The ice accretion on an operating wind turbine blade was observed by Seift and Schloz [64] in a wind farm with two 100 KW DEBRA-25 turbines with 3-blades and a pitch control system. Rong et al. [65] investigated a simulated site experiment with Enertech. A horizontal-axis, 3-blade, 13.4 m diameter wind turbine was studied. The ambient temperature varied between -2.7°C and 3°C , and the average wind speed was 7 m/s. The ice shapes were noted and the effect of icing on power loss was discussed.

Bose [66, 67] observed a natural icing event on a small wind turbine with two-bladed 1.06 m diameter blades. Various glaze ice profiles were recorded at different positions of the blades. The author noted that the ice built up much more on the tips of the blades than the roots of the blades. Also, ice accretion only covered the pressure side of the blade sections, but it was

clear on much of the suction side. Observations and records under icing conditions also recorded some power variation curves with wind speed. Bose [67] discovered that water droplets impinged and flowed some distance on the blades before icing occurred. An Acqua Spruzza test site for wind turbine operation was set up in harsh and complex terrain in Central Italy in 1996 and observed by Botta et al. [68]. The results showed that the performance of the wind turbine and the power output would be influenced by heavy icing, snow fall, high turbulence and other climate conditions. Winkelmeier and Trauttmansdorff [69] documented a wind farm with large scale wind turbines working under ice and snow accretion.

Over power production in cold temperatures of a wind turbine in Canada has been reported. This aspect is a severe cold weather issue. A 600 kW Tacke machine located in Tiverton, Ontario, reached 950 kW during a second-averaged power peaked at a -20°C and the generator overheated and tripped [70]. Also a 5-minute average power output of 89 kW was recorded for a 65 kW Bonus machine located in Kuujuaq (58°N), Nunavut [70]. These phenomena will be further examined in Section 4.4 during experiments.

2.7.2 Icing of airfoils on aircraft

Numerous past studies have focused on aerodynamic performance of different airfoil with different icing times and various simulated ice shapes, as well as spoilers to form two-dimensional flow conditions at higher Reynolds numbers. Past studies on aircraft aerodynamics normally concentrate on high Reynolds number conditions, due to the very high wind speed and relatively small water droplets. Also, aerodynamics with icing conditions

was originally studied because some aircraft disasters [71, 72] occurred when the wings were covered with ice.

Bragg et al. [73] has reviewed simulated and experimental studies on iced airfoil aerodynamics from the late of 1920s to present. Laminar separation bubble schematic and characteristic surface pressure distribution, separation streamlines with simulated ice shapes and contour plots of different ice geometries were the subject of this review. Roughness, horn ice, streamwise ice and spanwise-ridge ice were presented under different k/c (k : height of ice) and s/c (s : position of ice) for various airfoils at different Re_c and Ma (Mach number). The effect of various ice shapes at varying Reynolds number was reported for NACA airfoils, such as NACA 63A213, NLF 0414, GLC 305. The authors gave conclusions how ice geometries including height, density and surface positions affected the aerodynamics of the airfoils, flow fields, stream lines with varied Reynolds numbers and Mach numbers. The results were given [73] that $C_{L, \max}$ did not change significantly above a Reynolds number (varying with different airfoils); on the other hand, Mach numbers above 0.10 affected the performance of airfoil. This gives a conclusion that $C_{L, \max}$ would change in different trends between Re and Ma . Shin [74] investigated aerodynamic performance of a NACA 0012 with a 21-in chord, with comparison to the LEWICE model. The results [74] of C_L from the LEWICE model were much higher than the experiment. The roughness growth rate for the airfoil was different for the initial stage and later stages of accretion. A rapid initial growth followed by much slower growth was observed. A commercial airfoil and a business jet airfoil were investigated in the NASA Lewis Icing Research Tunnel by Addy et al. [75]. The focus of the investigation was various icing times at different temperatures to form glaze ice, rime ice and mixed ice shapes. Data showed that two minutes of glaze ice had a noticeable effect on lift coefficients, particularly at a high angle of attack. The drops in the lift coefficient differed as a result of

types of ice used. Lee et al. [76] experimentally studied a NACA 23012 airfoil with a quarter-round span-wise of $k/c = 0.0085$ (protuberance height over chord) and 0.0139 in height. A dramatic decrease in the maximum lift coefficients was observed. Papadakis et al. [77] researched aerodynamic characteristics for a Twin Otter tail section, with simulated ice shapes including 22.5 and 45 minutes of LEWICE ice shapes for a 57-in chord, SP22-1, Sp 45-1 spoiler ice shapes (24-in) and SP1 ~ SP7 for 4-in chord airfoils. Results showed that the aerodynamic performance with various ice conditions was controlled by specific configurations and flow conditions. More investigation with a range of airfoils and varying ice shapes is required to obtain more insight into the aerodynamics of airfoils under icing conditions.

The maximum lift and drag coefficients and stall angles of a NACA 23012 with ice shapes were investigated by Papadakis et al. [78], ranging from 2×10^6 to 10.5×10^6 in Reynolds number. The experiment with cast ice shapes at different icing times showed that the maximum lift coefficients would drop up to 60% while stall angles changed from 17° to 9° under icing conditions. Papadakis et al. [79, 80] studied the airfoil NACA0011 at the same height $k/c = 0.0625, 0.125$ for different chords of 24-in and 12-in. The research indicated that lift and drag were not significantly sensitive to Reynolds number. However, the pitch moment and pressure distribution were greatly affected by the Reynolds number for the iced airfoil. Another study [80] showed the maximum lift coefficient and stall angle at different Reynolds numbers with or without simulated ice. A maximum lift coefficient reduction of 150% and drag increase of 2000% with respect to a clean airfoil was reported and the stall angle decreased from 14° to 8° . The icing performance of a new business jet airfoil based on a GLC-305 airfoil was conducted by Addy et al. [81]. The maximum lift coefficient degraded up to 48% and large increases in the drag and pitching moment coefficient were obtained. A

simulated study of different airfoils, NACA 23012 and NFL 0414, were conducted by Pan et al. [82] to obtain the critical ice location. The critical ice locations, where the maximum lift coefficient and stall angle of attack were worst, changed with airfoil geometry. Changes in the Reynolds number and Mach number did not affect the iced-airfoil performance, as obtained by Addy [81] and Pan [82] for different airfoils. Broeren et al. [83] measured bubble and flow separation about a GLC-305 airfoil with simulated 22.5-minute and 45-minute leading edge ice shapes. The presence of a large separation bubble downstream of the ice shape, as well as the difference in size and integral boundary layer characteristics, could be used to explain the aerodynamics of the iced airfoil.

Various past papers studied airfoil aerodynamics with simulated icing conditions at high Reynolds numbers; these can be adapted for wind turbines at a high capacity when they are installed in cold climates. The following section discusses previous literature on wind turbine blades with ice.

2.7.3 Investigation of wind turbine blades with ice

Many researchers have studied the aerodynamics of iced blades in wind tunnels. Most experiments to investigate icing of wind turbine blades were conducted with simulated ice shapes at room temperatures. Hoskins et al. [84] experimentally investigated wind tunnel tests for the characteristics of a NASA LS (1)-0417 airfoil. The tests focused on a rime ice profile and two glaze ice profiles. A rime ice profile was simulated by wood fastened to the leading edge of the wing. The tested angle of attack ranged from -4° to 90° in a six component strain gauge dynamometer, in a tunnel of 1m by 1 m cross-section and a maximum air speed of about 14 m/s. The test Reynolds number was 0.1×10^6 . The authors compared different ice conditions and the resulting lift, drag and moment coefficients.

Seifert and Richer [85] developed a method to estimate the aerodynamic loads of iced rotator blades, based on NACA 4415 experimental tests. The “artificial” iced blade was 225 mm in chord and 500 mm in wing span. It investigated angles of attack ranging from -10° to 30° and a Reynolds number (based on chord length) of 6.3×10^5 in a 1.3 m wide wind tunnel. Three kinds of leading edge ice types were studied in this test. The approach could be used to calculate the drag, lift, mass load, power curves and energy output of different airfoils with various ice accretions. Also, Seifert and Schloz [64] investigated aeroelastics of an icing blade, with a simulated 37% chord length ice on the leading edge. The 0.29 m chord airfoil was tested and compared with a clean blade in the shape of a NACA 4415 airfoil with lift, drag and torsional moment coefficients, with Reynolds numbers (based on the chord length) between 1×10^6 and 1.5×10^6 . A comparison of power output and frequency under clean and iced conditions was reported for the test site.

A wind tunnel test was investigated by Kimura et al. [86] to measure the lift, drag and moment using a 2-D NACA0015 airfoil with 4 different ice shapes on the blade. The blade model with 2 arrays and 72 pressure taps was 2000 mm in length and 500 mm in width. It was tested at a 3×10^5 Reynolds number. The authors asserted that very little, if any, change occurred in both lift and drag coefficients during ice accretion. There was a reduction of maximum lift and stall angle, which changed the stall characteristics, and the drag increased in rime ice conditions.

Ice load models on offshore wind turbines were tested by Barker et al. [87] to simulate the ice loads and possibility of ice-induced vibration. The model tests and recommendations for an optimum angle and cone-size were presented. Also, Gravesen et al. [88] simulated ice loads

on the foundation of offshore wind turbines from large floating ice chunks. A hybrid grid generation and quad-dominant grid generation were adopted to simulate the iced shapes of the wind turbine blades by Koomullil et al. [89].

2.8 Research on anti-icing and de-icing for wind turbine blades

The problem of icing on wind turbines has led researchers to develop experiments to investigate the mechanism of de-icing and anti-icing. The next section will review previous literature about anti-icing and de-icing methods for wind turbines under icing conditions.

2.8.1 Simulation study

In order to obtain more data for applications of heating systems for de-icing, many researchers have used computational modeling to simulate the icing conditions and develop de-icing approaches. The heat and mass transfer with phase change in wind turbine rotor applications was investigated by Tao et al. [90]. The model used transport equations of momentum, energy and mass conservation for the ice surface. A commercial finite element code was used to simulate the air flow and temperature distribution over a 2-D airfoil with steady state, incompressible flow. The local heat transfer coefficients, average thickness and ice layer over 2 hours at various angles of attack around an NREL S809 airfoil were presented.

Marjaniemi et al. [91] developed a wind turbine blade icing model, TURBICE, to calculate the heating demand according to the shape of simulated ice in laminar or turbulent flow. Based on energy and mass balances between the blade surface and heating system, the model of TURBICE was tested in a case study. The numerical simulation of ice buildup and shapes

on the wind turbine blades were investigated by Makkonen et al. [92] using the TURBICE program. The local droplet collision efficiency was computed, at different angles of attack, as a function of the dimensionless surface length, while droplets impinged on a NACA 63213 airfoil. The heat and mass transfer were simulated with ice accretion over the airfoil surface. The results were compared with field observations from 18 operating wind turbines equipped with a de-icing system. Also, the NACA 63215 airfoil used by Kimura et al. [86] was numerically studied with ice growing up to 6% and 15% of the chord. The results showed that the electric power output would be reduced up to 78%, in stall control and 81.6%, in pitch control, due to different ice shapes on the blade.

2.8.2 Application of anti-icing or de-icing methods

Past research on heating systems for wind turbine blades with anti-icing and de-icing was reported by Seifert [93]. The ice shapes (such as leading edge icing, trailing edge icing and blade surface icing) were significantly different in various control systems having different pitch, stall and active stall control strategies. Seifert [93] described some recommendations and guidance on how to employ the heating system on the blade, according to various operational strategies.

Massardo and Farinazzo [94] developed a hot-film anti-icing system for an aircraft nacelle model. The hot film, formed with hot air injection, was used to keep a high temperature for nacelle intake ice protection. The experiment presented the inner heat transfer coefficient, hot air mass flow rate, and comparisons of weight reduction of the anti-ice system with a spray bar solution. The anti-ice system was an energy saving method, due to the high temperature bleed engine air of most aircraft. Ice-free anemometers were investigated by Tammelin et al. [95] in different site observations and heated anemometers. The results illustrated that an

inaccurate wind speed signal could significantly affect the operation of wind turbines. Using ice-free anemometers was recommended for a cold climate region, when wind turbines were operating.

Two heated and one unheated anemometers were used to measure the actual wind speed, icing time and sublimation time of ice in Northern Canada by Craig and Craig [96]. This is a possible method to estimate the icing time that a wind turbine would experience in an icing climate. One kind of blade heating system, using carbon fibre elements mounted to the blades near the surface, has the widest operating experience capability by Peltola et al. [97]. This heating system was applied in 18 wind turbines at various sites in France, with a total of nearly equivalent 100 operating winters [97] and obtained good anti-icing results.

Numerous experiences of operating wind turbines in low temperatures and severe in-cloud icing environments were reported by Yukon Energy Corporation. Installed in 1993 and 2000 respectively, two turbines, a 150 kW Mark III Bonus and a 660 kW V47 Vestas in Haeckel Hill, Yukon (altitude 1430 meters), have been operating in Yukon Territory for several years [98]. Low temperature steels, synthetic lubricants and heating systems for the gearbox, generator and electrical cabinets for the two wind turbines have been reported to work well by Maissan [98]. Heating strips for the ice detector, anemometers and aerial power lines and a black low adhesion type of paint for the wind turbine blades, were employed to de-ice and improve the operating performance of the wind turbine. In addition, the recommendation of that wind turbines be fitted with a full blade surface heater for ice protection was given as a solution for cold weather climates. De-icing of the rotor blades in the Enercon E-40 with a “hot-air” system, including a 12 kW ventilator on each blade, was used during slow rotation of the rotor (6 rpm). Results showed that de-icing was satisfactory (Horbaty [99]). Kraj [100]

studied the ice adhesive stress, volumetric accumulation amount, metric profile shape extension and the ice accumulation rate. The authors compared different mitigation strategies, including surface, thermal and thermface techniques in both anti-icing and de-icing regimes for different icing conditions.

All of these methods indicated that the method of using heat for anti-icing or de-icing would be an effective way to keep ice off. This research will perform experiments on heat transfer from an airfoil in order to develop better de-icing and anti-icing methods.

2.9 Convective heat transfer

2.9.1 Correlation of heat transfer without droplets

Previous studies have been conducted to discover empirical correlations for forced convective heat transfer from cylinders, plates and other geometrical configurations. For basic configurations such as a flat plate, analytical expressions can be developed for the Nusselt number, in terms of the Reynolds and Prandtl numbers. However, empirical correlations based on experimental data, are generally required for most bluff bodies including airfoils in an external flow. A standard functional form for these correlations involves a product of the Reynolds and Prandtl numbers, raised to exponents that depend on various factors including flow conditions and geometrical configurations [101]. Past studies have established non-dimensional correlations of the Nusselt number for various types of flow configurations and regimes. Heat transfer correlations were developed for a horizontal slender cylinder by Datta et al. [102], including effects of non-uniform slot injection and transverse curvature. Also, effects of viscous dissipation and varying Prandtl numbers on the resulting

skin friction and heat transfer coefficients were reported. Research presented in this thesis correlates experimental data into this standard functional form.

2.9.2 Analytical and numerical convection heat transfer

Past studies indicate that a wide diversity of methods and configurations of forced convection have been studied experimentally. In certain cases, analytical methods have been developed to gain additional insight into forced convection correlations. Turbulent mixed convection from a large vertical flat surface at high temperatures has been analyzed by Evans et al. [103]. Predicted temperature and velocity profiles showed good agreement with experimental data. Lachi et al. [104] analyzed transient heat transfer based on an integral method with fourth-order Karman–Pohlhausen polynomials and a similarity solution for velocity and temperature profiles within the boundary layer. The approximate solution was presented for a laminar forced convection problem, with a time-dependent heat flux over a flat plate. A differential method and similarity transformation were used to validate the approximate integral method.

Numerical methods have also been used extensively to develop forced convection correlations. Aydin et al. [105] analyzed steady, laminar mixed convection from a heated/cooled vertical flat plate in both opposing and assisting buoyant flows. Using a finite difference method, the Nusselt number (Nu) was correlated against the Prandtl number (Pr), Richardson number (Ri) and Eckert number (Ec). When predicting heat transfer coefficients numerically, near-wall grid refinement is needed to refine elements sufficiently to capture large spatial gradients of temperature near the wall. In certain cases (such as boundary layer separation), different procedures are required, depending on the surface location. As a result, numerical methods

often have limited applicability, when developing general correlations for forced convection over a range of flow conditions.

2.9.3 Experimental procedures of convection heat transfer

For heat transfer characterization presented in this thesis, an experimental procedure for developing correlations for forced convection past an airfoil is used. Past experimental studies of convective heat transfer have used various methods of measurement, including thermocouples, flux meters and other sensors. Adeyinka and Naterer [106] utilized methods of particle image velocimetry and particle induced fluorescence for heat transfer measurements, which could be extended to entropy production measurements [107].

Laguerre et al. [108] used a heated fluxmeter to determine the convective heat transfer coefficient between a wall and packed bed (3.8 cm diameter spheres) in a low velocity air crossflow. Akyol and Bilen [109] developed an experimental apparatus to study heat transfer and friction in a horizontal rectangular channel, with attachments of hollow rectangular profile fins over a heated surface. Temperatures were measured by thermocouples installed along the test section centerline. Correlation equations for the Nusselt number and friction coefficient were developed. Other experimental methods for convective heat transfer analysis include back-calculations from transient temperature data, mass-loss measurements and psychrometric methods [110]. Hanjalic [111] discussed various limitations of experimental techniques in measurements of turbulent forced convection. The studies included turbulence and magneto-hydrodynamic flows with heat transfer.

Convective heat transfer from in-line electronic chips in a vertical rectangular channel was studied experimentally by Bhowmik et al. [112]. The authors used chromel-alumel thermocouples along the chip centerline to measure temperatures between upstream and downstream locations within the channel. The results correlated the Nusselt number variations against the Reynolds number and Grashof number, with respect to the channel hydraulic diameter. Naterer [113, 114] has correlated transient variations of temperature measurements with entropy changes, which can provide useful insight regarding convective instabilities in the flow field. Kendoush et al. [115] performed an experimental study of fluid flow and convective heat transfer in the wake region of a circular disk, using thermistors and a Pitot tube to measure heat transfer and pressure distributions. The results established the local heat transfer coefficient along the diameter in the Reynolds number range between 1.4×10^3 and 5×10^4 . Kobus [116] presented an experimental method for obtaining convective heat transfer coefficients from thermistor measurements in a circular disk configuration. Self-heating thermistors were used to measure the convective heat transfer rate and the average wall temperature.

Van Fossen et al. [117] investigated heat transfer from a cylinder with four simulated ice shapes. Heat transfer correlations for a circular cylinder with different ice shapes and ice surface roughness were developed with the NASA Lewis Icing Research Tunnel, using heat flux gages, strip heaters and hot wires. Based on the mass and heat balance equations, the model was employed to simulate the roughness of ice accretion on aircraft wings. Regarding the water mass, roughness and heat transfer, the simulated ice shaped profiles showed close agreement with data collected in the wind tunnel experiments.

Those past studies show that many methods have been developed to measure heat transfer coefficients in convection problems for bluff bodies for external flows. These studies have generally focused on a cylinder, plate or wall. The experimental methods can measure the temperature or heat flux with thermocouples, thermostat and heat flux meters. This proposed research focuses on heat transfer from airfoils in an air flow, with and without water droplets impacting on the airfoil.

2.9.4 Characteristics of water droplet spray

Hedrih et al. [118] investigated the distribution of water droplets by an ultrasound sprayer. Also, the density distribution function was determined experimentally. The liquid water content (LWC) and temperature are two significant meteorological parameters for ice accretion at the leading edge of wings (Fuchs and Schickel [119]).

Based on an unsteady Reynolds-averaged Navier–Stokes (RANS) formulation, Yoon et al. [120] simulated and investigated the flow of water droplets over cylinders, both heated and unheated. Five K-type thermocouples and heaters were installed in an aluminum cylinder with a diameter of approximately 29.2 mm and 305 mm in length. Also, Phase Doppler Interferometry (PDI) was utilized to measure the droplet mean size and velocity, downstream of the cylinder. The simulated and provisional results showed good agreement, in terms of the mean size of droplet and velocity distributions. Kollár et al. [121] examined an air/dispersed water droplet two-phase flow in an icing wind tunnel. The gravity effects of large droplets and droplet collisions were considered. The results indicated that the liquid water content would concentrate in the bottom half of the wind tunnel for large droplets and low air speed. The droplet size distribution near the spray nozzle outlet is different with an icing object in the test

section due to movement of mixed flow. The phase change of super-cooled droplets to ice and the transformation, including heat and mass transfer with evaporation and sublimation, were studied both in experiments and modeling by Strub [122]. Visualization of the droplet crystallization was observed and compared with modeling results and close agreement was achieved. Kollár and Farzaneh [123] developed a theoretical model to simulate the evolution of droplet size distributions; it may be used to calculate two-phase flow under in-cloud icing and freezing drizzle conditions.

These previous studies indicate that a wide diversity of methods and configurations of forced convection with water droplets has been studied elsewhere. In particular cases, experimental methods have been developed to gain additional insight into the effect of water droplets. Jia and Qiu [124] investigated the dynamics of droplets and heat transfer in spray cooling, including a heating system, spray system and a droplet characterization system. Laser Phase-Doppler Anemometry (PDA), based on a dual-mechanism-scattering model, was used to obtain the diameter of water droplets. A hollow copper cylinder with a cartridge heater and K-type thermocouple was used to determine the temperature and heat flux. A multi-nozzle spray system range with mass fluxes from 0.156 to 1.20 kg/m²s supplied the water droplets. The results show the critical heat flux (CHF) can be avoided by water droplet cooling. Sawyer et al. [125] studied a horizontal, upward facing flat surface impacted by a stream of water droplets, to obtain the effects of the droplet diameter and collision velocity on the critical heat flux. Three experimental systems, including a heater system, instrument system and a fluid delivery system, were used in that research. The CHF was given as a function of the Weber and Strouhal numbers of the impacting droplets.

Chen et al. [126] employed a copper cylinder head with four 500-W cartridge heaters to investigate the impact of spray parameters on the CHF and heat transfer coefficient. They showed that the mean droplet velocity and mean droplet flux had the most significant effect on the CHF and heat transfer coefficient, while the CHF and heat transfer coefficient increased at higher mean droplet velocities. The temperature transition of freezing droplets in a cold air flow from a junction of a thermocouple, as well as a simulation to predict the temperature transition and the freezing time of a water droplet, were presented by Hindmarsh et al. [127].

2.9.5 Multi-phase convective heat transfer

Researchers have studied water droplets impinging on cables or cylinders, as well as some other shapes. Some performed analysis or simulations of heat transfer coefficients with water droplets for various types of flow configurations and regimes. Fortin et al. [128] developed a model of coupled mass and heat transfer during ice accretion on an airfoil surface. Naterer [129] analyzed the energy and mass equations in the ice and unfrozen water layers with incoming droplets. A single energy conservation equation was used to calculate the surface Joule heating rate for rime transition and combined rime/glaze ice conditions. Fu et al. [130] developed a novel, 2-D icing model to simulate the process of ice accretion on overhead power line cables. The water droplet trajectory, film thickness over the surface and water droplet flow direction, Local Collision Efficiency (LCE) and local Heat Transfer Coefficient (HTC) were computed. The predicted icing shapes under various conditions were obtained. Ge and Fan [131] simulated the impact of sub-cooled water and n-heptane droplets on a superheated flat surface to study the fluid dynamic behavior of the droplet. The phase change heat transfer and droplet dynamics were analyzed and compared with previous experimental data. The results showed that the heat flux and thickness of the vapor layer were strongly

influenced by the super-cooling magnitude. Naterer [132] performed a numerical analysis to simulate multiphase flow with impinging water droplets on an icing surface with a control-volume-based finite element method (CVFEM). Tsao and Rothmayer [133] reported a viscous–inviscid interaction model based on a triple-deck structure to simulate the heat transfer through an air boundary layer with ice and water films. The ice roughness on the leading edge of a NACA 0012 airfoil was discussed under glaze icing conditions in a high Reynolds number simulation.

Based on this survey, the previous research in heat transfer with water droplets and icing conditions has mainly concentrated on cylinders, flat surfaces and overhead cables. Some researchers studied the droplet dynamics and mechanics of water droplet collisions. However, no experimental correlations of Nusselt and Reynolds numbers of heat transfer from airfoils with water droplets could be found in past studies. This thesis addresses the lack of data on icing of wind turbine blades and heat transfer with water droplets impinging on an airfoil. This is an important aspect in the de-icing phase.

2.10 Operation of wind turbines

Various past studies have focused on operational problems of wind turbines, such as the lifetime, effectiveness, capacity factor, different control systems and so on. Some of these studies are reviewed here, since they contain relevant information that will be used to characterize wind turbine operation in a simulated icing event.

Krokoszinski [134] studied a systematic mathematical approach to the operation and maintenance (O&M) of wind turbines, including the general efficiency, productivity, effectiveness, Total Overall Equipment Effectiveness (TotalOEE), electrical energy production and delivered (sold) electrical energy. Also, the theoretical production time, available production time and valuable production time per unit of full load hours were studied. Krokoszinski [134] developed a calculation scheme to quantify wind farm production losses, in terms of planned or unplanned downtimes and speed losses, as well as the associated reduction of revenues relative to the theoretical maximum of annual wind park revenues. Torres et al. [135] developed an analytical expression to calculate site effectiveness in pitch regulated wind turbines. Different situations were considered, including the cut-in wind speed and maximum effectiveness values for constant-speed wind turbines.

A procedure based on an inverse reliability approach was presented by Saranyasoonorn and Manuel [136] to estimate nominal loads for a conventional load-and-resistance-factor-design format. The results from a 600 kW three-bladed horizontal-axis wind turbine showed that extreme design loads occurred by a full random characterization of both wind conditions and a short-term maximum response. The operational characteristics and the power output of grid-connected wind farms were reported by Abderrazzaq [137] during six years of operation. The variation of wind power output, wind speed and capacity factor were analyzed for single turbines and the entire wind farm. A correlation with external and internal factors affecting the wind turbines was shown. Ekelund [138] investigated the continuous control of a yaw servo in a 2-bladed wind turbine, including the tower bending structure and the motion of the turbine.

Riziotis and Voutsinas [139] carried out computational studies to test the impact of complex terrain wind conditions on the loading of wind turbines. Bianchi et al. [140] analyzed the control of variable-speed wind energy conversion systems (WECS), which were called linear parameter varying (LPV) systems. The control system attempted to maximize the conversion efficiency, safe operation, resonant mode damping and robust stability. Akhmatov et al. [141] used a dynamic simulation tool, PSSIE, to study a large offshore wind farm with many grid-connected wind turbines. A Matlab program was used to simulate the performance of a 5-kW wind turbine system by Sürgevil and Akpınar [142]. Bianchi et al. [143] studied a new approach to analyze variable-pitch control regulation, which considered various optimization criteria and compromised between limitations of the pitch actuator and the regulation performance.

Bouscayro et al. [144] investigated a control decomposition system for energy management of each part of a wind turbine, and global control, which performed power objectives and system constraints. Fernandez et al. [145] proposed equivalent models of wind farms with fixed speed wind turbines, by aggregating wind turbines into a matched wind turbine that operated on a substitute electrical network. These new models reduced the computation times and they were used to represent the dynamic behavior of wind farms on power systems, both for wind fluctuations and grid disturbances. Shokrieh and Rafiee [146] analyzed a fatigue damage model to predict the lifetime of a wind turbine, ranging from 18.7 to 24 years in worst and best case situations, respectively.

A 500-mm diameter wind turbine was developed for a series of tests, including the production of wind energy, rotation of wind turbines, power coefficients, and torque of wind turbines

over a wide range of wind speeds, by Hirahara et al. [147]. Also, PIV measurements around the wind turbine were made to visualize the flow field.

In addition to these previous papers, studies investigated other aspects of wind turbines and wind farms, such as hybrid systems in remote areas, grid connection, independent power supplies, simulation of wind turbine capacity and other problems of operation of wind turbines.

A novel approach to understanding turbine standstill and availability was developed to predict the monthly energy production, including the maintenance and fault hours (Abderrazzaqa and Hahn [148]). The authors showed that the frequency of the faults in 42% of turbine shutdowns was caused by network disturbances. Also, 70% was attributed to grid disconnections, whereas the voltage variations and the circuit breaker opening comprised almost 22% of these faults. The time distribution of the network faults was also investigated to illustrate the impact on the turbine standstill. Gómez-Elvira et al. [149] developed a calculation method based on an explicit algebraic model for the components of the turbulence stress tensor. The method was used to estimate an upper limit of the turbulent kinetic energy and the standard deviation of the three velocity components.

Harrison and Wallace [150] performed a sensitivity study involving wind and wave energy production, as well as economics based on wind and wave changes over the past few decades. A dynamic approach towards a Life Cycle Assessment (LCA) of renewable energy technologies was developed by Pehnt [151]. It showed that the input of finite energy resources and emissions of greenhouse gases were extremely low, compared with a conventional energy

system. Also, the other environmental impacts of renewable energies were not conclusive and further work would continue to reduce these impacts.

A grid cell approach was employed by Hoogwijk et al. [152] to assess technical and economic potential of onshore wind energy. Output of 96 PWh per year was estimated to be the technical potential in the world with 0.07 US\$ kW/h and lower in Canada, USA, South America, former USSR and OECD Europe. An analytical formula for the capacity credit based on the penetration level of the wind power, including an overall capacity factor or annual use of the wind turbines, has been developed by Voorspools and D'haeseleer [153]. The resulting analytical formula can be used to estimate the capacity credit, avoiding the use of elaborate stochastic reliability evaluations. The problems of wind farm generator displacement were investigated by Ozturk and Norman [154] for improving profits of wind farms. The authors applied a heuristic methodology to derive an effective solution.

2.11 Summary

Previous studies have provided information about wind turbines working under different climates and environments. The literature review regarding design of wind turbine blades in Section 2.4 helped to build a 3-blade wind turbine model. Specifically, Section 2.8 and 2.10 focused on anti-icing or de-icing and operation of wind turbines under cold climates that provided more informations wind energy losses under cold climates. However, no research has been reported on a wind turbine model under simulated icing conditions in a wind tunnel. An experimental investigation of losses of wind energy is conducted with the scaled 3-blade

turbine model using an electrical generator in the wind tunnel in Department of Mechanical and Manufacturing Engineering at the University of Manitoba. The HAWT model is used to measure ice accretion over the wind turbine model during a simulated icing event, when operating under various icing conditions. Energy losses and characterization of wind turbine operation during an ice event are investigated. Temperature, velocity of wind in the tunnel and current and voltage are the measured parameters used to understand the energy losses, ice accretion and irregular shedding during turbine operation (see Chapter 4).

Cold weather is one of the main challenges for wind energy utilization in North America. The thesis will concentrate on wind turbines operating under icing conditions, including heat transfer for de-icing, aerodynamics, blade characteristics and energy loss due to icing. Literature review in Section 2.5 – 2.7 provided previous findings about aerodynamics of airfoils with and without ice and wind turbines. Most past research on iced aerodynamics focused on aircraft high Reynolds numbers and Mach number (greater than 0.10). Therefore, the subject of the interest for the thesis is that Reynolds number in aerodynamic experiments of airfoils is less than 1.5×10^6 and Ma less than 0.10. The different of aerodynamics between iced airfoils in wind turbine blades and aircrafts is researched. The following chapters (Chapter 3 and 5) will give more explanations about the experimental setup of a 2D airfoil and the results of ice shapes over the airfoil and iced aerodynamics. In this research, ice shapes over the airfoil form under real-time icing conditions inside the wind tunnel. A force balance measurement system is utilized to achieve the objective of determining aerodynamics of wind turbine blades including the lift, drag and moment coefficient variations during a simulated icing event. Chapter 5 has the different characteristics obtained based on ice thicknesses, shapes and angles of attack of the airfoil. The results of aerodynamic

characteristics of airfoils give a better understanding of mechanics of wind turbine power losses under icing conditions.

Section 2.9 focused on research of convective heat transfer with or without LWC for different blunt bodys, such as a cylinder, plate or wall. Including experimental methods of heat transfer coefficient, temperature measurement, liquid water content and droplet distribution, flow visualization and various simulation codes were used in these studies. However, limited number of research concentrated on heat transfer coefficient for an air flow over an airfoil. In Chapter 6, the experiments will focus on heat transfer characterization of an airfoil, with and without water droplets. The results will show the relationships between Nusselt and Reynolds numbers under pre-icing conditions. The correlation of Nu and Re numbers of an airfoil for de-icing and anti-icing is developed from the new experimental data. Heat transfer characterization at various points along the blade will be presented in Chapter 6 to improve the understanding of heat and mass balance models. Also, characterization of the heat transfer from airfoils is used to predict energy requirements for thermal mitigation strategies and blade performance changes.

Chapter 3

Experimental setup and procedures

As may be seen in the literature survey in Chapter 2, many studies have contributed to our present understanding of the selection of airfoils for wind turbine blades, the aerodynamic effects of icing of wind turbine blades, and wind turbine operation under different climates and environments, especially extreme climates. Less research has focused on power losses in experimental icing conditions, the aerodynamic characteristics under simulated icing conditions created by super-cooled water droplets, the heat transfer from airfoils, with and without water droplets.

In order to achieve the objectives enunciated in Section 1.2, an icing wind tunnel, instrumentation and airfoils are required to simulate various climatic conditions. Table 3.1 summarizes the investigations that are carried out in this thesis.

Table 3.1: Test content in the investigation

	Test model	Content	
Power losses due to icing (Chapter 4)	3-blade wind turbine	Glaze ice	Rime ice
Aerodynamics of iced airfoil (Chapter 5)	NACA 63421 airfoil	Glaze ice	Rime ice
Convective heat transfer (Chapter 6)	NACA 63421 airfoil	AOA = 0 without LWC	
		Varying AOA without LWC	
		AOA = 0 with LWC	
		Varying AOA with LWC	

These proposed experiments require suitable facilities to generate the results. The following sections describe the experimental facilities and measurement apparatus.

3.1 Icing wind tunnel and instrumentation

3.1.1 Overall capability and sub-system components

This section describes the refrigerated wind tunnel shown in Figure 3.1 that will be used for the proposed experiments, described in Chapter 1, to perform the different studies of a 3-bladed wind turbine and the characterization of blades during various icing events. The icing tunnel test section is a rectangular duct of 916 mm width and 916 mm height. The wall of the test section 1.5 m in length is transparent, so observations and photographs can be readily obtained. The airfoil test piece is mounted horizontally within the test section. The velocity within the wind tunnel can reach up to 42 m/s at temperatures down to -35°C with small water droplets (from 10 μm to 1000 μm , MVD of 100 μm) sprayed into the cold chamber (see Figure 3.1 and Figure 3.2). Also, a constant air velocity can be varied from 5 m/s to 15 m/s, with large water droplets (MVD of 1 mm) sprayed into the cold chamber. LWC in the tunnel can be controlled varying from 0 to 2 g/m^3 . The air velocity is adjusted through an electrical control panel by varying the frequency of the fan blower motor. The wind tunnel setup was also presented by Naterer et al. [155]. In this thesis, the sub-duct and the high speed flow test section in Figure 3.2a will be used.

When an outer tunnel test is required, the sub-duct in the tunnel must be removed from the cold chamber. The removable ductwork was a special arrangement to ensure that it remains airtight, without vibrating in the airstream.

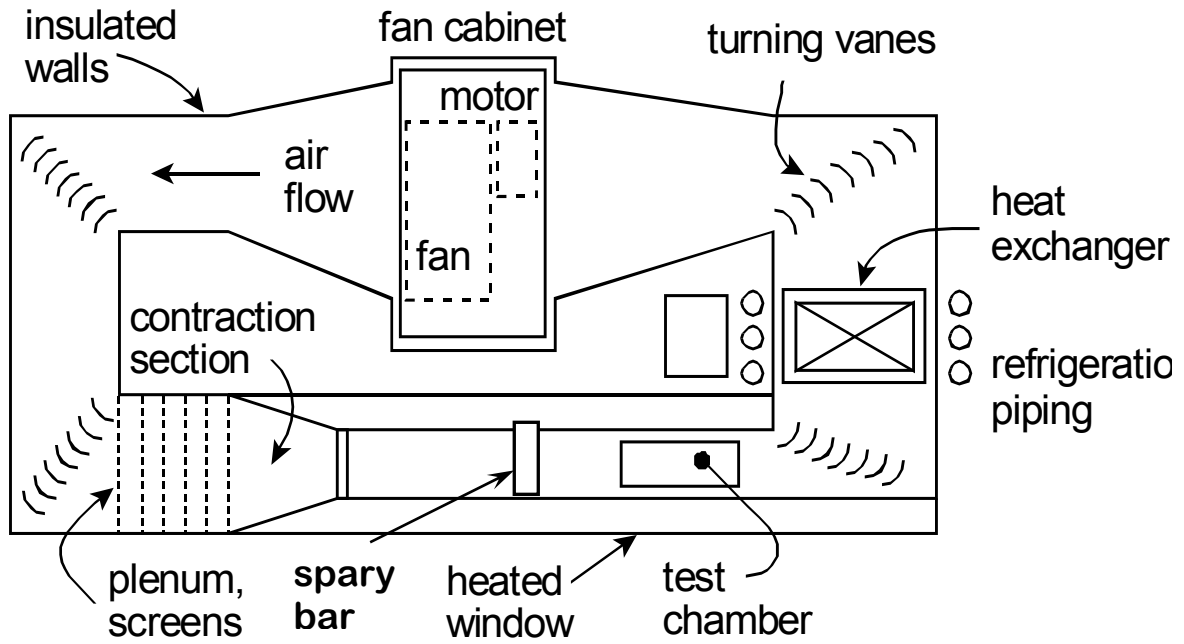


Figure 3.1: Top view of wind tunnel

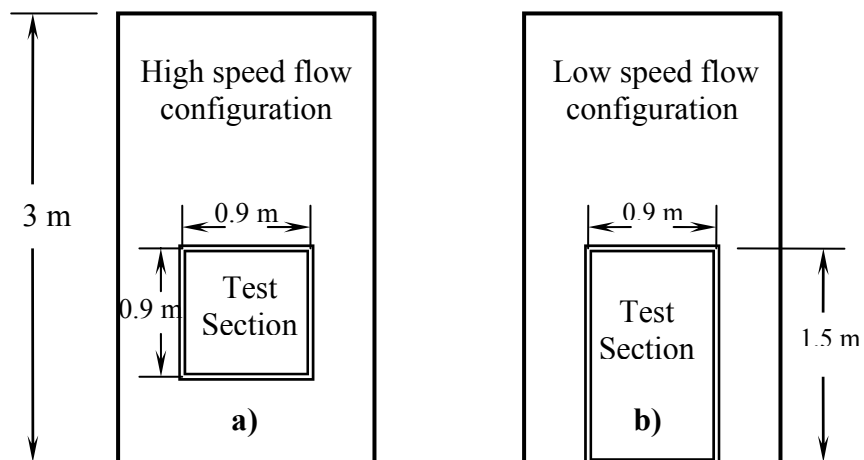


Figure 3.2: Side View of spray flow / ice tunnel: a) high speed and b) low speed

In order to keep the surface free of frost and allow visibility, the window of the outer cold chamber is heated. Windows are located on the front, back and top sides of the test area for viewing and reflection by laser light for PIV measurements. These can be seen in Figure 3.1 and Figure 3.2. Plenum screens after the contraction section provide a highly uniform flow,

reaching the test section. The entire ductwork of the test section is removable to permit different test sections for various test models. Doors are installed at various locations around the perimeter of the icing tunnel to allow access inside for spray and test piece adjustments, as well as cleaning of the ice after testing and regular maintenance of the various components. Also, a de-icing system is built within the floors and tied into the compressors for refrigeration of the icing tunnel.

Three evaporator heat exchanger systems are installed; each system can provide about 95,300 Btu per hour of cooling for a total capacity of 285,900 Btu per hour. The following systems are components of the icing tunnel:

- Electronic control panels
- Oil separators
- Head pressure control
- Receiver inlet and outlet shutoff valves
- Service and safety relief valves
- Compressor contactor, pump down switch
- Control transformer
- Solid-state protection or internal lines break for compressor
- Recycle pump down cycle

The type of compressor is a Copalmetric 30 hp discus, single stage compressor designed for refrigerant R422. The compressor housing is located in a separate room underneath the laboratory. In addition, a defrost system is included to remove an ice buildup should it occur during a test. The heater within the icing tunnel is designed to allow for a higher pressure drop, due to ice buildup throughout the duration of the tests.

3.1.2 Water spray system

There are many challenges to simulate natural icing conditions in a wind icing tunnel. A spray bar is mounted in the refrigerated wind tunnel to simulate icing conditions. The spray bar is designed with 4 nozzles in an aluminum streamlined shell. The spray bar is 910 mm long and the nozzles are installed with a uniform spacing interval, in order to establish a uniform spray. The shell of the spray bar is designed to contain the nozzles, as well as reduce large magnitude disruptions to the airflow in the tunnel. The shape of the bar is a thin symmetrical airfoil (152 mm wide wedge) with both ends rounded to reduce flow disturbances. Two heating strips are installed between the nozzles and the aluminum shell to prevent the water and nozzles from freezing during low temperature testing. The heating strips are resistive Ni-Chrome wires embedded in a silicone jacket. They are heated by a variable power supply using a 10 A transformer that can be adjusted from 0 to 120 V, thereby allowing variable heating up to 1,200 Watts (see Figure 3.3). The operating condition of the spray bar is monitored by a thermocouple mounted on one of the nozzles in the spray bar and the water pipe section, through the wall of the wind tunnel. The spray bar was commissioned as part of this research work.



Figure 3.3: Nozzle distribution with heaters and thermocouples inside the spray bar

In order to reduce flow field disturbances at the outlet of the duct module within the tunnel, where a test model will be set up, the spray bar is mounted 4,300 mm away from the outlet of wind tunnel. This distance allows the water droplets to have sufficient time to form ice in a low temperature environment. The flow to each nozzle is calibrated by controlling the atomizing air flow. Calibrating the mass flow to each nozzle is time-consuming and it requires adjustment of the valves until a uniform flow is obtained. Figure 3.4 shows the spray bar in the wind tunnel.

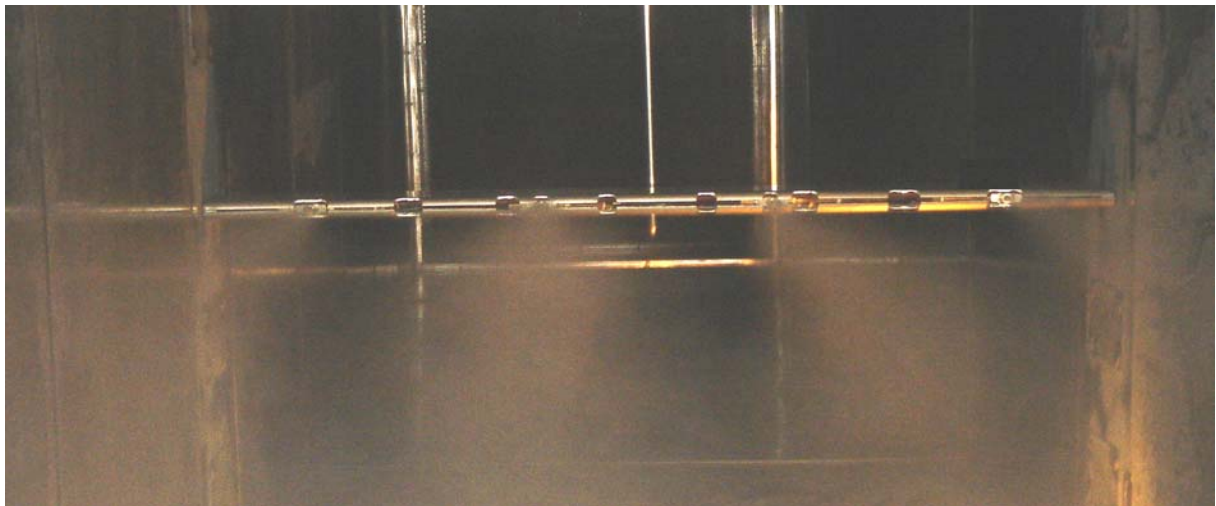


Figure 3.4: Spray bar in the icing wind tunnel

Super-cooled water is supplied by a fluid system including a water tank, cooling compressor, pump, temperature controller, water pressure controller, pipes and valves. The water temperature can be set close to 0 degrees and the water pressure can be adjusted up to 70 psi. Water flow is controlled by water valves and flow meters. Figure 3.5 shows the water flow-meters and air pressure indicators with valves. Insulated foil is used to keep the water temperature at cold levels. Also, an air filter, control key, manometer and cord for nozzle heaters can be seen in Figure 3.5.



Figure 3.5: Water flow meter and air pressure controller

Different types of ice will form in the wind tunnel by adjusting the air temperature in the tunnel, atomizing air flow and water droplet sizes, water temperature and water/air pressure. When glaze ice is required in an experiment, the air temperature in the tunnel is adjusted below 0°C and large water droplets are selected, by adjusting the water and air pressure in the spray bar. If the atomizing air pressure is increased, the water flow is decreased, and the air temperature is lowered, rime ice will occur over the test piece surface. The significant difference between glaze and rime ice is obtained through different ice accretion surface temperatures and sizes of water droplets.

3.2 HAWT with 3-D twisted blade operation under icing conditions

3.2.1 Fabrication of small wind turbine model

The prototype blade of a scaled wind turbine model was acquired from a wind blade manufacturing company. It is 1,300 mm long and it was scaled down to 420 mm to fit the test section of the icing wind tunnel. A 3-D scanner (ShapeGrabber 3D Scanning systems, Model: LM 1250 GT [156]) was used to obtain 3-D profiles of the blade. After the profile of the blade

was scanned, all scanned data were merged together to form a digital blade. Merging the data of the blade together was a challenge and it was very time consuming, because the blade is so thin and the profile data obtained from the blade tip has little variation. Also, there are no obvious characteristic points (used to identify the scanned object in reverse engineering) near the tip of the blade. Figure 3.6b shows the blade after digitization (merged all scanned data together) through Geomagic Studio [157] developed by the Raindrop Company, showing flaws in the surface.

In order to manufacture the blade model, the rough profiles were smoothed to avoid faults in the surface. Also, the blade centre was hollowed to reduce the weight of the blade using Autodesk Inventor software. Specific sections from the digitized blade were chosen and then flaws were modified in each airfoil. After all flaws were repaired, all airfoils were joined together to form a whole blade. Figure 3.6a shows the blade after being processed by Autodesk Inventor, which is the method used to fabricate each of the 3 blades, with a rapid prototype machine. It uses resin to fabricate the model.

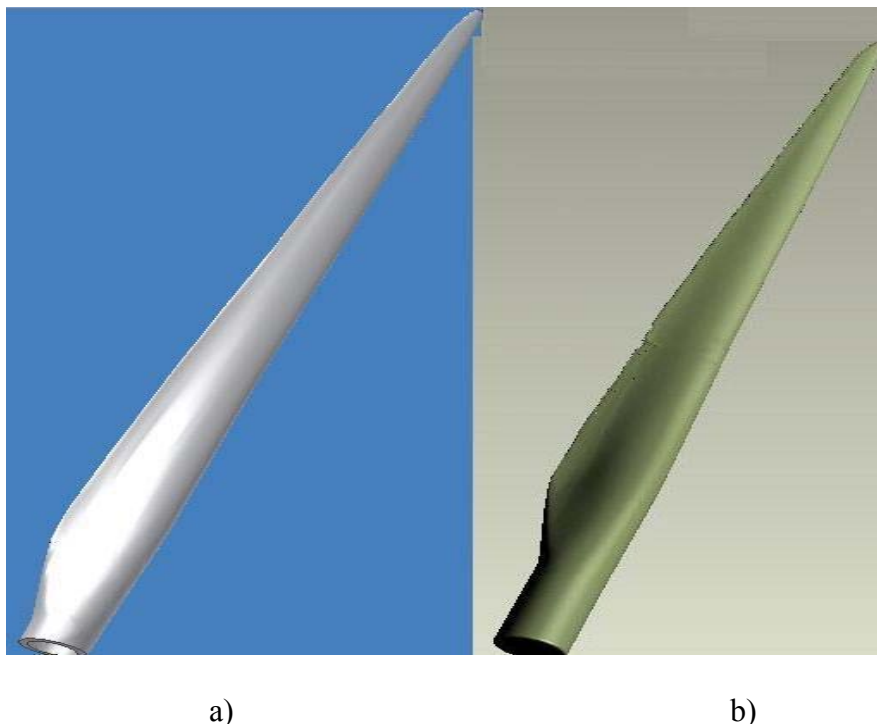


Figure 3.6: Digitized blade: a) smooth blade and b) blade before smoothing

With a twisted blade, the pitch angle changes along the length. The pitch angle of a blade is important when a wind turbine extracts energy from the wind. The blade pitch angle affects the energy output and operational characteristics of the wind turbine. The initial pitch angle is important to ensure that the small turbine works efficiently in the tunnel with this blade model. An important aspect of blade design is to define the twist angle as a function of μ ($\mu = r/R$) from 0 to 1. Most references such as Refs [53] and [158] assume that the pitch angle is 0 at $\mu=1$. Simulation studies on the aerodynamics of 3-D airfoils by Johansen and Niels [159] indicate that the local pitch angles at the tips of wind turbine blades are zero. Adaptors with a small columella have been used to adjust the pitch to connect blades and the hub. Figure 3.7 shows that the blade model was set to 0 pitch angle at the tip and the blades were glued with adaptors. The pitch angles of the blades in the model are changed by adding or removing 0.5mm thickness washers, as shown in the following section.

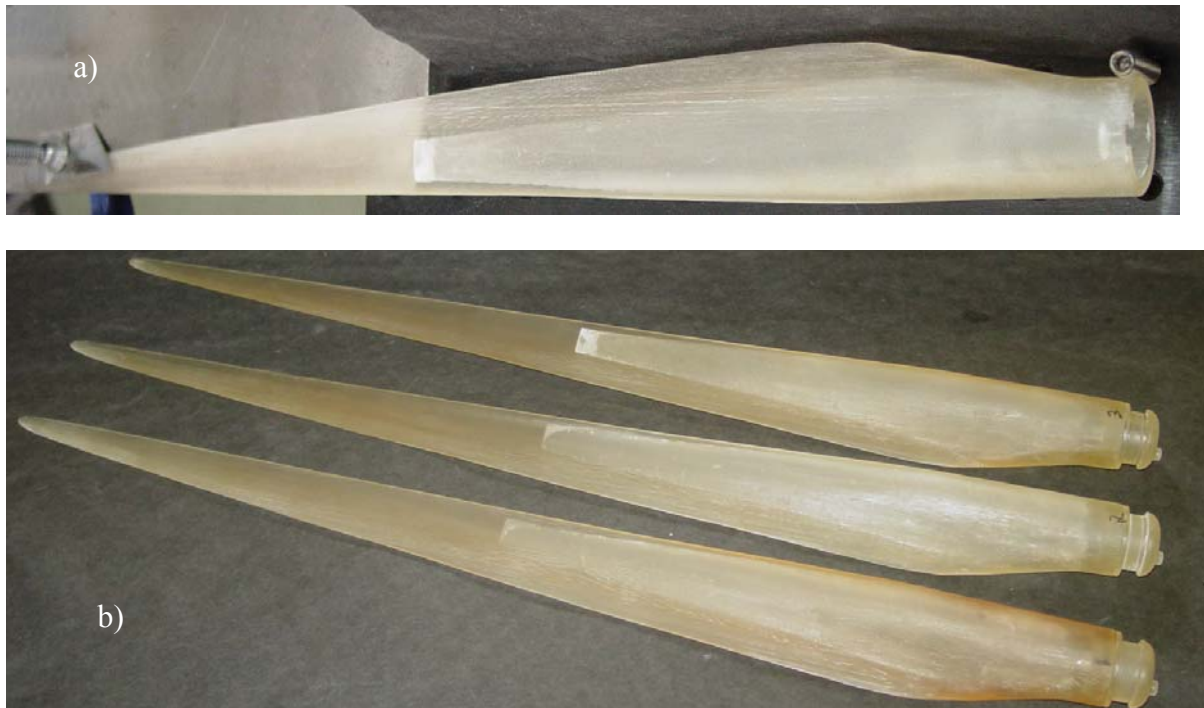


Figure 3.7: a) a blade model at 0 pitch angle and b) blades with adaptors

A hub was designed to connect the blades to the DC generator and also allow varying pitch angles of each blade during an icing event. This aspect is important to the study, in order to determine whether varying the pitch angles of the blades can help during various icing conditions. Figure 3.8 shows the manufactured hub and hub centre. A set screw can be used to change the pitch angle of the wind turbine blades by changing the position of the hub centre with 0.5 mm washers (also shown in the figure). The brass hub has an 8-mm diameter hole to accommodate the shaft of the generator.

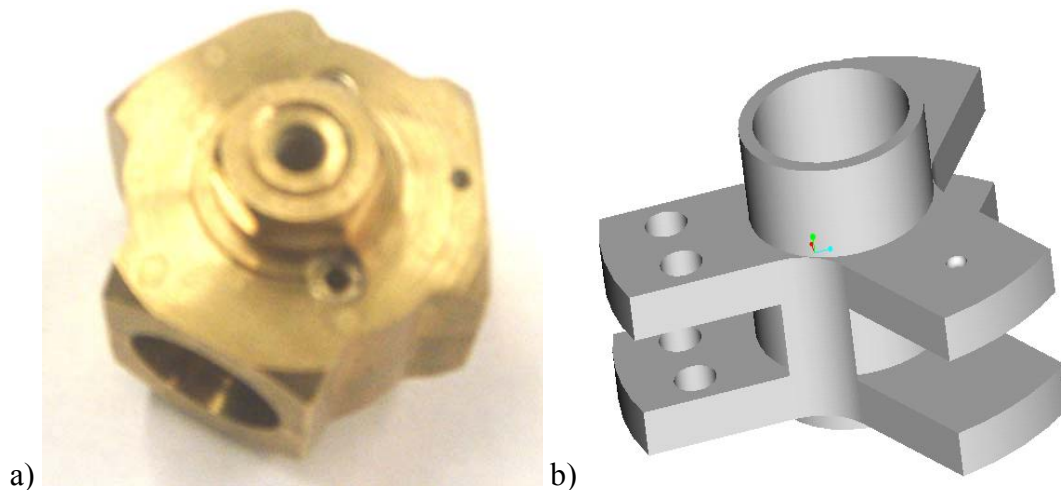


Figure 3.8: a) hub and b) hub center

The 3-D blades, hub and generator are assembled to construct a prototype wind turbine. The washers between the hub centre and hub are able to adjust the pitch of the blades. The washers were made from brass with 0.5 mm thickness and one can adjust the angles by 2.8° . The 0 degree of the blade installation depends on the angle of the tip of the blade. Figure 3.9 shows the wind turbine working in the wind tunnel.



Figure 3.9: Wind turbine model with DC generator in the wind tunnel

The generator is a permanent magnet DC generator made by Windstream Power Systems Inc. The voltage of the output is 48 V and the maximum power is 144 Watts. The three-blade scaled wind turbine model is supported by a shaft (see Figure 3.9) during operation. By measuring the generator current, voltage, temperature, and wind speed in the tunnel, it is possible to study wind turbine operation during an icing event. The following section will discuss the measurement of twisted blade wind turbines.

3.2.2 Measurement of rotation, current and voltage

All sensors in the icing tunnel are built to handle icing and cold temperatures.

Remote optical sensor: The blade rotation rate of the wind turbine in the tunnel is measured by a remote optical sensor made by Monarch Instruments of Monarch International Inc. [161].

The sensor is capable of detecting a reflected pulse from a reflective tape target at distances up to 1 m from a rotating object and angles up to 45 degrees. In the experiment, the sensor is mounted on top of the wind tunnel at a distance of approximately 0.5 m from the shaft of the wind turbine and a slight angle from the perpendicular direction. The lights are turned off, so that only pulses from a reflective marker are received by the sensor. Water-proof reflective tape is applied to a blade. Also, the sensor is optically aligned to illuminate the target once per revolution. The green LEN On-Target indicator will blink at the input frequency rate when the sensor is properly aimed. The sensor power requirement is 5 V DC, provided by Connector Block SCB-100. The output from the sensor is a 0 - 5 V DC TTL pulse. It is connected to the PCI-7033E data acquisition board via Connector Block SCB-100. The speed range of the sensor (ROS-5 W) is 1~250,000 rpm and the operating temperature is -23°C to 121°C.

Transducers of current and voltage: The Series LTS current transducers are used to achieve a total accuracy better than $\pm 0.2\%$ at 25°C. In contrast to the majority of closed-loop current transducers available, the measuring resistor has been integrated into the transducer with an accuracy of $\pm 0.5\%$ and a temperature drift of 50 ppm/K maximum [162]. In this experiment, the LTS 6-NP is selected. This type of current transducer is a closed loop (compensated) current transducer using the Hall Effect, unipolar voltage supply (+5 V from the Connector Block SCB-100 box) and a compact design for PCB (Printed Circuit Board) mounting, which incorporates a measuring range and extended measuring range. The primary nominal r.m.s. current is 6 A, with a primary current measuring range of $0 \sim \pm 18$ A and an analog output voltage of 2.5 ± 0.625 V that can be obtained by the PCI 6033E. We also can change the measuring range for different connections in the transducer output side.

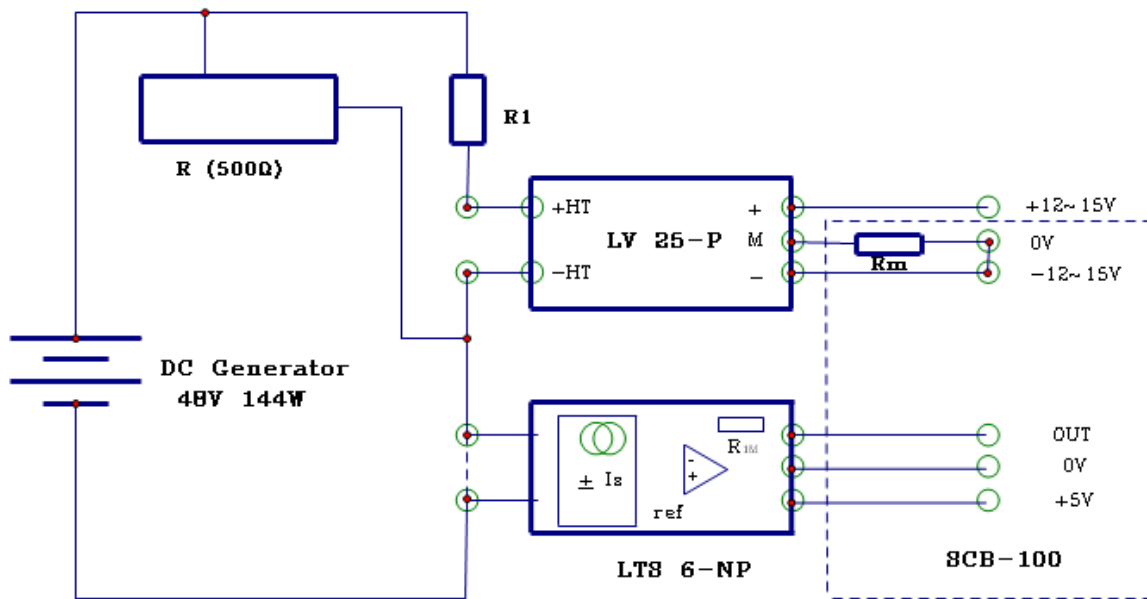


Figure 3.10: Circuit diagram of current and voltage transducer with DC generator

The voltage transducer LV 25-P is used to measure the voltage of the generator. The voltage transducer is based on the closed loop Hall Effect. The main difference between a current and voltage transducer is the addition of an internal primary winding with a large number of turns, allowing the voltage transducer to create the necessary ampere turns to measure the small primary current that is directly proportional to the voltage of interest. The electronics data of the LV 25-P is summarized as follows:

$$I_{PN} = 10 \text{ mA}$$

$$V_{PN} = 10 \sim 500 \text{ V}$$

$$\text{Supply voltage: } +12 \text{ V}$$

$$R_p = 250 \Omega, R_l = 5.8 \text{ K}\Omega, R_m = 150 \Omega.$$

Figure 3.10 shows the connection of the current and voltage transducer in the DAQ system.

Figure 3.11 shows the PC-based data acquisition system, including all parameters measured by softwares except for force measurement.

The results of the small wind turbine operating in the wind tunnel under icing conditions are presented in Chapter 4. Data acquisition of current, voltage and rotation will be presented in Section 3.4.

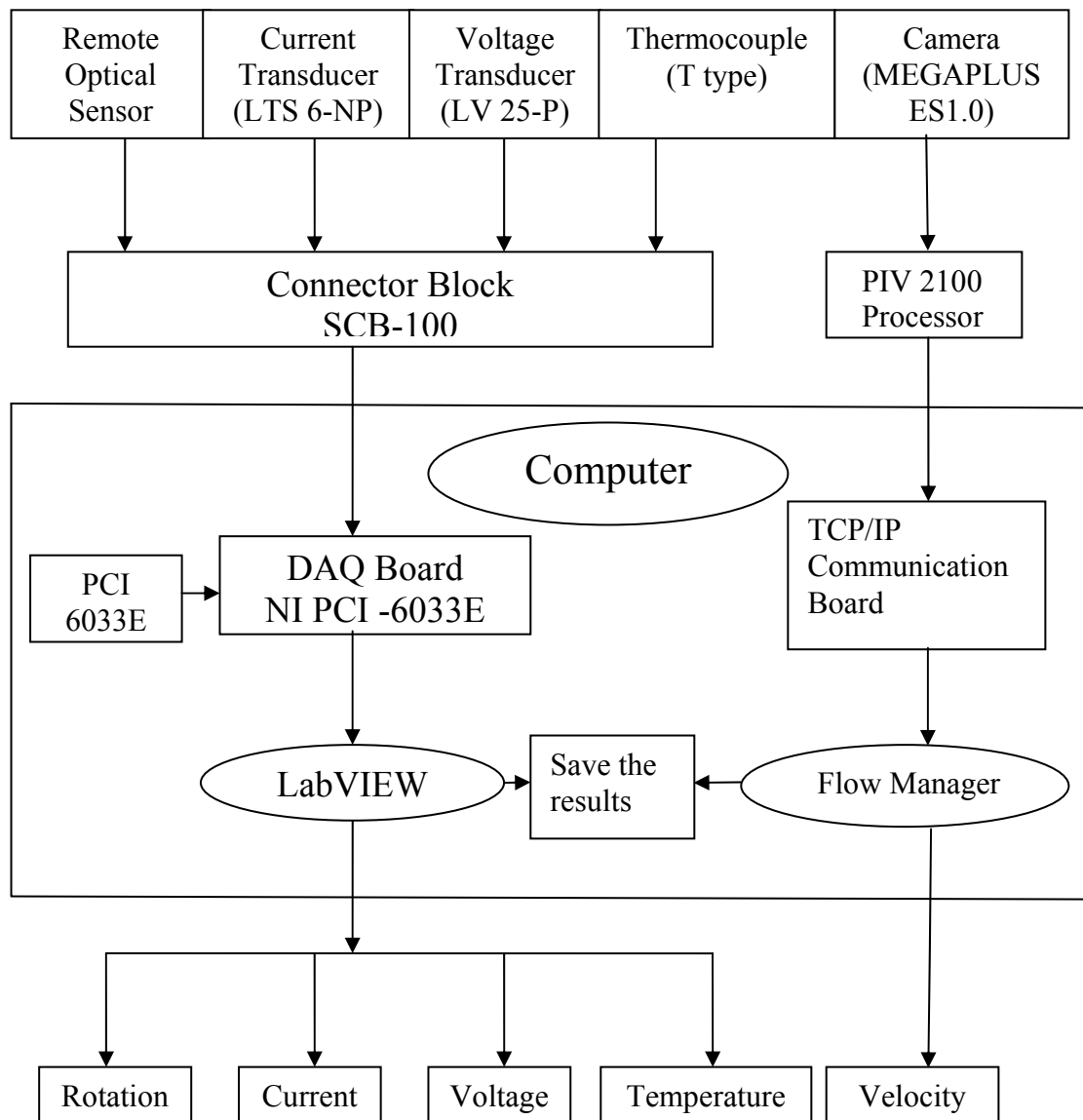


Figure 3.11: PC-based data acquisition system

3.3 Aerodynamic force characterization during icing

3.3.1 Force balance measurements

In order to study the aerodynamics of an airfoil under icing conditions, a customized force balance is used to measure the drag, lift and moment, based on 6 strain gauges on each side that can measure 3 directional forces and 3 directional moments. Figure 3.12 illustrates the force balance, which was custom designed to fit within the icing wind tunnel [163].

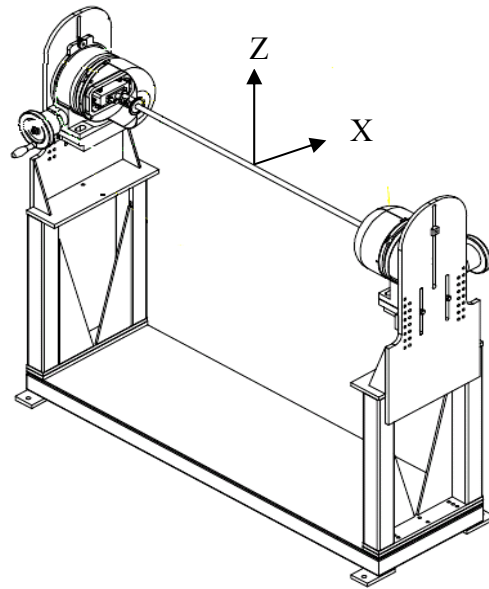


Figure 3.12: Structure of the side wall force balance



Figure 3.13: Side view of one balance wall with a shaft coupler

As illustrated in Figure 3.13, it can be seen that the force balance is very sensitive, due to the special structure of the C-beam configurations. The forces including normal force (Z axis direction), axial force (X axis direction) and moments in 3 directions can be measured and recorded by a computer. Figure 3.14 shows the data acquisition system, including a HBM MGC Plus laptop computer connected via Ethernet. HBM MGC Plus provides all necessary amplifiers, filters and digital conversion for each of the balance channels.



Figure 3.14: Data acquisition system: HBM MGC Plus and a Laptop

The force balance system is provided with a standalone data acquisition/processing system called FMS (Force Measurement System). The Windows 2000 operating system and FMS can be used to obtain data from the force balance. Table 3.2 shows the standard deviation of the calibration of the force balance from calibration results in April 2006 [163]. The force balance is calibrated to obtain the coefficient matrix constants to translate the voltages to forces and moments. A separate program is available to perform this calibration using weights applied to a calibration beam. The maximum force measures 111 N in a single direction included weight.

Table 3.2: Standard deviation of calibration results (6×39 Non-Iterative)

	File #	FX	FY	FZ	MX	MY	MZ
Loading	743	0.037%	-N/A-	0.128%	0.205%	0.271%	0.849%
	Point						

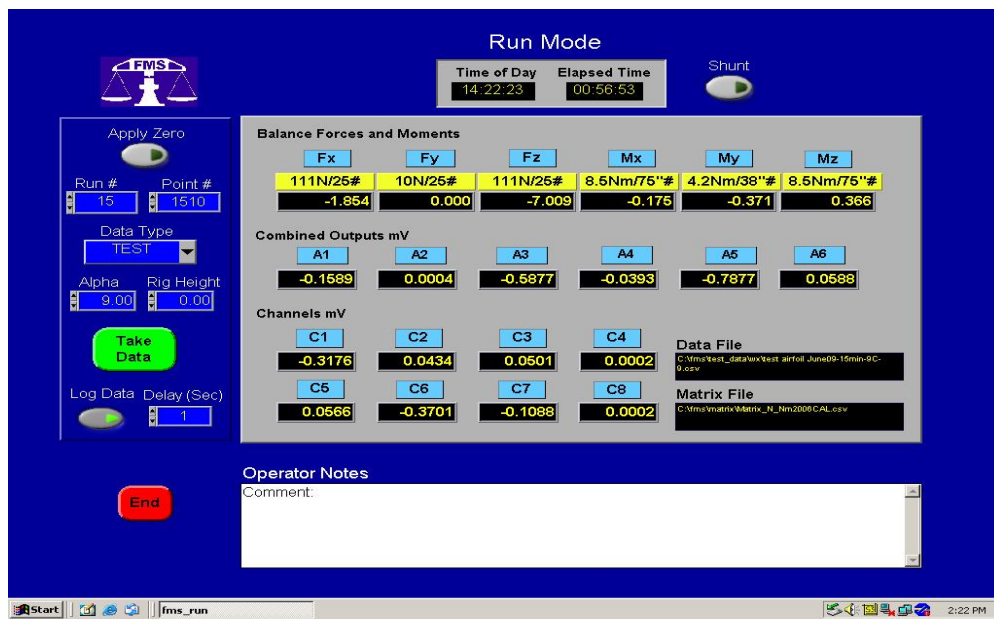


Figure 3.15: Acquisition of data from FMS force measurement system

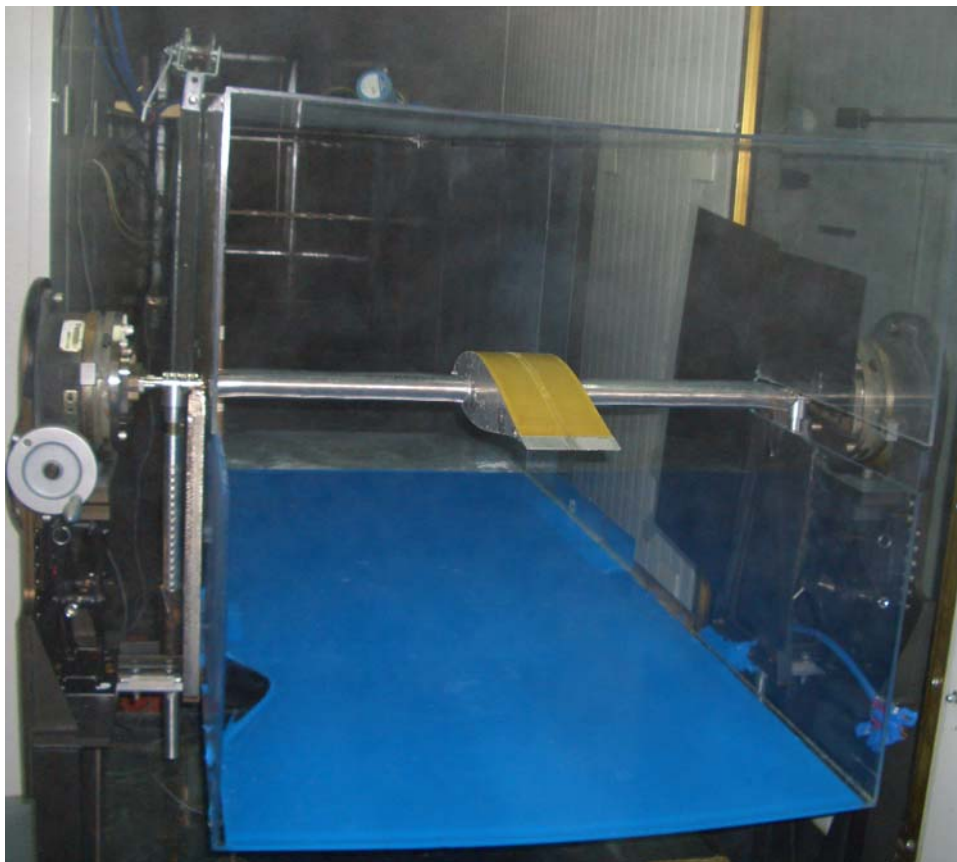


Figure 3.16: Tunnel setup for icing of airfoil measurements

The force balance is very sensitive and it requires care when operating. In order to protect the force balance, a section of a removable glass duct was made to be easily pulled out and pushed in when the test piece is installed or removed (see Appendix B: Manual of operating the Force Balance). Also, a flow blocker for zero wind speed is installed before the spray bar in the tunnel for re-zeroing of the force balance during an icing event to remove the static force component due to the weight of the ice accretion. Shaft protectors are made from stainless pipes to protect the shaft from additional force. Shaft holders are installed to keep the force off when a test piece is put into the shaft couples. All these components are designed to ensure that the force balance provided the required measurement during an icing event without damaging the strain gauges from excessive force.

3.3.2 Aerodynamics measurements

In order to characterize the aerodynamic forces during an icing event, a scaled airfoil is placed inside the icing tunnel and the force balance, described in Section 3.3.1, is used to measure the forces during a transient icing event for glaze and rime icing regions. To achieve the objective of studying the aerodynamics of icing of the wind turbine, a 2-D blade was fabricated with fiberglass and mounted in an aluminum frame.

Table 3.3 lists some airfoils employed by authors in previous literature. There are more airfoils used by researchers than listed. However, from Table 3.3, one can see that the NACA 63 series airfoils are often employed in wind turbine blades. The aircraft range of Reynolds numbers is different than that for wind turbines. According to the results and the comparison with the wind turbine blade model from one manufacturer, the shape of the test model selected in this research is a NACA 63421 airfoil. Figure 3.17 shows the side view of the shape of the airfoil. The selected airfoil is a NACA 63 series airfoil to simulate a wind turbine

blade. The shaft hole of the blade model is set at the dynamic centre (the position of one quarter chord of the airfoil). Each airfoil model was 62.5 mm in span. Eight pieces can be used as 500 mm in span for each force measurement. In order to reduce the force scale and protect the force balance from excessive stress, only two pieces of airfoil model are employed together to measure iced blades.

Table 3.3: Past literature for airfoils and range of Reynolds numbers

Authors	Application	Airfoils	Reynolds number	Ref.
Coton et al.	Wind turbine	S809	$5 \times 10^5 \sim 1 \times 10^6$	[16]
Sohn et al.	Wind turbine	NACA 63 series		[17]
Kong et al.	Wind turbine	NACA 63 series		[18]
Jackson et al.	Wind turbine	FB series and S series		[19]
Bak et al.	Wind turbine	NACA 62 ₂ -415		[21]
Grant al et.	Wind turbine	NACA 4 digital series		[22]
Schreck al et.	Wind turbine	full-scale	$7.4 \times 10^5 \sim 1.12 \times 10^6$	[23]
Timmer al et.	Wind turbine	DU97-W-300	$1 \times 10^6 \sim 10 \times 10^6$	[24].
Bak et al.	Wind turbine	NACA 63415		[40]
Devinant et al.	Wind turbine	NACA 65 ₄ -421		[41]
Yurdusev et al.	Wind turbine	NACA 4415, LS-1		[43]
Kishinami et al.	Wind turbine	NACALS04 series		[52]
Hoskins et al.	Wind turbine	NASA LS(1)-0417	0.1×10^6	[84]
Seifert et al.	Wind turbine	NACA 4415	$6.3 \times 10^5, 1 \times 10^6$ 1.5×10^6	[85], [64]
Kimura et al.	Wind turbine	NACA 0015, 63215	3×10^5	[86]
Makkonenet et al.	Wind turbine	NACA 63213		[92]
Papadakis et al.	Aircraft	NACA 23012	2×10^6 to 10.5×10^6	[78]
Addy et al.	Aircraft	GLC-305	3×10^6 to 10.5×10^6	[81]
Lee et al.	Aircraft	NACA 23012	1.8×10^6	[76]
Shin	Aircraft	NACA 0012		[74]
Pan et al.	Aircraft	NACA 23012, NFL 0414	3×10^6 to 10.5×10^6	[82]

Test procedures: The wind tunnel air temperature is initially set. After a steady state has been achieved, the force balance is zeroed to obtain the voltage offset, with no flow in the wind tunnel. The LWC is then set and the air velocity set from a range from 0 to 35 m/s. Rime or glaze ice is then simulated. During ice accretion, the forces are continuously measured. All forces are checked to not damage the strain gauges of the force balance. Periodically the flow in the tunnel is stopped to re-obtain a new zero offset to account for the added weight of the ice.

Analysis: The measured aerodynamics of the airfoil is obtained by measuring the forces on the airfoil under different conditions in the wind tunnel. Drag, lift and moment measurements for the airfoil are achieved via the instruments described in Section 3.3.1.

The force balance can obtain the forces in the X and Z axis directions: F_X and F_Z . Also, the angle of attack, α , can be set for an airfoil. The following equations can be used to obtain the drag and lift forces.

$$F_L = F_Z \cos \alpha - F_X \sin \alpha \quad (3-1)$$

$$F_D = F_X \cos \alpha + F_Z \sin \alpha \quad (3-2)$$

The drag coefficient C_D can be calculated as:

$$C_D = \frac{2F_D}{\rho u_\infty^2 Lc} \quad (3-3)$$

where F_D is the mean drag force, ρ is the fluid density, L is the span of the airfoil and c is the chord of the airfoil. The lift coefficient C_L can be calculated as:

$$C_L = \frac{2F_L}{\rho u_\infty^2 Lc} \quad (3-4)$$

where F_L is the mean lift force.

Preliminary results are shown in Chapter 5 for force measurements on a cylinder and a NACA airfoil with various icing shapes.

3.4 Convective heat transfer characterization of wind blades

3.4.1 Setup of heat transfer for an airfoil

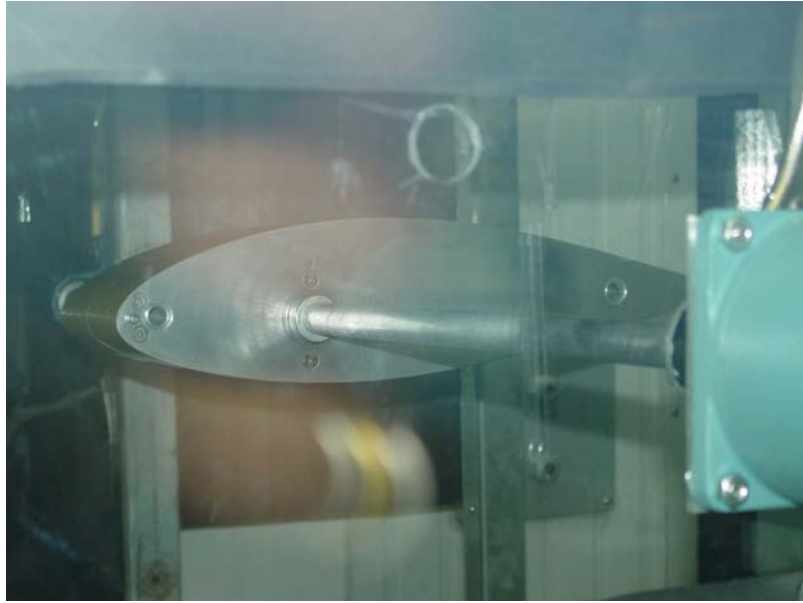
In order to characterize the convective heat transfer for wind blades during icing conditions, three separate tests are performed, each corresponding to the three icing regions, as shown in Table 3.4.

Table 3.4: Heat transfer and simulated icing conditions

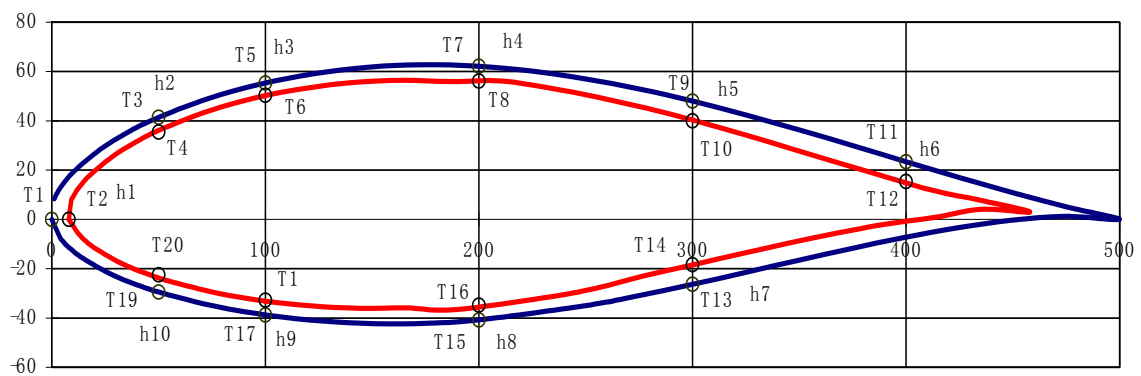
Heat Transfer tests	Icing Region	Icing Condition Simulated
Airfoil in air	Pre-icing	This focuses on the single-phase convection coefficient occurring before an icing event is initiated. The convective heat transfer coefficient variation from the leading edge of the wind blade is required to be known, especially when developing ice mitigation techniques.
Airfoil in air and water droplets (no phase change)	Start of icing conditions	Water droplets caused by precipitation start to impact the blade surface and flow along the blade. This region is composed of convection, air with a known liquid content and water partially covering the blade surface. Both phases need to be tested.
Airfoil in air and super-cooled droplets with phase change	Post icing	Water droplets have turned to rime or glaze ice and more super-cooled water droplets are deposited on the outer surface. The blade profile has changed, impacting not only the aerodynamics, but also the convective heat transfer.

Figure 3.17 shows the NACA 63421 airfoil used to perform these tests. The airfoil length and width are 500 mm and 65 mm, respectively. The fiberglass airfoil has a wall thickness of 3 mm. This airfoil used for heat transfer characterization is fixed within an aluminum frame and positioned in the icing wind tunnel using a vertical support bar that can be rotated to change the pitch. T-type thermocouples are embedded at both inner and outer edges of the airfoil surface. The thermocouple junctions are carefully flush-mounted with each surface at several positions around the airfoil, as shown in Figure 3.17. The thermocouple lead wires are collected within the hollow section of the airfoil and exit through the side of the airfoil. The airfoil has 25 thermocouples mounted at various locations within the airfoil (see Figure 3.17), including 22 thermocouples installed along the inner and outer surfaces of the airfoil. Temperature differences between inner and outer surfaces are measured at 11 locations.

Heater strips are installed along the inner edges of the airfoil. The dimensions of the heating strips are 40-mm in width and 880-mm in length. The operating voltage of the heating strip is 120 V and the power input is fixed at 500 W for all tests. The heater can be adjusted by a variable transformer over a range of voltages from 0 V to 120 V. The heater strips are attached inside of the airfoil with double-sided adhesive tape, after all thermocouples are secured (see Figure 3.18: Test airfoil with a heater and thermocouples). The thermocouples are connected to the data acquisition system of the icing tunnel, as described in Section 3.3.2.



a) Photo of airfoil inside tunnel



b) Location of thermocouples

Figure 3.17: NACA 63421 airfoil with thermocouple locations (note: dimensions in mm)

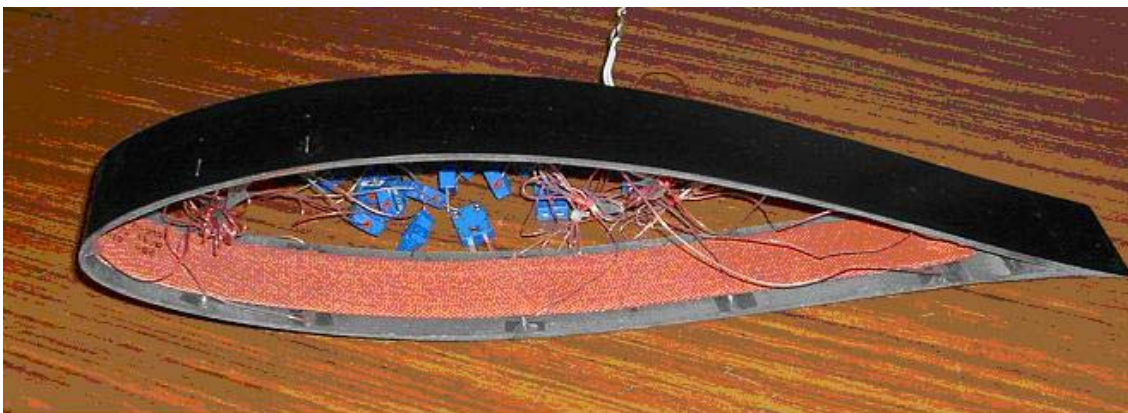


Figure 3.18: Test airfoil with a heater and thermocouples

3.4.2 Temperature measurements

Heat transfer characterization of airfoils is performed by measuring the temperatures along the airfoil, including inner and outer surfaces. T-type thermocouples are adopted with a differential connection mode. With differential measurements, each channel uses two signal leads and the voltage difference between the leads is measured. A direct-reading temperature sensor is used to measure the temperature of the reference junction for cold-junction compensation. The measurement system is controlled by a LabVIEW program [164] (see Figure 3.19) that is customized for the icing wind tunnel. The air temperature is measured with a sheathed thermocouple inserted into the midplane of the wind tunnel.

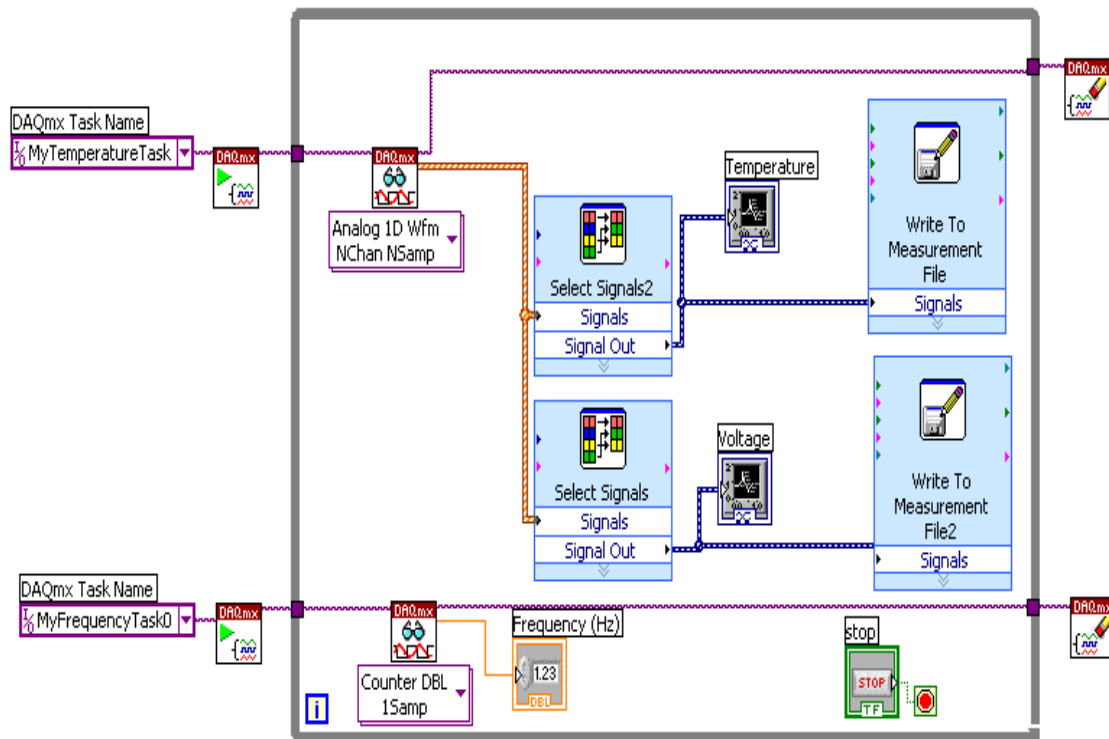


Figure 3.19: Block panel of LabVIEW: temperature, voltage and frequency measurement

A PC-based data acquisition system was developed for the temperature measurements. The system consists of a PC with a Plug-in PCI 6033E DAQ board and an SCB-100 shielded

connector block. The thermocouples are connected to the SCB-100 connector block box. There is a built-in temperature sensor on the SCB-100 shielded connector block for cold-junction compensation. This SCB-100 connector block box uses an isothermal design to minimize temperature gradients across the screw terminals.

The SCB-100 connector block is connected directly to the PCI 6033E and data acquisition board by a cable. The DAQ board converts analog data to digital data via a software program. The temperature data acquisition system was also reported previously by Wang et al. [165]. Temporal averaging of temperature measurements is performed for steady-state results at each location on the airfoil. Measurements are collected 100 times per second and averaging is performed over a period of 60 seconds. Figure 3.20 shows the front panel of temperature, rotation and voltage measurements with LabView 8.

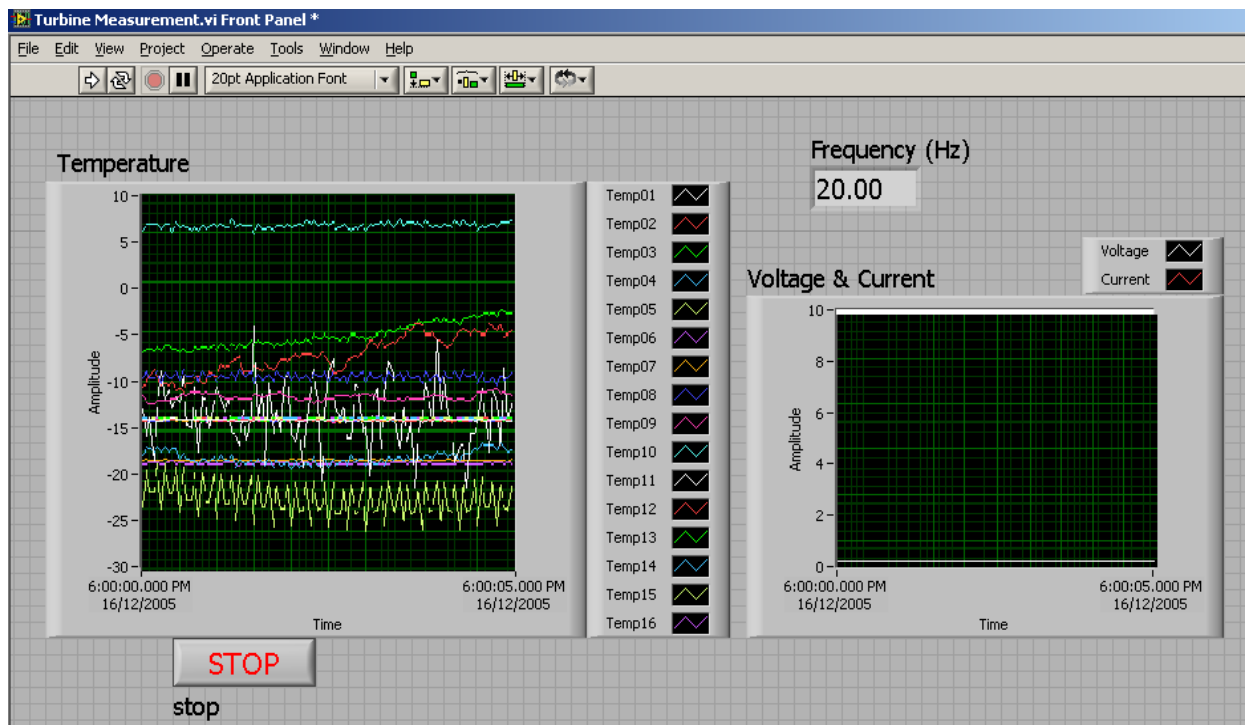


Figure 3.20: The front panel of temperature, rotation and voltage measurements

3.4.3 Test procedures and analysis

Test procedures: The test procedure consists of placing the airfoil inside the wind tunnel and measuring the wind velocity, air temperature and wall temperatures. Water droplets are injected to simulate the air-liquid tests. Experiments are performed for air temperatures varying from -30°C to 20°C, wind speed from 5 m/s to 40 m/s and LWC from 0 to 2 g/m³ and water droplet MVD ranges from 10 µm to 1000 µm.

Analysis: Spatial averaging of heat transfer coefficients is performed to obtain the average Nusselt number. Temperature measurements recorded at various locations around the NACA airfoil are used to determine the convective heat transfer coefficient. The rate of convective heat transfer per unit area from the airfoil is determined by:

$$q_{con} = h(T_{\infty} - T_o) \quad (3-5)$$

which can be re-arranged to give

$$h = \frac{q_{con}}{T_{\infty} - T_o} \quad (3-6)$$

Heater strips below the airfoil surface provide a source of heat input, which is transported through the thin airfoil surface by conduction, then convection to the external air stream. Heat conduction perpendicular to the surface is much larger than lateral heat conduction due to the high temperature difference across the thin surface. The perpendicular Fourier heat flux balances the rate of convective heat transfer to the surrounding air stream, i.e.,

$$q_{con} = q_{cd} = \frac{k(T_{in} - T_o)}{\delta} \quad (3-7)$$

Substituting Eq. 3-7 into Eq. 3-6, the resulting heat transfer coefficient can be expressed in the following manner,

$$h = \frac{k(T_{in} - T_o)}{\delta(T_{\infty} - T_o)} \quad (3-8)$$

The average heat transfer coefficient was obtained from spatial averaging around the airfoil.

$$\bar{h} = \frac{1}{s} \int_s h dx = \frac{1}{s} \sum_i^{11} h_i \Delta s_i \quad (3-9)$$

Then, the average Nusselt number becomes

$$\overline{Nu} = \frac{\bar{h}c}{k_{air}} \quad (3-10)$$

The results are presented in Chapter 6 for both average and local Nusselt numbers under the following test conditions:

1. Heat transfer from the airfoil without droplets for air temperatures ranging from -30°C to 20°C at AOA = 0;
2. Heat transfer from the airfoil with droplets having the same temperature as the air with different liquid water contents at AOA = 0;
3. Heat transfer from the airfoil without droplets for temperatures ranging from -30°C to 20°C at varying AOA;
4. Heat transfer from the airfoil with droplets having the same temperature of the air with different liquid water contents at various AOA.

Chapter 6 will provide the detailed results.

This chapter has presented the wind tunnel facility at the University of Manitoba and experimental instruments, including the force balance and thermocouples installed in the airfoil. The following aspects are covered in upcoming chapters.

Chapter 4

Wind turbine operation under icing conditions

In the previous chapters, a 3-blade rotating wind turbine model was described to operate under icing conditions. Ice changes the profiles of the wind turbine blades. Different ice types affect the performance of a wind turbine and this will be studied in this chapter. Table 4.1 summarizes the main operating conditions of the wind turbine experiments.

Table 4.1: Wind turbine operating conditions

	Glaze ice	Rime ice
Temperature	-1°C to -3°C , -5°C	-10°C, -20°C, -30°C
LWC	0.6 g/m ³	0.6 g/m ³
T (water)	32°F (0°C)	32°F (0°C)
Spraying Time	5, 10, 15, 20, 25, 30, 35 minutes	5, 8, 12, 15, 20, 25, 30 minutes
Air speed	From 12 m/s to 33 m/s	From 12 m/s to 33 m/s

4.1 Characteristics of the 3-blade wind turbine model

In this section, two parts will be presented to determine power losses under different icing conditions. Low temperatures close to 0°C and lower temperatures down to -30°C degrees will be discussed. The correlation of power losses will be expressed in terms of the Reynolds number, Re_D :

$$Re_D = \frac{\rho u_{\infty} D}{\mu} , \quad (4-1)$$

where D = diameter of wind turbine, m,

ρ = density of free stream, kg/m³,

u_∞ = velocity of free stream, m/s,

μ = viscosity of free stream, kg/ms.

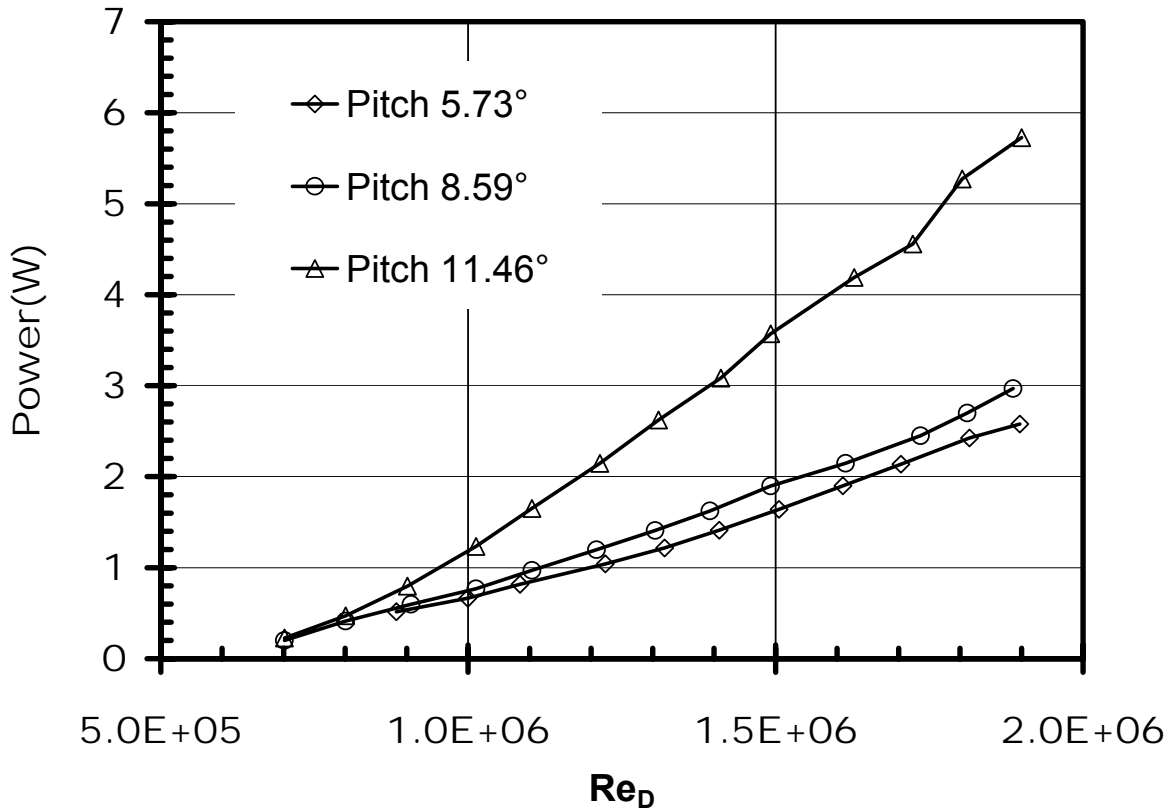


Figure 4.1: Power output at different pitch angles for tests at 20°C

The dimensionless power, $\frac{P}{P_{\max}^*}$ will be presented in terms of the maximum power output,

P_{\max}^* (P^* in figures), with the wind turbine at an optimized pitch and highest velocity. In this study, pitch angles of 0°, 2.86°, 5.73°, 8.59°, 11.46° and 14.32° are tested in the wind tunnel to determine a reference point and optimized pitch. However, the power output at 0°, 2.86° and 14.32° pitch angles so small, are not included in Figure 4.1. The power loss measured includes the DC generator losses. From the results, the best pitch angle tested is 11.46° and the reference point selected is $Re_D^* = 1.9 \times 10^6$, $P_{\max}^* = 5.73$ W, RPM = 370 rpm, at a surrounding temperature of 20°C. Figure 4.1 shows the power output and Figure 4.2 shows the rotation curve with respect to Re_D at 5.73°, 8.59° and 11.46°. These pitches are used

because the wind turbine operates at very low rotation when the pitches are 0° , 2.86° and 14.32° . These show that different pitch affect the power output and optimal pitch angle, depending on the direction of wind. In this thesis, an optimal pitch is employed under different icing conditions, due to the wind flow being only in one direction in the icing tunnel.

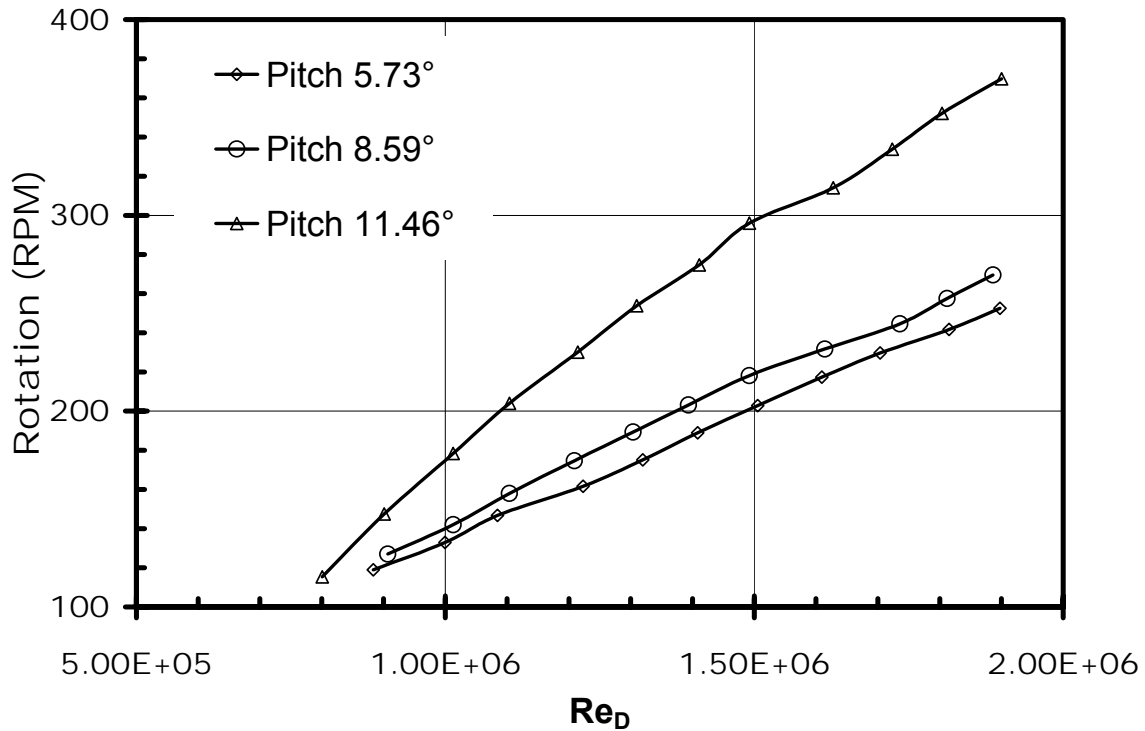


Figure 4.2: Rotation at different pitch for tests at 20°C

The thickness of ice, δ , over the wind turbine blade is measured at the root and middle of the blade, using a digital caliper. The ice thickness is reported at the widest point on the root of the wind turbine blade. Temperature is a significant factor that affects the power output when a wind turbine operates. Conditions at temperatures of 20°C , 10°C , 0°C , -10°C , -15°C , -20°C , -25°C and -30°C are measured to test different operating characteristics of the wind turbine. Figure 4.3 and 4.4 show the power output and rotation at varying Re_D . From the curves, a low temperature has more energy potential due to higher air density. At the same wind speed, the power output at a lower temperature is higher than that at a high temperature as Re_D increasing because of higher air density at low temperature. In Figure 4.4, all curves of RPM/RPM^* are lower than 1 at the highest wind velocity.

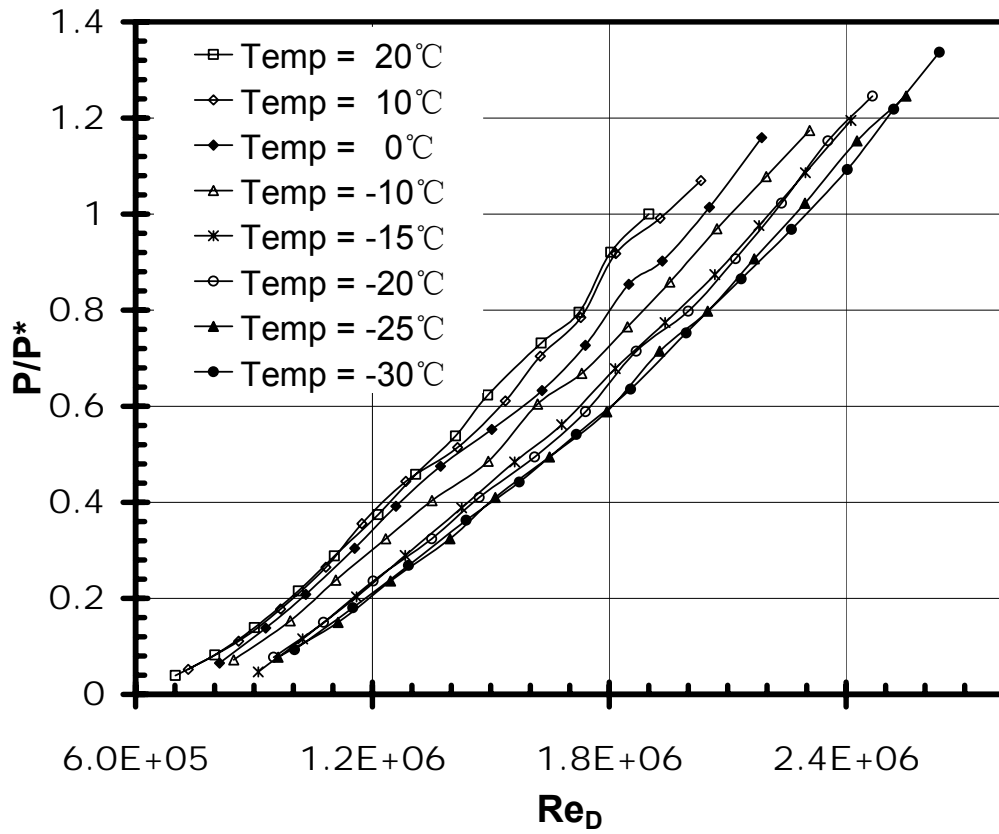


Figure 4.3: Power output at different temperatures

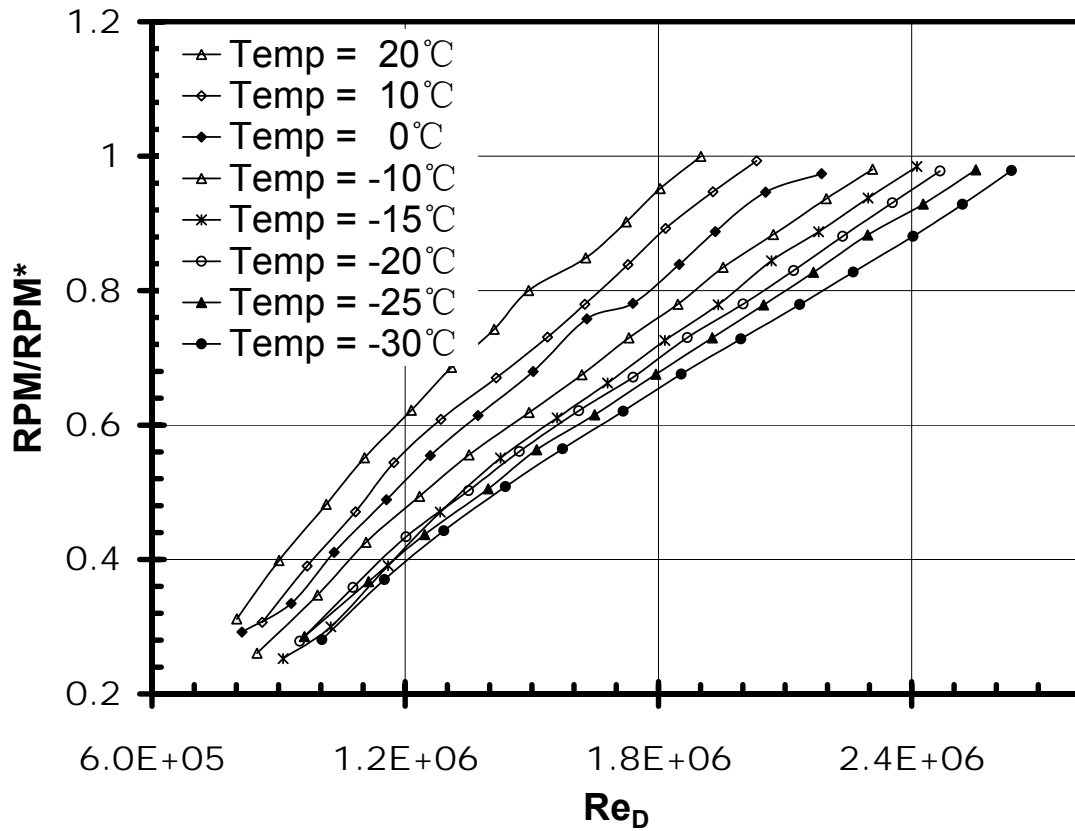


Figure 4.4: Rotation variation at different temperatures

4.2 Ice thickness over the wind turbine blades

The wind turbine model is operating in the wind tunnel with water droplets at different spraying times. The water droplets adhere to the wind turbine blades and accrete. The spraying time and temperature are two significant factors that affect the ice thickness. Table 4.2 presents ice accretions over the wind turbine blades at $LWC = 0.6 \text{ g/m}^3$, droplet size from $10 \text{ }\mu\text{m}$ to $1000 \text{ }\mu\text{m}$, wind speed at 12.5 m/s and a temperature of -3°C . R1, R2, R3 are ice thickness in mm at the root of wind turbine No.1, 2, 3 blades. M1, M2, M3 are ice thickness in mm at the middle of wind turbine No. 1, 2, 3 blades. From this table, it can be found that the ice thickness doesn't scale up with spraying time at the same LWC. From Table 4.2, the ice thickness at 35 minutes is almost the same as 30 minutes, because the air temperature is changing during a long duration running of the tunnel. In the experiments, the wind tunnel temperature is set as -3°C , however, it varies from -1°C to -5°C due to the difference in temperature of 2°C in the control system.

Table 4.2: Glaze ice thicknesses over the wind turbine blades (-3°C) (mm)

Time	R1	R2	R3	Avg R	M1	M2	M3	Av M
5	3.0	2.2	2.1	2.4	2.7	3.2	2.9	2.9
10	4.9	5.1	4.3	4.8	5.1	5.4	5.4	5.3
15	6.2	6.2	6.1	6.2	6.3	7.2	6.3	6.6
20	8.0	7.9	8.2	8.04	8.2	8.3	8.4	8.3
25	11.3	11.1	11.1	11.2	11.6	11.3	11.6	11.5
30	13.8	13.1	13.0	13.3	13.9	13.9	13.8	13.9
35	13.3	13.5	13.5	13.4	12.3	13.9	13.3	13.2

Table 4.3 and Table 4.4 show the ice accretion when the wind turbine operates at lower temperatures of -10°C , -20°C and -30°C . It can be that the rime ice thickness at 5 minutes is thicker than the glaze ice condition. The reason of this phenomenon is higher collective

efficiency when water droplets hit the airfoil surface at lower temperature. For this temperature range, also -30°C has thicker ice accretion over the blades.

Table 4.3: Rime ice thicknesses over the wind turbine blades (-10°C) (mm)

Time	R1	R2	R3	Avg R	M1	M2	M3	Avg M
5	4.5	4.8	4.5	4.6	4.3	3.9	4.0	4.1
8	7.0	7.4	7.3	7.2	5.9	6.0	5.9	5.9
12	8.8	9.0	9.0	8.9	8.5	9.0	8.9	8.8
16	14.8	15.7	15.5	15.3	12.7	13.1	12.7	12.8
20	18.4	18.6	18.2	18.4	14.6	14.2	14.8	14.5
25	24.9	24.8	25	24.9	18.3	17.9	17.8	18.0
30	28.9	29.6	29.6	29.4	20.5	21.0	20.9	20.8

Table 4.4: Rime ice thicknesses at -20°C and -30°C on the wind turbine blades (mm)

Time	R1	R2	R3	Avg R	M1	M2	M3	Avg M
Temp = -20°C								
5	5.1	5.0	5.2	5.1	4.3	4.5	4.3	4.4
8	7.2	7.6	7.5	7.4	6.0	6.2	5.8	6.0
12	11.9	11.9	12.2	12.0	9.3	9.4	9.5	9.4
16	16.2	16.6	16.8	16.5	12.5	12.5	12.4	12.5
20	19.7	19.8	20.0	19.8	14.8	15.0	15.3	15.0
Temp = -30°C								
5	5.6	5.6	5.5	5.6	3.9	4.0	4.2	4.0
8	8.5	8.4	8.5	8.5	5.8	6.3	6.1	6.1
12	12.5	12.7	12.8	12.7	8.9	9.1	9.2	9.1

4.3 Glaze ice over wind turbine

Glaze ice with a hard, smooth and transparent appearance is the result of liquid water droplets striking a surface whose temperature is just below the freezing point. Figure 4.5 shows a glaze ice sample over the wind turbine, formed at -5°C for 10 minutes and 12.5 m/s wind speed.

Figure 4.6 shows icing of wind turbine blades formed at -2°C for 2, 5 and 10 minutes, separately. The icing conditions are 0.6 g/m^3 of LWC.



Figure 4.5: Glaze ice over a wind turbine at -5°C for 10 minutes and 12.5 m/s and 0.6 g/m^3

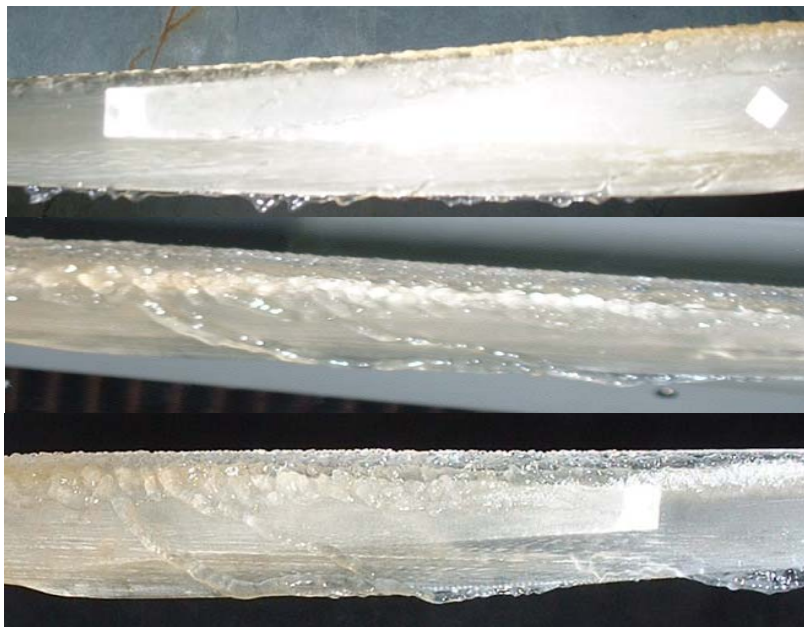


Figure 4.6: Icing of blades at -2°C for 2, 5 and 10 minutes (from top to bottom)

Figure 4.7 shows that the ice thickness will significantly affect the power output of a wind turbine. As the ice thickness increases, the energy losses increase rapidly. When ice thickness is 0.12 mm, the power output is 90.5% of the total, as well as 85.2% output with a 0.72 mm ice thickness. Power losses are 62% when the ice thickness is 9.4 mm. Figure 4.8 shows that the ice thickness also affects the rotation, compared to the turbine rotation with no ice (no control on rpm in these tests). It shows that the rotation speed of a wind turbine varies with wind velocity in the wind tunnel. The curve illustrates that the rotation of a wind turbine normally is less than the maximum, when the blade is covered with ice.

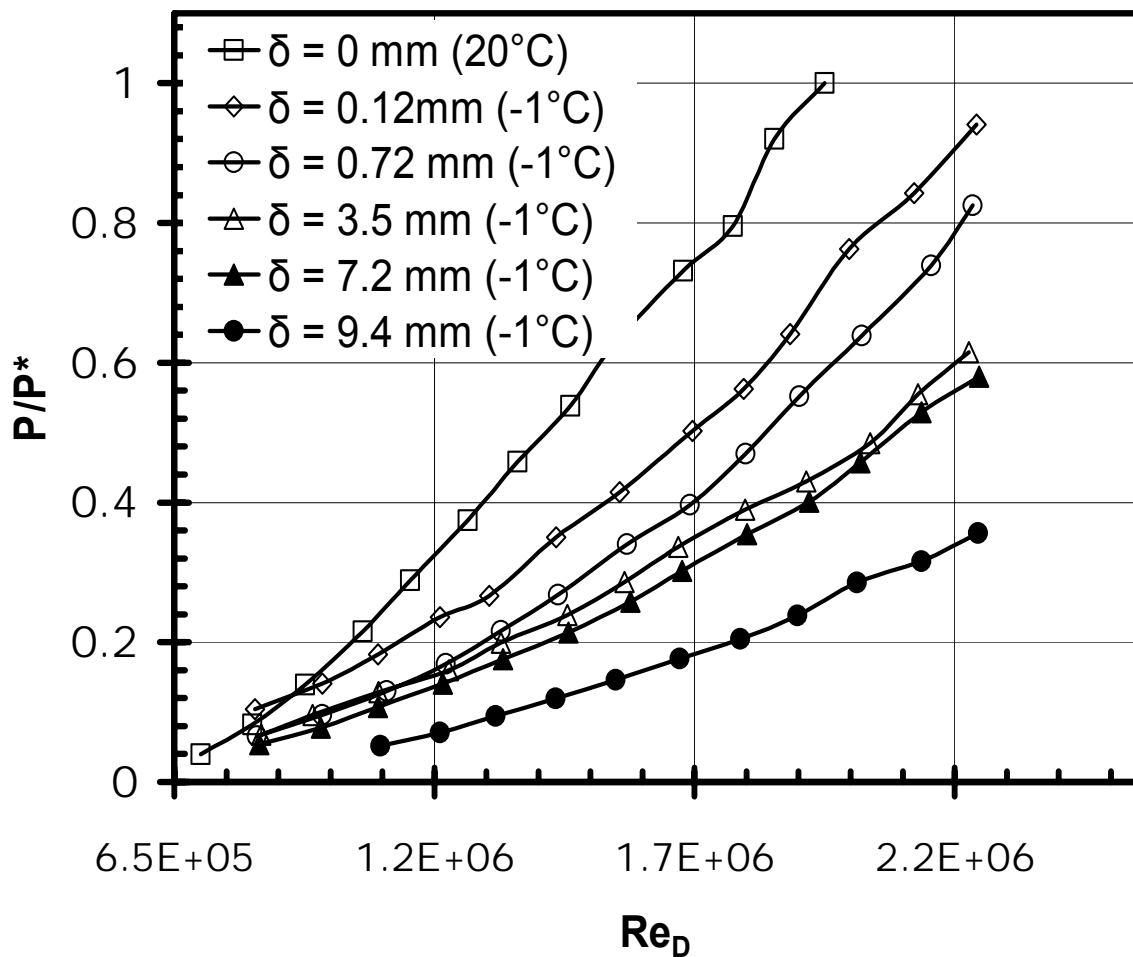


Figure 4.7: Power output with average ice thicknesses

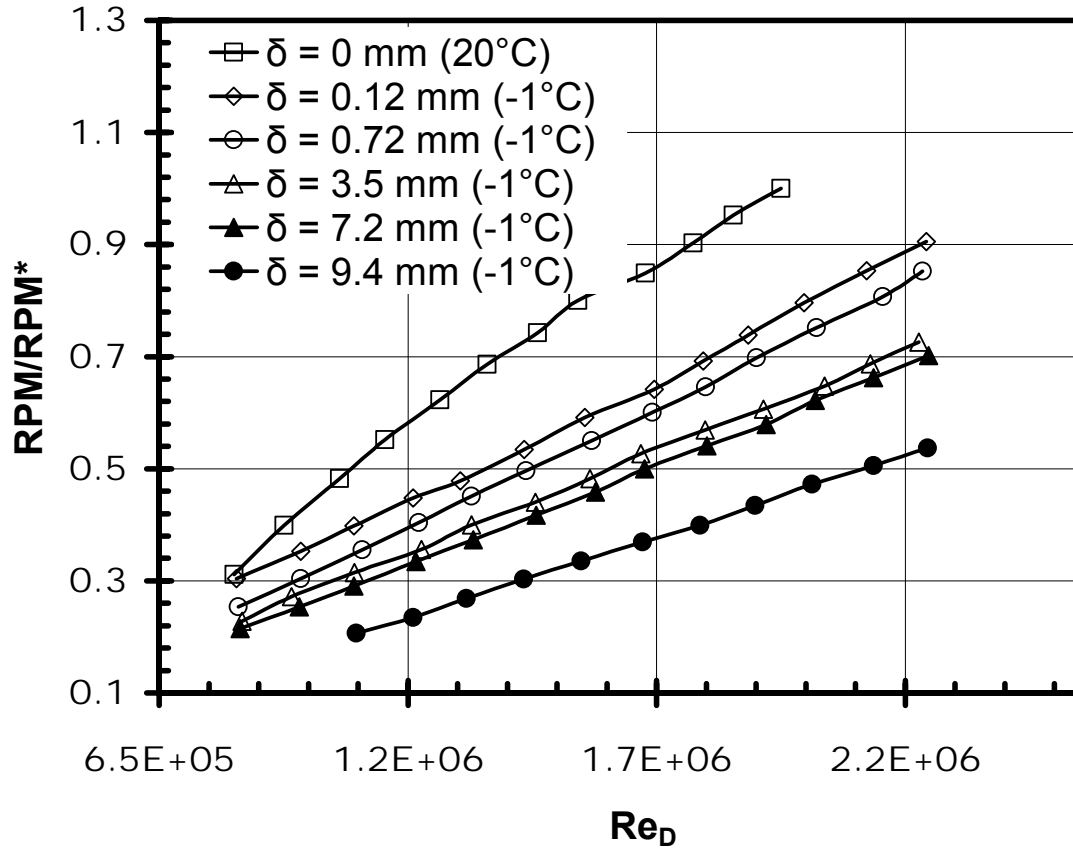


Figure 4.8: Rotation rate with average ice thicknesses

Figure 4.9 shows additional characteristics while a wind turbine is working under icing conditions. The 4.2 mm ice thickness formed at -3°C temperature, 0.6 g/m^3 LWC and wind speed 12.5 m/s. The curve jumps from 0 to 47% power output when $\text{Re}_D = 1.4 \times 10^6$. This occurs because the shape of the blade significantly changed due to ice. Ice changes the airfoil shape of the wind turbine blade, making the turbine rotate at low RPM and it suddenly jumps to a high rotation, due to different aerodynamic characteristics of a different airfoil shape with various ice thicknesses. When the blade is covered by glaze ice, the shape of the blade is changed by ice. This change decreases the lift force. This phenomenon will be explained in Chapter 5. However, the rotational speed is not more than regular rotation rate, and the power output is higher than the regular power output (see Figure 4.9). This is also observed when the wind turbine is subjected to rime ice conditions.

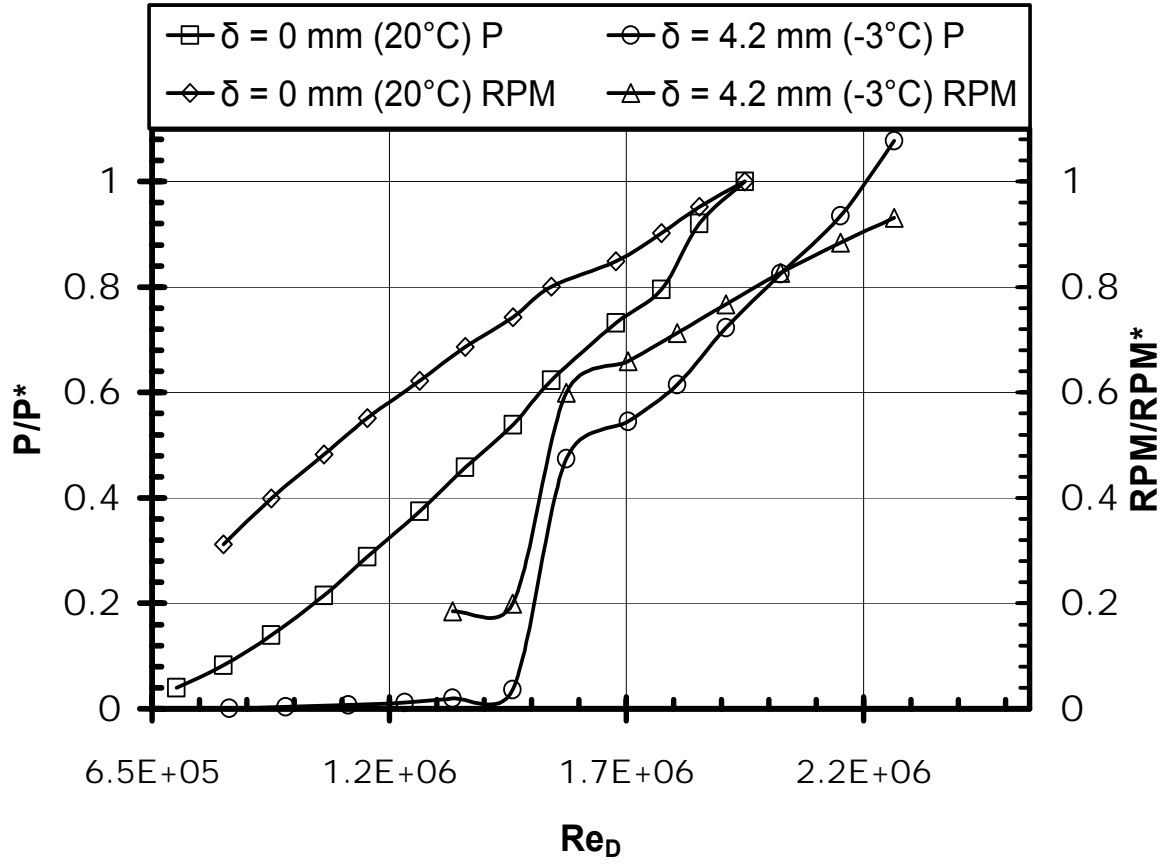


Figure 4.9: Power output for a 4.2 mm average ice thickness

4.4 Power losses with rime iced blades

Rime ice has a rough and opaque appearance and it forms when the surface temperature is below the freezing point and exposed to super-cooled water droplets. Due to the presence of trapped air bubbles, rime ice is opaque and its density ranges from 0.59 to 0.9 g/cm³, depending on accretion conditions. Figure 4.10 shows an example of rime ice on the wind turbine and blades.



Figure 4.10: Rime ice on the wind turbine blade (-30°C , 0.6 g/m^3 and 12.5 m/s)

Comparing the icing of the blades in Figure 4.6 and Figure 4.10, there is a clear difference between rime ice and glaze ice. Glaze ice over the blade will have some trace of water flow over the blade, due to an air temperature just below the freezing point. In comparison, rime ice is white and it covers the whole leading edge. The blade leading edge is elongated. This changes the shape of the airfoil and its aerodynamic characteristics. Operation of the wind turbine will change, depending on the thickness of ice.

Figure 4.11 presents results of the various average ice thicknesses when the turbine operates at -30°C . It shows that the power output has been affected by ice accretion. When the ice thickness is 5.6 mm at -30°C , the power is 104% when $\text{Re}_D = 2.6 \times 10^6$. However, at a low wind speed, the power loss is comparable with the wind turbine without ice accretion. When the ice thickness is 8.5 mm, the power output is just 20% when $\text{Re}_D = 2.4 \times 10^6$. It can be found that the wind turbine rotates slowly in Figure 4.12. But the power output suddenly rises to 190%, once the wind velocity continues to increase. These indicate that the aerodynamic characteristics of the wind turbine blades including lift and drag coefficient have changed significantly due to ice accretion. Comparing glaze ice accretion over the whole blades, rime ice just covers the leading edge (shown in Figure 4.10). Rime ice accretion prolongs the chord of the blades. Ice transforms the characteristic of the airfoil. How ice accretion transforms the aerodynamic characteristics of the airfoil will be tested in Chapter 5.

Figure 4.12 shows the variation of rotation speed as the ice thickness increases. When ice thickness causes the rotational speed to accelerate, this will damage the generator, as well as the electric equipment. Ice affects the operational characteristic of the wind turbine more seriously when the ice thickness increases. When blades have a 5.6 mm ice thickness, the power output has decreased significantly. However, the power output will suddenly jump to 200% of the regular power output, with ice thickness up to 8.5 mm. When the ice thickness increases to 12.7 mm, the power output is 15% of the regular power. This trend also can be observed in Figure 4.13, when the wind turbine model operates at -20°C .

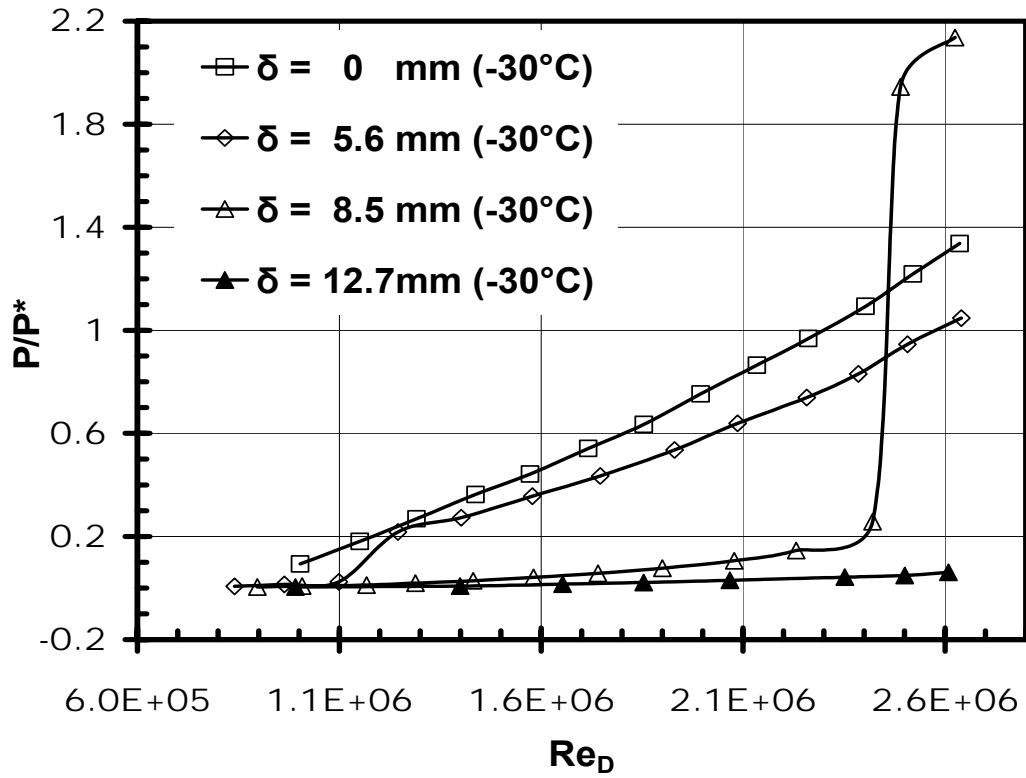


Figure 4.11: Power losses under extreme icing conditions

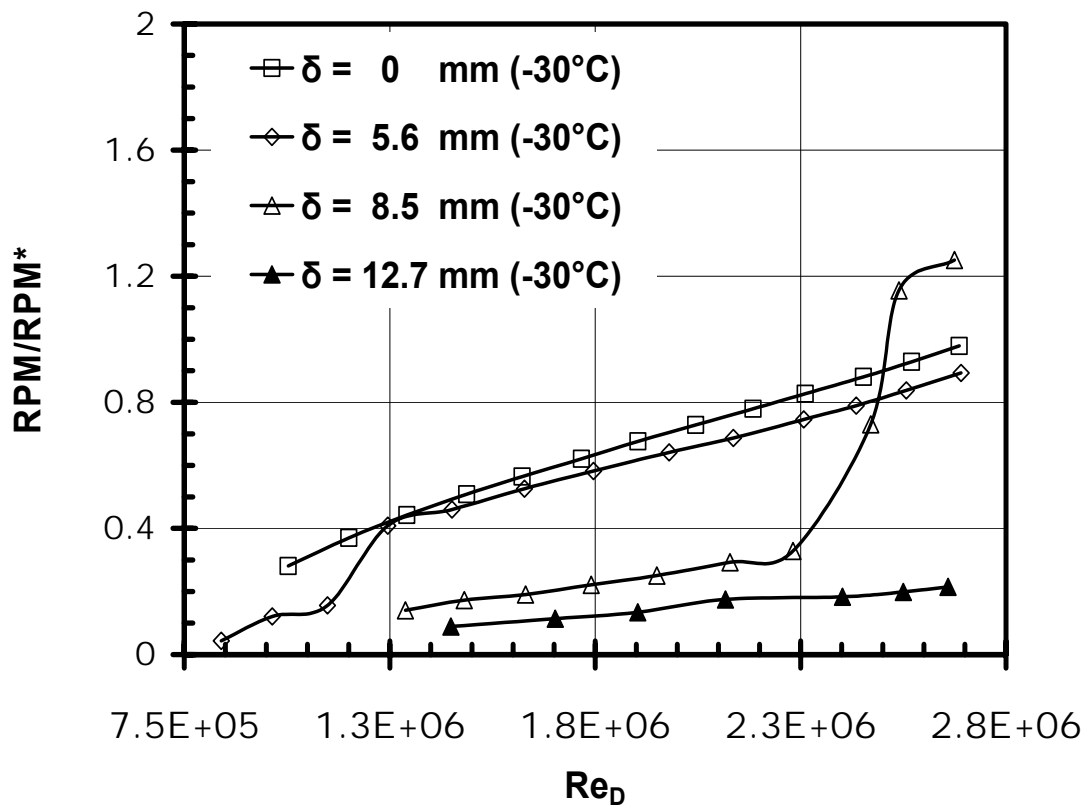


Figure 4.12: Rotation of the turbine in extreme weather conditions for different ice thickness

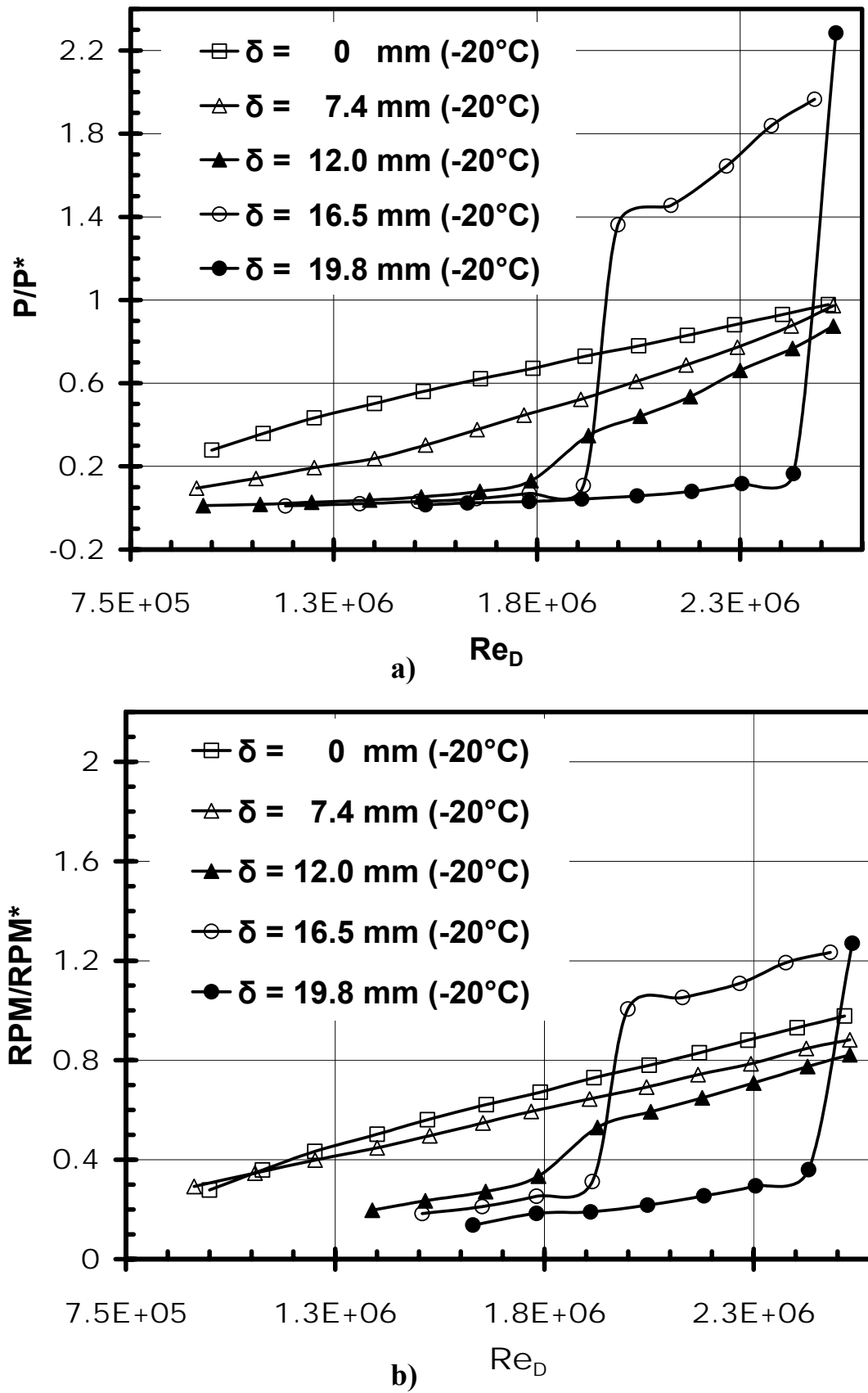
Figure 4.13: Wind energy losses at -20°C : a) power output; b) rotation

Figure 4.13 shows that the power output changes with different ice thicknesses at -20°C . Compared with -30°C , the ice thickness of the wind turbine blades is thicker, while the power output suddenly jumps to a higher power output at the lower wind velocity. When ice accretes over the blades, 19.8 mm of ice thickness leads to a transition at $\text{Re}_D = 2.5 \times 10^6$. Ice accretion creates different ice shapes at different temperatures. Various ice shapes affects the lift coefficient in different way.

4.5 Summary

The experimental results in this chapters showed that icing of a wind turbine blade significantly affects energy output, regardless of what kind of ice accretes on the blades. The power output of a wind turbine is seriously affected by icing. With more glaze ice accretion, higher power losses occur. With more rime ice accretion, power losses or power increases depense on ice shapes and wind conditions.

For similar event duration, extreme cold temperatures will form a larger ice thickness on the blades than will form under glaze ice conditions. Rime ice forms on the blades of a wind turbine and changes the airfoil shape of wind turbine blades. These blades with ice will increase the rotation speed of wind turbines in extreme ice conditions. In our experimental icing conditions, the power output increases to 214%, with 8.5 mm of rime ice thickness and the rotation speed of the wind turbine increase to 125%. This is dangerous for a wind turbine

because a high rotation speed and more power output will make the mechanical and electrical components overheat and partially fail.

Power losses and high rotation speeds are two important aspects of iced wind turbine blades. Both of these aspects are dangerous for wind turbines operating in cold climates under icing conditions. The following chapters will focus on the aerodynamics and convective heat transfer from the airfoils.

Chapter 5

Aerodynamics of iced airfoils

The previous chapter has shown experimental data on power loss during icing of wind turbines. When blades have ice accretions, the blade shapes and aerodynamics change and affect the power output of the wind turbine. This chapter will examine the aerodynamic characteristics of an airfoil to understand more concerning iced wind turbines. Different icing times at varying AOAs (angles of attack) will be discussed in this chapter. Table 5.1 summarizes the airfoil icing tests.

Table 5.1: Icing conditions for aerodynamics studies

	Glaze ice	Rime ice
Temperature	-3°C	-9°C
AOA	0°, 3°, 6°	0°, 3°, 6°, 9°
LWC	0.8 g/m ³	0.8 g/m ³
T (water)	32°F (0°C)	32°F (0°C)
Wind speed	10 m/s	10 m/s
MVD	10 µm to 1000 µm	10 µm to 1000 µm
Spraying duration	15, 30, 45 minutes	15, 30, 45 minutes

5.1 Cylinder measurements

An experiment is first performed on a cylinder. In order to measure the forces on cylinders, the measurement setup described in Chapter 3 is used. A force balance is used to measure normal and axial forces, as well as moments.

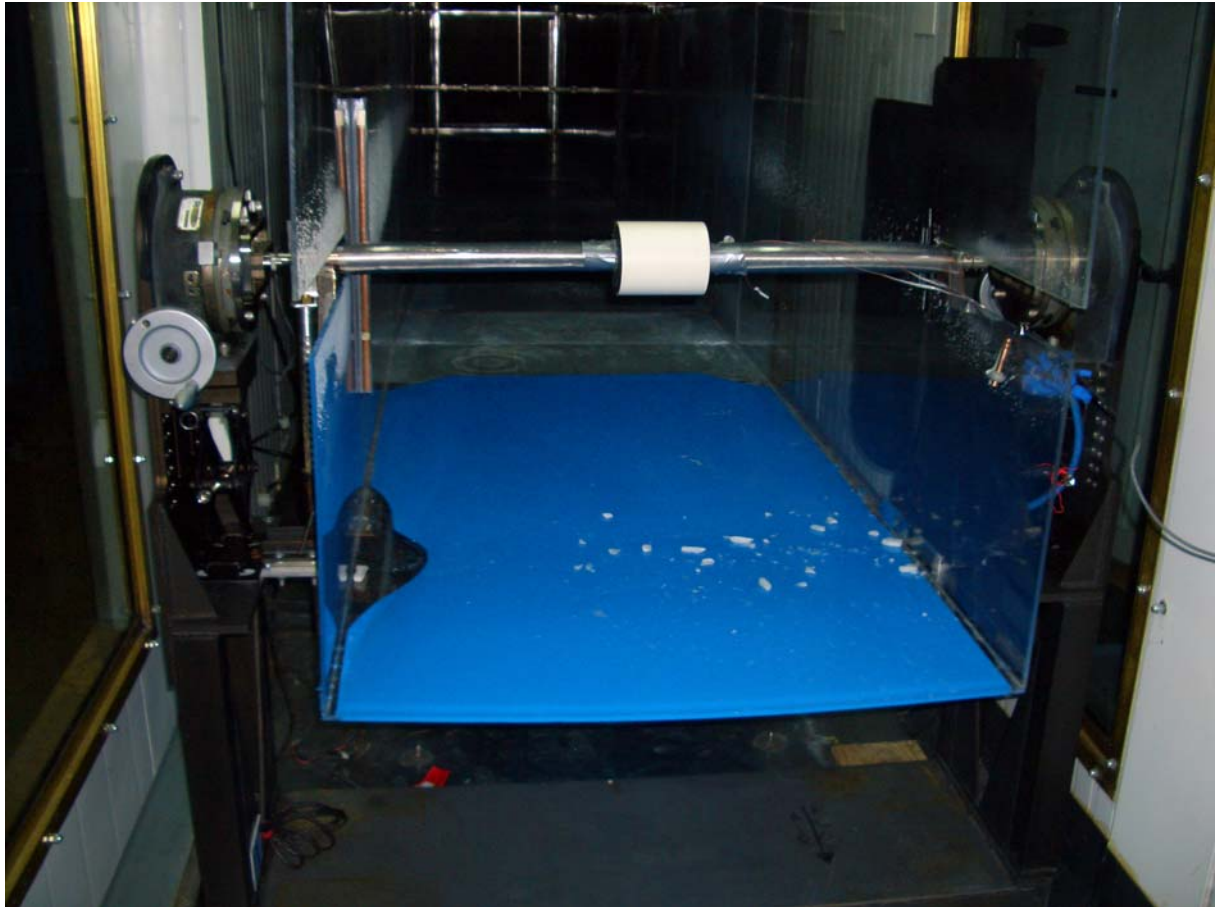


Figure 5.1: Shorter cylinder installed in the wind tunnel with force balance and shaft protectors

The measurement of aerodynamic forces on cylinders was processed in two spans with the same diameters to test experiments consistently. The 106 mm diameter is the same size as the airfoil thickness. The span of 125 mm is the same size as the span of the airfoil (Figure 5.1).

Also, longer spans of 916 mm cylinder were tested for C_D measurements. These cylinders were used to commission the force balance and verify its accuracy. The diameters, D , of the cylinders were 16.0 mm, 28.7 mm, 48.3 mm, 60.7 mm, 89.5 mm and 114.7 mm. All cylinders are 916.0 mm in length.

The drag coefficient C_D can be calculated as:

$$C_D = \frac{2F_D}{\rho u_\infty^2 LD} \quad (5-1)$$

Where F_D is the mean drag force, ρ is the fluid density, and L is the span of the cylinder.

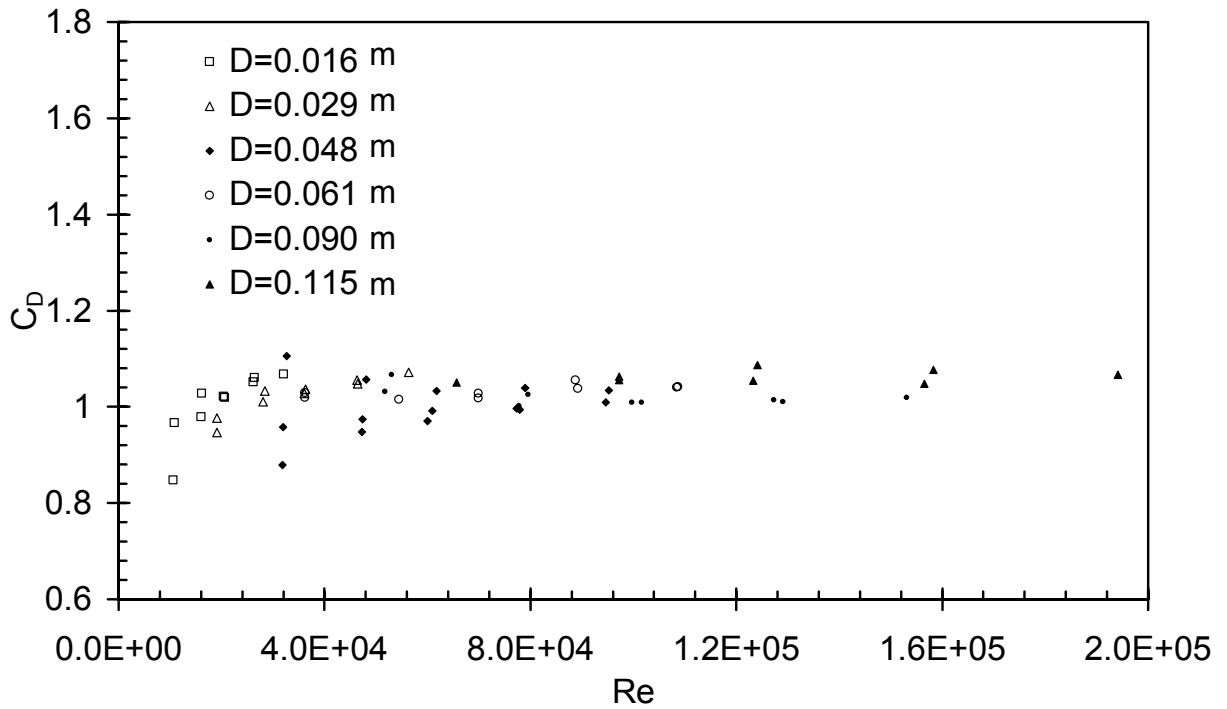


Figure 5.2: C_D of different diameter cylinders as a function of Reynolds numbers

Several past studies investigated C_D for a single isolated cylinder in a uniform planar shear flow. Adachi and Kato [166] experimentally studied drag and lift coefficients, with $C_D = 1.080$, $C_L = 0.037$ when dimensionless shear parameter $K = 0.04$ and $Re = 0.8 \times 10^4$. Values of $C_D = 1.14 \pm 0.02$, $C_L = -0.03 \pm 0.02$ when dimensionless shear parameter $K = 0.05$

and $Re = 5 \times 10^4$ were obtained by Sumner and Akosile [167]. Also, Hayashi et al. [168] obtained the experimental results of $C_D = 0.997$ and $C_L = -0.109$ when $K = 0.15$ and Reynolds number $Re = 6 \times 10^4$. The results in Figure 5.2 agree with this previous work.

A test with a 125 mm cylinder was then conducted with and without sprayed water droplets. A comparison was performed with a longer cylinder, 890 mm in span, with the same diameter without water spraying. The results are presented in the Figure 5.3. Figure 5.3 shows that the short cylinder has a lower C_D and higher C_L . It suggests that 3-D effects are present. The edge effects are large when measuring the aerodynamics without end plates, for a shorter cylinder or 2 or 3 piece airfoil. This is the reason that C_L in the measurements, with or without ice, is smaller than results in past literature. Other measurements of the ice shapes on the airfoil are obtained as anticipated. However, C_L , C_D and C_m are 3-D airfoil measurements and include edge effects.

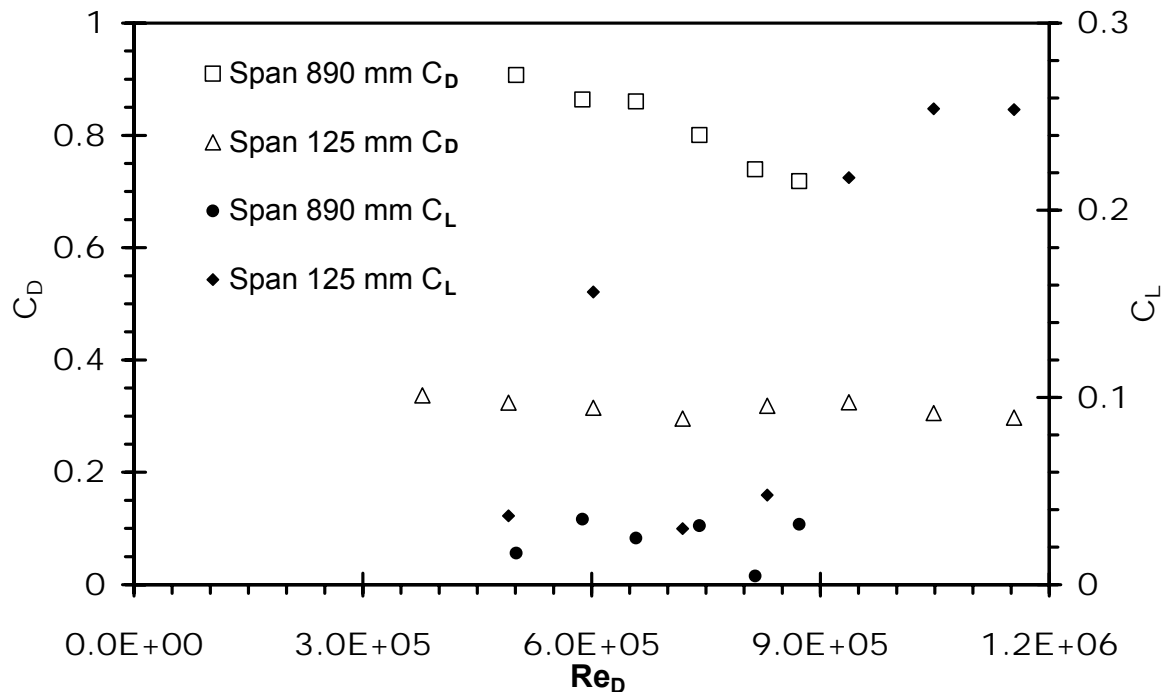


Figure 5.3: Comparisons with short and long cylinders for C_L and C_D

A correlation between ice shapes and C_L , C_D , C_m are difficult because the ice shape is complex and there is no correlation of C_L with AOA. A method is used wherein $\Delta C_L = C_L(\text{no ice}) - C_L(\text{ice})$, and similarly for ΔC_D and ΔC_m . The lift coefficient is affected by ice. However, the lift coefficient is not reduced with icing time. It means that the ice shapes are not the only significant factor for a decrease in the lift coefficient. The results suggested that one correlation with the ice shape and lift coefficient could not be obtained. Although the aerodynamic tests were made in 3-D conditions, without end plates to keep the tested airfoil free of edge effects; some 2-D iced cylinders will be considered here.



Figure 5.4: Rime iced cylinder at -9°C , 0.8 g/m^3 and 10 m/s at 30 minutes spraying duration

The results of drag coefficients for cylinders indicate that the technique to measure forces in the wind tunnel is suitable. But the force balance procedures and data reduction need to be modified to account for the weight change of the test specimen during ice build-up as discussed in Appendix D.

5.2 Ice shapes on an airfoil

As presented at the beginning of this chapter, the aerodynamics of an iced NACA 63421 airfoil will be tested in this section. Figure 5.5 depicts two airfoil pieces that are installed in tandem in the movable duct, for icing in the wind tunnel. Also, the shaft to hold test pieces is protected by the shaft protectors to avoid transfer force to the balance. The angle of attack can be adjusted by turning the hand wheel on one side of the Force Balance. Details of the Force Balance can be found in Section 3.3.

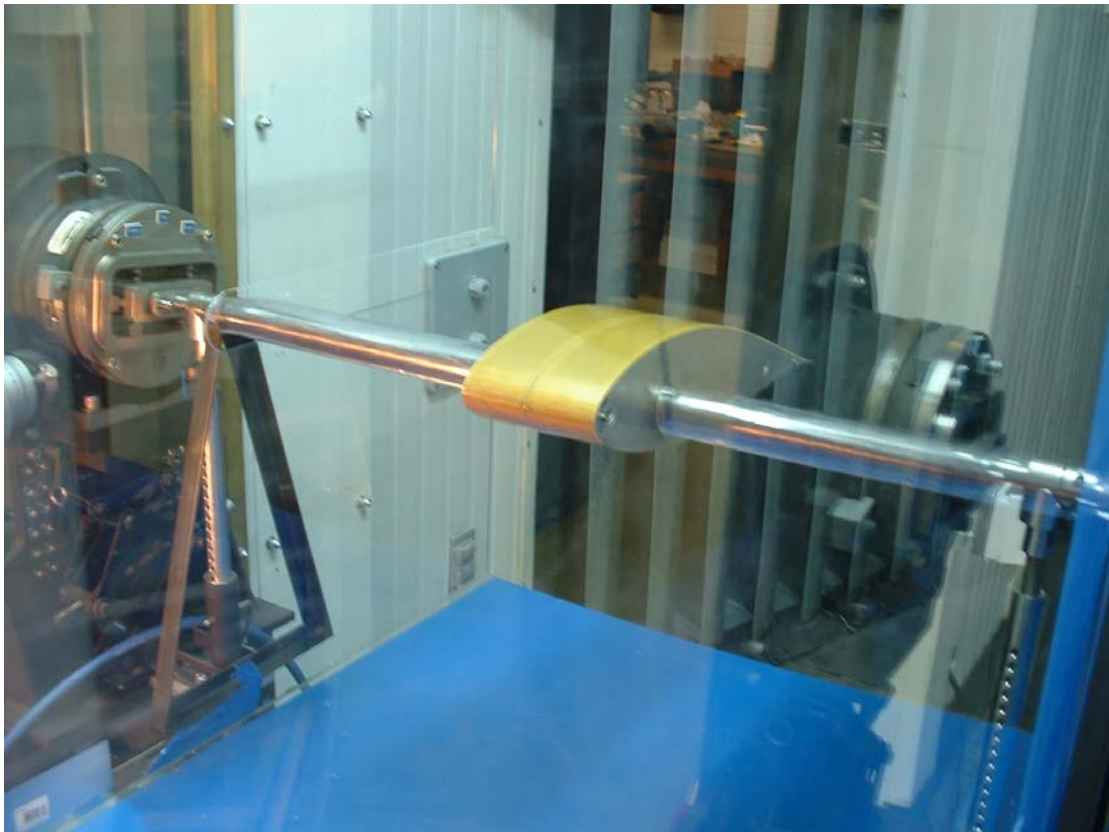


Figure 5.5: Two airfoils in tandem installed in the icing wind tunnel

The ice shapes on the airfoil were recorded using a digital camera. A special aluminum plate was installed in the shaft holder of the lift side for the camera in Figure 5.6. The camera must be installed at the same level with the shaft of the test pieces, in order to capture suitable pictures. The pictures are taken manually. The camera is a Fuji digital Camera FinePix with 3Mp and $3 \times$ optical zoom.

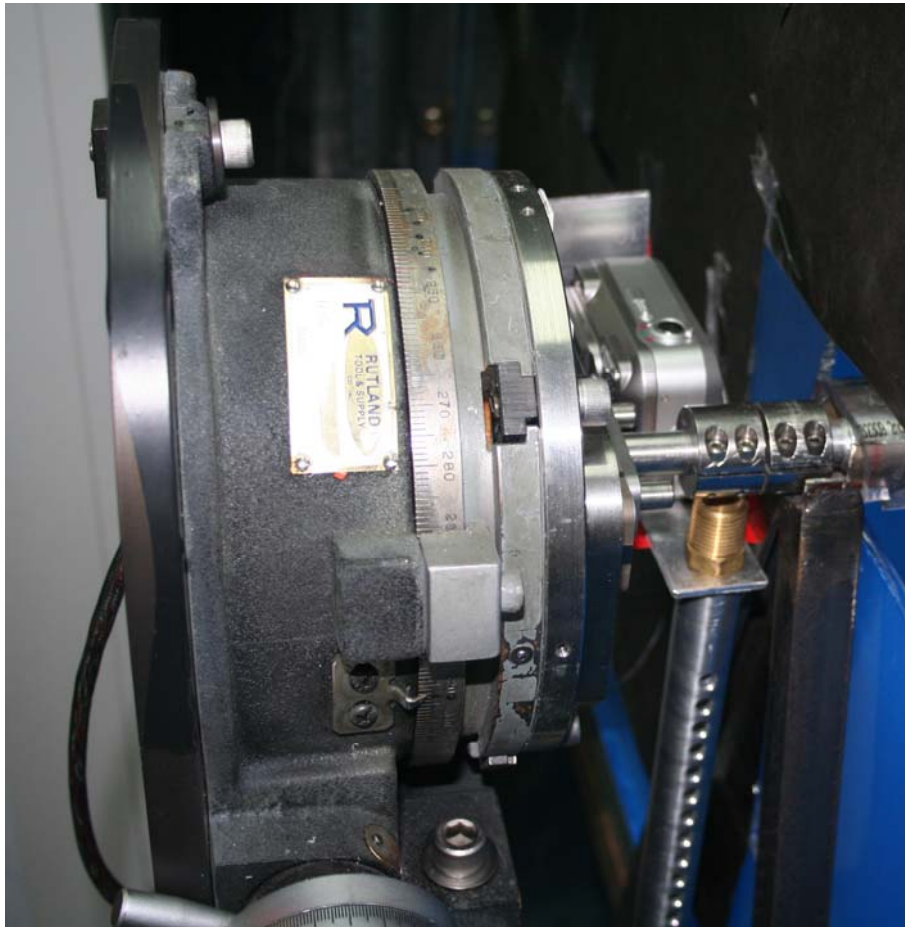


Figure 5.6: Left side of the force balance with a camera

The iced airfoil exhibits various ice shapes when the test piece is set up at different times under spraying water conditions, including the spraying time, air temperature and air speeds. Table 5.2 presents photographs of ice shapes in the wind tunnel, when the airfoil is exposed to super-cooled spraying. All ice shapes at glaze conditions are above -5°C (tunnel temperature)

with a water temperature of 0°C . It was observed that the ice becomes thicker and thicker as time advances. Table 5.3 shows how AOA affects the ice shapes.

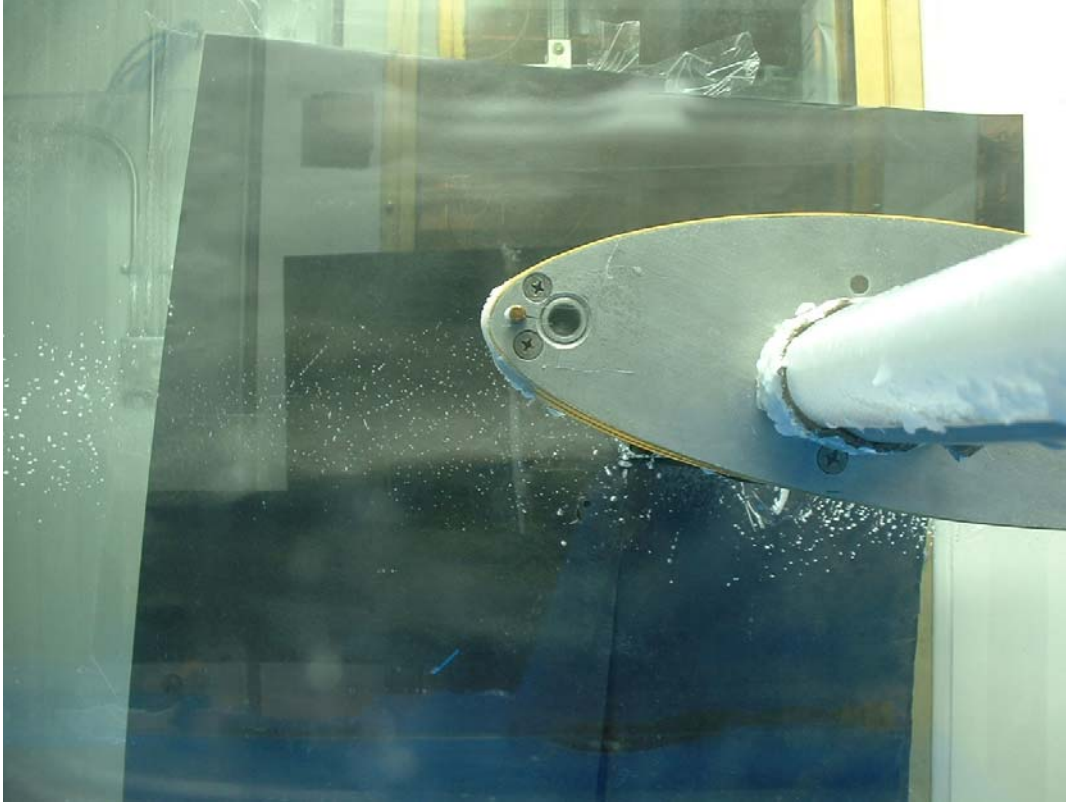


Figure 5.7: Photograph of an iced airfoil at -9°C , 10 m/s and 0.8 g/m^3

Figure 5.7 shows an original photograph of an iced airfoil at a -9°C tunnel temperature with a 10 m/s wind speed and during 15 minutes spraying time at 0.8 g/m^3 LWC when $\text{AOA} = 9^{\circ}$. The black paper is used to obtain clear ice shapes accreted on the airfoil. The side behind the black paper is another window that can be used to put camera for photos. It is a challenge to capture ice shapes over the airfoils. Original photos were processed using MATLAB software, in order to obtain ice shapes. The glaze ice shapes over the airfoil are smooth and became longer along the lower surface, when AOA increases. The reason is a stagnation point that is different than $\text{AOA} = 0$. The stagnation point moves to the lower surface as AOA increases.

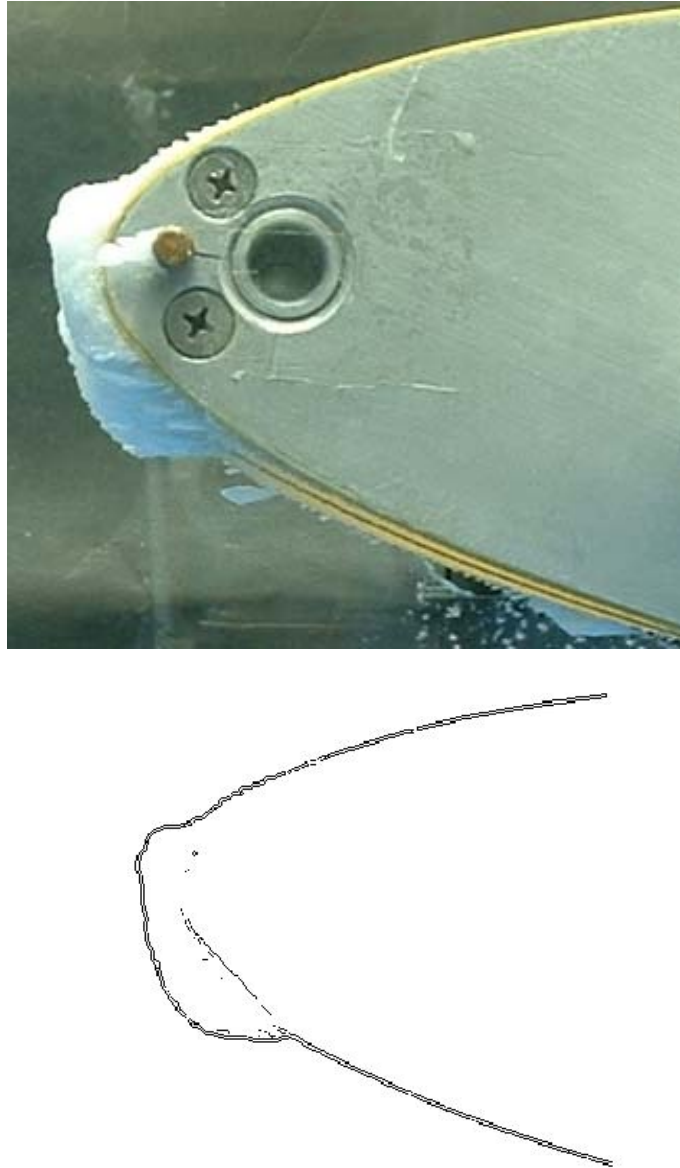


Figure 5.8: Ice shape over the airfoil at -9°C , 10 m/s and 0.8 g/m^3 during 45 minutes

Figure 5.8 presents an ice shape over the airfoil at a -9°C tunnel temperature, 10 m/s wind speed and 0.8 g/m^3 when $\text{AOA} = 9^{\circ}$ during 45 minutes spraying. It shows how the ice shape is captured from the original photograph. Tables 5.4 and Table 5.5 show the ice shapes over an airfoil under rime ice conditions. The temperature is -9°C and the spraying water temperature is 0°C . Comparing the glaze ice and rime ice conditions, the ice thickness is greater at lower temperatures, at the same wind speed and LWC. The significant difference in

ice thickness between glaze and rime ice is the different collection coefficient. Lower temperature has the higher collection coefficient.

Table 5.2: Photos of glaze ice at various AOAs and spraying times at -5°C and 10 m/s










AOA	Spraying water, 15 minutes	Spraying water, 30 minutes	Spraying water, 45 minutes
0			
3			
6			

Table 5.3: Glaze ice shapes at various AOA and spraying duration at -5°C and 10 m/s





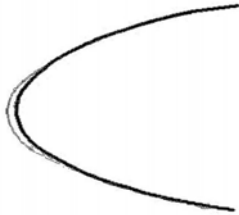



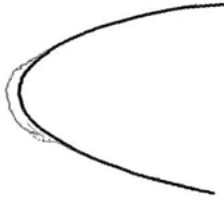
AOA	Spraying water, 15 minutes	Spraying water, 30 minutes	Spraying water, 45 minutes
0			
3			
6			

Table 5.4: Pictures of rime ice at various AOA and spraying duration at -9°C and 10 m/s













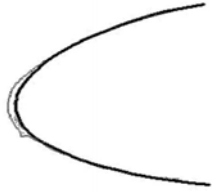




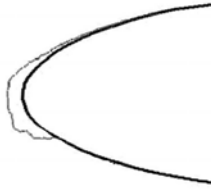

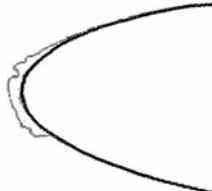




AOA	Spraying water, 15 minutes	Spraying water, 30 minutes	Spraying water, 45 minutes
0			
3			
6			
9			

Table 5.5: Rime ice shapes at various AOA and spraying duration at -9°C and 10 m/s

AOA	Spraying water, 15 minutes	Spraying water, 30 minutes	Spraying water, 45 minutes
0			
3			
6			
9			

5.3 Aerodynamics of the iced airfoil

The last section presented the observations of ice thickness on a NACA 63421 airfoil under glaze and rime ice conditions. The ice thickness increases with icing time. Ice changes the airfoil profile resulting in different aerodynamics. This section will illustrate some experimental results regarding aerodynamic characteristics of the iced airfoil.

Table 5.6 shows results when airfoils are exposed to spray at an air temperature of -5°C for various spraying durations and AOAs, ranging from 0° to 9° . The Reynolds number varies from 8.3×10^5 to 1.2×10^6 . It can be observed that C_L was significantly affected by the ice. The maximum change in C_L is a drop of 96% of the uniced value when $\text{Re} = 8.3 \times 10^5$ ($\text{AOA} = 0$) when spraying water for 30 minutes. The Reynolds number affects the lift coefficient. The lift coefficient decreases more at low than at high Reynolds numbers. This is different than the results at high Reynolds number, reported by Addy et al. [81]. They found that at a Reynolds number greater than 3×10^6 , changes in the Reynolds number did not significantly affect the iced airfoil performance coefficients. Also, previous research on iced airfoils shows that the aerodynamics of an iced airfoil is relatively insensitive to variations of Re ([169, 170]). Figure 5.9 suggests that the aerodynamic coefficients of an iced airfoil are not a strong function of Reynolds number between 8.3×10^5 and 1.2×10^6 . When the Reynolds number is low, ΔC_L of an iced airfoil is greater than at high Reynolds numbers for the same spraying duration. For C_D , at a low Reynolds number, the maximum increase is 55% at $\text{AOA}=6^{\circ}$, while spraying durations of 30 minutes.

Table 5.6: Glaze ice ΔC_L , ΔC_D and ΔC_m at -5°C (LWC of 0.8 g/m^3 and wind speed of 10 m/s)

AOA	Icing time	Re	ΔC_L	$\Delta C_L/C_L$	ΔC_D	$\Delta C_D/C_D$	ΔC_m	$\Delta C_m/C_m$
0	15	8.30E+05	0.057	0.859	0.011	0.156	0.0031	0.860
		9.37E+05	0.027	0.392	0.004	0.066	0.0012	0.399
		1.05E+06	0.019	0.279	0.007	0.107	0.0006	0.277
		1.15E+06	0.020	0.287	0.008	0.114	0.0006	0.292
	30	8.30E+05	0.063	0.963	0.014	0.190	0.0034	0.963
		9.39E+05	0.031	0.447	0.008	0.120	0.0013	0.455
		1.04E+06	0.021	0.308	0.010	0.149	0.0007	0.305
		1.15E+06	0.022	0.309	0.011	0.160	0.0006	0.307
	45	8.23E+05	0.031	0.469	0.015	0.206	0.0017	0.469
		9.26E+05	0.041	0.587	0.011	0.160	0.0017	0.589
		1.02E+06	0.028	0.405	0.007	0.100	0.0009	0.384
		1.16E+06	0.027	0.383	0.009	0.138	0.0007	0.385
3	15	8.33E+05	0.023	0.254	0.004	0.063	0.0013	0.264
		9.44E+05	0.005	0.057	0.004	0.062	0.0002	0.057
		1.05E+06	0.021	0.230	0.005	0.067	0.0007	0.217
		1.15E+06	0.015	0.168	0.004	0.060	0.0004	0.162
	30	8.17E+05	0.026	0.287	0.008	0.120	0.0014	0.282
		9.35E+05	0.022	0.260	0.008	0.117	0.0009	0.253
		1.05E+06	0.026	0.283	0.007	0.101	0.0008	0.271
		1.16E+06	0.022	0.243	0.006	0.090	0.0006	0.241
	45	8.17E+05	0.041	0.453	0.012	0.169	0.0022	0.450
		9.35E+05	0.034	0.406	0.009	0.136	0.0014	0.400
		1.05E+06	0.027	0.294	0.008	0.125	0.0009	0.285
		1.15E+06	0.018	0.206	0.008	0.125	0.0005	0.198
6	15	8.26E+05	0.014	0.105	-0.010	-0.166	0.0007	0.105
		9.30E+05	0.014	0.104	-0.009	-0.144	0.0006	0.109
		1.04E+06	0.017	0.128	-0.007	-0.111	0.0007	0.142
		1.15E+06	0.017	0.125	-0.005	-0.084	0.0005	0.128
	30	8.23E+05	0.019	0.147	-0.034	-0.552	0.0010	0.141
		9.26E+05	0.020	0.148	-0.013	-0.210	0.0009	0.152
		1.04E+06	0.022	0.160	-0.010	-0.166	0.0008	0.171
		1.16E+06	0.019	0.144	-0.009	-0.152	0.0006	0.155
	45	8.11E+05	0.025	0.192	-0.022	-0.361	0.0012	0.170
		9.28E+05	0.034	0.254	-0.016	-0.253	0.0015	0.262
		1.04E+06	0.030	0.222	-0.015	-0.245	0.0010	0.228
		1.16E+06	0.023	0.172	-0.012	-0.196	0.0007	0.178
9	15	8.11E+05	0.069	0.329	-0.029	-0.340	0.0036	0.316
		9.25E+05	0.065	0.297	-0.020	-0.226	0.0025	0.279
		1.04E+06	0.057	0.258	-0.020	-0.241	0.0017	0.240
		1.14E+06	0.047	0.212	-0.015	-0.194	0.0011	0.187
	30	8.10E+05	0.076	0.362	-0.006	-0.070	0.0038	0.340
		9.23E+05	0.069	0.315	-0.002	-0.018	0.0027	0.294
		1.02E+06	0.053	0.240	-0.008	-0.095	0.0015	0.205
		1.12E+06	0.045	0.203	-0.010	-0.132	0.0010	0.161
	45	8.07E+05	0.039	0.184	-0.011	-0.126	0.0017	0.151
		9.04E+05	0.042	0.194	-0.008	-0.095	0.0013	0.141
		1.01E+06	0.033	0.152	-0.013	-0.154	0.0007	0.093
		1.11E+06	0.028	0.124	-0.012	-0.146	0.0004	0.067

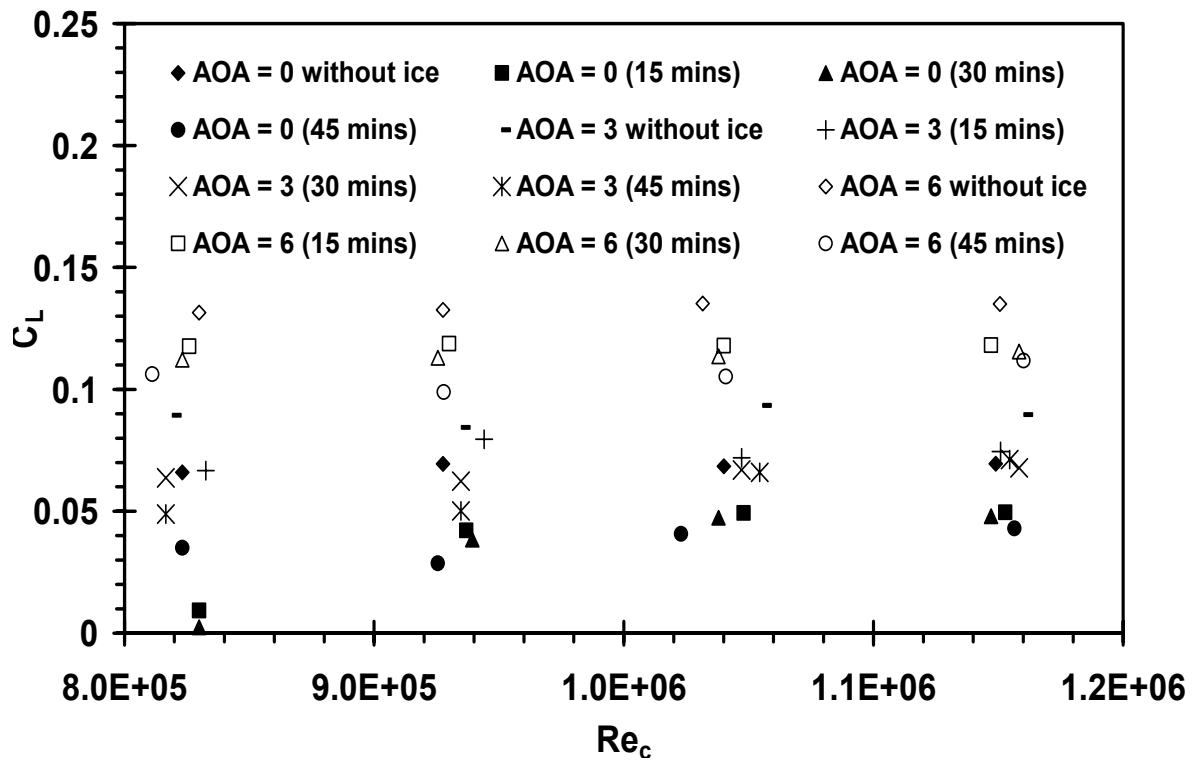


Figure 5.9: Aerodynamics of iced airfoils with glaze ice at various AOA

From Figure 5.9, it can be observed that the glaze ice affects the lift coefficient significantly. Regardless of AOA, the ice accretion over the blade degrades the lift coefficient. However, rime ice has a different effect. Table 5.7 presents the results for an iced airfoil at different Reynolds numbers, with varying spraying durations and AOAs. The maximum decrease of lift coefficients is 45% at AOA = 0° and the spraying duration is 15 minutes. However, it may be observed that the lift coefficient increases when the airfoil accretes some ice. For example, the lift coefficient increases by 10% when AOA = 3° with a spraying duration of 15 minutes and $Re = 1.12 \times 10^6$. The lift coefficient increases by 0.5% when AOA = 6° at 30 minutes spraying duration and $Re = 1.06 \times 10^6$. This phenomenon may help to explain why an iced wind turbine can give more power output in Section 4.4. However, there is not enough data obtained to illustrate every condition in Section 4.4. Also, the temperature in this test is 11°C higher than the conditions in Section 4.4 (-20°C and -30°C).

Table 5.7: Rime ice aerodynamics of the iced airfoil at tunnel temperature -9°C

(LWC 0.8 g/m³ and wind speed 10 m/s)

AOA	Icing time	Re	ΔC_L	$\Delta C_L/C_L$	ΔC_D	$\Delta C_D/C_D$	ΔC_m	$\Delta C_m/C_m$
0	15	8.41E+05	0.038	0.458	-0.034	-0.644	0.0022	0.476
		9.48E+05	0.019	0.227	-0.027	-0.539	0.0010	0.255
		1.05E+06	0.029	0.342	-0.023	-0.475	0.0011	0.363
		1.17E+06	0.039	0.430	-0.016	-0.310	0.0012	0.458
	30	8.16E+05	0.022	0.259	-0.031	-0.595	0.0013	0.269
		9.15E+05	0.017	0.204	-0.027	-0.535	0.0008	0.209
		1.02E+06	0.010	0.123	-0.025	-0.517	0.0004	0.134
		1.12E+06	0.031	0.343	-0.019	-0.372	0.0009	0.346
	45	8.27E+05	0.016	0.192	-0.024	-0.461	0.0010	0.208
		9.36E+05	0.024	0.277	-0.029	-0.572	0.0011	0.292
		1.05E+06	0.020	0.239	-0.026	-0.540	0.0008	0.255
		1.17E+06	0.020	0.224	-0.019	-0.378	0.0006	0.242
3	15	8.15E+05	0.001	0.008	-0.027	-0.460	-0.0002	-0.040
		9.19E+05	0.002	0.017	-0.022	-0.382	-0.0002	-0.047
		1.03E+06	-0.007	-0.076	-0.018	-0.302	-0.0004	-0.135
		1.13E+06	-0.010	-0.102	-0.013	-0.221	-0.0004	-0.164
	30	8.19E+05	0.004	0.046	-0.039	-0.662	0.0000	0.000
		9.33E+05	0.018	0.191	-0.033	-0.564	0.0006	0.148
		1.05E+06	0.020	0.206	-0.022	-0.379	0.0005	0.169
		1.15E+06	0.020	0.209	-0.016	-0.279	0.0005	0.173
	45	8.38E+05	0.018	0.190	-0.016	-0.267	0.0010	0.190
		9.51E+05	0.008	0.083	-0.016	-0.269	0.0003	0.069
		1.07E+06	-0.092	-0.964	-0.014	-0.238	0.0001	0.036
		1.18E+06	0.007	0.073	-0.011	-0.191	0.0002	0.076
6	15	8.41E+05	0.012	0.087	-0.013	-0.197	0.0007	0.098
		9.46E+05	0.011	0.079	-0.011	-0.166	0.0004	0.070
		1.06E+06	0.004	0.033	-0.008	-0.120	0.0001	0.029
		1.17E+06	0.007	0.053	-0.005	-0.081	0.0002	0.046
	30	8.34E+05	0.005	0.040	-0.019	-0.292	0.0002	0.027
		9.43E+05	0.001	0.007	-0.016	-0.237	0.0000	-0.008
		1.06E+06	-0.001	-0.005	-0.013	-0.192	0.0000	-0.005
		1.17E+06	0.000	0.000	-0.010	-0.156	0.0000	-0.007
	45	8.41E+05	0.025	0.184	-0.016	-0.253	0.0013	0.179
		9.51E+05	0.020	0.147	-0.013	-0.197	0.0009	0.147
		1.06E+06	0.015	0.109	-0.010	-0.147	0.0005	0.105
		1.18E+06	0.023	0.163	-0.007	-0.098	0.0006	0.168
9	15	8.37E+05	0.009	0.043	0.008	0.081	0.0001	0.012
		9.53E+05	0.010	0.047	0.011	0.111	0.0003	0.037
		1.07E+06	0.006	0.028	0.009	0.097	0.0001	0.009
		1.17E+06	0.008	0.041	0.010	0.107	0.0001	0.019
	30	8.37E+05	0.017	0.083	0.010	0.106	0.0006	0.053
		9.58E+05	0.020	0.100	0.013	0.137	0.0008	0.100
		1.07E+06	0.010	0.049	0.008	0.091	0.0002	0.030
		1.18E+06	0.015	0.072	0.010	0.112	0.0003	0.059
	45	8.42E+05	0.044	0.220	-0.006	-0.066	0.0021	0.205
		9.58E+05	0.042	0.204	0.000	0.005	0.0017	0.204
		1.07E+06	0.029	0.144	0.000	0.000	0.0008	0.127
		1.18E+06	0.030	0.146	0.000	0.002	0.0007	0.135

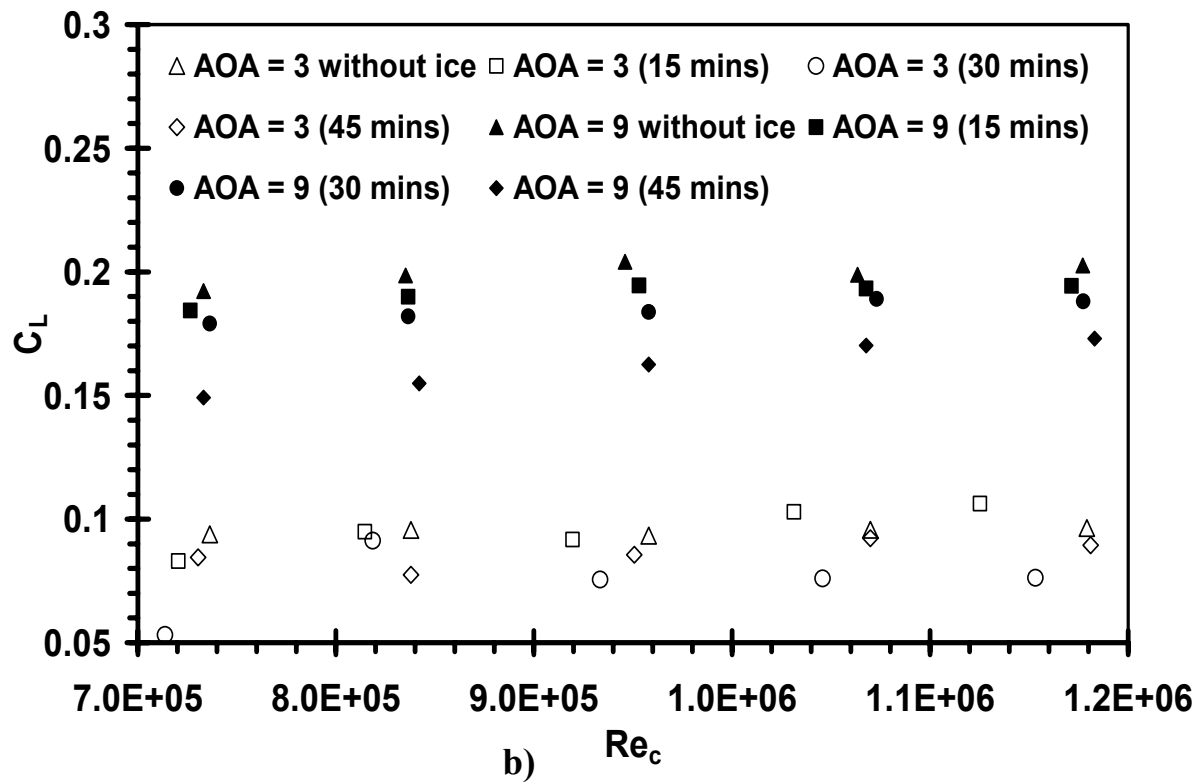
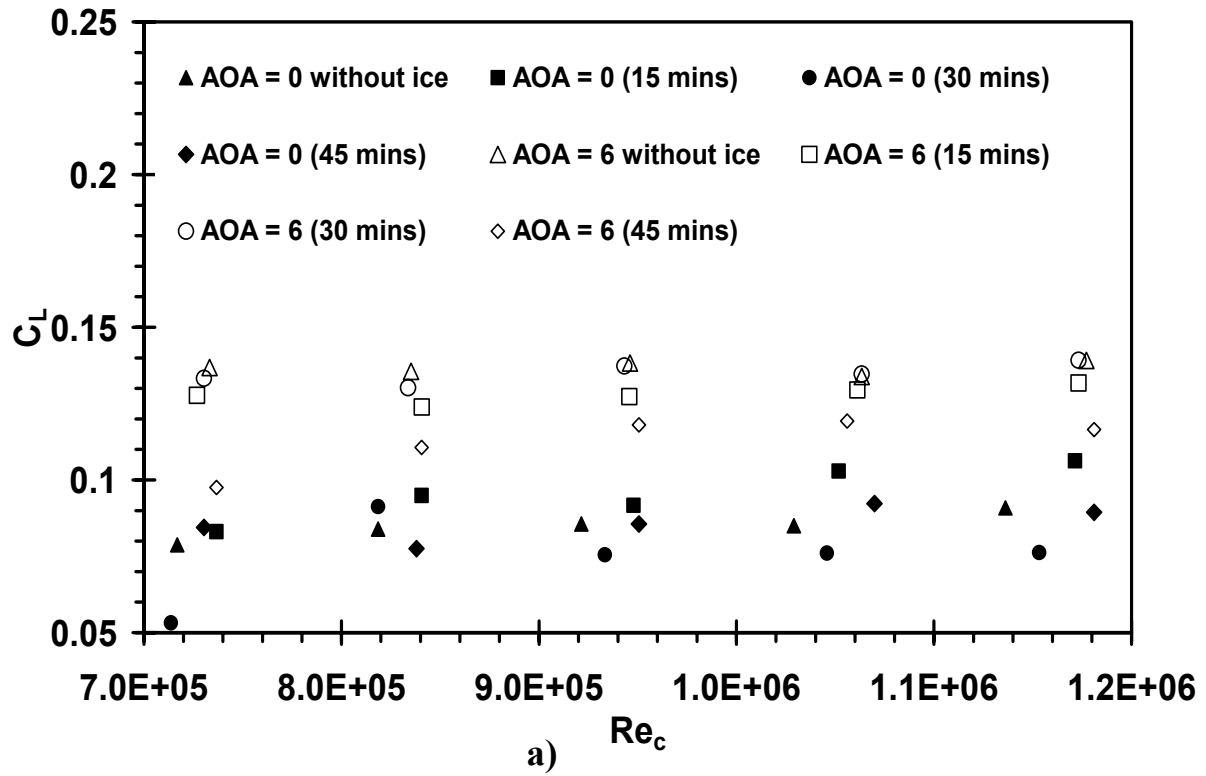


Figure 5.10: Aerodynamics of iced airfoils with rime ice at various AOA and spraying duration: a) AOA = 0°& 6°; b) AOA = 3°& 9° with 0.8 g/m³ LWC at 10 m/s wind speed

Figure 5.10 illustrates the aerodynamics of a rimed airfoil at varying AOA from 0° to 9° . As ice thicknesses increases, the lift coefficient drops. As AOA increases, the lift coefficient drops less than AOA = 0.

The rime ice drag coefficient also can be found in Table 5.7. The maximum increase oin the drag coefficient is 66% at $Re_c = 8.18 \times 10^5$, AOA = 3° and a spraying duration of 30 minutes. The increase in drag coefficient is higher at smaller AOA. Normally, as AOA varying from 0° to 9° , the changes in drag coefficient decrease from high to low.

5.4 Discussion of iced wind turbine results

Experimental results in Chapter 4 show that ice accretion changes the wind turbine blade profiles and therefore decreases the wind turbine power output. The glaze iced wind turbine blades are almost all covered by ice in Figure 4.5 and Figure 4.6. Ice can cover the blades from the leading edge to the trailing edge. However, the rime iced blades are normally covered only on the leading edge, as shown in Figure 4.10, as ice accumulates along the leading edge under rime ice conditions because of the very low temperature of the blades when water droplets impact on the surface. A water droplet impinges on a wind turbine blade in the liquid state under glaze ice conditions. Before a water droplet changes to ice, it can flow along the surface from the leading edge to the trailing edge, then release latent heat, turn to ice and adhere to the blade. For rime ice conditions, the water droplets are super-cooled in the wind tunnel before they collide with the blades, and then change to ice when they hit the blades, thus there is no time for droplets to move along a blade. Thus, ice accretion is more confined to the leading edge.

Comparing Figure 4.5 and Table 5.2, different ice shapes between the rotating wind turbine blades and the 2-D airfoil are observed, under glaze ice conditions. The ice roughness on the airfoil occurs along the leading edge of the airfoil. For the rotating 3-blade wind turbine, glaze ice can adhere from the leading edge to the trailing edge of the blades, due to the shorter chord of the blades and rotation of the 3-blade wind turbine. The centrifugal force lets water droplets move when they impact the blades. Another reason is the varying pitch angles along the twisted blades, used in most wind turbines. There are different ice shapes for iced rotating blades and iced static blades under glaze ice conditions. Glaze ice conditions occur at just below zero degrees Celsius. Worldwide climate change may lead to more drizzle and freezing

rain storms, so glaze ice conditions during wind turbine operation would become more common. Figure 4.10 and Table 5.5 show nearly the same ice shapes along the rotating blades and static airfoils. The basic difference between rime ice and glaze ice is the temperature when ice is occurring. Lower temperatures make water droplets change more readily to ice. The ice thickness on a rotating blade is higher than a static airfoil if they have the same LWC and spraying time, due to a higher relative velocity when a water droplet hits a rotating blade.

Comparison with Tables 5.3 and 5.5, the ice shapes are different under rime ice and glaze ice conditions at the same spraying time and AOA. This can be explained by lower temperatures that lead to a higher collection coefficient. A varying AOA can also change the ice shapes, especially at the leading edge.

Ice modifies the profile of wind turbine blades, regardless of glaze or rime ice conditions. Iced blades affect the power generation as measured in Chapter 5, so appropriate methods need to be considered when turbines are operating in cold climates. Further research on coating materials [100] provides methods for anti-icing, de-icing and ice-phobic materials. Using ice-phobic material surface coatings is insufficient, so a heating surface provides an additional method for anti-icing and de-icing, when wind turbines operate under icing conditions. Results in Chapter 6 have provided heat transfer correlations of the heat transfer coefficient for these purposes.

From Chapters 4 and 5, it was examined how ice adheres to the leading edge of a wind turbine blade. The heat transfer correlations in Chapter 6 provide average values for the entire airfoil. According to recommendations in Ref. [98], an entire heater over the blade surface is better

for anti-icing and de-icing, under extreme cold conditions. These trends were observed in experimental results in Chapter 4, for glaze ice conditions. For most drizzle and freezing rain conditions, a heater over an entire wind turbine blade is necessary for de-icing and anti-icing. Also, the heat transfer correlation at the leading edge (10% chord along the blades, $0.1c$) is higher than 1.7 times the average correlation. The heat transfer correlation at the leading edge (20% chord along the blades, $0.2c$) is higher than 1.4 times the average correlation. This can be used to calculate the heat transfer correlation for a heater at the leading edge. From Chapters 4 and 5, most ice cover lies in the range of $0.1c$. According to results in Ref. [100], a useful method is an ice-phobic material and a heater strip at the leading edge up to $0.1c$, for most blade sections in icing condition areas. The results provide a useful method to calculate the energy required when wind turbine blades need to be installed with a heater or a built-in heat strip.

Chapter 6

Convective heat transfer from a NACA 63421 airfoil

The previous chapters depicted the icing of wind turbines and blades under experimental icing conditions. Wind turbines have power losses due to ice modified profiles of the blades. De-icing and anti-icing are important objectives to achieve for wind turbines operating under icing conditions. This chapter examines a key aspect of de-icing methods – convective heat transfer – with air flowing over the NACA 63421, airfoil with or without impinging water droplets. The heat transfer will alter the ice accretion described in Chapter 5.

The experimental systems include the force balance for a 2-D airfoil, temperature measurements, and current, voltage and rotation measurements of a wind turbine system in the refrigerated wind tunnel. The 3-blade HAWT model provided evidence about power losses under icing conditions (see Chapter 4). The 2-D blade (NACA 63421) was used to study aerodynamics under icing conditions as presented in Chapter 5. The results have shown that wind turbines have lower power output, when the blades are iced. Also, an airfoil would produce less lift and more drag during an icing event. The results presented in the previous two chapters suggest that heat transfer is necessary to keep ice off when wind turbines are operating under icing conditions. This chapter will focus on the mechanism of heat transfer, when air flows over a turbine blade under various icing conditions. Table 6.1 summarizes the cases to be examined in this chapter.

Table 6.1: Experimental conditions during convective heat transfer

	Without LWC		With LWC	
AOA	0°	5°, 10°, 15°, 20°, 25°	0°	5°, 10°, 15°, 20°, 25°
Temperature	10°C, 0°C, -5°C, -10°C, -15°C, -20°C, -25°C, -30°C		3°C, 10°C	
LWC	0 g/m ³		0 ~ 2 g/m ³	
T (water)	N/A		10°C	
Heater	45 V, 1.3 A		50 V, 1.5 A	
Wind speed	0 ~ 33 m/s		0 ~ 33 m/s	

6.1 Heat transfer characterization at 0 AOA

In this section, experimental results are presented for convective heat transfer from a NACA 63421 airfoil at varying Reynolds numbers. These variations are obtained by changing the icing tunnel air velocity and the air temperature in order to vary the air viscosity, density and thermal diffusivity. Within the refrigerated wind tunnel (Figure 3.1), air temperatures were varied between 20°C and -30°C. This temperature range yields Prandtl numbers in Table 6.2.

Table 6.2: The range of Prandtl numbers in the experiments

Prandtl Number	Temperature
0.7098	20°C
0.7125	10°C
0.715	0°C
0.7166	-5°C
0.7181	-10°C
0.7196	-15°C
0.7211	-20°C
0.7226	-25°C

Data was collected at lower temperatures (-30°C), but measured data at these temperatures becomes highly uncorrelated when normalized against other data at warmer temperatures. It is observed that all data collapsed closely onto a single normalized curve, except data at -30°C . Although droplets were not sprayed inside the wind tunnel, moisture within the air may condense and freeze along a thin surface film at very low temperatures. This phase change releases latent heat into the surface thermocouple, which distorts the heat balance involving conduction and convection. As a result, data was primarily analyzed over a range of temperatures that yielded uniform normalizations of the Nusselt numbers, this indicated consistency and useful verification that experimental data was collected accurately.

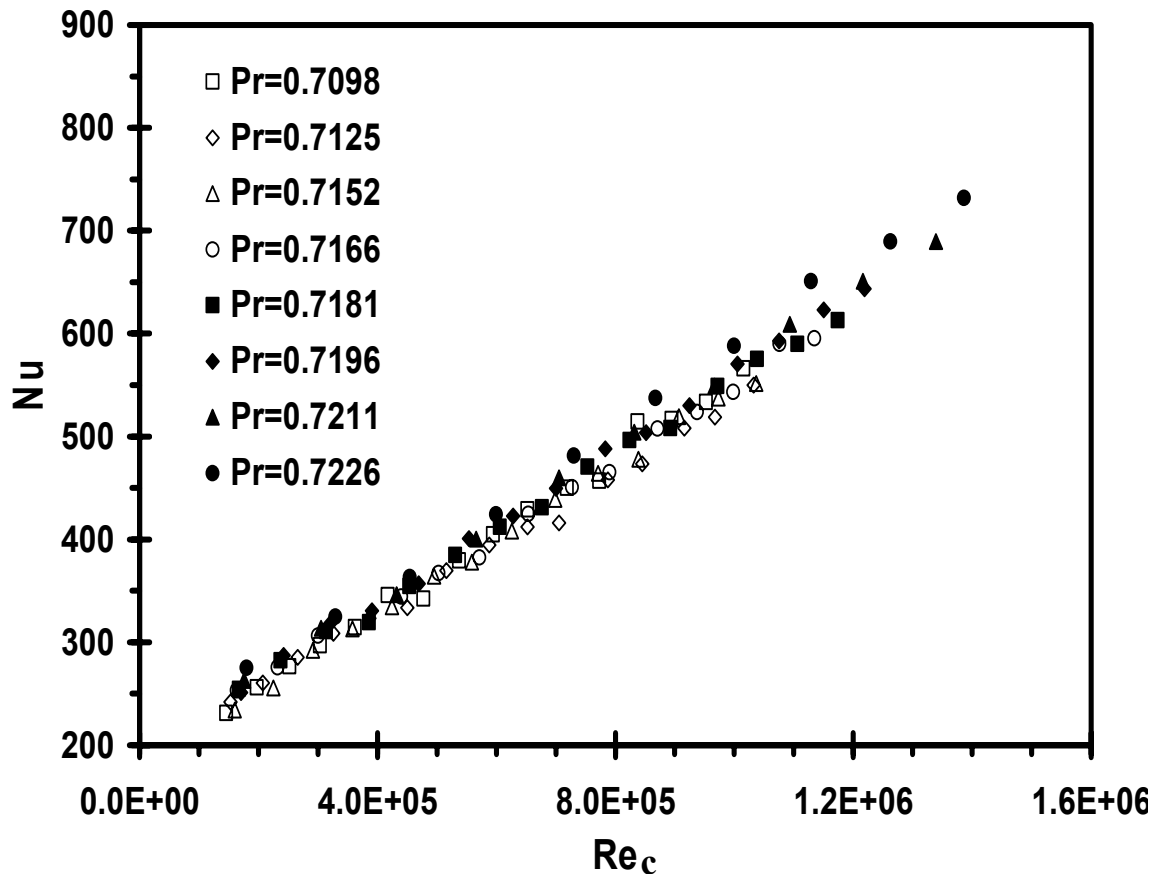


Figure 6.1: Average Nusselt number for a NACA 63421 airfoil at varying Reynolds and Prandtl numbers

A Reynolds number of $Re_c > 5 \times 10^5$ characterizes transition to turbulence of the boundary layer over the airfoil. This transition also occurs for a flat plate, as well as a cylinder, although

the transition number for a cylinder in cross flow occurs at a Re_D of 2×10^5 . Due to these similarities, experimental data is correlated against the following functional form of the Nusselt number, which is equivalent to the Hilpert correlation for a cylinder in cross flow[171],

$$\overline{Nu} = c Re^m Pr^{1/3} \quad (6-1)$$

Figure 6.1 shows that experimental data exhibits similar behavior over a range of Reynolds and Prandtl numbers. A modified Hilpert correlation accurately reflects the measured data over a similar range of Reynolds numbers shown in Figure 6.2. The coefficients, c and m , are found based on a least squares curve fit of measured data. The data points lie close to the correlated curve and measured data for each Prandtl number, which is determined independently at different temperatures. This close agreement provides useful verification that measurements exhibit consistent behavior under appropriate normalization at varying Reynolds numbers.

Figure 6.3 shows the local Nusselt numbers, Nu_x , at different positions and Reynolds numbers. The stagnation point is $x/c = 0$. The Nusselt number decreases dramatically after the stagnation point, due to the rapidly thickening boundary layer along the top and bottom surfaces. It falls to a minimum at a position of $0.2c$ along the chord of the airfoil, after which it increases. Although both surfaces of the airfoil have the same trends near the leading edge of the airfoil, the lowest value of Nu_x occurs along the bottom surface, due to the different streamline pattern for a non-symmetric airfoil. It would have the same local Nusselt number, if the airfoil was symmetric in shape and orientation, with respect to the freestream. The local Nusselt number for the NACA 63421 airfoil has different trends below and above the stagnation point, due to the non-symmetrical profile of the airfoil.

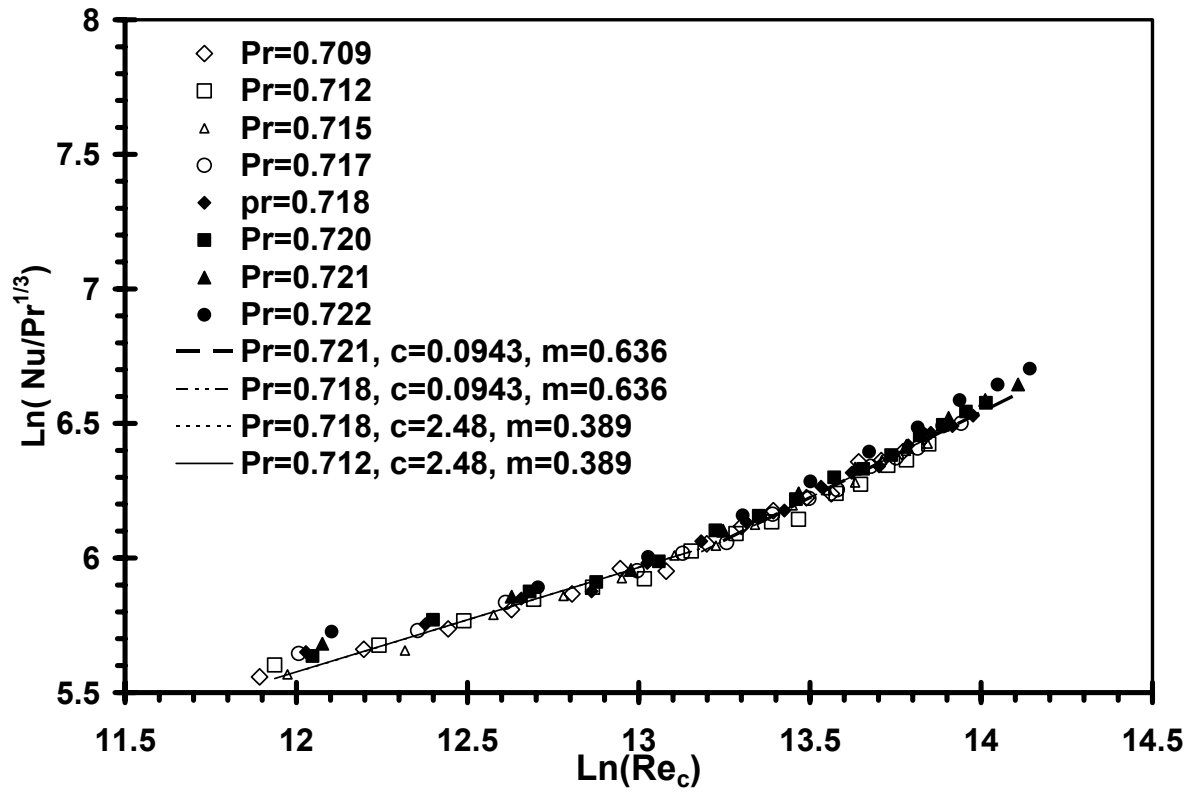
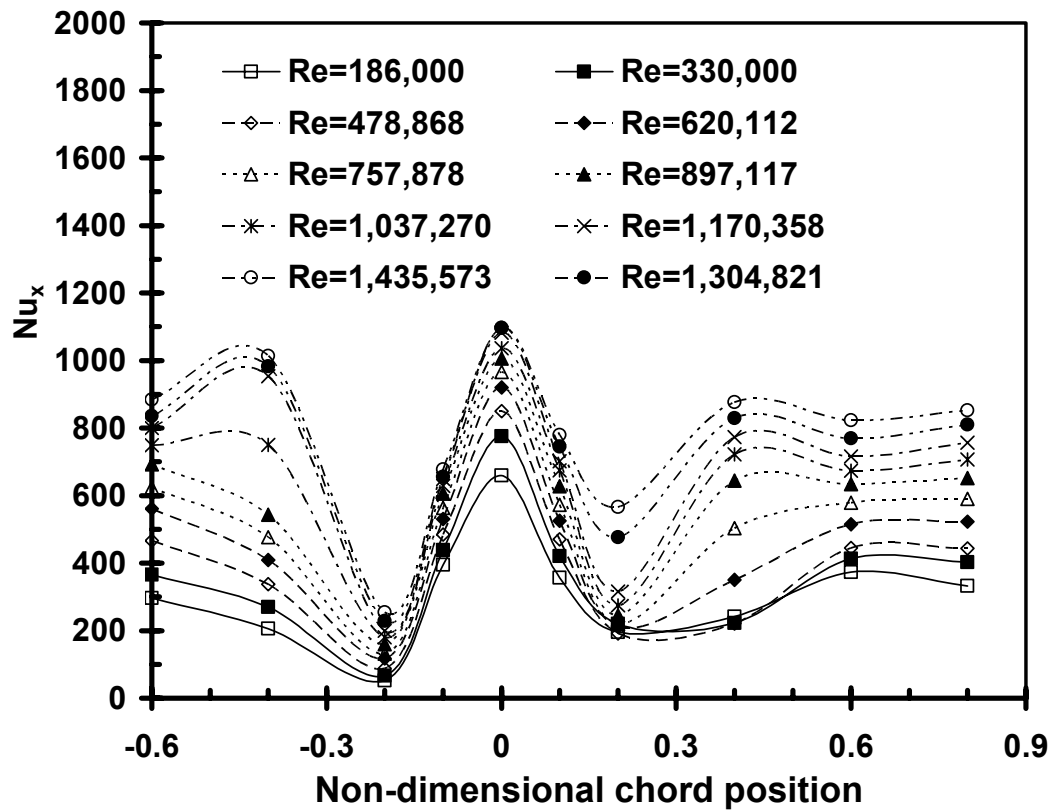


Figure 6.2: Normalized Nusselt function correlation

Figure 6.3: Local Nusselt number at varying chord positions (x/c)

6.1.2 Sensitivity study for correlation coefficients

Sensitivity studies involving the effects of varying correlation coefficients, c and m , are illustrated in Figure 6.4 (0°C, $Pr = 0.715$) and Figure 6.5 (-10°C, $Pr = 0.718$). The purpose of these studies is to better understand sensitivity of the correlation to changes of the empirical coefficients. In Figure 6.4a, the central line represents $c = 2.483$ and $m = 0.389$. The following correlation of \overline{Nu} closely agrees with the experimental data,

$$\overline{Nu} = 2.483 Re^{0.389} Pr^{1/3} \quad (\text{for } Re \leq 5 \times 10^5) \quad (6-2)$$

In Figure 6.4a, the m -coefficient is kept constant, while the c -coefficient varies over a range of values to show sensitivity of the correlation with respect to the c -coefficient. In contrast, Figure 6.4b shows sensitivity with respect to the m -coefficient, while the c -coefficient is kept constant. Unlike Reynolds numbers below $Re = 5 \times 10^5$ (laminar flow regime) in Figure 6.4, sensitivity studies at higher Reynolds numbers (turbulent flow regime) are illustrated in Figure 6.5a and b. Similar trends are observed both in Figure 6.4 and 6.5, with respect to sensitivity to the c -coefficient and m -coefficient. The following correlation is obtained for turbulent flow conditions: $c = 0.0943$ and $m = 0.636$.

$$\overline{Nu} = 0.0943 Re^{0.636} Pr^{1/3} \quad (\text{for } Re > 5 \times 10^5) \quad (6-3)$$

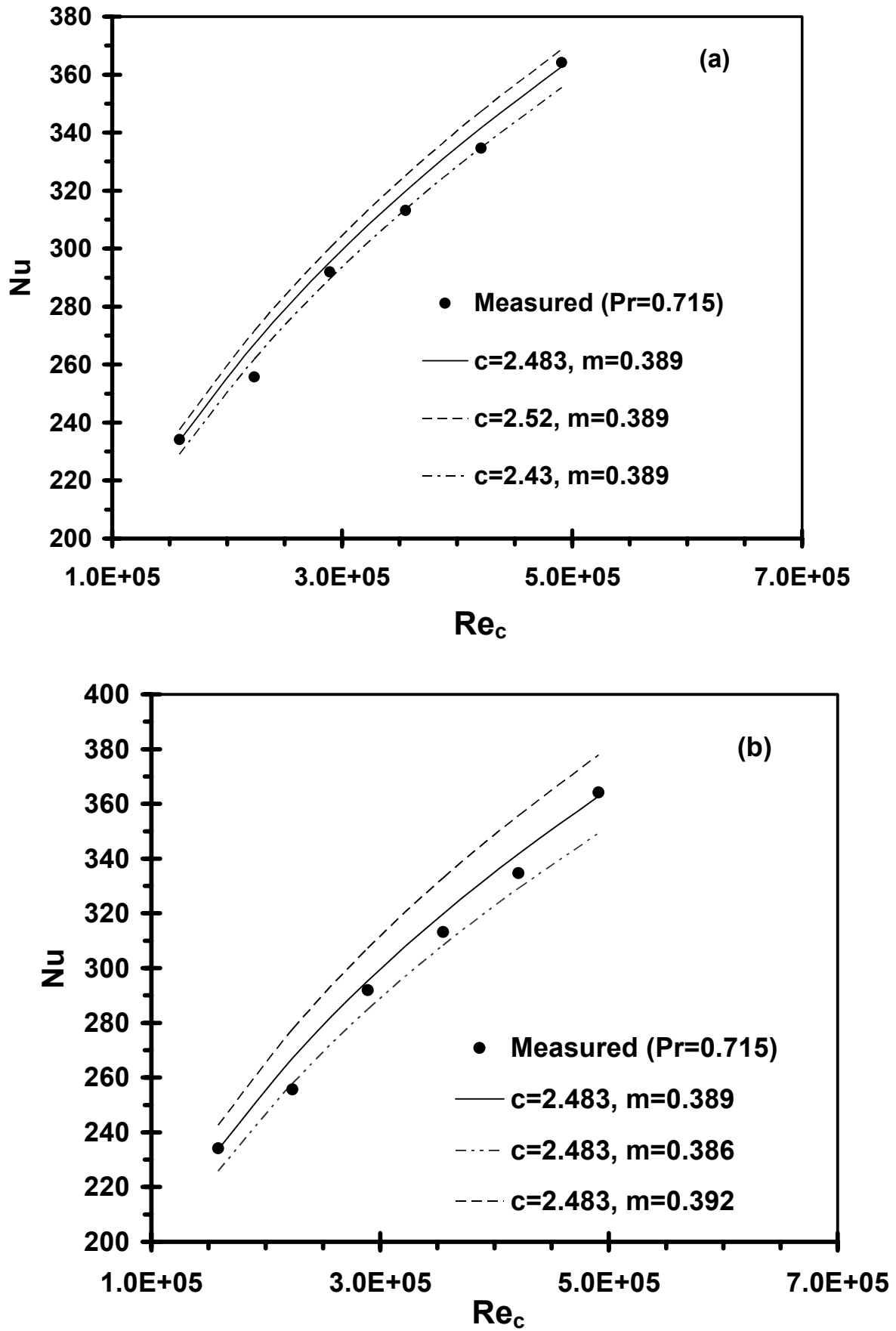


Figure 6.4: Average Nusselt number at varying a) c and b) m ($Re_c \leq 5 \times 10^5$)

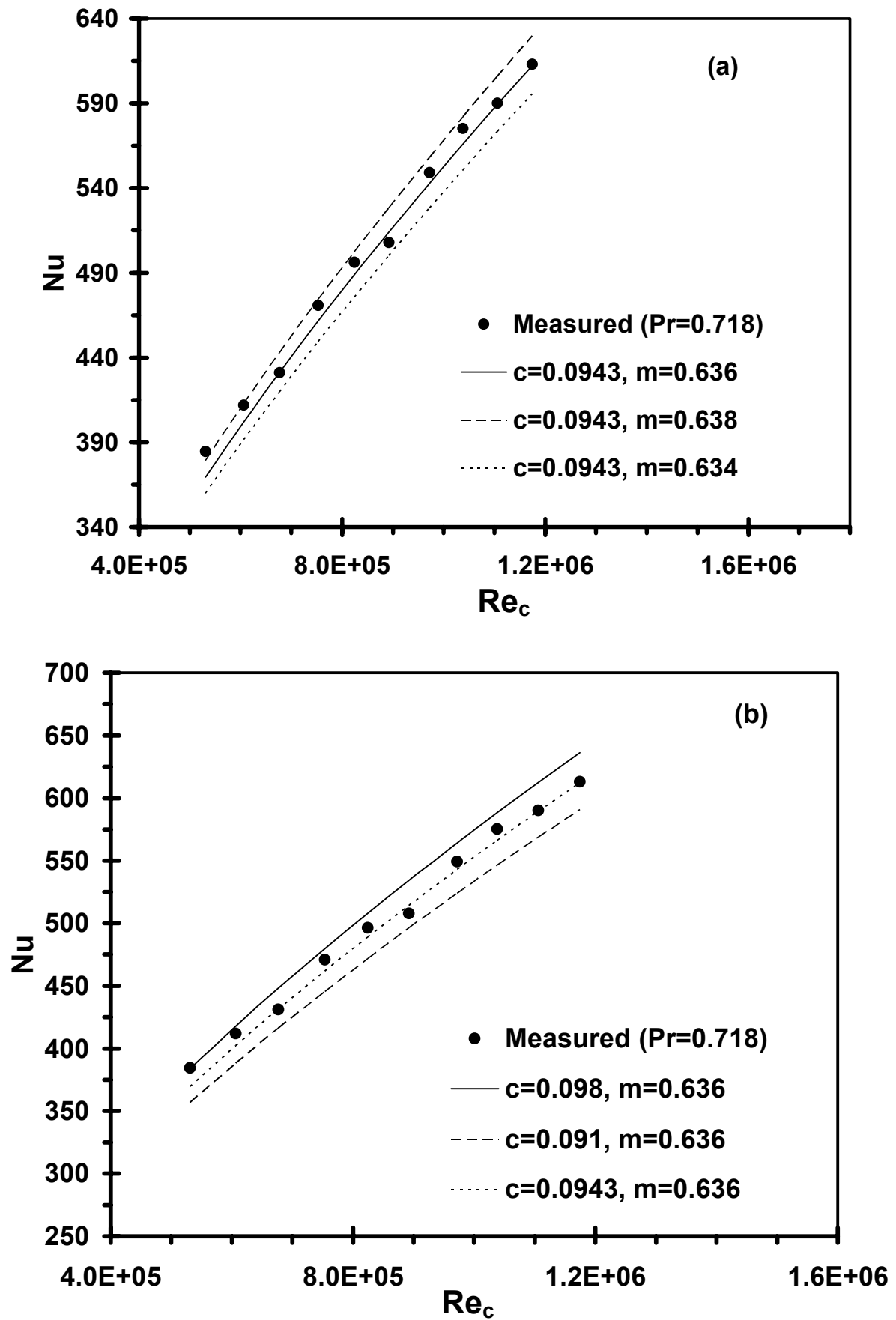


Figure 6.5: Average Nusselt number at varying a) c and b) m ($Re_c > 5 \times 10^5$)

6.1.3 Comparison with past methods

The previous study used thermocouples to measure surface temperatures, which were subsequently used in heat balances to establish the convective heat transfer coefficients. Many similar past studies have shown that thermocouple measurements can provide an effective method for determining these coefficients. Sanitjai and Goldstein [172] measured both local and average convection coefficients for a circular cylinder, with eight T-type (copper–constantan) thermocouples installed under the heated surface. The authors studied Reynolds numbers between 2,000 and 90,000 and Prandtl numbers between 0.7 and 176, in air, water and six mixtures of ethylene glycol and water. In a similar way as Equations 6-2 and 6-3, the authors separated the empirical correlations into distinct regions, namely the laminar boundary layer, reattachment and periodic vortex flow regions. Chang and Mills [173] used an RdF microfoil heat flux sensor with T-type thermocouples installed on the center plane of a cylinder to measure local surface temperatures and convection coefficients for a cylinder in cross flow. The authors presented correlations for the average Nusselt numbers, while including effects of wind tunnel blockage and freestream turbulence on the correlations.

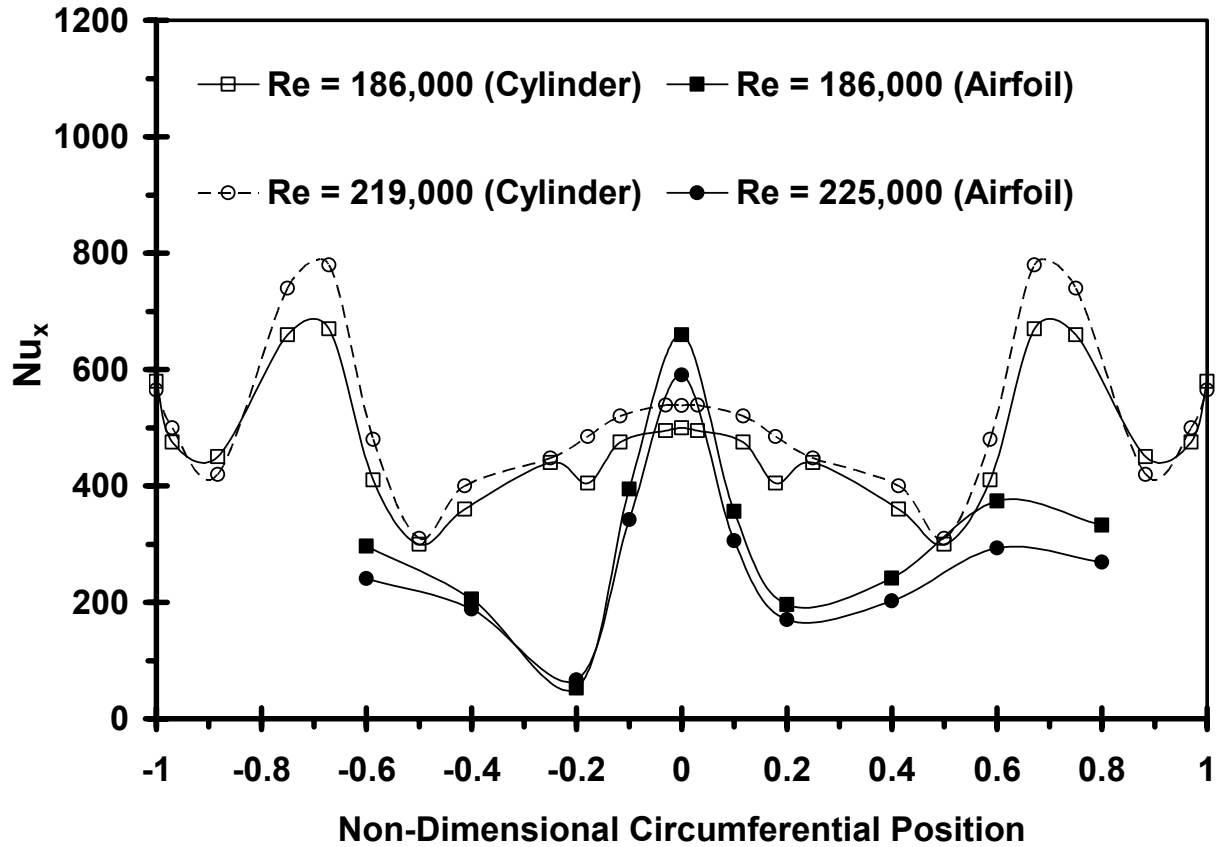


Figure 6.6: Local Nusselt number for cylinder and airfoil cases

Previous studies have shown that heat flux sensors and other techniques can also determine convective heat transfer coefficients at varying Reynolds and Prandtl numbers [174]. For example, Nakamura and Igarashi [175] used heat flux sensors to measure heat transfer from a circular cylinder in cross flow at Reynolds numbers between 3,000 and 15,000. The heat flux sensor was used to measure fluctuating heat transfer rates, while an infrared thermograph gathered time-spatial characteristics of the heat exchange. Naylor [176] gave an overview of classical and holographic interferometers, which can also be used for measurements of convective heat transfer coefficients. Interferometric systems are advantageous since they are non-intrusive, while thermocouples provide other advantages of low cost and reliability over a wide range of temperatures.

The circular cylinder and flat plate are the most common geometrical configurations, which have received most attention of past research studies. Correlations have been reported in textbooks [171] and review articles [177].

Figure 6.6 compares the local Nusselt number for a circular cylinder with an airfoil. Two curves at different Reynolds numbers are shown for each case. For the cylinder, it can be observed that the local Nusselt number variation is symmetric, with respect to the upper and lower surfaces. Also, two minimum points of the local Nusselt number are observed. This occurs from the laminar boundary layer development after the stagnation point, followed by boundary layer transition from laminar to turbulent flow. A second minimum of the local Nusselt number arises on the downstream side of the cylinder. After the separation point in the wake region, the local Nusselt number increases due to turbulent mixing in the wake. Turbulent flow conditions occur when $Re > 2 \times 10^5$. Both cases in Figure 6.6 exceed this Reynolds number.

The local Nusselt number distribution for the airfoil is significantly different than for the circular cylinder. Only a single minimum value is observed and the maximum occurs at the stagnation point. The boundary layer growth causes the local Nusselt number to decrease, as the air flows over the airfoil downstream of the stagnation point. The local Nusselt number reaches a minimum at $0.2c$ and Nu_x along the lower surface becomes smaller than values on the upper surface. The local Nusselt number increases after $0.2c$. The maximum Nusselt number at the stagnation point (not at $0.6c$) is significantly different than the cylinder.

A comparison of the average Nusselt number at varying Re numbers is shown in Figure 6.7, for the cases of an airfoil, cylinder and flat plate. For the circular cylinder, the following Hilpert and Churchill correlations are investigated,

$$\overline{Nu} = 0.027 Re_D^{0.805} Pr^{1/3} \quad (\text{for } 4,000 < Re_D < 40,000; \text{Hilpert [171]}) \quad (6-4)$$

$$\overline{Nu} = 0.3 + \frac{0.62 Re^{1/2} Pr^{1/3}}{\left[1 + (0.4/Pr)^{2/3}\right]^{1/4}} \times \left[1 + \left(\frac{Re}{282,000}\right)^{4/5}\right]^{4/5}$$

(for $10^2 < Re \leq 10^7$; Churchill [178]) (6-5)

For a flat plate, the following correlations are adopted [171],

$$\overline{Nu} = 0.664 Re_x^{1/2} Pr^{1/3} \quad (\text{for } Re \leq 5 \times 10^5) \quad (6-6)$$

$$\overline{Nu} = (0.0037 Re_L^{4/5} - 871) Pr^{1/3} \quad (\text{for } 5 \times 10^5 < Re < 10^8) \quad (6-7)$$

In Figure 6.7, significant differences between different Nusselt numbers can be observed. When $Re \leq 5 \times 10^5$, the average Nusselt number for the airfoil is almost the same as for flow across a flat plate, due to fully laminar flow over the surface. The situation changes when $Re > 5 \times 10^5$. The average Nusselt numbers for the airfoil are not affected significantly by turbulence along the airfoil. In Figure 6.7, the average Nusselt number for the cylinder and flat plate has a large variation with Reynolds number, as compared with the airfoil.

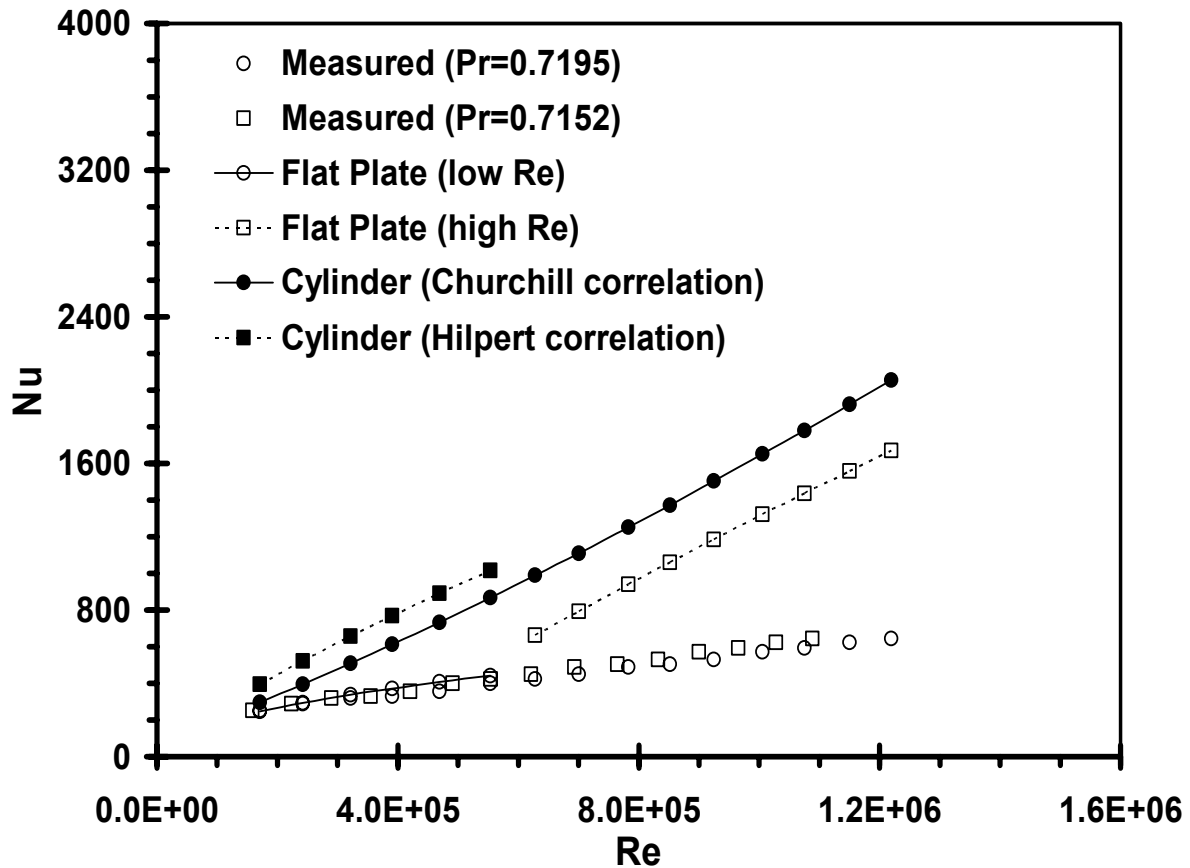


Figure 6.7: Comparison between NACA 63421 airfoil, flat plate and circular cylinder results

The experimental uncertainty of the measured Nusselt number depends on the uncertainty of the local heat transfer coefficient, airfoil chord, thermal conductivity and other factors. The local heat transfer coefficient depends on the temperature difference between the surface and freestream, as well as the net convective heat loss for each test case. The estimated uncertainties [179] of the heat transfer coefficient and Nusselt number is $\pm 7.32\%$ and $\pm 7.34\%$, respectively (see Appendix B – Measurement uncertainties). The major portion of the measurement uncertainty arises from varying temperatures during the experiments, resulting in a 6.2% precision error. The uncertainties of velocity measurements and Reynolds numbers are 0.62% and 0.95%, respectively, mainly due to an error bias in the air velocity measurements.

The current method of using thermocouples and balancing heat conduction with forced convection to measure heat transfer from a bluff body is a well-known and conventional technique for heat flux measurements. In the next section, measured results from this experimental study will be presented at varying angles of attack. The results will be correlated with respect to the Nusselt number at varying Reynolds and Prandtl numbers. It will be shown that the experimental results can be modeled accurately with a modified Hilpert correlation, thereby providing a common functional form of classical correlations for bluff bodies.

6.2 Nusselt number at varying AOA

The previous section introduced a modified correlation with airflow over the airfoil at zero AOA. This section will discuss experimental results at varying AOA. The experimental results will show that the angle of attack (AOA) substantially affects the heat transfer coefficient. Figure 6.8 shows the measured local Nusselt numbers, Nu_x , at different positions and Reynolds numbers. The stagnation point is located at $x/c = 0$. The curve with $AOA = 0$ shows that the Nusselt number decreases after the stagnation point, due to the thickening boundary layer along the top and bottom surfaces. It falls to a minimum at a position of $0.2c$ along the chord of the airfoil, then it increases thereafter. Although both surfaces of the airfoil have the same trends near the leading edge of the airfoil, the lowest value of Nu_x occurs along the lower surface. It would have the same local Nusselt number, if the airfoil was symmetric in shape and orientation with respect to the freestream, but non-symmetry leads to different Nusselt number fields on each side of the stagnation point. The thickness of the laminar boundary layer increases when x increases from the leading edge to the trailing edge. At some

points along each surface, the boundary layer transition occurs and the boundary layer becomes turbulent. In the laminar region, the heat transfer coefficient decreases as the thickness of the boundary layer increases. The heat transfer coefficient increases as the boundary layer becomes turbulent.

In Figure 6.8a, it can be observed how the Nusselt number changes with AOA, for the case of low Reynolds number ($Re \leq 5 \times 10^5$). At the stagnation point, the Nusselt number remains nearly uniform at different values of AOA. However, it can change significantly with AOA along the chord of the airfoil. The Nusselt number decreases significantly at $\pm 0.1c$, $-0.4c$ and $0.6c$, and it increases at $-0.2c$, $-0.6c$ and $0.4c$. Figure 4b shows the Nusselt number results for cases of high Reynolds numbers. At angles of attack of 5° and 10° , the local Nusselt number at the stagnation point is lower than the case for 0° . Also, values of the Nusselt number at $0.4c$ and $+0.6c$ are lower than AOA of zero at those points. In contrast, the values of Nusselt number at $-0.1c$, $-0.2c$ and $-0.6c$ are higher than an AOA of zero at the same points. As AOA increases, the changes of local Nu with AOA become more pronounced at higher Reynolds numbers. The Nusselt number at the stagnation point is higher than the value of Nu at the stagnation point when the angle of attack is 0° . Also, only two points of the local Nu number along the airfoil, $-0.4c$ and $+0.6c$, have lower values than the Nusselt number at 0° for the same points. Furthermore, Nu_x for the other points along the airfoil are larger than the value of the local Nu number at the same points for 0° . The average Nu number is expected to have similar distinct trends at high Reynolds numbers.

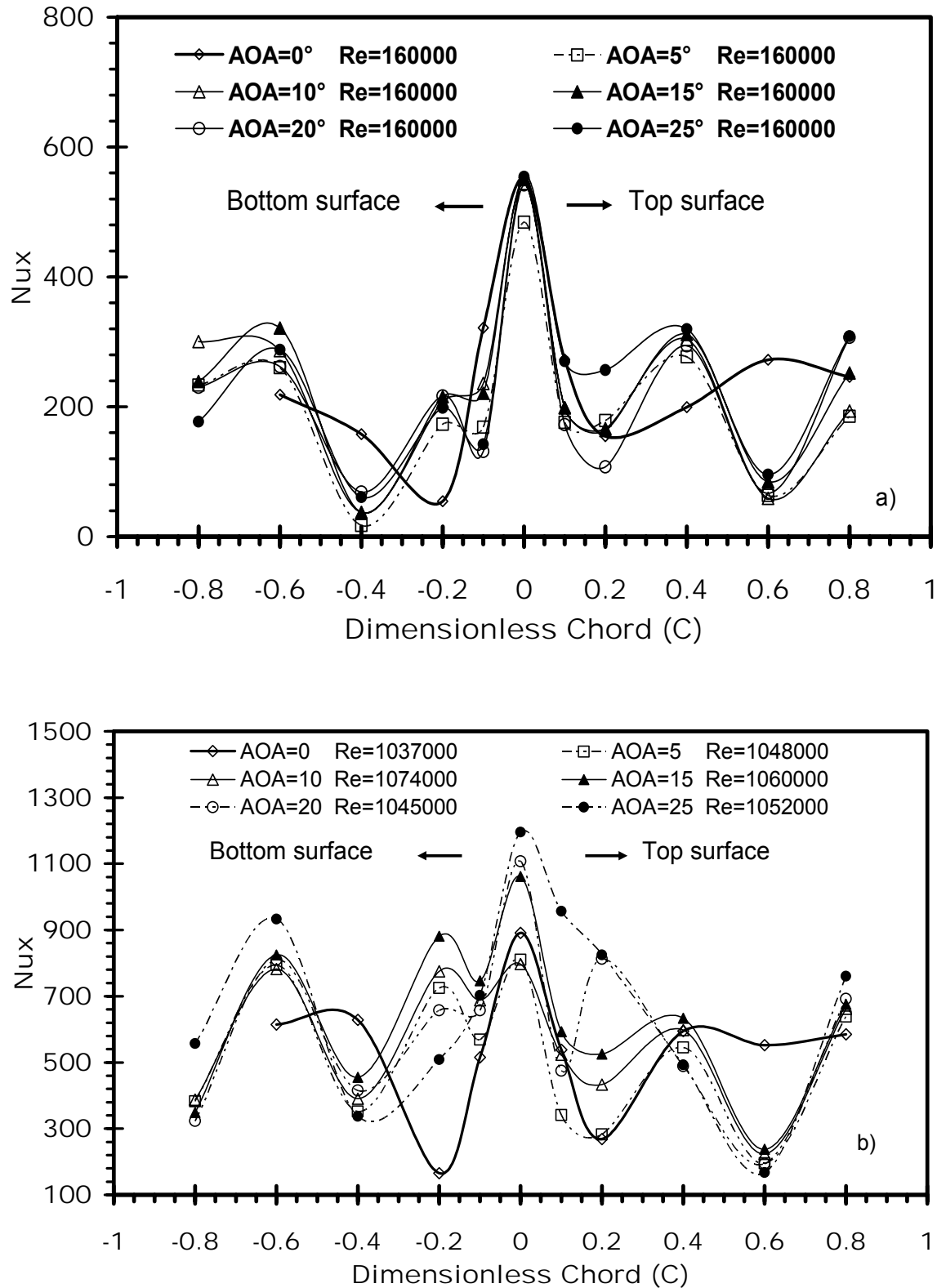


Figure 6.8: Local Nusselt number distribution along the dimensionless chord of a NACA 63421 airfoil: a) low Re , and b) high Re

Figure 6.9 shows additional results for other angles of attack: 5° , 10° , 15° , 20° and 25° at a higher Reynolds number. In each case, the correction factors for the Nu number correlations have yielded good agreement between the predicted and measured data. The Nusselt number increases at higher angles of attack, since the separation point moves upstream, induces turbulence and enhances heat exchange between the surface and fluid. At lower Reynolds numbers, close agreement is also achieved, both at 10° in Figure 6.10 and higher angles of attack in Figure 6.11. As observed previously for higher Reynolds numbers, the Nusselt number increases at higher angles of attack. The results indicate that a standard Hilpert form of convection correlation can be used to predict heat transfer from a NACA 63421 airfoil at varying angles of attack. A correction factor on a standard Hilpert correlation has yielded relatively close agreement with measured data for the Nusselt number.

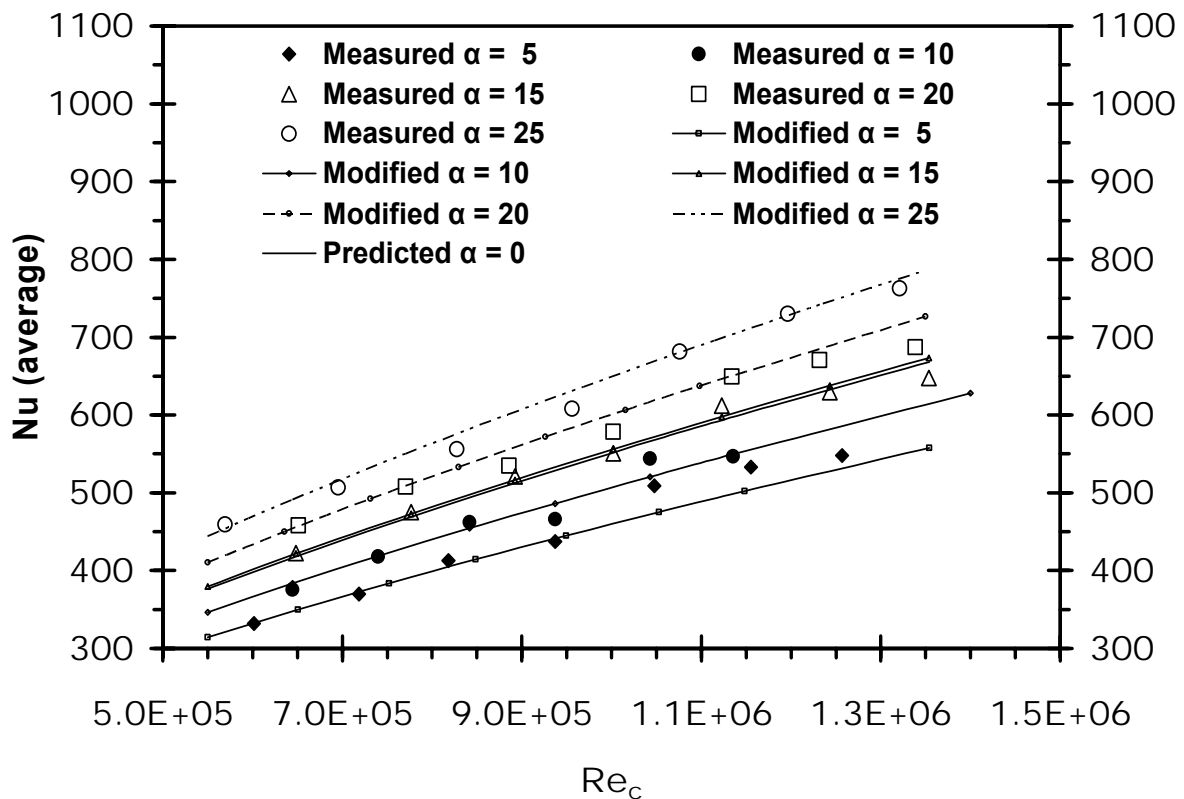
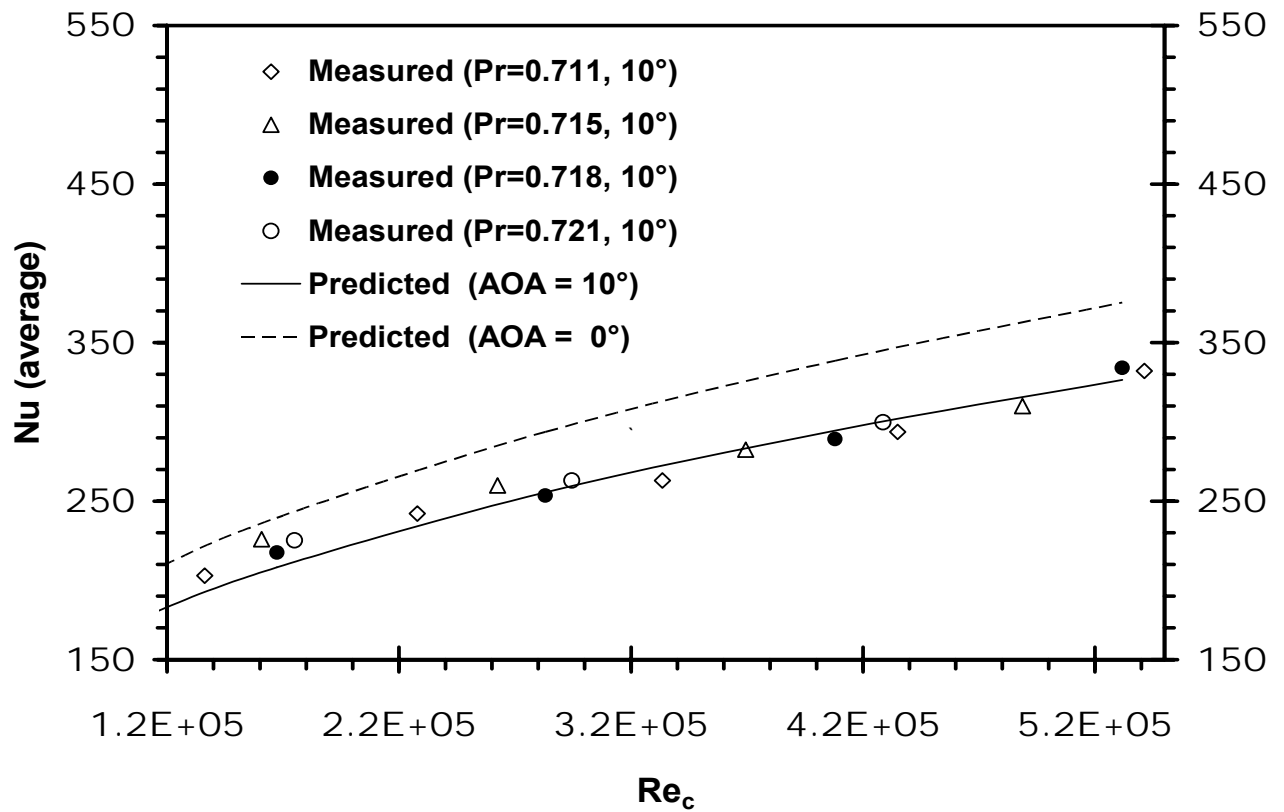
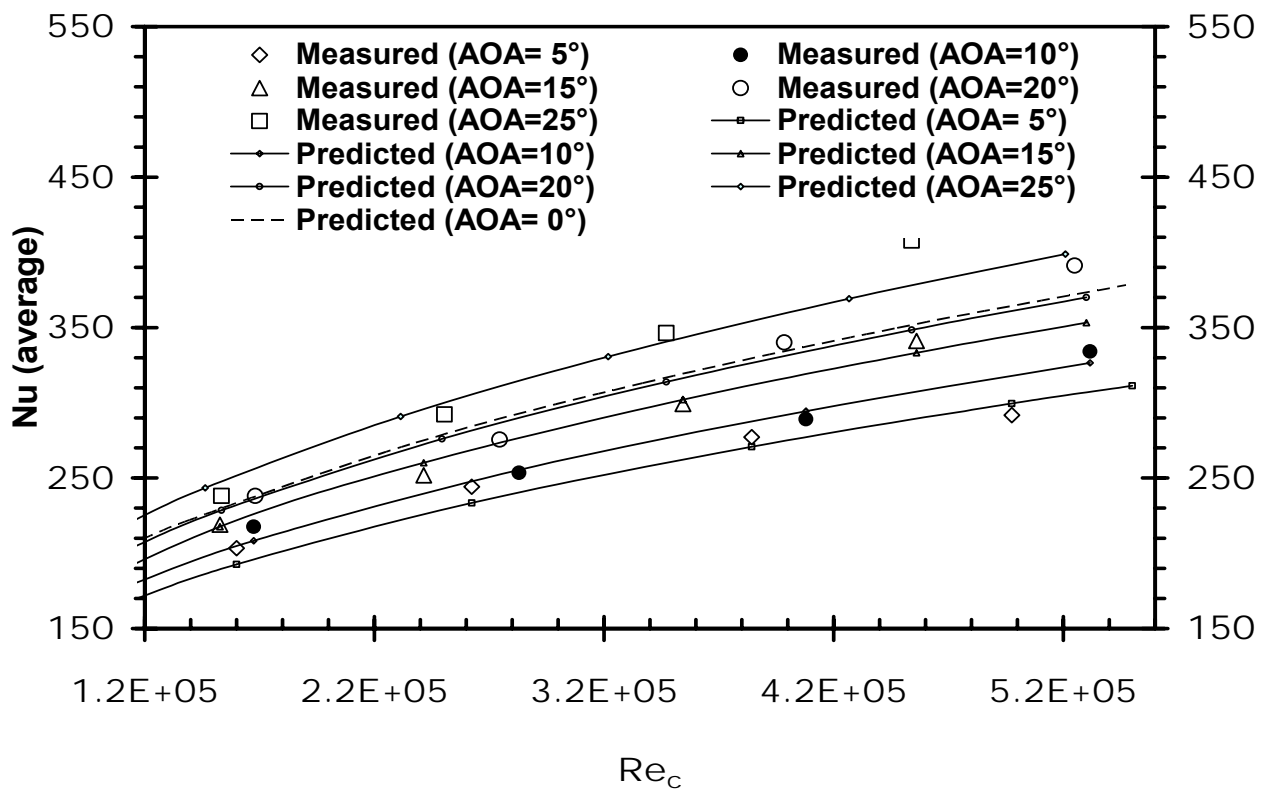


Figure 6.9: Measured data and average Nusselt number correlation with Re_c at various AOA (high Re_c)

Figure 6.10: Measured data and Nu correlation at 10° AOA (low Re_c)Figure 6.11: Measured data and Nu correlation at varying AOA from 5° to 25° (low Re_c)

The movement of the point of separation depends on the adverse pressure gradient, which depend on angle of attack and Reynolds number [180]. When the Reynolds number increases, the separation point moves toward the leading edge. Higher turbulence over the airfoil will enhance the heat transfer at a higher Reynolds number. Okong'o and Knight [181] predicted 2-D laminar flow over a pitched airfoil, by using a second-order discretization with Roe's method. The results showed that a larger Reynolds number leads to a primary recirculation region that forms closer to the leading edge. When the AOA was varied from 14.5° to 22.5°, the air flow over a NACA 0012 airfoil developed a flow reversal at 14.5°. The primary recirculation region formed at 16.5°. The primary recirculation region with critical points formed at 19.5°, while the secondary recirculation region with critical points and primary recirculation occurred at 21°. A tertiary recirculation region, with secondary recirculation and critical points, occurred at 22.5°. This implies that a recirculation region developed and moved towards the leading edge, when the angle of attack increased. The results also showed that a higher Reynolds number will lead to a circulation region at a smaller angle of attack, while the centre of recirculation moves forward to the leading edge. The flow and movement of the point of separation over the NACA 0012 airfoil is different than for the NACA 63421. These results are helpful to understand the current heat transfer trends along the airfoil at different AOA and Reynolds numbers.

The following form of correlation has been used for an iced blade by van Foseen [117]:

$$\overline{Nu} = A Re_c^B \quad (6-8)$$

where A and B are coefficients that depend on flow conditions. This functional form is similar to Nu correlations obtained previously by Wang et al. [182] for convective heat transfer from an airfoil at 0 degrees AOA and associated formula corrections. The relationships between Reynolds and Nusselt number coefficients (c and m) were determined based on a least squares

curve fit of measured data by Wang et al. [182]. The correlations in Equations 6-2 and 6-3 were obtained for convective heat transfer from an airfoil. For different AOAs, a similar functional form is used, but modified for varying angles of attack. A modified heat transfer correlation is developed according to the following functions,

$$\overline{Nu} = 0.0943(C_1 + D_1\alpha)\text{Re}_c^{0.636}\text{Pr}^{1/3} \quad (6-9)$$

$$\overline{Nu} = 2.483(C_1 + D_2\alpha)\text{Re}_c^{0.389}\text{Pr}^{1/3} \quad (6-10)$$

where, α , C_1 , D_1 and D_2 refer respectively to the angle of attack (AOA) and coefficients used as correction factors for the correlations developed for the limiting case of zero angle of attack. The normalized chord of the airfoil (c) and dynamic centre (c_m) are used to define the first coefficient, $C_1 = 1 - c_m/c = 1 - 0.25/1 = 0.75$. The remaining coefficients are found from a unit angle and exchange factor from 1° to the maximum arc length: $D_1 = \pi/180 = 0.017$ and $D_2 = C_1 \times D_1 = 0.013$.

These coefficients aim to provide a functional expression that accounts for movement of the point of separation along the airfoil surface, due to the varying angle of attack. By including the AOA correction factor based on this movement, the expected Nu trends for varying angles of attack can be established for the heat transfer correlation.

The coefficient D_2 must be modified differently than D_1 and C_1 , for cases of lower turbulence when movement of the transition point changes at low Reynolds numbers. Using these resulting factors in Equations 6-9 and 6-10, the following correlations are obtained for the Nusselt number in low and high Reynolds number cases, respectively,

$$\overline{Nu} = 0.0943(0.75 + 0.017\alpha)Re_c^{0.636} Pr^{1/3} \quad (\text{for } Re_c > 5 \times 10^5) \quad (6-11)$$

$$\overline{Nu} = 2.483(0.75 + 0.013)\alpha Re_c^{0.389} Pr^{1/3} \quad (\text{for } Re_c \leq 5 \times 10^5) \quad (6-12)$$

Figure 6.12 shows better agreement between measured data and predictions at $AOA = 10^\circ$, when the above corrections factors are applied to the Nu correlation. Measured data at varying temperatures (different Prandtl numbers) is illustrated in Figure 6.12. Without the above correction factors, the zero AOA correlation would over-predict the measured data across the range of Reynolds numbers. For the results in Figure 6.12, the curve regression coefficient is $R^2 = 0.955$.

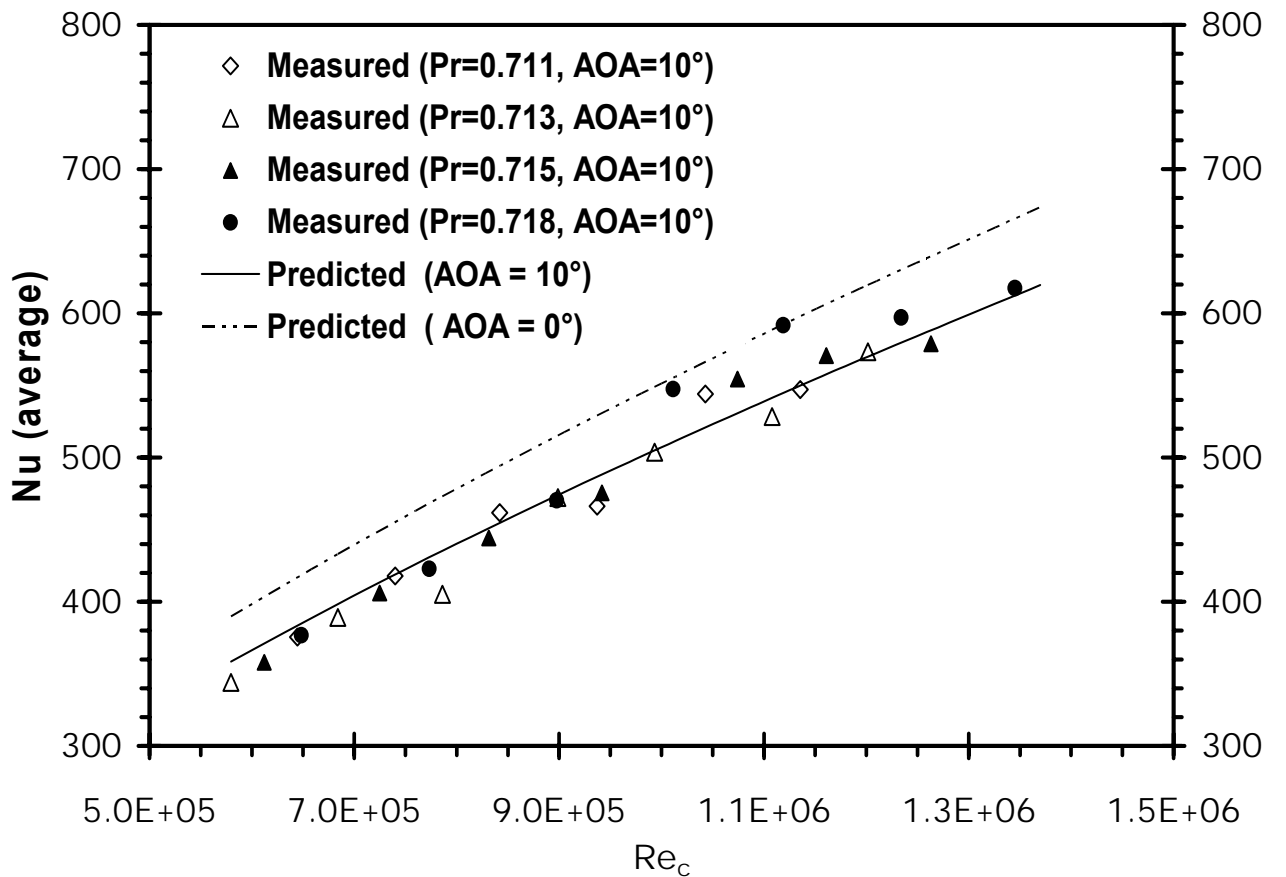


Figure 6.12: Comparison of measured data at 10° and Nu correlations at 0° & 10° AOA

6.3 Heat transfer characterization with water droplets at 0 AOA

In the previous section, experimental results were presented for convection heat transfer from a NACA 63421 airfoil at varying Reynolds numbers, by changing the icing tunnel air flow velocity, air viscosity and thermal diffusivity. In this section, the liquid water content is also varied. Within the refrigerated wind tunnel in Figure 3.1 and Figure 3.2, air temperatures are varied between 20°C and -30°C. In addition, liquid droplets are also added to the air. The quantity of liquid water flow rate varies from 0 to 20 L/h, while the liquid water content ranges from 0 - 2 g/m³. Data was collected at an air temperature of 10°C with the same temperature for the air and the water droplets. Data was analyzed over a range of liquid water contents that yielded uniform normalizations of the Nusselt numbers; this procedure indicated consistency of the data and provided a useful verification that the experimental data were collected accurately.

According to the analysis of Section 6.1, experimental data can be correlated by Equations 6.2 and 6.3, in terms of the Nusselt number, which is expressed equivalently to the Hilpert correlation for an airfoil in cross flow without water droplets, separately for low and high Reynolds numbers. In this investigation, the liquid water content is expected to substantially affect the heat transfer coefficient. The average Nusselt number rises by 26.7% and 27.4%, respectively, for $Re_c \leq 5 \times 10^5$ and $Re_c > 5 \times 10^5$, relative to the average Nu without water droplets. In Figure 6.13, it can be noticed that the experimental data has higher values than the correlation of Nusselt number with Reynolds number, from low to high in Figure 6.13 a) and b). The correlations of Nu and Re in Figure 6.13 are Eqs. 6-2 and 6-3 for convection heat transfer from an airfoil. Their modified correlation will be discussed in the following section.

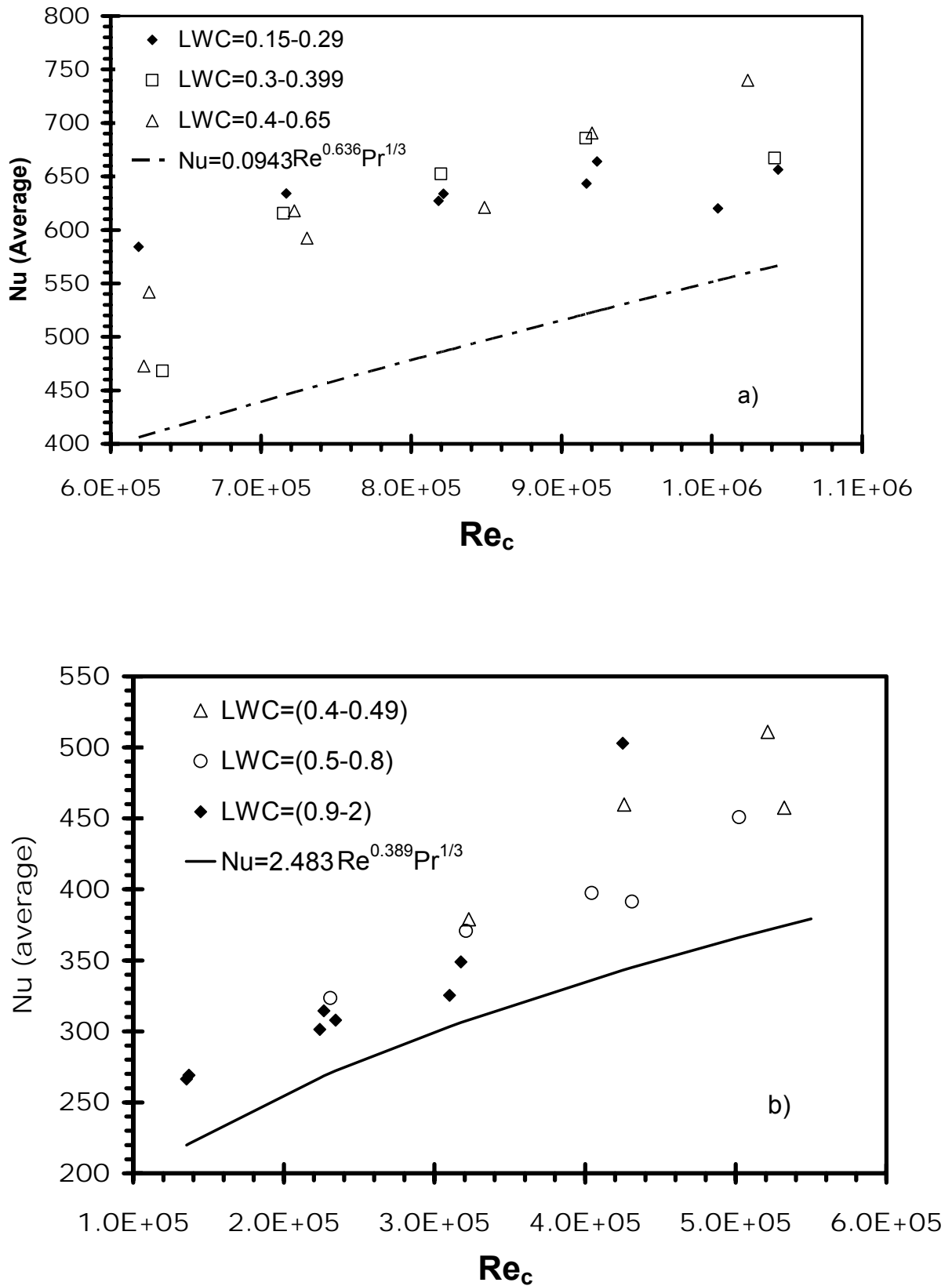


Figure 6.13: Comparison of experimental data with LWC (g/m^3) and Nusselt function correlations without LWC: a) high Re and b) low Re

The relationship between Reynolds and Nusselt number coefficients (c and m) are determined based on a least squares curve fit of measured data. The definition in Equations 6-2 and 6-3 obtained for airfoil heat transfer will be corrected for heat transfer arising from droplet impact on the airfoil.

Extensions to cases with impinging droplets were made based on correlations in Eqs. 6-2 and 6-3. It was determined that a new multiphase Reynolds parameter, $Re_m = Re_c (1+W)$, leads to a promising method of normalizing the experimental data, where W represents a non-dimensional liquid water content. In other words, the Nusselt number correlation was established as follows:

$$\overline{Nu} = c(Re_c (1+W))^m Pr^{1/3} \quad (6-13)$$

$$W = \frac{LWC}{LWC_0} \quad (6-14)$$

where LWC_0 refers to a reference value of the liquid water content.

Figure 6.14 shows the local Nusselt numbers, Nu_x , at different positions and corrected Reynolds numbers. The stagnation point is $x/c = 0$. The Nusselt number decreases significantly after the stagnation point, due to the rapidly thickening boundary layer along the upper and lower minmium surfaces. It falls to a minmium at a position of $0.2c$ along the chord of the airfoil, after which it increases. Although both surfaces of the airfoil have the same trends near the leading edge of the airfoil, the lowest value of Nu_x occurs along the lower surface. It would have the same local Nusselt number, if the airfoil was symmetric in shape and orientation, with respect to the freestream. The local Nusselt number for the NACA 63421 airfoil has different trends below and above the stagnation point, due to the non-symmetrical profile of the airfoil. On the airfoil, the thickness of laminar boundary layer increases as x increases from the leading edge to the trailing edge. Afterwards, boundary layer

transition occurs and the boundary layer becomes turbulent. These trends can be clearly seen in Figure 6.14.

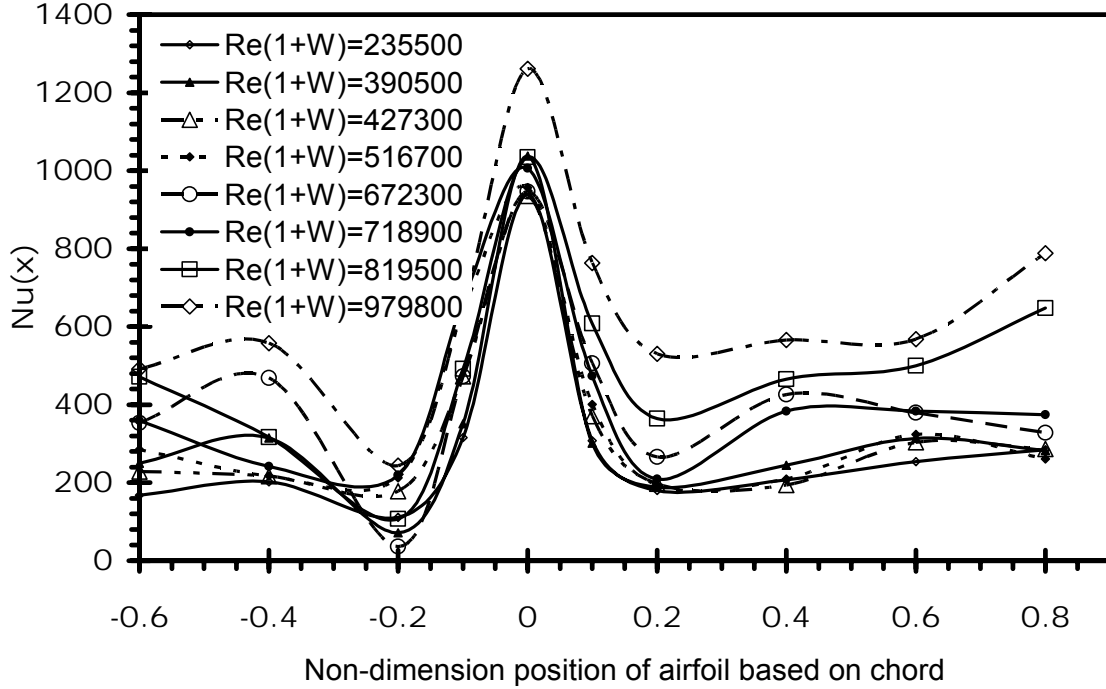


Figure 6.14: Local Nusselt number at varying chord positions (x/c)

By selecting the reference value equal to one-fourth of the maximum water content in air at the average temperature, it was observed that the same Nusselt number correlation could be used for both single-phase (without droplets) and two-phase flows (with droplets), provided the Reynolds number is replaced with the multiphase Reynolds parameter. At the average temperature of -0.16°C for the low speed set of experiments, the maximum water content in air is 4.98 g/m^3 , so the reference water content was taken as 1.25 g/m^3 . The average temperature is -4.55°C for the higher speed set of experiments, so the maximum liquid water content (LWC) at this temperature is 3.69 g/m^3 and the reference liquid water content becomes 0.92 g/m^3 .

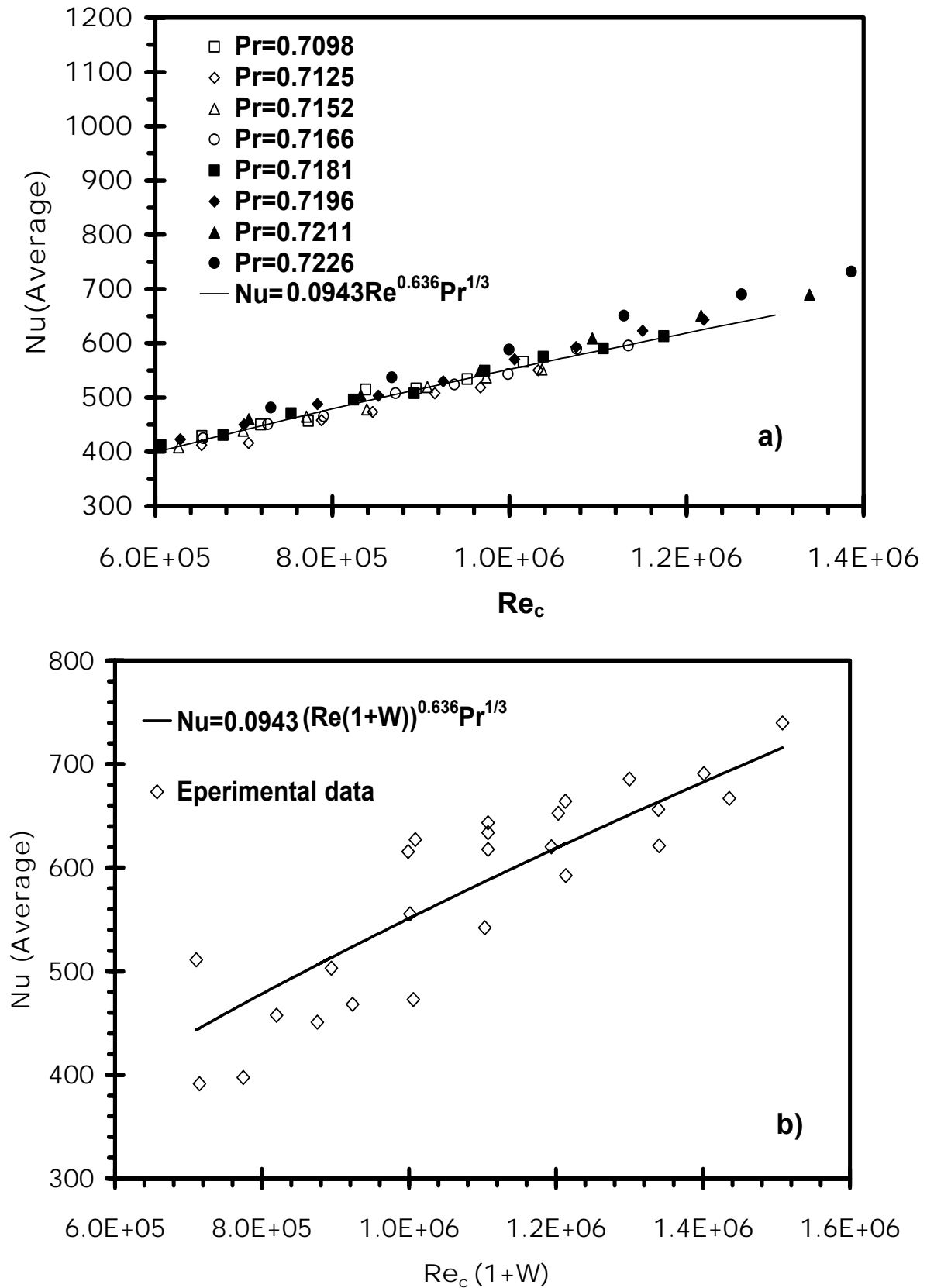


Figure 6.15: Predicted and measured Nu a) without liquid water droplets and b) with droplets for $Re_c(1+W) > 6 \times 10^5$

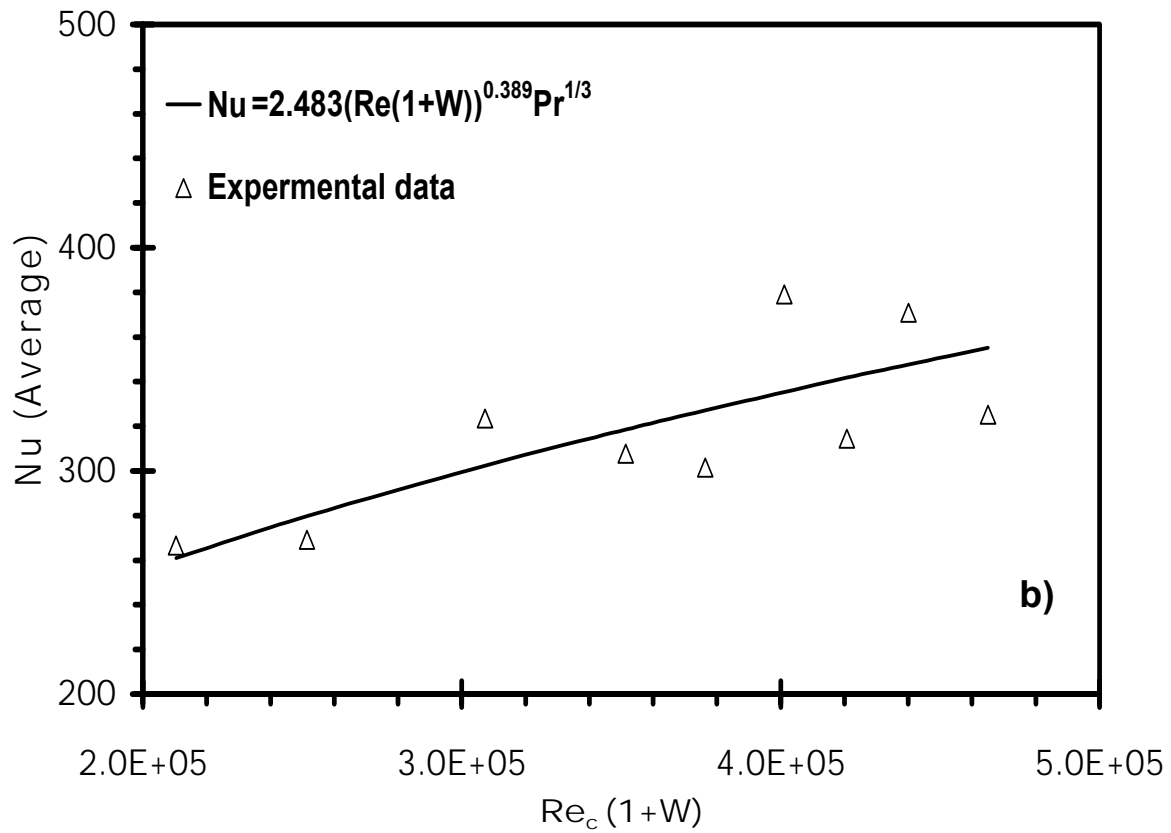
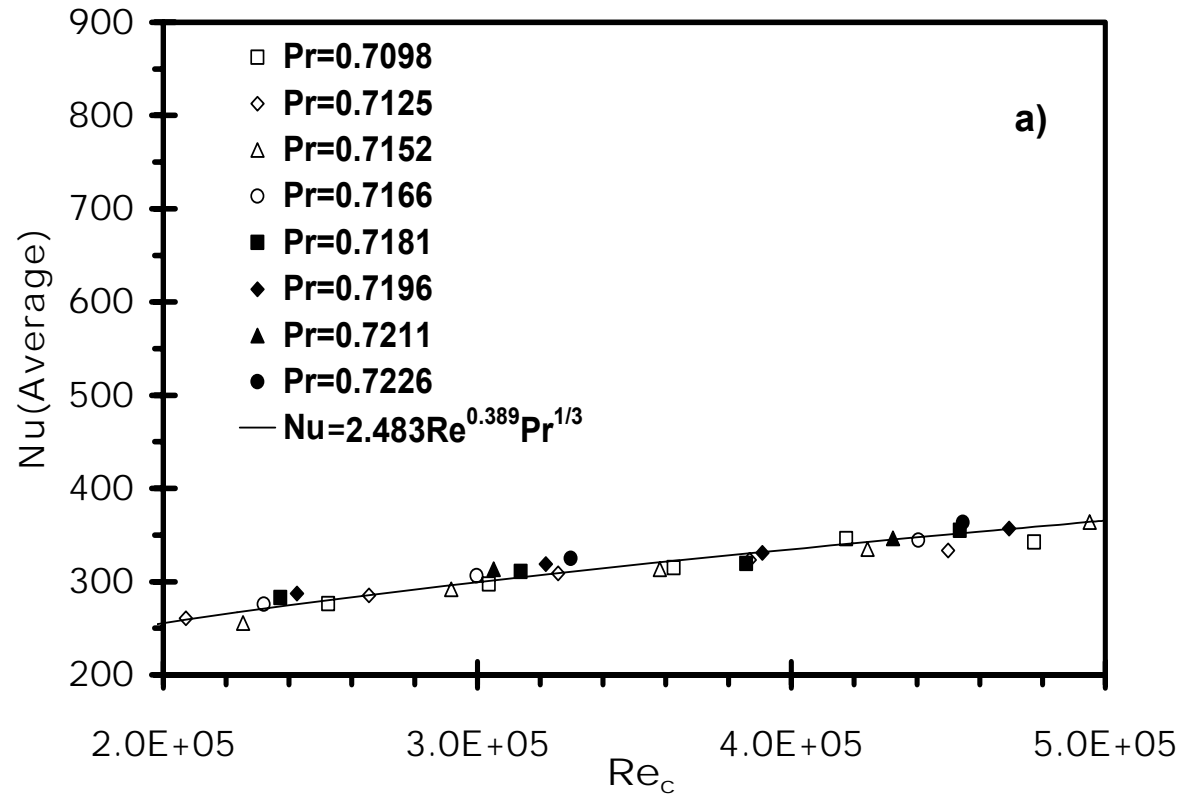


Figure 6.16: Predicted and measured Nu a) without liquid water droplets and b) with droplets for $Re_c (1+W) \leq 6 \times 10^5$

$$\overline{Nu} = 2.483(\text{Re}_c(1+W))^{0.389} \text{Pr}^{1/3} \quad (\text{for } \text{Re}_c(1+W) \leq 6 \times 10^5) \quad (6-15)$$

$$\overline{Nu} = 0.0943(\text{Re}_c(1+W))^{0.636} \text{Pr}^{1/3} \quad (\text{for } \text{Re}_c(1+W) > 6 \times 10^5) \quad (6-16)$$

The experimental data shows close agreement with this formula in Figure 6.15b and 6.16b. The data points all lie close to the correlated curve and measured data for each LWC value. The standard deviation between experimental data and the correlation coefficient for the best curve fit was 8.25 and 11.9 for the Nusselt number at low and high Reynolds numbers, respectively. Also, R^2 was 0.8517 and 0.8149, separately. This close agreement provides useful verification that measurements exhibit consistent behavior under appropriate normalization at varying Reynolds numbers. Without the multiphase Reynolds parameter, a consistent trend could not be observed with the data. But the definition of $\text{Re}_c(1+W)$ allows effective normalization of measured data and it incorporates effects of both the Reynolds number and LWC, thereby reducing the number of independent variables in plotted figures.

In Figure 6.15, the measured Nusselt number is shown without droplets (Figure 6.15a) and with droplets (Figure 6.15b) at $\text{Re}_c(1+W) > 6 \times 10^5$. When using the single-phase Reynolds parameter in Figure 6.15a and multiphase parameter in Figure 6.15b, it can be observed that very similar trends are obtained. Such close similarity would not be achieved without the multiphase Reynolds parameter proposed. Values at different Prandtl numbers in Figure 6.15a are obtained through varying temperatures within the wind tunnel, which alter the dynamic viscosity and thermal diffusivity of the air stream. Analogous trends and close proximity between correlated data with and without droplets can be observed in Figure 6.16b at lower Reynolds numbers ($\text{Re}_c(1+W) \leq 6 \times 10^5$). The multiphase Reynolds parameter is shown to give promising normalization against single-phase correlations over a wide range of Reynolds numbers.

Several key differences should be noted between Figure 6.13, Figure 6.15 and Figure 6.16. In Figure 6.13, measured data is shown at different values of the liquid water content (two-phase flow with droplets), while Figure 6.15a and Figure 6.16a show Nusselt numbers at varying temperatures and Prandtl numbers (without droplets). The measured data in Figure 6.15a and Figure 6.16a was used to develop the empirical correlations Eqs. 6-2 and 6-3 in Figure 6.13. Also, Figure 6.15b and Figure 6.16b plot the Nusselt numbers against the multiphase Reynolds parameter, while Figure 6.13 plots the Nusselt number against the conventional, single-phase Reynolds number (without droplets) obtained in Section 6.1. The results in Figure 6.15b and Figure 6.16b are nearly independent of the Prandtl number, since the temperature range and variations of the Prandtl number are small. The data is the same as results in Figure 6.13a and b, except that it is normalized by LWC_0 and plotted against the multiphase Reynolds parameter, rather than the conventional single-phase Reynolds number. The number of measured data points in Figure 6.13, Figure 6.15 and Figure 6.16 is different since the Reynolds number on the horizontal axis is different, thereby affecting the number of data points within a given range.

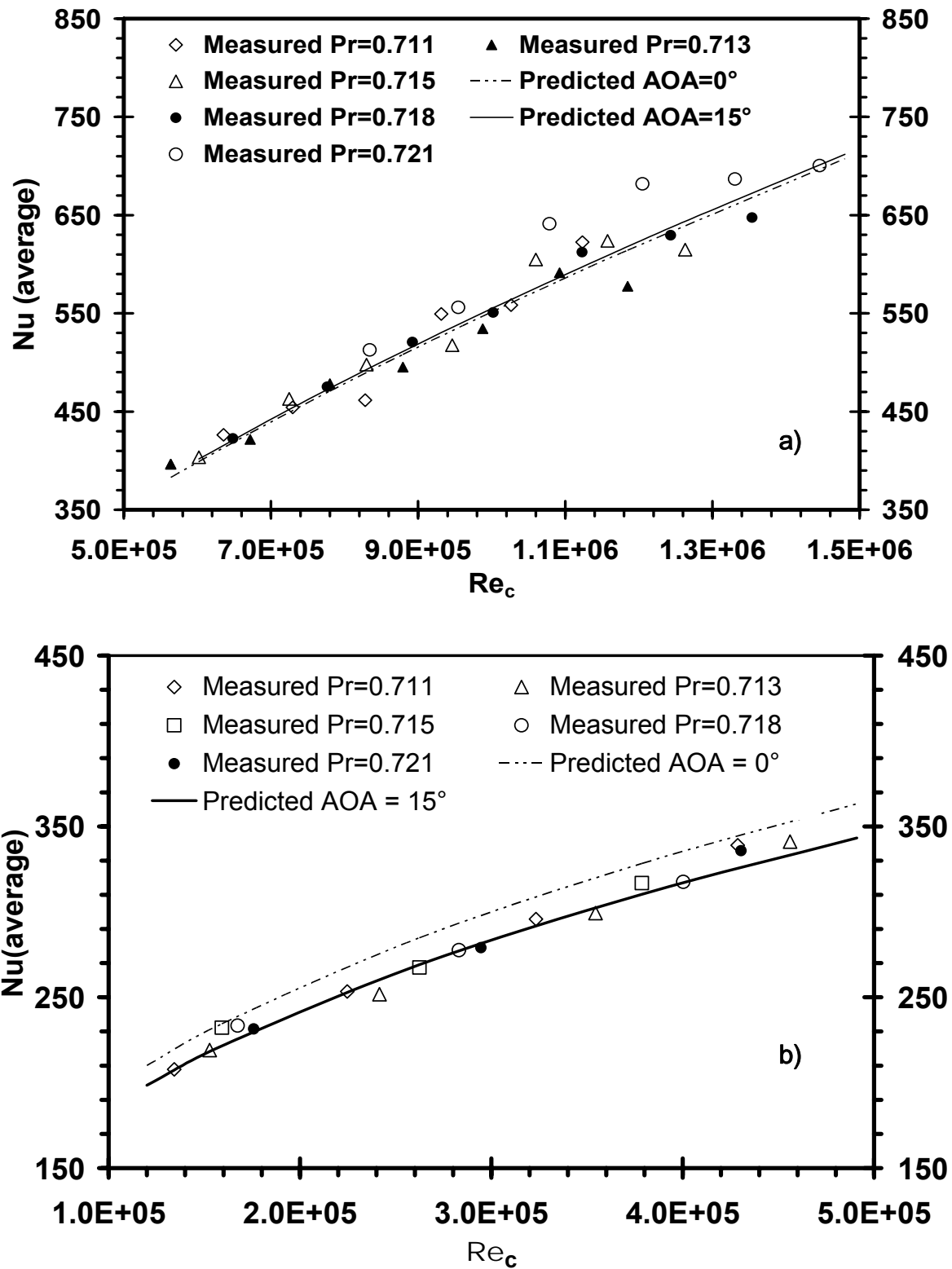
6.4 Modified hilpert correlation with LWC at varying AOA

In this section, experimental results will be presented for convective heat transfer from a NACA 63421 airfoil at varying AOA between 0° and 25° . The Reynolds number is varied by changing the air velocity in the icing tunnel and air viscosity (by changing the air temperature). The liquid water content is also varied through different spray flow conditions. Within the refrigerated wind tunnel, air temperatures are varied between -30°C and 20°C . The liquid water content varies from 0 to 45 liters per hour. Data is collected over a range of temperatures and liquid water contents that yielded uniform normalization of the Nusselt

numbers. For example, normalized data collapsed onto a single curve fit at different temperatures which indicated consistency and provided useful verification that experimental data was collected accurately.

Particular effort was taken to ensure uniformity of the droplet distribution. Atomizing nozzles were adjusted iteratively with the air and water streams to improve the uniformity. This was a time-consuming process, since they affect each other. Also, Particle Image Velocimetry (PIV) was used to analyze the uniformity of the droplet distribution at each step. Furthermore, icing patterns were observed on the airfoil and the uniformity of ice buildup provided another way to improve uniformity of the droplet distribution. These efforts and others were taken to provide as uniform a droplet distribution as possible.

From the manufacturer's specifications of the spray nozzles, the average droplet size is 100 microns. The air atomizing nozzles can produce a reliable spray pattern with water mean droplet diameters ranging between 10 and 1,000 microns. At the nozzle exit, droplet ejection is air-assisted since the air stream drives the emission from the nozzle, rather than ejection at a particular velocity, so the droplet velocity is close to the air stream velocity. Droplet sizes are controlled by variation of the air pressure. Figure 6.17 compares the measured data and correlations for both high and low Reynolds numbers at a 15° angle of attack. The results illustrate that the average Nusselt number increases at a higher Reynolds number. Measured data at varying temperatures (different Prandtl numbers) is illustrated in the figure. For the low Reynolds number, without the AOA correction factors developed in the previous section, the zero AOA correlation would over-predict the measured data across the range of Reynolds numbers. The AOA correction to the Hilpert correlation was determined empirically from the curve fit of measured data.

Figure 6.17: Measured data and predicted Nu correlation at a) high Re_c and b) low Re_c at 15°

AOA without LWC

Results of measured data at various values of the LWC are plotted in Figure 6.18, together with a correlated curve fit of experimental data without water droplets, which was derived by conducting the experiments at the same operating AOA, but with the spray nozzles closed. In Figure 6.18, the solid curves represent empirical correlations without droplets when angle of attack $\alpha = 15^\circ$. The markers correspond to measured data with droplets at 15° AOA and the dotted line illustrates predictions of the Nusselt number with the multiphase Reynolds parameter, $Re_c(1+W)$. The curve of Eq. 6-12 in Figure 6.18 has a higher Reynolds number due to the data modification by $(1+W)$. Neither the correlation of Nusselt number and Reynolds number in Eq. 6-11, nor Eq. 6-16, can be used to predict the heat transfer correlation with liquid water droplets at varying AOA, although the multiphase Reynolds number can be used to include effects on the heat transfer coefficient. A new heat transfer coefficient is needed in this situation. The experimental data indicates that the average Nusselt number at a fixed AOA rises about 26.4% for $Re_c > 6 \times 10^5$, when water droplets are introduced into the air stream. Impinging droplets enhance the rate of heat exchange between the surface and air stream, as they enhance fluid mixing along the wall, thereby increasing the convective heat exchange and Nusselt number.

Experimental results show that the angle of attack substantially affects the heat transfer coefficient, both with and without water droplets. Figure 6.19 shows the measured local Nusselt numbers, Nu_x , at different positions with a LWC of 0.58 g/m^3 and 0.75 g/m^3 at high and low Re . The stagnation point is located at $x/c = 0$. The curve with $AOA = 0$ shows that the Nusselt number decreases after the stagnation point, due to the thickening boundary layer along the top and bottom surfaces. It falls to a minimum point at a position of $0.2c$ along the chord of the airfoil, and then increases thereafter. Although both surfaces of the airfoil have

the same trends near the leading edge of the airfoil, the lowest value of Nu_x occurs along the bottom surface.

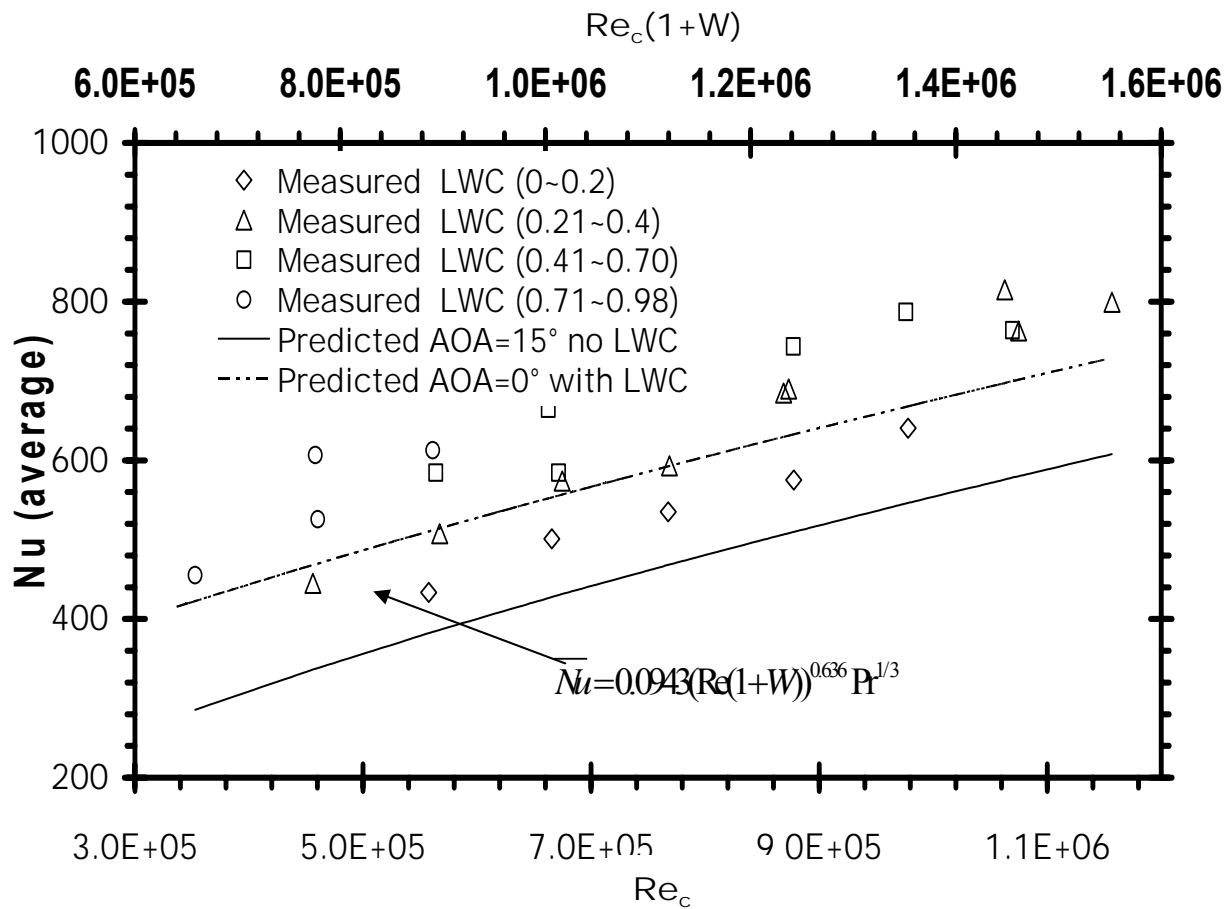


Figure 6.18: Comparison of measured data with LWC, and Nu correlations without LWC, at 15° AOA, as well as the predicted Nu correlation with LWC at 0° AOA

It would have the same local Nusselt number if the airfoil was symmetric in shape and orientation with respect to the freestream, but non-symmetry leads to the different Nusselt number results on each side of the stagnation point. The thickness of the laminar boundary layer increases when x increases from the leading edge to the trailing edge. In the laminar region, the heat transfer coefficient decreases when the thickness of the boundary layer increases. The heat transfer coefficient increases when the boundary layer becomes turbulent.

In Figure 6.19a, it can be observed how the local Nu changes with AOA at $LWC = 0.75 \text{ g/m}^3$, for cases of low Reynolds numbers. At the stagnation point, the Nusselt number changes with LWC. Without droplets in the air stream, it remains nearly uniform at different values of AOA, whereas the Nusselt number increases higher than $AOA = 0$ with a non-zero LWC, although it doesn't depend on the angle of attack. It also changes significantly with AOA along the chord of the airfoil. The Nusselt number decreases at $\pm 0.1c$, $-0.4c$, $0.6c$ and it significantly increases at $-0.2c$, $-0.6c$ and $+0.4c$ and $+0.8c$. Figure 6.19b shows the Nusselt number results for cases of high Reynolds numbers at various AOA and $LWC = 0.51 \text{ g/m}^3$. At angles of attack of 5° , the local Nusselt number at the stagnation point is lower than the case for 20° and 25° , but higher than the case for 10° and 15° .

All values of the Nusselt number at the stagnation point are higher than the case for 0° AOA. Values of the Nusselt number at $-0.1c$, $+0.1c$ and $+0.6c$ change depending on the AOA at those points. The values at $-0.2c$, $-0.6c$, $+0.2c$ and $+0.4c$ are higher than a zero AOA at the same points. As AOA increases, the changes of local Nu with AOA become more pronounced at higher Reynolds numbers. Also, no points of the local Nusselt number along the chord of the airfoil have lower values than the Nusselt number at 0° for the same points. Furthermore, Nu_x for the other points along the chord of the airfoil are larger than the values at the same points for 0° . The average Nusselt number is expected to have similar trends at high multiphase Reynolds numbers.

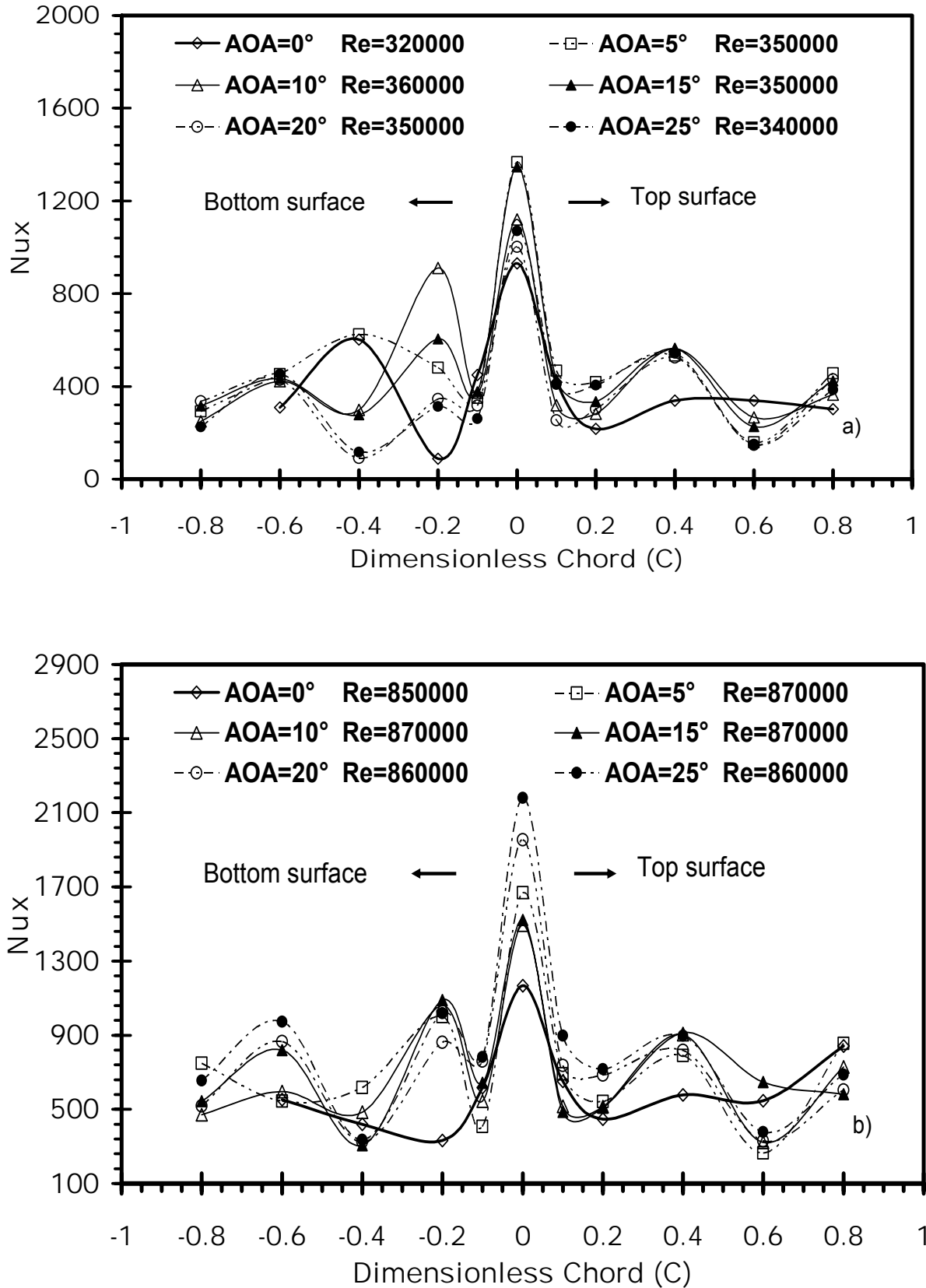


Figure 6.19: Nusselt number at a) low Reynolds numbers with $LWC = 0.75 \text{ g/m}^3$ and b) high Reynolds numbers with $LWC = 0.51 \text{ g/m}^3$ at varying AOA

The results also showed that a higher Reynolds number will lead to a circulation region at the smaller angle of attack, while the centre of recirculation moves forward to the leading edge. These mechanisms of the recirculation zone affect the convective heat exchange, so the Nusselt correlation requires a suitable dependence on AOA, which reflects the physical processes in the boundary layer. A modified Hilpert correlation is used to fit measured data obtained from the experiments according to Eqs. 6-11 and 6-12 to 6-15 and 6-16 as follows:

$$\overline{Nu} = 2.483(C_1 + D_3\alpha)(Re_c(1+W))^{0.389} Pr^{1/3}, \text{ and} \quad (6-17)$$

$$\overline{Nu} = 0.0943(C_2 + D_4\alpha)(Re_c(1+W))^{0.636} Pr^{1/3}, \quad (6-18)$$

Where, α , C_1 , C_2 , D_3 and D_4 refer to the angle of attack (AOA) and coefficients used as correction factors for the correlations developed in the limiting case of zero angle of attack. The normalized chord of the airfoil, c , and dynamic centre, c_m , are used to define the first coefficient, $C_1 = 1 - c_m/c = 1 - 0.25/1 = 0.75$. The remaining coefficients are found from a unit angle and exchange factor from 1° to the maximum arc length: $\pi/180 = 0.017$ and $D_3 = C_1^2 \times 0.017 = 0.01$. These coefficients provide a functional expression that accounts for movement of the point of separation along the airfoil surface, due to the varying angle of attack.

The coefficient D_4 must be modified differently by D_3 and C_1 , for cases of higher turbulence to decrease the effect of the angle of attack under conditions of impinging droplets. Movement of the transition point changes at high Reynolds numbers, so $D_4 = C_1 \times D_3 = 0.007$. The other chord coefficient is: $C_2 = c/c = 1$. Higher turbulence increases the heat transfer coefficient in droplet flow conditions, regardless of the angle of attack. Using the resulting factors in Eqs. 6-17 and 6-18, the following correlations are obtained for the Nusselt number in low and high Reynolds number cases, respectively,

$$\overline{Nu} = 2.483(0.75 + 0.01\alpha)(Re_c(1+W))^{0.389} Pr^{1/3} \quad \text{for } Re_c(1+W) \leq 6 \times 10^5, \quad (6-19)$$

$$\overline{Nu} = 0.0943(1 + 0.007\alpha)(Re_c(1+W))^{0.636} Pr^{1/3} \quad \text{for } Re_c(1+W) > 6 \times 10^5. \quad (6-20)$$

Figure 6.20 compares the measured data and predictions at AOA=15°, when the above corrections factors are applied to the Nusselt number correlation. Measured data at varying temperatures (different Prandtl numbers) is illustrated in Figure 6.20 by using the multiphase Reynolds parameter. Without the previous correction factors, the zero AOA correlation would over-predict the measured data across the range of Reynolds numbers. For the results in Figure 6.20, the curve regression coefficient is $R^2 = 0.961$. Without the multiphase Reynolds parameter, a consistent trend could not be observed with the data. But the definition of the multiphase Reynolds number $Re_c(1+W)$ and modification for the angles of attack allow an effective normalization of measured data. The correlation incorporates effects of both Reynolds number and LWC, thereby reducing the number of independent variables in plotted figures.

Figure 6.21 shows additional results for other angles of attack: 5°, 10°, 15°, 20° and 25° at the higher Reynolds number. In each case, the correction factors for Nu number correlations have yielded good agreement between the predicted and measured data. The Nusselt number increases at higher angles of attack, since the separation point moves upstream, induces turbulence and enhances heat exchange between the surface and fluid. At lower Reynolds numbers, close agreement is also achieved, both at 15° in Figure 6.22 and higher angles of attack in Figure 6.23. As observed previously for higher Reynolds numbers, the Nusselt number increases at higher angles of attack. The results indicate that a standard Hilpert form of convection correlation can be used to predict heat transfer from a NACA 63421 airfoil at

varying angles of attack. A correction factor in a standard Hilpert correlation has yielded relatively close agreement with measured data involving the Nusselt number.

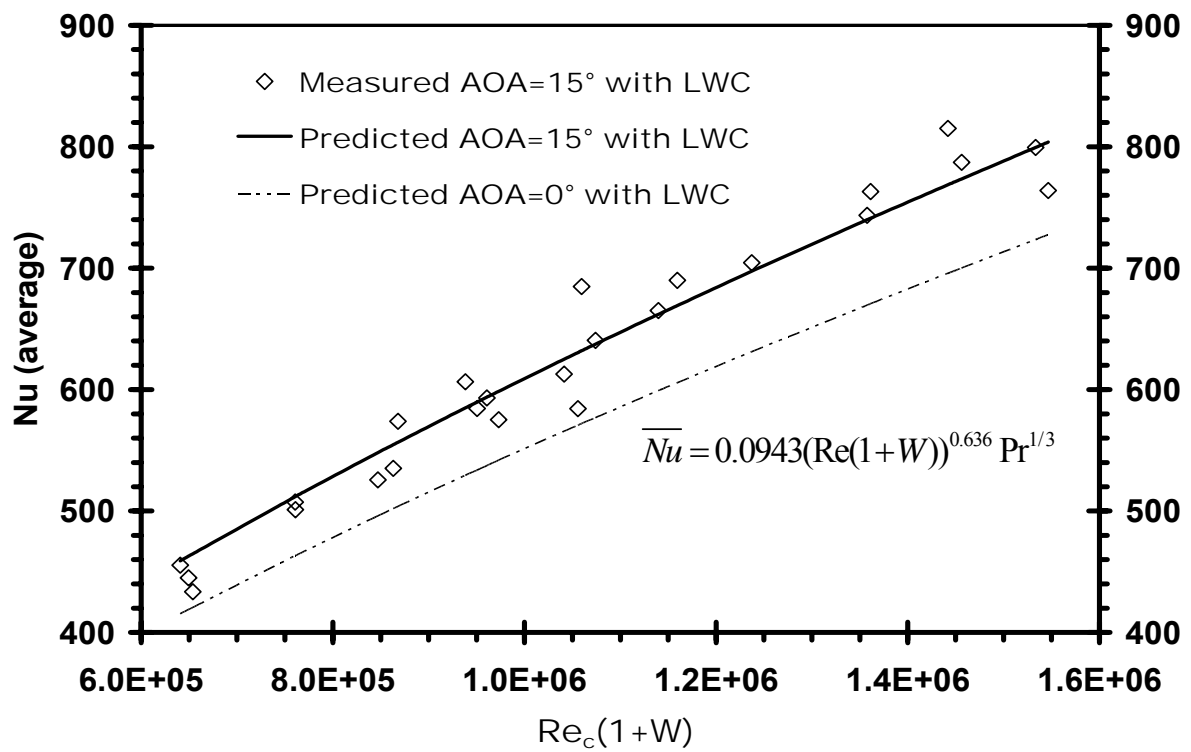


Figure 6.20: Predicted and measured Nu with droplets for $Re_c(1+W) > 6 \times 10^5$ at 15° AOA

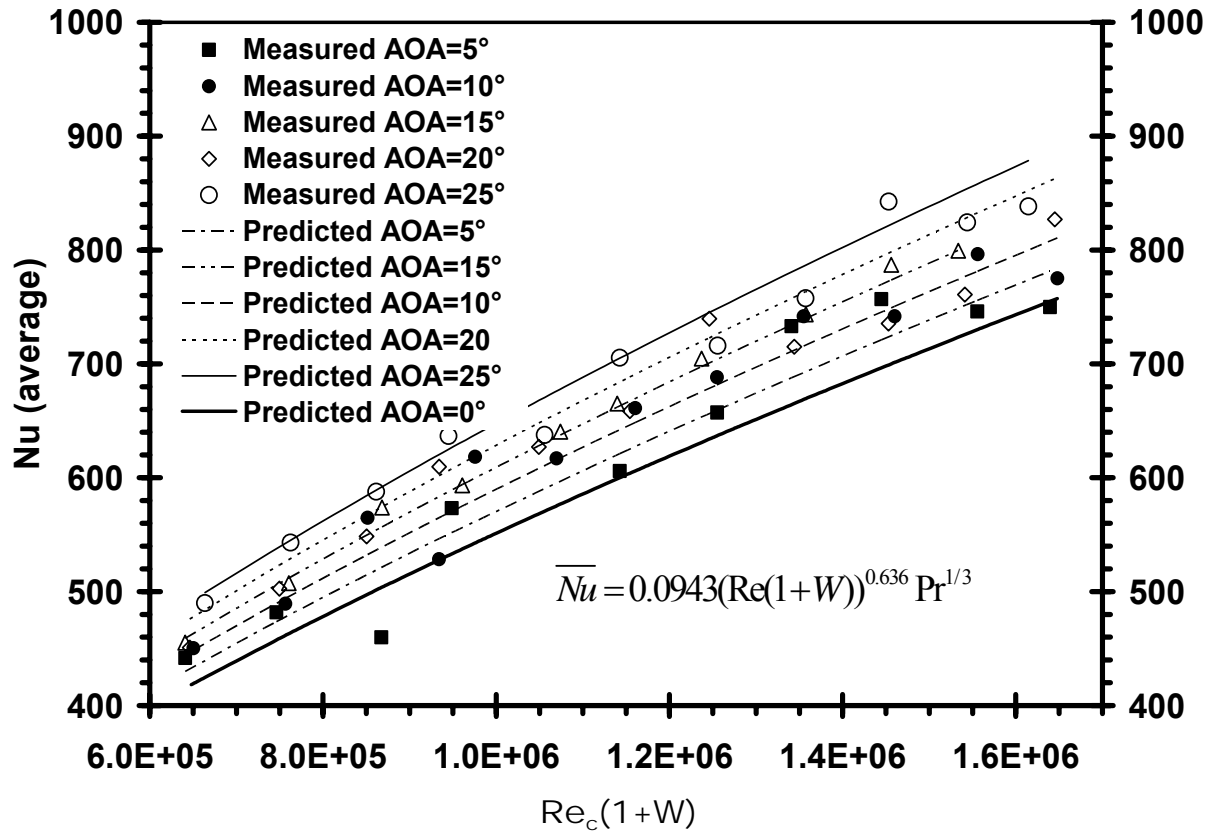


Figure 6.21: Measured data and predicted Nu with droplets at varying angles of attack for high $Re_c(1+W)$

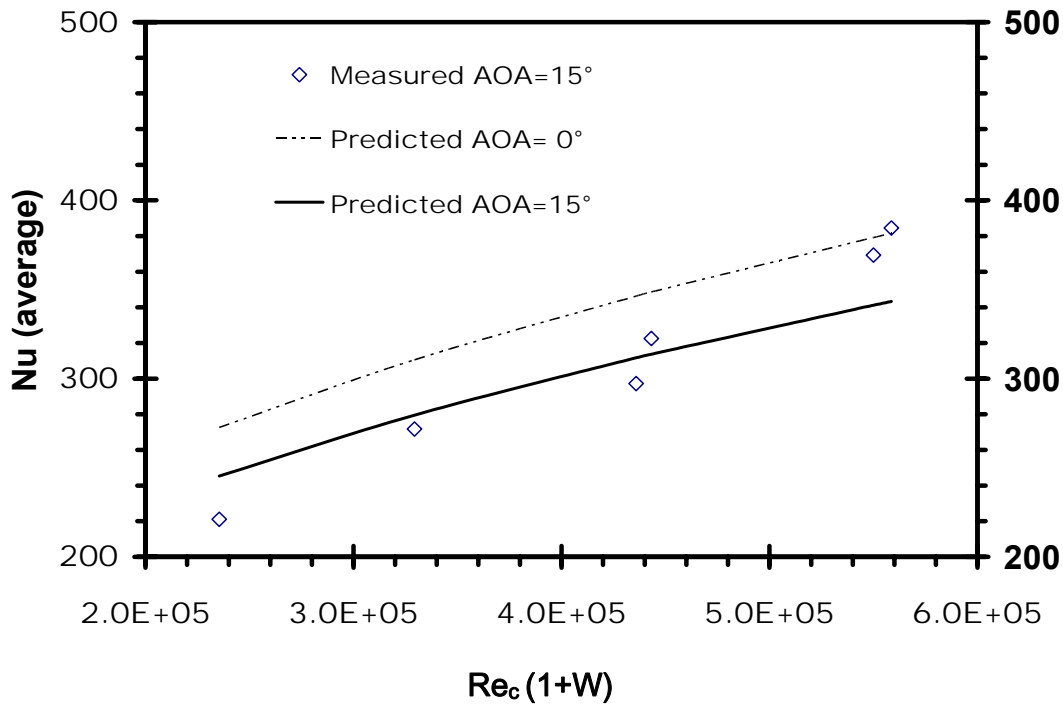


Figure 6.22: Predicted and measured Nu with droplets for $Re_c(1+W) \leq 6 \times 10^5$ at 15° AOA

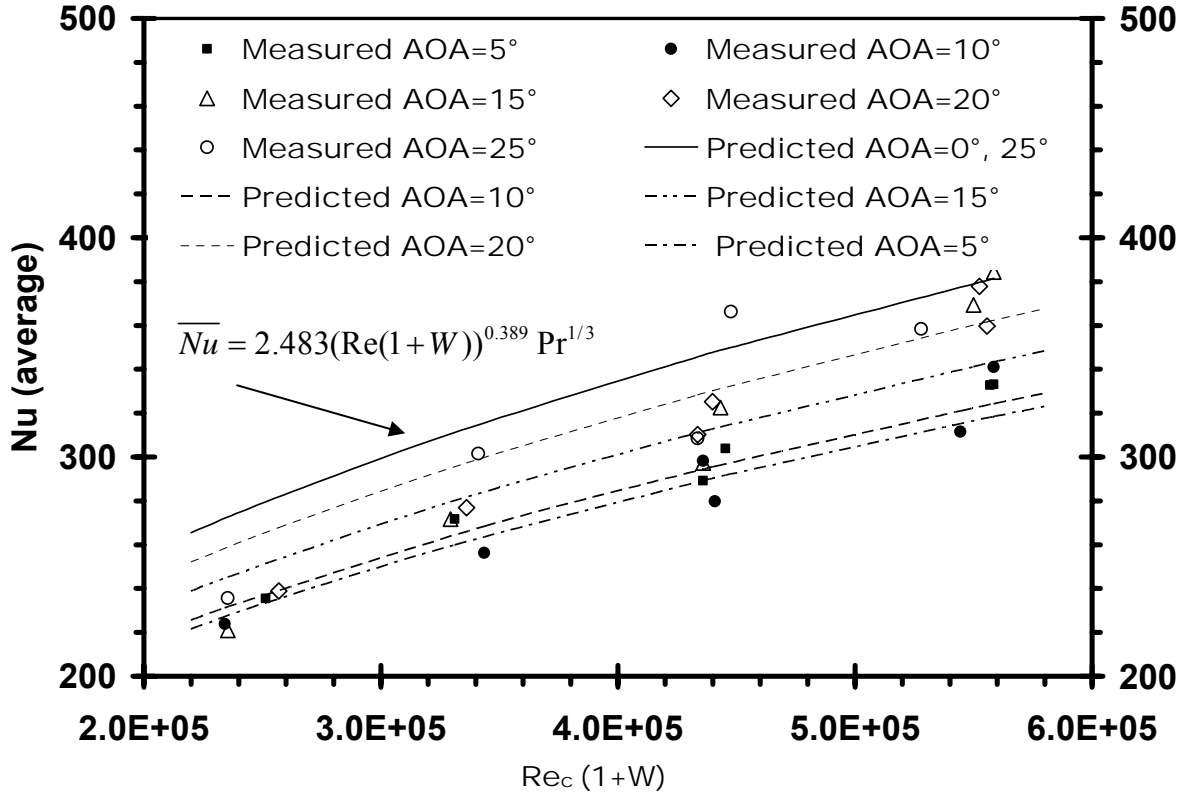


Figure 6.23: Predicted and measured Nu with droplets for $Re_c(1+W) \leq 6 \times 10^5$ at varying AOA

6.5 Summary

The results of an experimental investigation of the heat transfer coefficients for forced convection from a NACA 63421 airfoil were presented in Section 6.1. Wind tunnel measurements of convection coefficients were obtained for air flow temperatures from -30°C to 20°C . The experimental data is correlated with the Nusselt and Reynolds numbers. Conduction within the airfoil balances heat transfer by convection from the airfoil surface in steady-state conditions. Both average and spatial variations of the heat transfer coefficients are non-dimensionalized through modifications of a classical Hilpert correlation for cylinders in cross flow. It was shown that the functional form of the Hilpert correlation can effectively accommodate measured data for the NACA 63421 airfoil over a range of Reynolds numbers. In Section 6.2, experimental correlations of heat transfer at different blade angles of attack

(NACA 63421 airfoil) were developed. Various angles of attack (AOA) between 0 to 25 degrees were investigated at different Reynolds numbers. The correlations provide important characterization of convective heat transfer from the airfoil surface to the cold surrounding air. Experimental studies of heat transfer with water droplets impinging on a NACA 63421 airfoil were studied to simulate anti-icing conditions in Section 6.3. Various liquid water contents (LWC) were investigated. The measurements can provide important characterization of heat convection between the airfoil surface and cold surrounding air, just before ice accumulation. These experimental measurements can be used to develop better methods to reduce the impact of icing of wind turbines in cold weather climates.

A new non-dimensional correlation of convective heat transfer with impinging droplets on a NACA airfoil at varying angles of attack was presented in Section 6.4. The experimental study was performed to develop correlations of heat transfer from a NACA 63421 airfoil at different angles of attack (AOA) between 0 to 25 degrees and different Reynolds numbers with impinging droplets. A modified Hilpert correlation of convective droplet heat transfer from the NACA airfoil at varying AOA was determined with respect to the Reynolds number, Prandtl number, liquid water content and AOA. The modified Hilpert correlation includes the effects of droplet-air interactions on the effective heat transfer coefficient at varying AOA. Increasing the AOA leads to flow separation and reattachment on the airfoil surface, which affect the structure of the thermal boundary layer and energy exchange through kinetic energy of impinging droplets and the thin flowing film along the surface of the airfoil. The results show that both average and local Nusselt numbers vary with AOA. The results indicate that variation of air velocity, liquid water content and AOA can be normalized into a modified Hilpert correlation, by using empirical coefficients that involve the chord dimensions, AOA and non-dimensional liquid water content.

Chapter 7

Conclusions and recommendations for future research

7.1 Conclusions

Iced wind turbine blades and convective heat transfer from a NACA airfoil were investigated in this thesis. In this chapter, conclusions will be presented for the following aspects of wind energy: wind power losses under icing conditions, aerodynamic losses under icing conditions and convective heat transfer at varying AOA, with or without LWC.

The experimental results presented in Chapter 4 show that icing of a wind turbine blade will significantly affect power output. Normally, glaze ice will reduce power output progressively as the ice thickness increases. Extreme cold temperatures will form a larger thickness of rime ice on the blades, for the same icing duration, compared to glaze ice conditions. Rime ice that forms on the wind turbine blades will change the profile of the wind turbine blades and these iced blades may increase their rotation rate under extreme ice conditions. For experimental icing conditions, the power output increased to 214% with 8.5 mm of rime ice thickness and the rotation rate of the wind turbine increased to 125% at -30°C. This is dangerous for the wind turbine because the high rotation speed and increased power output may cause the mechanical and electrical parts to overheat and fail. Power losses and high rotation are two consequences of iced wind turbine blades in extreme climates.

The iced airfoil aerodynamics affects the power output, due to the changing blade profile. From the ice shapes on an airfoil, glaze ice conditions will form smoother ice over the airfoil than rime ice conditions. Also, the ice thickness for the same spraying duration is different, due to the difference of air temperatures. When the temperature is lower, the ice thickness will be large. The lift coefficient and drag coefficient are also changing, as glaze ice conditions and rime ice conditions change. The aerodynamics of an iced airfoil was slightly affected by the higher Reynolds number. When the Reynolds number is lower, the lift coefficient of an iced airfoil will decrease, more than the higher Reynolds number, at the same ice thickness. Also, the rime ice and glaze ice have different effects on drag and lift coefficients, when varying the Reynolds number, spraying time and AOA.

Heat transfer results were presented in Chapter 6, including modified Hilpert correlations to predict heat transfer by forced convection from a NACA airfoil, with and without LWC, at 0 and varying AOA. Initially, a modified Hilpert correlation was used for heat transfer by forced convection from a NACA airfoil at zero AOA, without liquid water content. Under steady-state conditions, heat conduction through the airfoil was balanced against heat transfer by convection to the air stream. Experimental data was shown to collapse consistently onto a single normalized correlation of $Nu/Pr^{1/3}$ at varying Prandtl numbers. Representative coefficients of the modified Hilpert correlation were obtained. It was observed that the average Nusselt number for an airfoil is smaller than a flat plate and cylinder at the same Reynolds number, as a result of the differences between turbulent boundary layer behaviors after the transition point.

A modified Hilpert correlation of forced convection heat transfer from the NACA airfoil was presented for different angles of attack. An experimental method was developed with

thermocouples embedded at different locations along the surface of the airfoil. Representative coefficients of the modified Hilpert correlation were reported. The modifications of AOA are $(0.75 + 0.013\alpha)$ and $(0.75 + 0.0017\alpha)$, separately for low and high Reynolds numbers, respectively. It was observed that the average Nusselt number varied with angles of attack, due to movement of the transition point and turbulence. The correction factors and modified correlations have provided useful new predictive tools for convective heat transfer from airfoils at varying angles of attack.

Results were presented on the investigation of heat transfer coefficients for forced convection from the NACA airfoil with effects of impinging liquid water droplets. Wind tunnel measurements of the convection coefficients were obtained for air flows with LWC ranging from 0 - 2 g/m³ at AOA = 0. The experimental data were correlated with the Nusselt and Reynolds numbers. Both average and spatial variations of the heat transfer coefficients were non-dimensionalized through modifications of the Hilpert correlation for cylinders in cross flow, while the Reynolds number was corrected by the LWC. The corrected $W = LWC/LWC_0$ uses $LWC_0 = 0.92$ for LWC less than 1 g/m³ and $LWC_0 = 1.25$ when LWC ranges from 1 to 2 g/m³.

Another experimental study of heat transfer was conducted for forced convection with droplet impact on the NACA 63421 airfoil at varying angles of attack from 5° to 25°. Wind tunnel studies were conducted at varying wind speeds and LWC values ranging between 0 - 2 g/m³. The experimental data were correlated with the Nusselt number, angle of attack and a newly defined multiphase Reynolds number. Both average and local Nusselt numbers were obtained and non-dimensionalized in a modified Hilpert correlation. An uncertainty analysis was performed to give a measurement uncertainty of 7.34% for the measured Nusselt numbers,

(Appendix B – Measurement uncertainties). The new correlations have provided useful new predictive tools for convective heat transfer from airfoils, with and without LWC, at varying AOA.

7.2 Recommendations for future research

The following suggestions are recommended for further study of aerodynamics and heat transfer related to wind turbine icing.

1. The LWC and MVD in the wind tunnel should be tested further with experimental facilities. They affect the results significantly. Uniform droplet sizes are important for the aerodynamic investigation.
2. The aerodynamics experiment of the iced airfoil should be investigated further with two end plates within the tunnel. A 2-D or 3-D investigation for the airfoil is different. The 3-D experiments have different values, due to the side effects, than 2-D airfoil investigations.
3. Flow visualization of the airfoil at various AOA in a water tunnel would be helpful for the flow field over the airfoil. This would provide deeper insight for more understanding of the convective heat transfer coefficient, when air flow passes over the blade.
4. An infrared Temperature Measurement System is a possible method to measure surface temperatures of an iced airfoil. A combined temperature measurement system, with thermocouples inside the airfoil, can be used to obtain the heat transfer coefficient of the iced airfoil.
5. An iced airfoil will be tested over a very short time to compare an un-iced airfoil and iced airfoil. Results obtained from an iced airfoil indicate that the spraying

time affects the aerodynamics. A minute or a shorter time test would disclose ice accretion information with a high speed camera.

6. Computer simulation studies with CFD for the iced airfoil would be helpful to simulate various ice conditions.

References

- [1] EWEA (the European Wind Energy Association), “Green Peace International, Wind Force 12 A blueprint to achieve 12% of the world’s electricity from wind power by 2020,” June 2005. <http://www.greenpeace.org/international/press/reports/windforce-12-2005>. Accessed on Feb. 06, 2006.
- [2] GWEC (Global Wind Energy Council), Global wind 2007 report. http://www.gwec.net/uploads/media/Global_Wind_2007_Report_final.pdf. Accessed on May 17, 2008.
- [3] GWEC (Global Wind Energy Council), [http://www.gwec.net/index.php?id=30&no_cache=1&tx_ttnews\[pointer\]=1&tx_ttnews\[tt_news\]=24&tx_ttnews\[backPid\]=4&cHash=26e173f378](http://www.gwec.net/index.php?id=30&no_cache=1&tx_ttnews[pointer]=1&tx_ttnews[tt_news]=24&tx_ttnews[backPid]=4&cHash=26e173f378). Accessed on June 06, 2006.
- [4] Canadian Wind Energy Association http://www.canwea.ca/images/uploads/File/WindSight/windsight_jul07.pdf. Accessed on Sep. 07, 2007.
- [5] T. Laakso, E. Peltola, “A statistical evaluation of icing and low temperature failures in Finland 1996 – 2002,” *BOREAS VI Proceedings*, April 2003.
- [6] G. Ronsten, “Svenska erfarenheter av vindkraft i kallt klimat—nedisning, iskast och avisning,” *Elforsk rapport 04:13*, May, 2004.
- [7] J. Druez, D.D. Nguyen, Y. Lavoie, “Mechanical properties of atmospheric ice,” *Cold Region Science and technology*, vol. 13, pp. 67 - 74, 1986.

-
- [8] EWEA, “Prioritizing wind energy research strategic research agenda of the wind energy sector. July 2005.” <http://www.ewea.org/index.php?id=15>. Accessed on 06.02, 2006.
 - [9] IEA, “2005 IEA Wind Energy Annual Report”. http://ieawind.org/ar_two_o_five.html. Accessed on July 16, 2006.
 - [10] Wind energy in the NWT and Nunavut, “Arctic experience”, <http://www.yec.yk.ca/wind/presentations/May%2027/Project%20Development%20&%20Success%20Stories%20II/SteveKerr%20LeeDouglas%20Wind%20Energy%20-%20NWT%20and%20Nunavut.pdf>, Accessed on July 28, 2006.
 - [11] J. Woods, “Ice & wind factors in wind turbine output in Southern Manitoba,” report to Manitoba Hydro, 2007.
 - [12] T. Laakso, “Wind energy projects in cold climates,” report to the Executive Committee of the International Energy Agency Programme, edition 2005.
 - [13] <http://virtual.vtt.fi/virtual/arcticwind/>. Accessed on September 12, 2007.
 - [14] <http://www.lmglassfiber.com/News/Archive/View%20News.aspx?id={0DEFA898-82D4-4662-9BAF-B3E66570D2A6}&y=2007>. Accessed on Sep.11, 2007.
 - [15] EWEA, “Execute summary, wind energy the facts, An analysis of wind energy in the EU-25,” [http://www.ewea.org/index.php?id=91&no_cache=1&sword_list\[\]=facts](http://www.ewea.org/index.php?id=91&no_cache=1&sword_list[]=facts). Accessed on Sep. 12, 2007.
 - [16] F. N. Coton, T. Wang, R. A. McD. Galbraith, “An examination of key aerodynamic modelling issues raised by the NREL blind comparison,” *Wind Energy*, vol. 5, pp. 199 - 212, 2002.
 - [17] Y. U. Sohn, Ch. H. Chun, Y. C. Kim, C. W. Chung, Y. H. Kim, K. S. Han, J. Y. Ryu, D. H. Kim, R. Schmidt, M. Rees, “Blade design of a 750 kW direct-drive wind turbine generator system,”

- <http://scholar.google.com/scholar?hl=en&lr=&q=related:FJBZ26E8mZsJ:scholar.google.com/>. Accessed on Aug 21, 2007.
- [18] C. Kong, J. Bang, Y. Sugiyama, "Structural investigation of composite wind turbine blade considering various load cases and fatigue life," *Energy*, vol. 30, pp. 2101 - 2114, 2005.
 - [19] K. J. Jackson, M. D. Zuteck, C. P. van Dam, K. J. Standish, D. Berry, "Innovative design approaches for large wind turbine blades," *Wind Energy*, vol. 8, pp. 141 - 171, 2005.
 - [20] P. Fuglsang, C. Bak, "Development of the Risø wind turbine airfoils," *Wind Energy*, vol. 7, pp. 145 - 162, 2004.
 - [21] C. Bak, P. Fuglsang, "Modification of the NACA 62₂-415 leading edge for better aerodynamic performance," *Journal of Solar Energy Engineering*, vol. 124, pp. 327 - 334, 2002.
 - [22] I. Grant, M. Mo, X. Pan, P. Parkin, J. Powell, H. Reinecke, K. Shuang, F. Coton, D. Lee, "An experimental and numerical study of the vortex filaments in the wake of an operational, horizontal-axis, wind turbine," *Journal of Wind Engineering and Industrial Aerodynamics*, vol. 85, no. 2, pp. 177 - 189, 2000.
 - [23] S. Schreck and M. Robinson, "Rotational augmentation of horizontal axis wind turbine blade aerodynamic response," *Wind Energy*, vol. 5, pp. 133 - 150, 2002.
 - [24] W. A. Timmer, A. P. Schaffarczyk, "The effect of roughness at high Reynolds Numbers on the performance of aerofoil DU 97-W-300Mod," *Wind Energy*, vol. 7, pp. 295 - 307, 2004.
 - [25] K. Y. Maalawi, H. M. Negm, "Optimal frequency design of wind turbine blades," *Journal of Wind Engineering and Industrial Aerodynamics*, vol. 90, pp. 961 - 986, 2002.

-
- [26] J. M. Mejía, F. Chejne, R. Smith, L. F. Rodríguez, O. Fernández, I. Dyner, "Technical note simulation of wind energy output at Guajira, Colombia," *Renewable Energy*, vol. 31, pp. 383 - 399, 2006.
- [27] M. Jureczko, M. Pawlak, A. Mężyk, "Optimization of wind turbine blades," *Journal of Materials Processing Technology*, vol. 167, pp. 463 - 471, 2005.
- [28] Norwin 46/47-ASR-600/750KW Main feature of design, http://www.norwinna.com/turbine_750.htm. Accessed on Oct 12, 2007.
- [29] J. S. R. Anttonen, P. I. King, P. S. Beran, "Applications of multi-POD to a pitching and plunging airfoil," *Mathematical and Computer Modeling*, vol. 42, pp. 245 - 259, 2005.
- [30] R. Giering, T. Kaminski, T. Slawig, "Generating efficient derivative code with TAF adjoint and tangent linear Euler flow around an airfoil," *Future Generation Computer Systems*, vol. 21, pp. 1345 - 1355, 2005.
- [31] S. Mittal, P. Saxena, "Hysteresis in flow past a NACA 0012 airfoil," *Comput. Methods Appl. Mech. Engrg*, vol. 191, pp. 2179 - 2189, 2002.
- [32] M. H. Akbari and S. J. Price, "Simulation of the flow over elliptic airfoils oscillating at large angels of attack," *Journal of Fluids and Structures*, vol. 14, pp. 757 - 777, 2000.
- [33] O.P. Le Maître, R.H. Scanlan, O.M. Knio, "Estimation of the flutter derivatives of an NACA airfoil by means of Navier–Stokes simulation," *Journal of Fluids and Structures*, vol. 17, pp. 1 - 28, 2003.
- [34] T. Slawig, "Domain optimization of a multi-element airfoil using automatic differentiation," *Advances in Engineering Software*, vol. 32, pp. 225 - 237, 2001.

-
- [35] M. Meyer, H. G. Matthies, "State-space representation of instationary two-dimensional airfoil aerodynamics," *Journal of Wind Engineering and Industrial Aerodynamics*, vol. 92, no. 3 - 4, pp. 263 – 274, 2004.
- [36] Y.W. Jung, S.O. Park, "Vortex-shedding characteristics in the wake of an oscillating airfoil at low Reynolds number," *Journal of Fluids and Structures*, vol. 20, pp. 451 - 464, 2005.
- [37] M.R. Ahmed, S.D. Sharma, "An investigation on the aerodynamics of a symmetrical airfoil in ground effect," *Experimental Thermal and Fluid Science*, vol. 29, pp. 633 - 647, 2005.
- [38] M. Amitay, A. Glezer, "Controlled transients of flow reattachment over stalled airfoils," *International Journal of Heat and Fluid Flow*, vol. 23, pp. 690 - 699, 2002.
- [39] C. Hillenherms, W. Schröder, W. Limberg, "Experimental investigation of a pitching airfoil in transonic flow," *Aerospace Science and Technology*, vol. 8, pp. 583 - 590, 2004.
- [40] C. Bak, P. Fuglsang, J. Johansen, I. Antoniou, "Wind tunnel tests of the NACA 63-415 and a modified NACA 63-415 Airfoil," Riso National Laboratory, Roskilde Denmark RISO-R-1193(EN), December, 2000.
- [41] Ph. Devinant, T. Laverne, J. Hureau, "Experimental study of wind-turbine airfoil aerodynamics in high turbulence," *Journal of Wind Engineering and Industrial Aerodynamics*, vol. 90, pp. 689 - 707, 2002.
- [42] L. Bermúdez, A. Velázquez, A. Matesanz, "Viscous–inviscid method for the simulation of turbulent unsteady wind turbine airfoil flow," *Journal of Wind Engineering and Industrial Aerodynamics*, vol. 90, pp. 643 - 661, 2002.

-
- [43] M.A. Yurdusev, R. Ata, N.S. Çetin, "Assessment of optimum tip speed ratio in wind turbines using artificial neural networks," *Energy*, vol. 31, no. 12, pp. 2153 - 2161, 2006.
- [44] R. Younsi, I. El-Batanony, J. Tritsch, H. Naji, B. Landjerit, "Dynamic study of a wind turbine blade with horizontal axis," *Eur. J. Mech. A/Solids*, vol. 20, pp. 241 - 252, 2001.
- [45] K. Abe, M. Nishida, A. Sakurai, Y. Ohya, H. Kihara, E. Wada, K. Sato, "Experimental and numerical investigations of flow fields behind a small wind turbine with a flanged diffuser," *Journal of Wind Engineering and Industrial Aerodynamics*, vol. 93, pp. 951 - 970, 2005.
- [46] L. Bermúdez, A. Velázquez, A. Matesanz, "Numerical simulation of unsteady aerodynamics effects in horizontal-axis wind turbines," *Solar Energy*, vol. 68, no. 1, pp. 9 - 21, 2000.
- [47] K. Badreddinne, H. Ali, A. David, "Data bank: Optimum project for horizontal axis wind turbines 'OPHWT'," *Renewable Energy*, vol. 30, pp. 2019 - 2043, 2005.
- [48] L.J. Vermeer, J.N. Sørensen, A. Crespo, "Wind turbine wake aerodynamics," *Progress in Aerospace Sciences*, vol. 39, pp. 467 - 510, 2003.
- [49] P. R. Ebert, D. H. Wood, "The near wake of a model horizontal-axis wind turbine--I. Experimental arrangements and initial results," *Renewable Energy*, Vol. 12, No. 3, pp. 225 - 243, 1997.
- [50] P.R. Ebert, D.H. Wood, "The near wake of a model horizontal-axis wind turbine --II. General features of the three-dimensional flow field," *Renewable Energy*, vol. 18, pp. 513 - 534, 1999.

-
- [51] P.R. Ebert, D.H. Wood, "The near wake of a model horizontal-axis wind turbine Part 3: properties of the tip and hub vortices," *Renewable Energy*, vol. 22, pp. 461 - 472, 2001.
- [52] K. Kishinami, H. Taniguchi, J. Suzuki, H. Ibano, T. Kazunou, M. Turuhami, "Theoretical and experimental study on the aerodynamic characteristics of a horizontal axis wind turbine," *Energy*, vol. 30, pp. 2089 - 2100, 2005.
- [53] T. Burton, D. Sharpe, N. Jenkins, E. Bossanyi, *Wind Energy Handbook*, John Wiley & Sons, 2001.
- [54] M. Durstewitz, C. Ensslin, M. Hopper-Kilpper, K. Rohrig, "External conditions for wind turbine operation-results from the German '250MW wind' programme," *European Union Wind Energy Conference*, Goeteborg, 1996.
- [55] B. Schaffner, "Long term experience in the Swiss Alps," *METEOTEST*, 2003.
- [56] C. Morgan, E. Bossanyi, H. Seifert, "Assessment of safety risks arising from wind turbine icing," *BOREAS IV* 31March- 2 April, Hetta, Finland, 1998.
- [57] J. Peinke, S. Barth, F. Böttcher, "Turbulence, a challenging problem for wind energy," *Physica A*, vol. 338, pp. 187 - 193, 2004.
- [58] P.W. Cheng, W.A.A.M. Bierbooms, "Distribution of extreme gust loads of wind turbines," *Journal of Wind Engineering and Industrial Aerodynamics*, vol. 89, pp. 309 - 324, 2001.
- [59] E. Aarnio and S. Partonen, "Operational experience of arctic wind farms," *BORES V*, 29 November to 1 December, Levi Finland, 2000.
- [60] B. Tammelin and K. Santti, "Icing in Europe," *BOREAS IV*, Hetta, Finland, Mar 31-April 2, 1998.
- [61] P. Antikainen and S. Peuranen, "Ice loads, case study," *BORES V*, 29 November to 1 December, Levi Finland, 2000.

-
- [62] B. Tammelin and H. Seifert, "Large wind turbines go into cold climate regions," *EWEC*, Copenhagen, 02-06, 07, 2001.
- [63] B. Tammelin, "New ice tools – Experimental wind energy data from cold climate sites in Europe," *DEWI Magazin*, Nr.21 August, 2002.
- [64] H. Seifert and C. Schloz, "Additional loads caused by ice on rotor blades during operation," *European Community Wind Energy Conference*, Madrid Spain, 10-14 Sep. 1990.
- [65] J. Rong, N. Bose, Carl Brothers and Malcolm Lodge, "Icing test on a horizontal axis wind turbine," *Wind Engineering*. vol.15, no. 2, pp. 109 - 113.
- [66] N. Bose, "Icing on a small horizontal-axis wind turbine – Part 1: Glaze ice profiles," *Journal of wind engineering and Industrial Aerodynamic*, vol. 45, pp. 75 - 85, 1992.
- [67] N. Bose, "Icing on a small horizontal-axis wind turbine – Part 2: Three dimensional ice and wet snow formations," *Journal of wind engineering and Industrial Aerodynamic*, vol. 45, pp. 87 - 96, 1992.
- [68] G. Botta, M. Cavaliere, S. Viani, S. Pospisil, "Effects of hostile terrains on wind turbine performances and loads: The Acqua Spruzza experience," *Journal of Wind Engineering and Industrial Aerodynamics*, vol. 74-76, pp. 419 - 431, 1998.
- [69] H. Winkelmeier and J. Trauttmansdorff, "Tauern wind park berzeiring 13MW wind power plant at an alpine site with severe weather conditions," *BORES V*, 29 November to 1 December, Levi Finland, 2000.
- [70] C. Leclerc, C. Masson, "Abnormal high power output of wind turbine in cold weather: a preliminary study," *Proceedings of the CanWEA Seminar and the 15th CanWEA Conference & Trade Show '99*, pp.190-199, Setp. 27-29, Rimouski, Canada, 1999.
- [71] http://www.ec.gc.ca/science/sandejan00/article4_e.html, accessed on may 18, 2008.
- [72] http://en.wikipedia.org/wiki/American_Eagle_Flight_4184, accessed on may 18, 2008.

-
- [73] M.B. Bragg, A.P. Broeren, L.A. Blumenthal, "Iced-airfoil aerodynamics," *Progress in Aerospace Sciences*, vol. 41, pp. 323–362, 2005.
- [74] J. Shin, "Characteristics of surface roughness associated with leading edge ice accretion," *AIAA Paper 94-0799*, 1994.
- [75] Jr. HE Addy, M.G. Potapczuk, DW. Sheldon, "Modern airfoil ice accretions," *AIAA Paper 97-0174*, 1997.
- [76] S. Lee, T. Dunn, H. Gurbaki, M.B. Bragg, E. Loth, "An experimental and computational investigation of spanwise-step-ice shapes on airfoil aerodynamics," *AIAA Paper 98-0490*, 1998.
- [77] M. Papadakis, B.E. Gile-Laflin, G.M. Youssef, T.P. Ratvasky, "Aerodynamic scaling experiments with simulated ice accretions," *AIAA Paper 2001-0833*, 2001.
- [78] M. Papadakis, H.W. Yeong, R. Chandrasekharan, M. Hinson, T.P. Ratvasky, "Effects of roughness on the aerodynamic performance of a business jet tail," *AIAA Paper 2002-0242*, 2002.
- [79] M. Papadakis, S. Alansatan, M. Selmann, "Experimental study of simulated ice shapes on a NACA 0011 airfoil," *AIAA Paper 99-0096*, 1999.
- [80] M. Papadakis, S. Alansatan, S. Wong, "Aerodynamic characteristics of a symmetric NACA section with simulated ice shapes," *AIAA Paper 2000-0098*, 2000.
- [81] Jr, H. Addy, A.P. Broeren, JG Zoeckler, S. Lee, "A wind tunnel study of icing effects on a business jet airfoil," *AIAA Paper 2003-0727*, also NASA TM-2003-212124, 2003.
- [82] J. Pan, E. Loth, M.B. Bragg, "RANS simulations of airfoils with ice shapes," *AIAA Paper 2003-0729*, 2003.
- [83] A.P. Broeren, H.E. Addy, M.B. Bragg, "Flow field measurements about an airfoil with leading-edge ice shapes," *AIAA Paper 2004-0059*, 2004.

-
- [84] P. S. Hoskins, N. Bose and J. Rong, "Experimental characteristics of a NASA LS (1)-0417 airfoil with simulated Icing." 1989.
- [85] H. Seifert, F. Richert, "A recipe to estimate aerodynamics and loads on iced rotor blades," *BOREAS IV*, Hetta, Finland Mar31-April 2, 1998.
- [86] S. Kimura, B. Tammelin and K. Santti, "Estimation of reduction of power production due to icing from the existing meteorological data," *BORES V*, 29 November to 1 December, Levi Finland, 2000.
- [87] A. Barker, G. Timco, H. Gravesen, P. Vølund, "Ice loading on Danish wind turbines Part 1: Dynamic model tests," *Cold Regions Science and Technology*, vol. 41, pp. 1 - 23, 2005.
- [88] H. Gravesen, S. L. Sørensen, P. Vblund, A. Barker, G. Timco, "Ice loading on Danish wind turbines Part 2. Analyses of dynamic model test results," *Cold Regions Science and Technology*, vol. 41, pp. 25 - 47, 2005.
- [89] R.P. Koomullil, D.S. Thompson, B.K. Soni, "Iced airfoil simulation using generalized grids," *Applied Numerical Mathematics*, vol. 46, pp. 319 - 330, 2003.
- [90] Y.X. Tao, G. Liu and P. Tu, "Modeling ice layer growth on a wind turbine rotor blade," *AIAA/ASME Joint Thermochemical and Heat Transfer Conference*, vol. 4, ASME 1998.
- [91] M. Marjaniemi, L. Makkonen and T. Laakso, "TURBICE- the wind turbine blade icing model," *BORES V*, 29 November to 1 December, Levi Finland, 2000.
- [92] L. Makkonen, T. Laakso, M. Marjaniemi and K. J. Finstad, "Modelling and prevention of ice accretion on wind turbines," *Wind Engineering*, vol. 25, No.1, pp. 3 - 21, 2001.
- [93] H. Seifert, "Technical requirements for rotor blades operation in cold climate," *BOREAS IV*, 9-11 April, Pyhae, Finland, 2004.

-
- [94] A.F. Massardo and E. Farinazzo, "Experimental investigation of a new and energy-saving nacelle anti-icing system," *Journal of Aircraft*, vol. 33, no. 6, 1996.
- [95] B. Tammelin, M. Cavaliere, S. Kimura, C. Morgan, A. Peltomaa, "Ice free anemometers," *BOREAS IV*, Hetta, Finland Mar31-April 2, 1998.
- [96] D. F. Craig, D. B. Craig, "Monitoring of icing events on fjells in northern Canada," In proceedings of BOREAS II (Ed. B. Tammelin et al.), Finnish meteorological institute, pp.154 -163, 1994.
- [97] E. Peltola, M. Marjaniemi, H. Stiesdal and J. Jävelä "An ice prevention system for the wind turbine blades," In Proc. of 1999 European Wind Energy Conference, 1-5 March, , Nice, France, pp. 1034 -1037, 1999.
- [98] J. F. Maissan, "Wind power development in sub-arctic conditions with severe rime icing," Report by Yukon Energy corp. Yukon, Canada, May 2000.
- [99] R. Horbaty, "Wind energy in cold climates — The Swiss experience," Proceedings of the 2005 BOREAS VII, Saariselkä, Finland, March, 2005.
- [100] A. G. Kraj, *Icing characteristics and mitigation strategies for wind turbines in cold climates*, Master thesis, University of Manitoba, 2007.
- [101] G. F. Naterer, *Heat Transfer in Single and Multiphase Systems*, CRC Press, Boca Raton, FL, 2003.
- [102] P. Datta, D. Anilkumar, S. Roy, N. C. Mahanti, "Effect of non-uniform slot injection (suction) on a forced flow over a slender cylinder," *International Journal of Heat and Mass Transfer*, vol. 49, no. 13-14, pp. 2366 - 2371, 2006.
- [103] G. Evans, R. Greif, D. Siebers, S. Tieszen, "Turbulent mixed convection from a large, high temperature, vertical flat surface," *International Journal of Heat and Fluid Flow*, vol. 26, pp. 1 - 11, 2005.

-
- [104] M. Lachi, M. Rebay, E. C. Mladin, J. Padet, "Alternative models for transient convection heat transfer in external flows over a plate exposed to a variable heat flux," *International Journal of Thermal Sciences*, vol. 43, pp. 809 - 816, 2004.
- [105] O. Aydin, A. Kaya, "Mixed convection of a viscous dissipating fluid about a vertical flat plate," *Applied Mathematical Modelling*, vol. 31, no. 5, pp. 843 - 853, 2007.
- [106] O. B. Adeyinka, G. F. Naterer, "Particle image velocimetry based measurement of entropy production with free convection heat transfer," *ASME Journal of Heat Transfer*, vol. 127, no. 6, pp. 615 - 624, 2005.
- [107] G. F. Naterer, O. B. Adeyinka, "New laser based method for non-intrusive measurement of available energy loss and local entropy production," *Experimental Thermal and Fluid Science*, vol. 31, no. 2, pp. 91 - 95, 2006.
- [108] O. Laguerre, S. Ben Amara, D. Flick, "Heat transfer between wall and packed bed crossed by low velocity air flow," *Applied Thermal Engineering*, vol. 26, no. 16, pp. 1951 - 1960, 2006.
- [109] U. Akyol, K. Bilen, "Heat transfer and thermal performance analysis of a surface with hollow rectangular fins," *Applied Thermal Engineering*, vol. 26, no. 2-3, pp. 209 - 216, 2006.
- [110] J. K. Carson, J. Willix, M. F. North, "Measurements of heat transfer coefficients within convection ovens," *Journal of Food Engineering*, vol. 72, pp. 293 - 301, 2006.
- [111] K. Hanjalic, "Synergy of experiments and computer simulations in research of turbulent convection," *International Journal of Heat and Fluid Flow*, vol. 26, pp. 828 - 842, 2005.
- [112] H. Bhowmik, C. P. Tso, K. W. Tou, F. L. Tan, "Convection heat transfer from discrete heat sources in a liquid cooled rectangular channel," *Applied Thermal Engineering*, vol. 25, pp. 2532 - 2542, 2005.

- [113] G. F. Naterer, "Establishing heat - entropy analogies for interface tracking in phase change heat transfer with fluid flow," *International Journal of Heat and Mass Transfer*, vol. 44, no. 15, pp. 2903 - 2916, 2001.
- [114] G. F. Naterer, "Applying heat - entropy analogies with experimental study of interface tracking in phase change heat transfer," *International Journal of Heat and Mass Transfer*, vol. 44, no. 15, pp. 2917 - 2932, 2001.
- [115] A. A. Kendoush, A. W. Izzat, "Experiments of fluid flow and heat convection in the wake of a disk facing a uniform stream," *International Journal of Thermal Sciences*, vol. 44, pp. 894 - 902, 2005.
- [116] C. J. Kobus, "Utilizing disk thermistors to indirectly measure convective heat transfer coefficients for forced, natural and combined (mixed) convection," *Experimental Thermal and Fluid Science*, vol. 29, pp. 659 - 669, 2005.
- [117] G. J. Van Fossen, R. J. Simoneau, W. A. Olsen, R. J. Shaw, "Heat transfer distributions around nominal ice accretion in the LEWIS icing research tunnel," AIAA 22nd Aerospace Science Meeting, Reno, Nevada, AIAA paper 84-0017, 1984.
- [118] K. (Stevanović) Hedrih, V. Babović, D. Šarković, "An auxiliary size distribution model for the ultrasonically produced water droplets," *Experimental Thermal and Fluid Science*, vol. 30, pp. 559 - 564, 2006.
- [119] W. Fuchs, K.-P. Schickel, "Aircraft icing in visual meteorological conditions below low stratus clouds," *Atmospheric Research*, vol. 36, pp. 339 - 345, 1995.
- [120] S.S. Yoon, P.E. DesJardin, C. Presser, J.C. Hewson, C.T. Avedisian, "Numerical modeling and experimental measurements of water spray impact and transport over a cylinder," *International Journal of Multiphase Flow*, vol. 32, pp. 132 - 157, 2006.

-
- [121] L. E. Kollár, M. Farzaneh, A. R. Karev, "Modeling droplet collision and coalescence in an icing wind tunnel and the influence of these processes on droplet size distribution," *International Journal of Multiphase Flow*, vol. 31, pp. 69 - 92, 2005.
- [122] M. Strub, O. Jabbour, F. Strub, J.P. Bédécarrats, "Experimental study and modeling of the crystallization of a water droplet," *International Journal of Refrigeration*, vol. 26, pp. 59 - 68, 2003.
- [123] L. E. Kollár, M. Farzaneh, "Modeling the evolution of droplet size distribution in two-phase flow," *International Journal of Multiphase Flow*, vol. 33, pp. 1255 - 1270, 2007.
- [124] W. Jia, H.-H. Qiu, "Experimental investigation of droplet dynamics and heat transfer in spray cooling," *Experimental Thermal and Fluid Science*, vol. 27, pp. 829 - 838, 2003.
- [125] M. L. Sawyer, S. M. Jeter and S. I. Abdel-Khaliks, "A critical heat flux correlation for droplet impact cooling," *International Journal of Heat Mass Transfer*, vol. 40, no. 9, pp. 2123 - 2131, 1997.
- [126] R.H. Chen, L. C. Chow, J. E. Navedo, "Effects of spray characteristics on critical heat flux in subcooled water spray cooling," *International Journal of Heat and Mass Transfer*, vol. 45, pp. 4033 - 4043, 2002.
- [127] J.P. Hindmarsh, A.B. Russell, X.D. Chen, "Experimental and numerical analysis of the temperature transition of a suspended freezing water droplet," *International Journal of Heat and Mass Transfer*, vol. 46, pp. 1199 - 1213, 2003.
- [128] G. Fortin, J. L. Laforte, A. Ilinca, "Heat and mass transfer during ice accretion on aircraft wings with an improved roughness model," *I. J. of Thermal Sciences*, vol. 45, pp. 595 - 606, 2006.

- [129] G.F. Naterer, "Coupled liquid film and solidified layer growth with impinging super cooled droplets and Joule heating," *International Journal of Heat and Fluid Flow*, vol. 24, pp. 223 - 235, 2003.
- [130] P. Fu, M. Farzaneh, G. Bouchard, "Two-dimensional modeling of the ice accretion process on transmission line wires and conductors," *Cold Regions Science and Technology*, vol. 46, no. 2, pp. 132 - 146, 2006.
- [131] Y. Ge, L.-S. Fan, "3-D modeling of the dynamics and heat transfer characteristics of sub cooled droplet impact on a surface with film boiling," *International Journal of Heat & Mass Transfer*, vol. 49, pp. 4231 - 4249, 2006.
- [132] G.F. Naterer, "Dispersed multiphase flow with air-driven runback of a liquid layer at a moving boundary," *International Journal of Multiphase Flow*, vol. 29, pp. 1833 - 1856, 2003.
- [133] J.C. Tsao, A.P. Rothmayer, "Application of triple-deck theory to the prediction of glaze ice roughness formation on an airfoil leading edge," *Computers & Fluids*, vol. 31, pp. 977 - 1014, 2002.
- [134] H.-J. Krokoszinski, "Efficiency and effectiveness of wind farms—keys to cost optimized operation and maintenance," *Renewable Energy*, vol. 28, pp. 2165 - 2178, 2003.
- [135] J.L. Torres , E. Prieto , A. Garcia , M. De Blas , F. Ramirez , A. De Francisco, "Effects of the model selected for the power curve on the site effectiveness and the capacity factor of a pitch regulated wind turbine," *Solar Energy*, vol. 74, pp. 93 - 102, 2003.
- [136] K. Saranyasoontorn, L. Manuel, "Efficient models for wind turbine extreme loads using inverse reliability," *Journal of Wind Engineering and Industrial Aerodynamics*, vol. 92, pp. 789 - 804, 2004.

-
- [137] M.H. Abderrazzaq, "Technical note: Energy production assessment of small wind farms," *Renewable Energy*, vol. 29, pp.2261 - 2272, 2004.
- [138] T. Ekelund, "Yaw control for reduction of structural dynamic loads in wind turbines," *Journal of Wind Engineering and Industrial Aerodynamics*, vol. 85, pp. 241 - 262, 2000.
- [139] V. A. Riziotis, S. G. Voutsinas, "Fatigue loads on wind turbines of different control strategies operating in complex terrain," *Journal of Wind Engineering and Industrial Aerodynamics*, vol. 85, pp. 211 - 240, 2000.
- [140] F.D. Bianchi, R.J. Mantz, C.F. Christiansen, "Gain scheduling control of variable-speed wind energy conversion systems using quasi-LPV models," *Control Engineering Practice*, vol. 13, pp. 247 - 255, 2005.
- [141] V. Akhmatov, H. Knudsen, A. H. Nielsen, J. K. Pedersen, N. K. Poulsen, "Modelling and transient stability of large wind farms," *Electrical Power and Energy System*, vol. 25, pp. 123 - 144, 2003.
- [142] T. Sürgevil, E. Akpınar, "Data bank modeling of a 5-kW wind energy conversion system with induction generator and comparison with experimental results," *Renewable Energy*, vol. 30, pp. 913 - 929, 2005.
- [143] F.D. Bianchi, R.J. Mantz, C.F. Christiansen, "Technical note: Power regulation in pitch-controlled variable speed WECS above rated wind speed," *Renewable Energy*, vol. 29, pp. 1911 - 1922, 2004.
- [144] A. Bouscayro, Ph. Delarue, X. Guillaud, "Power strategies for maximum control structure of a wind energy conversion system with a synchronous machine," *Renewable Energy*, vol. 30, pp. 2273 - 2288, 2005.
- [145] L. M. Fernández, J. R. Saenza, F. Juradob, "Dynamic models of wind farms with fixed speed wind turbines," *Renewable Energy*, vol. 31, no. 8, pp. 1203 - 1230, 2006.

-
- [146] M. M. Shokrieh, R. Rafiee, "Simulation of fatigue failure in a full composite wind turbine blade," *Composite Structures*, vol. 74, no. 3, pp. 332 - 342, 2006.
- [147] H. Hirahara, M. Z. Hossain, Y. Nonomura, M. Kawahashi, "Technical note: Testing basic performance of a very small wind turbine designed for multi-purposes," *Renewable Energy*, vol. 30, pp. 1279 - 1297, 2005.
- [148] M.A. Abderrazzaqa, B. Hahnb, "Analysis of the turbine standstill for a grid connected wind farm (case study)," *Renewable Energy*, vol. 31, pp. 89 - 104, 2006.
- [149] R. Gómez-Elvira, A. Crespo, E. Migoya, F. Manuel, J. Hernández, "Anisotropy of turbulence in wind turbine wakes," *Journal of Wind Engineering and Industrial Aerodynamics*, vol. 93, pp. 797 - 814, 2005.
- [150] G. P. Harrison, A. R. Wallace, "Climate sensitivity of marine energy," *Renewable Energy*, vol. 30, pp. 1801 - 1817, 2005.
- [151] M. Pehnt, "Dynamic life cycle assessment (LCA) of renewable energy technologies," *Renewable Energy*, vol. 31, pp. 55 - 71, 2006.
- [152] M. Hoogwijk, B. de Vries, W. Turkenburg, "Assessment of the global and regional geographical, technical and economic potential of onshore wind energy," *Energy Economics*, vol. 26, pp. 889 - 919, 2004.
- [153] K. R. Voorspools, W. D. D'haeseleer, "An analytical formula for the capacity credit of wind power," *Engineering Structures*, vol. 27, pp. 1209 - 1219, 2005.
- [154] U. Aytun Ozturk, Bryan A. Norman, "Heuristic methods for wind energy conversion system positioning," *Electric Power Systems Research*, vol. 70, pp. 179 - 185, 2004.
- [155] G. F. Naterer, N. Popplewell, W. Barrett, J. Anderson, E. Faraci, D. McCartney, W. Lehmann, "Experimental facility for new hybrid ice / spray flow tunnel with laser based droplet measurement," AIAA Paper 2002-2867, AIAA 32nd Fluid Dynamics Conference, St. Louis, Missouri, June 24 - 27, 2002.

-
- [156] ShapeGrabber 3D Scanning systems User's Manual, ShapeGrabber Incorporated, 2004.
- [157] Geomagic Studio manual 7, <http://www.geomagic.com/en/products/studio/>, accessed on May 2005.
- [158] J.F. Manwell, J.G. McGowan and A.L. Rogers, *Wind energy explained: theory, design and application*, Chichester, New York: Wiley, 2002.
- [159] J. Johansen, N.N. Sørensen, "Aerofoil characteristics from 3D CFD rotor computations," *Wind Energy*, vol. 7, pp. 283 – 294, 2004.
- [160] Autodesk Inventor manual, <http://www.inventor-certified.com/graphics/>. Accessed on Aug. 2005
- [161] Remote Optical Sensor, <http://www.monarchinstrument.com/>. Accessed on September 06 2005.
- [162] Isolated Current and Voltage Transducers Characteristics Applications Calculations, LEM Components. Third Edition 05.04. 2005.
- [163] Force measurement systems, Side Wall Balance Performances Summary April 2006 Calibration report, Allied Aerospace, 2006.
- [164] Manual of LabVIEW 8.0, National Instruments, <http://digital.ni.com/manuals.nsf/websearch/4ADECE27D5C390498625709200644635>, 2005
- [165] X. Wang, G. F. Naterer, E. Bibeau, "Experimental study of 3-D blades and wind turbines under icing conditions," The Second International Green Energy Conference, Oshawa, ON, June 25 - 29, 2006.
- [166] T. Adachi, E. Kato, "Study on the flow about a circular cylinder in shear flow," *Journal of the Japan Society for Aeronautical and Space Sciences*, vol. 23, pp. 311 - 319, 1975.

- [167] D. Sumner, O.O. Akosile, "On a circle cylinder in a uniform planar shear flow at sub critical Reynolds number," Proceedings of the Fifth International Symposium on Fluid - Structure Interactions, Aero elasticity, Flow – Induced Vibration & Noise, New Orleans, USA, No. IMECE2002-32170, ASME, New York, 2002.
- [168] T. Hayashi, F. Yoshino, R. Waka, "An analytical evaluation of the aerodynamic forces acting on a circular cylinder in a uniform shear flow," Forum on Turbulent Flows - 1991; ASME and JSME Joint Fluids Engineering Conference, 1st, Portland, OR; UNITED STATES; 23-27 June 1991. pp. 83 - 88. 1991.
- [169] S. Lee, H.S. Kim, M.B. Brag, "Investigation of factors that influence iced-airfoil aerodynamics," AIAA Paper 2000-0099, 2000.
- [170] S. Lee, M.B. Brag, "Investigation of factors affecting iced-airfoil aerodynamics," *Journal of Aircraft*, vol. 40, no. 3, May-June 2003
- [171] F. P. Incropera, D. P. deWitt, *Fundamentals of Heat and Mass Transfer*, Fourth Edition, John Wiley and Sons, Chapter 7, 1996.
- [172] S. Sanitjai, R. J. Goldstein, "Forced convection heat transfer from a circular cylinder in crossflow to air and liquids," *International Journal of Heat and Mass Transfer*, vol. 47, pp. 4795 - 4805, 2004.
- [173] B. H. Chang, A. F. Mills, "Effect of aspect ratio on forced convection heat transfer from cylinders," *International Journal of Heat and Mass Transfer*, vol. 47, pp. 1289 - 1296, 2004.
- [174] A. Amarante, J. L. Lanoisell, "Heat transfer coefficients measurement in industrial freezing equipment by using heat flux sensors," *Journal of Food Engineering*, vol. 66, pp. 377 - 386, 2005.

-
- [175] H. Nakamura, T. Igarashi, "Optimized complexity unsteady heat transfer from a circular cylinder for Reynolds numbers from 3000 to 15,000," *International Journal of Heat and Fluid Flow*, vol. 25, pp. 741 - 748, 2004.
- [176] D. Naylor, "Recent developments in the measurement of convective heat transfer rates by laser interferometry," *International Journal of Heat and Fluid Flow*, vol. 24, pp. 345 - 355, 2003.
- [177] R. J. Goldstein, W. E. Ibele, S. V. Patankar, T. W. Simon, T. H. Kuehn, P. J. Strykowski, K. K. Tamma, J. V. R. Heberlein, J. H. Davidson, J. Bischof, F. A. Kulacki, U. Kortshagen, S. Garrick, V. Srinivasan, "Heat transfer - a review of 2003 literature," *International Journal of Heat and Mass Transfer*, vol. 49, pp. 451 - 534, 2006.
- [178] S.W. Churchill, M. Bernstein, "A correlating equation for forced convection from gases and liquids to a circular cylinder in cross flow," *ASME Journal of Heat Transfer*, vol. 99, pp. 300 - 306, 1977.
- [179] S.J. Kline, F.A. McClintock, "Describing uncertainties in single-sample experiments," *Mechanical Engineering*, vol. 75, pp. 3 - 8, 1953.
- [180] S. Montelpare, R. Ricci, "A thermographic method to evaluate the local boundary layer separation phenomena on aerodynamic bodies operating at low Reynolds number," *International Journal of Thermal Sciences*, vol. 43, no.3, pp. 315 - 329, 2004.
- [181] N. Okong'o, D. D. Knight, "Implicit unstructured Navier-Stokes simulation of leading edge separation over a pitching airfoil," *Applied Numerical Mathematics*, vol.27, no. 3, pp. 269 – 308, 1998

- [182] X. Wang, E. Bibeau, G. F. Naterer, “Experimental correlation of forced convection heat transfer from a NACA airfoil,” *Experimental Thermal and Fluid Science*, vol.31, no. 8, pp.1073 - 1082, 2007.

Appendix A – Lists of published papers

- [1] X. Wang, E. Bibeau, G. F. Naterer, 2008, “Convective Heat Transfer from a NACA airfoil at Varying Angles of Attack,” *AIAA Journal of Thermophysics and Heat Transfer*, vol. 22, no. 3, pp. 457—463.
- [2] X. Wang, G. F. Naterer, E. Bibeau, 2008, “Multiphase Nusselt Correlation for the Impinging Droplet Heat Flux from a NACA Airfoil,” *AIAA Journal of Thermophysics and Heat Transfer*, vol. 22, no. 2, pp. 219 - 226.
- [3] X. Wang, E. L. Bibeau, G. F. Naterer, 2008, “Multiphase flow with convective droplet impact on a NACA airfoil at varying Angles of attack,” 46th AIAA Aerospace Sciences Meeting and Exhibit, Reno, Nevada, U.S.A, Jan. 10.
- [4] X. Wang, E. L. Bibeau, G. F. Naterer, 2007, “Experimental Investigation of Energy Losses due to Icing of a Wind Turbine,” *International Conference on power engineering-2007*, Hangzhou, China, Oct 23-27.
- [5] X.Wang, E. Bibeau G. F. Naterer, 2007, “Experimental Correlation of Forced Convection Heat Transfer from a NACA Airfoil,” *Experimental Thermal and Fluid Science*, vol. 31, no. 8, pp. 1073-1082.
- [6] X. Wang, G. F. Naterer, E. Bibeau, 2007, “Convective droplet impact and heat transfer from a NACA airfoil,” *AIAA Journal of Thermophysics and Heat Transfer*, vol. 21, no.3, pp. 543 - 547.
- [7] X. Wang, G. F. Naterer, E. Bibeau, 2007, “Wind tunnel measurements of convective heat transfer with droplet impact on a wind turbine NACA63-421 blade,” 2007 ASME-JSME Thermal Engineering Conference and Summer Heat Transfer Conference, Vancouver, BC, Canada, July 8-12.

- [8] X. Wang, E. Bibeau, G. F. Naterer, 2007, "Modified Hilpert Correlation for Turbulent Convective Heat Transfer from a NACA Profile of Wind Turbine Blades," AIAA 39th Thermophysics Conference, Miami, FL, June 25 – 28.
- [9] X. Wang, G. F. Naterer, E. Bibeau, 2006, "Experimental study of 3-D blades and wind turbines under icing conditions," The Second International Green Energy Conference, Oshawa, Ontario, June 25 - 29.
- [10] X. Wang, E. Bibeau, G. F. Naterer, 2006, "Experimental investigation of wind energy losses under icing Conditions," Canada Wind Energy Association Conference, Winnipeg, Oct. 22-25. Poster presentation.
- [11] X. Wang, T. Xu, J. Wang, 2004, "Experimental Study of Aerodynamic Fields of α -shaped Flame," The 4th International Symposium on Measurement Techniques for Multiphase Flows, Huangzhou, China, Oct.

Appendix B – Measurement uncertainties

This appendix uses the method of Kline and McClintock [179] to determine the measurement uncertainties in the reported experiments. From Equation (3-8), the heat transfer coefficient was determined as follows,

$$h = \frac{k(T_{in} - T_o)}{\delta(T_{\infty} - T_o)} \quad (B-1)$$

In the experiments, the parameters T_o , T_i and δ were measured. The total uncertainty, U_h , includes a precision uncertainty, P_h , and B_h (bias contribution to the uncertainty).

$$U_h = \sqrt{P_h^2 + B_h^2} \quad (B-2)$$

$$P_q^2 = \left(\frac{\partial h}{\partial T_{in}} \right)^2 P_{Ti}^2 + \left(\frac{\partial h}{\partial T_o} \right)^2 P_{To}^2 + \left(\frac{\partial h}{\partial T_{\infty}} \right)^2 P_{T\infty}^2 + \left(\frac{\partial h}{\partial \delta} \right)^2 P_{\delta}^2 + \left(\frac{\partial h}{\partial k} \right)^2 P_k^2 \quad (B-3)$$

$$\left(\frac{P_h}{h} \right)^2 = \left(\frac{P_{Ti}}{\Delta T_1} \right)^2 + \left(\frac{P_{To}}{\Delta T_2} \right)^2 + \left(\frac{P_{T\infty}}{\Delta T_2} \right)^2 + \left(\frac{P_{\delta}}{\delta} \right)^2 + \left(\frac{P_k}{k} \right)^2 \quad (B-4)$$

Also,

$$\begin{aligned} \left(\frac{B_h}{h} \right)^2 &= \frac{B_{Ti}^2 + B_{To}^2 - 2B'_{Ti}B'_{To}}{\Delta T_1^2} + \frac{B_{To}^2 + B_{T\infty}^2 - 2B'_{To}B'_{T\infty}}{\Delta T_2^2} + \frac{2}{\Delta T_1 \Delta T_2} B_{To}^2 - \frac{2}{\Delta T_1 \Delta T_2} B'_{To}B'_{Ti} \\ &\quad + \frac{2}{\Delta T_1 \Delta T_2} (B'_{T\infty}B''_{Ti} - B'_{To}B'_{T\infty}) + \frac{B_k^2}{k^2} + \frac{B_{\delta}^2}{\delta^2} \end{aligned} \quad (B-5)$$

$$\begin{aligned} \left(\frac{B_h}{h} \right)^2 &= \frac{B_{Ti}^2}{\Delta T_1^2} + \left(\frac{1}{\Delta T_1} + \frac{1}{\Delta T_2} \right) B_{To}^2 - 2 \left(\frac{1}{\Delta T_1^2} + \frac{1}{\Delta T_1 \Delta T_2} \right) B'_{To}B'_{Ti} + \frac{2}{\Delta T_1 \Delta T_2} B'_{T\infty}B'_{Ti} \\ &\quad - 2 \left(\frac{1}{\Delta T_2^2} + \frac{1}{\Delta T_1 \Delta T_2} \right) B'_{To}B'_{T\infty} + \frac{B_{T\infty}^2}{\Delta T_2^2} + \frac{B_k^2}{k^2} + \frac{B_{\delta}^2}{\delta^2} \end{aligned} \quad (B-6)$$

where B'_{Ti} , B'_{To} and $B'_{T\infty}$ are the portions of B_{Ti} , B_{To} and $B_{T\infty}$, respectively, which arise from an identical error source, so they are assumed to be perfectly correlated. The bias contribution to the uncertainty is reduced to

$$\left(\frac{B_h}{h}\right)^2 = \frac{B_k^2}{k^2} + \frac{B_\delta^2}{\delta^2} \quad (\text{B-7})$$

The total uncertainty of the heat transfer coefficient becomes:

$$\frac{U_h}{h} = \sqrt{\left(\frac{P_h}{h}\right)^2 + \left(\frac{B_h}{h}\right)^2} \quad (\text{B-8})$$

In this study, temperatures were measured 100 times per second and 10-second average values were calculated, so $P_{Ti} = P_{To} = P_{T\infty} = 0.64 \text{ K}$. Additional variables are $\Delta T_1 = 10.25 \text{ K}$, $\Delta T_2 = 42.42 \text{ K}$, $P_\delta = 0.095 \text{ mm}$, $\delta = 2.999 \text{ mm}$ and $B_\delta = 0.005 \text{ mm}$. It was assumed that $P_h/k = 0$ and $B_k/k = 0$. Hence, the uncertainty of the heat transfer coefficient becomes $U_h/h = 7.32\%$.

For the Nusselt number in the experiments, $\overline{Nu} = \overline{hc}/k$, and the total uncertainty can be expressed in the following manner,

$$\begin{aligned} \frac{U_{\overline{Nu}}}{\overline{Nu}} &= \sqrt{\left(\frac{P_{\overline{Nu}}}{\overline{Nu}}\right)^2 + \left(\frac{B_{\overline{Nu}}}{\overline{Nu}}\right)^2} = \sqrt{\left(\frac{U_h}{h}\right)^2 + \left(\frac{B_c}{c}\right)^2 + \left(\frac{B_k}{k}\right)^2} \\ &= \sqrt{0.00732^2 + \left(\frac{0.5}{498.5}\right)^2 + 0.005^2} = 7.34\% \end{aligned} \quad (\text{B-9})$$

where it has been assumed that $B_k/k = 0.5\%$.

The measurement uncertainty of the average freestream velocity is given as follows,

$$\frac{U_u}{u} = \sqrt{\left(\frac{1}{2} \frac{U_{\rho_l}}{\rho_l}\right)^2 + \left(\frac{1}{2} \frac{U_{\rho_{air}}}{\rho_{air}}\right)^2 + \left(\frac{1}{2} \frac{B_{\Delta h}}{\Delta h}\right)^2} = \sqrt{\left(\frac{1}{2} \times 0.005\right)^2 + \left(\frac{1}{2} \times \frac{0.005}{1.371}\right)^2 + \left(\frac{1}{2} \times 0.005\right)^2}$$

(B-10)

which yields an uncertainty of 0.397%. The uncertainties of the tabulated density of air and manometer fluid for the Pitot tube measurements of velocity are $\frac{U_{\rho_l}}{\rho_l} = \frac{U_{\rho_{air}}}{\rho_{air}} = 0.5\%$. The uncertainty of Reynolds number is 0.818% based on the uncertainty of velocity, density of air, viscosity and bias of chord length.

In conclusion, the measurement uncertainty of the measured Nusselt number was 7.34% for heat transfer in Chapter 6.

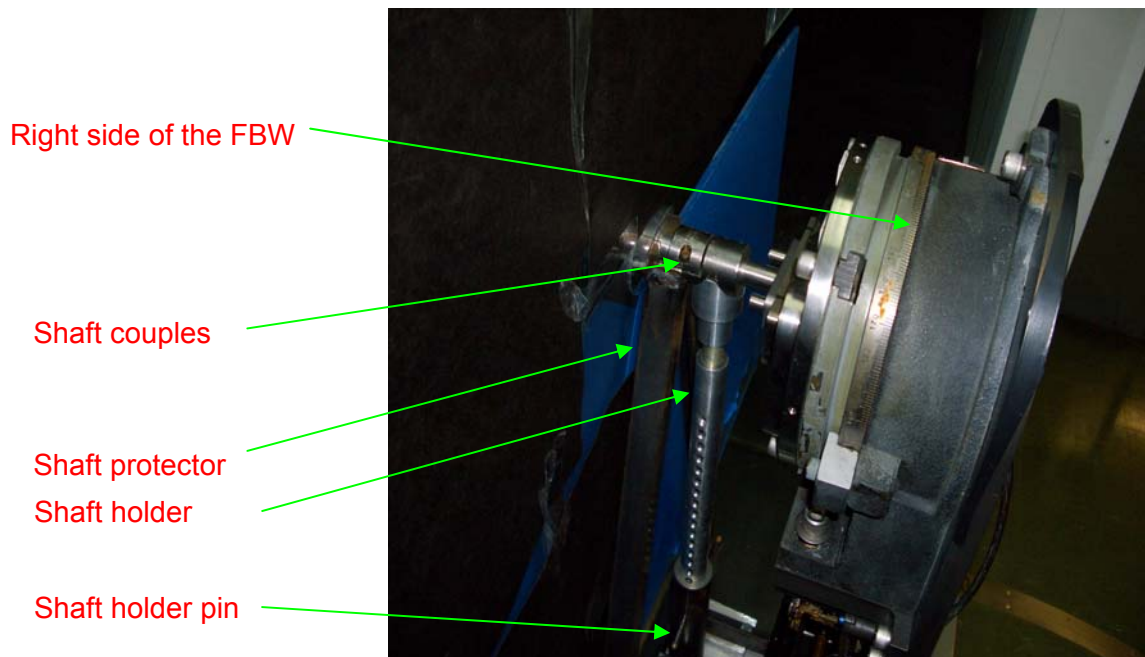
Appendix C – Operation manual for force balance (A)

(Test piece outside of the duct)

The following operational steps were developed to ensure proper functioning of the sensitive instruments inside the ice tunnel.

1. The operation must keep the force balance force safe.
2. Remove the left covers of the walls carefully. Then remove the right covers.
3. Raise the left shaft holder up to the center of the wall.
4. Adjust the screws of the left shaft holder and put the pin into a hole to keep the holder at the same level with the shaft center.
5. Put the shaft couples in carefully, and let the shaft holder softly connect to the shaft couples. If necessary, adjust the screw of the left shaft holder a little. Put the “A” shaft clamp into the “A” side wall (left side).
6. Then do the same with right side of the wall. Put the “B” shaft clamp into the “B” side wall.
7. Remove the top pieces of the shaft couples (A and B) carefully. Don’t let more force work on the walls of the force balance (FBW).
8. Put the shaft of a test piece in the shaft couples with care. One person holds the test piece and another person puts the top piece of the left shaft couples, then screws two pieces of shaft couples together. Don’t screw the top piece of the shaft couples too tight. And then do the same for the right side wall. Make sure the shaft can move and tighten enough to hold the test piece.
9. One person adjusts the angle of the test piece if needed, and another tightens the shaft couples one side by one side, when the angle of attack is correct.

10. Pull out the pin in the left shaft holder carefully. Let the shaft holder down 4 inches away from the test piece. Then put the pin in; don't touch the test piece. After you finish the left side, do the right side. Let the test piece clear and don't touch the test piece anywhere.



11. Put the left side covers in, and make sure the covers don't touch the test piece and shaft.
Screw the side covers tight. Make sure it doesn't move when the test is operating on. Then put the right side covers on and tighten them.
12. Don't touch the test piece or side of the wall during testing.
13. After the test is finished, stop the fan initially.
14. When the wind stops, remove the left and right side covers carefully.
15. Next raise the shaft holder up to touch the shaft clamps on the left side, and adjust the screw. Make sure the holders are attached to the clamp. Then adjust the right side following the same procedure.

16. One person holds the test piece, and the another person loosens the screws of the left shaft clamp carefully. Repeat with the right side. When the tops of the shaft clamps have been removed, hold the test piece and remove it from the force balance.
17. Reinstall the wall covers side by side. Make sure the walls of the force balance are protected by the covers at all times.

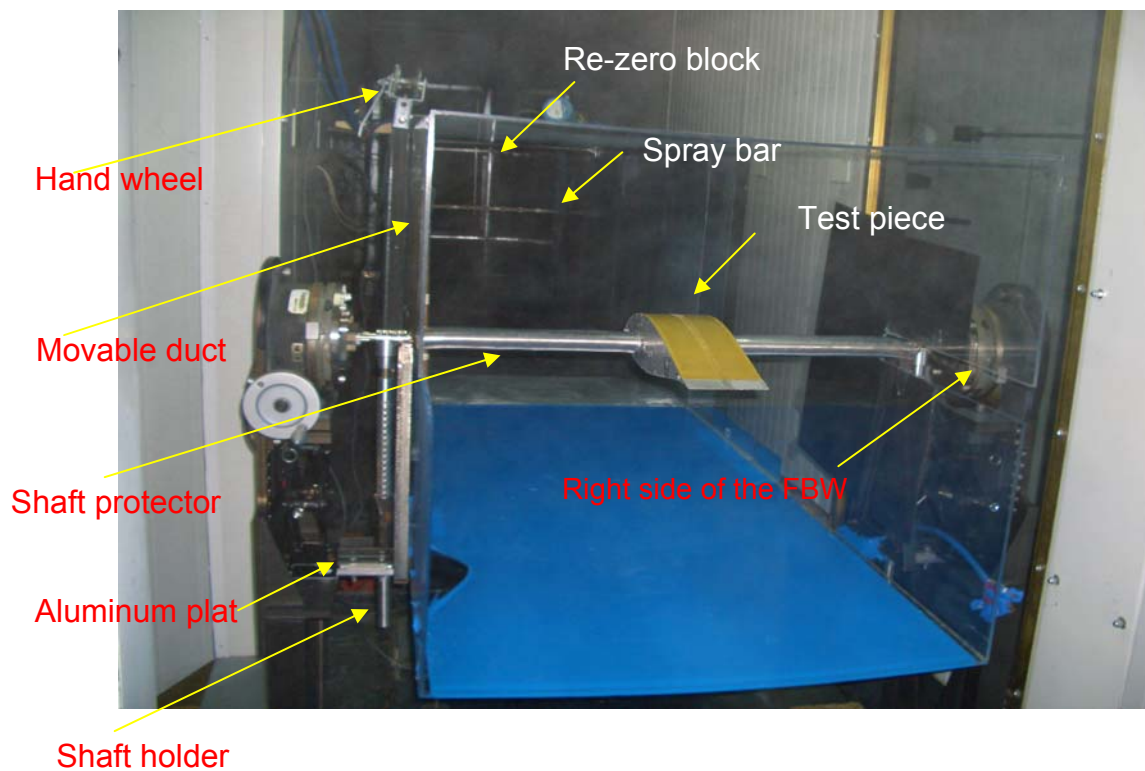
Appendix D – Operation manual for force balance (B)

(Test piece inside of the duct)

The operation must keep the force balance safe and force free. When a test piece is working inside of the duct, attention must be paid to the installation. The following operations must be completely by two people.

1. The operation must keep the force balance safe and force free. When a test piece is working inside of the duct, attention must be paid to the installation. The following operations must be completely by two people.
2. Two people push the force balance near the plexiglass duct. Let the base of the force balance be close to the edge of the glass duct. Be careful, do not touch the side covers.
3. Then put two pieces of wood of ½ inch thickness under both side balance base. Push the force balance close to the inside wall (the glass window side) of the tunnel, while making sure that the shaft is in the centre of the duct. Make sure the test axis of the force balance is at the same level with the slot of the plexiglass duct. Remove the covers of the walls carefully, and then put the shaft couples onto the force walls (see the Test Manual for the Force Balance, when a test piece is working outside of the Duct).
4. Put the lift shaft protectors in, make sure they don't touch the balance wall and haft clamps. If required, adjust the screws in the aluminum plate to make sure the shaft protector doesn't touch the shaft couple.
5. Next adjust the shaft protectors in the right position compared to the shaft couples. Make sure the two pieces of shaft protectors are in the same line. This requires two people for completion.

6. Follow the instructions of the test manual of the force balance when the test piece is working outside of the duct when installing a test piece into the Force Balance.
7. Raise the shaft holders up to the centre of the two walls, one by one.
8. Remove the top pieces of the shaft couples carefully, don't let more force work on the walls of the force balance than necessary.
9. See 7, 8, 9 in the Test Manual of the Force Balance, when the test piece is working outside of the duct to install a test piece.



10. One person pulls one corner as the other person pulls the other corner of the plexiglass duct, out two feet. Make sure the shaft lies in the centre of the slot and don't let the shaft touch the shaft protectors.
11. Install two nuts into the plexiglass duct and make sure it connects to the tunnel extension.
This makes the plexiglass duct solid when the tunnel is working.

12. After the test, stop the fan. Unscrew the nuts of the plexiglass duct. Two people at different sides (left and right) of the duct push the plexiglass duct into the tunnel. Don't touch the force balance and test piece, when pushing on the plexiglass duct.
13. Raise the shaft holders up to touch the shaft couples. Lift the left side first and then the right side. Loosen the screws and remove the test piece with care. This requires two people to complete this job.
14. Remove the shaft protectors carefully. One person loosens the screws in the aluminum plate, while the other person holds the protectors.
15. Finally, install the side covers to protect the side walls of the force balance.